Semiconductor Structures in the Quantum Size Regime

Thesis by

Peter C. Sercel

In Partial Fulfillment of the Requirements

for the Degree of

Doctor of Philosophy

California Institute of Technology

Pasadena, California

1992

(Defended May 6, 1992)

©1992

Peter C. Sercel

All Rights Reserved

To my mother,

Jill Sercel,

and to the memory of my father,

John Sercel, WGFP

Acknowledgments

I have found the process of earning a Ph.D. to be a lot like running a 100 mile race in that it is a long haul, and having a coach and support crew is essential.

Kerry Vahala has been my "coach" in this challenging process. I thank him for the excellent example he set of how to do science – with energy, and excitement. All of the work presented in this thesis bears the mark of his creativity. Harry Atwater was a second advisor to me. The cluster synthesis work in chapters 6 and 7 was largely made possible by his expertise and that of Richard Flagan. Planning the next step of my career has made me realize that the responsibility of supporting students is often not as fun as doing science. I sincerely thank Kerry, Harry, and Rick for their conscientious efforts which have enabled me to do the work I love. I also thank Stanley Bashkin at the University of Arizona for providing me the opportunity as an undergraduate to experience the excitement of research.

If Kerry, Harry and Rick have been my coaches, I have had the benefit of an incredible support crew as well. Winston Saunders continually inspired me with his playful creativity and experimental genius. The exploding wire concept described in chapter 6 is an idea only he could have come up with, and his sense of fun lightened up many a long growth run on the "Harry-Kerry" arsine reactor. My friend John Lebens' quiet technical acuity has been the foundation of much of the experimental effort in our lab, especially the lithography, and I have missed him tremendously since he went to work at Kodak. Hal Zarem introduced me to semiconductor processing skills and was the originator, with Kerry Vahala, of the selective impurity diffusion experiment described in chapter 5. Mike Hoenk built the cathodoluminescence system used in chapter 5. My collaboration and friendship with Hal and Mike has been a bright point in my stay at Caltech.

There have been many other faculty, students, and staff at Caltech that have helped me in the course of my graduate work. I thank Amnon Yariv for encouragement and the use of lab equipment. Thanks are due to Dave Goodwin for the use of his Nd:Yag laser. I thank Mike Newkirk, Charles Tsai, Namkyoo Park, Jay Dawson, Lars Eng, Channing Ahn, Michael Mittelstein, Ali Ghaffari, and especially Carol Garland for their assistance at various stages of this work. I thank them, and Shouleh Nikzhad, Jianhui Zhou, Bihn Zhou, and Steve Sanders for many excellent discussions and a lot of fun. I am indebted to Larry Begay for sharing his design expertise and I thank him for the quality hardware he built for me. Thanks are due to Jeff Sercel and Pat Sercel for help in excimer laser processing experiments conducted at Resonetics, Inc.

The companionship of Mark Sargent, Joel Sercel, and Dale Capewell has enriched many miles up in the Gabes and elsewhere. The hours spent by Mark and Julie Sargent, Joe and Cindi Sercel, John Lebens, and especially Stephanie Leifer in proofreading this manuscript is much appreciated.

Lastly, I give special thanks to my fiance, Stephanie Leifer, for her love and patience. She is a dear friend and kindred soul. Our future together looks bright.

I am grateful to the National Science Foundation and to the A.T.T. Foundation for providing support for my graduate studies.

Abstract

The physics of quantum wires and quantum dots is investigated theoretically. We develop an analytical formalism for determining the energy eigenstates and bandstructure of spherical quantum dots and cylindrical quantum wires. The technique is based upon a reformulation of second order $\vec{K} \cdot \vec{P}$ theory in a basis of eigenstates of total angular momentum. We are led by analysis of quantum wires and dots based upon the InAs-GaSb material system to propose a novel class of self-doping nanostructures for carrier transport experiments and possible future application. The polarization dependence of linear optical absorption and gain spectra in cylindrical quantum wires is calculated. Applicability of the results derived for cylindrical quantum wires to the case of wires with lower symmetry is addressed using symmetry group theory.

Fabrication of quantum wires and dots is attempted by several techniques. A method for fabricating nanometer-scale GaAs wire structures from quantum well material by selective impurity induced disordering is demonstrated. The technique produces lateral bandgap modifications on a 100 nm scale, as verified by cathodoluminescence imaging and spectroscopy. We demonstrate vapor phase synthesis of nanometer-scale III-V semiconductor clusters in the 5 to 20 nm diameter regime. Clusters form by homogeneous nucleation from a non-equilibrium vapor created by the explosive vaporization of a bulk semiconductor filament in an inert atmosphere. The clusters produced have zincblende crystal structure and are faceted. The optical absorption spectra of the clusters are suggestive of quantum confinement effects. A second method of cluster formation utilizes homogeneous nucleation from volatile metal-organic and hydride precursors to produce nanometer-scale, zincblende GaAs clusters.

Contents

1 Introduction 1

1.1 Semiconductor structures in the quantum size regime 1

1.2 Quantum wells 2

1.3 Quantum wires and quantum dots 5

1.4 Outline of the thesis 7

2 Quantum wire and quantum dot bandstructure 16

2.1 Introduction 16

2.2 Conventional techniques for studying quantum confinement effects 18

2.3 The envelope function method in centrosymmetric problems 22

2.4 Bandstructure in a spherical representation 26

2.5 Electronic structure of the spherical quantum dot 35

2.6 Bandstructure in a cylindrical representation 49

2.7 Electronic structure of the cylindrical quantum wire 53

2.8 Conclusions 67

2.9 Appendix: The conventional $\vec{K} \cdot \vec{P}$ Hamiltonian 68

3 Self-doping semiconductor quantum structures 75

3.1 Introduction 75

3.2 InAs-GaSb heterostructures 76

3.2.1 InAs-GaSb quantum dots 78

3.2.2 InAs-GaSb quantum wires 82

3.3 Potential fabrication schemes 82

3.4 Conclusions 84

4 Optical absorption and gain in quantum wires 86

4.1 Introduction 86

4.2 Electronic structure of the cylindrical quantum wire 89

4.2.1 Conduction subbands 89

4.2.2 Valence subbands 90

4.3 Interband optical transitions in cylindrical quantum wires 97

4.3.1 Polarization dependence of the optical matrix element 97

4.3.2 Joint density of states 105

4.4 Optical spectra 107

4.4.1 Absorption spectra 107

4.4.2 Gain spectra 110

4.5 Quantum wires of lower symmetry 114

4.6 Conclusions 120

4.7 Appendix: One-band models of polarization anisotropies 120

5 Nanometer-scale wire structures fabricated by diffusion induced selective

disordering of a GaAs-$Al_xGa_{1-x}As$ quantum well **125**

5.1 Introduction 125

5.2 Disorder of GaAs-$Al_xGa_{1-x}As$ heterostructures by zinc diffusion 127

5.3 Selective disordering of a shallow quantum well to produce 100 nm scale wire structures 128

5.3.1 Electron-beam lithography 130

5.3.2 The diffusion 132

5.3.3 Cathodoluminescence 134

5.3.4 Experimental results 136

5.4 Conclusions 143

6 Nonequilibrium vapor phase synthesis of nanometer-scale III-V semiconductor clusters **147**

6.1 Introduction 147

6.2 Cluster sources 150

6.2.1 The exploding wire cluster source 150

6.2.2 Clusters formed by pulsed laser ablation 156

6.3 Optical characterization of GaAs clusters 163

6.4 Conclusion 166

7 Nanometer-Scale GaAs Clusters from Organometallic Precursors **170**

7.1 Introduction 170

7.2 Reactor design 173

7.2.1 Process configuration 173

7.2.2 Safety issues and reactor construction 174

7.3 Synthesis of nanometer-scale GaAs clusters from organometallic precursors 177

7.4 Passivation experiments 187

7.5 Conclusions 193

List of Figures

1.1 Quantum wells, wires and dots. 3

1.2 The physics of quantum confinement. 6

2.1 Quantum wells, quantum wires and quantum dots. 19

2.2 Model of a cylindrical quantum wire and a spherical quantum dot. 21

2.3 Confinement energy of the conduction band states in a spherical GaAs dot. 38

2.4 Confinement energy of conduction band states in an InAs dot embedded in GaSb. 41

2.5 Confinement energy of bound valence band states in a spherical GaAs quantum dot versus dot radius. 46

2.6 Confinement energy of bound valence band states in a spherical GaAs quantum dot versus dot radius calculated in the one-band model. 48

2.7 Confinement energy at zone-center ($K_z = 0$) for bound valence band states in a cylindrical GaAs quantum wire. 60

2.8 Confinement energy at zone-center ($K_z = 0$) for bound valence band states in a cylindrical GaAs quantum wire. 61

2.9 Valence subband dispersion for a 5 nm radius GaAs quantum wire. 63

2.10 Valence subband dispersion for a 2.5 nm radius GaAs quantum wire. 64

3.1 Confinement energy of the lowest conduction band state in a spherical InAs dot embedded in a GaSb barrier. 81

3.2 Possible scheme for fabricating InAs quantum wires or dots embedded in GaSb using a selective epitaxial growth technique. 83

4.1 Two possible designs for a quantum wire laser. 88

4.2 Valence subband dispersion $E(k_z)$ for a 5 nm radius GaAs quantum wire. . 94

4.3 Valence band DOS for a 5 nm radius GaAs quantum wire. 96

4.4 Polarization dependence of the squared optical transition matrix element for transitions between the lowest electron subband, C(0), and the highest two valence subbands. 100

4.5 Squared overlap integral for transitions between C(0) and valence subbands. 101

4.6 Squared optical matrix elements for the transitions between C(1) and valence subbands with quantum number $F_z = \pm 1/2$. 103

4.7 Squared overlap integral for transitions between C(1) and valence subbands with quantum number $F_z = \pm 3/2$. 104

4.8 Joint density of states for k_z-conserving optical transitions in a 5 nm radius GaAs quantum wire embedded in $Al_{0.3}Ga_{0.7}As$. 106

4.9 Absorption spectra for a 5 nm radius GaAs quantum wire embedded in an $Al_{0.3}Ga_{0.7}As$ barrier. 108

4.10 Absorption spectra for different linewidths. 109

4.11 Relative polarization dependence of the two lowest energy peaks in Figures 4.9 and 4.10. 111

4.12 Calculated gain spectra for a 5 nm radius GaAs quantum wire. 113

4.13 Symmetry of the eigenstates of square, rectangular, and triangular quantum wires. 116

4.14 Effect of weak lateral coupling in a quantum wire array. 119

5.1 Schematic of selective impurity diffusion experiment. 129

5.2 Schematic of electron-beam lithography system. 131

5.3 Scanning electron micrograph of a typical array of silicon-stripe diffusion masks. 133

5.4 Schematic of cathodoluminescence imaging system. 135

5.5 Cathodoluminescence spectra under a large area mask and an unmasked region. 137

5.6 Secondary electron and cathodoluminescence images of several wire arrays and an isolated wire. 139

5.7 Cathodoluminescence spectra from wire arrays taken at 10 keV. 140

5.8 Cathodoluminescence spectra from wire arrays taken at 3 keV. 142

6.1 Schematic diagram of the exploding wire apparatus 151

6.2 A high resolution transmission electron micrograph of GaAs clusters. . . . 154

6.3 Measured interplanar spacings for electron diffraction pattern of GaAs clusters produced by the exploding wire method. 155

6.4 A high resolution transmission electron micrograph of an InAs cluster produced by the exploding wire method. 157

6.5 Bright field transmission electron micrograph of InP clusters produced at two different explosion energies. 158

6.6 Apparatus used for laser ablation experiment. 160

6.7 Bright field transmission electron micrograph of GaAs cluster produced by pulsed laser ablation. 161

6.8 Measured interplanar spacings for electron diffraction pattern of GaAs clusters produced by pulsed laser ablation. 162

6.9 The measured optical extinction of a colloidal suspension of GaAs particles produced by the exploding wire technique. 164

7.1 Conceptual schematic of gas-phase synthesis of passivated nanometer-scale GaAs clusters from organometallic precursors. 172

7.2 Instrumentation diagram of the OMVPE reactor used for GaAs cluster synthesis and passivation. 175

7.3 Simplified schematic of the experimental apparatus for gas-phase synthesis of nanometer-scale GaAs clusters. 178

7.4 Transmission electron micrograph of GaAs clusters from organometallic precursors 180

7.5 Interplanar spacings for GaAs clusters formed from organometallic precursors versus bulk interplanar spacings. 181

7.6 High resolution transmission electron micrograph of GaAs clusters. 182

7.7 Typical size distribution of GaAs clusters produced from organometallic precursors. 184

7.8 Analysis of the size distribution of GaAs clusters produced at various temperatures. 185

7.9 Bright field transmission electron micrograph of Ga droplets produced by pyrolysis of TMG. 188

7.10 GaAs clusters produced by reaction of nanometer-scale Ga droplets with arsine. 189

7.11 Drawing of OMVPE reactor process tube used for passivation experiments. 191

List of Tables

2.1 Explicit representations for basis states of total angular momentum corresponding to quantum numbers F=1/2 and $F_z = 1/2$. 31

2.2 Matrix representation, $\mathbf{H}_{\mathbf{F_Z}}$, of the $\vec{K} \cdot \vec{P}$ Hamiltonian in a cylindrical wave basis. 52

2.3 Effective mass of the highest valence subband in a GaAs quantum wire for several wire radii. 62

2.4 Comparison of valence subband effective mass in quantum wells and quantum wires. 66

2.5 The full 8×8 $\vec{K} \cdot \vec{P}$ Hamiltonian. 71

Chapter 1

Introduction

1.1 Semiconductor structures in the quantum size regime

Progress in semiconductor device fabrication technology in the last two decades has produced a new field of study in condensed matter physics – the physics of materials in the quantum size regime. Quantum structures with physical dimensions smaller than the characteristic length scales of several key physical processes exhibit macroscopic behavior governed by quantum mechanical effects. This "mesoscopic" size scale is distinct from the microscopic world of atoms, molecules, and elementary particles, because mesoscopic systems can be *engineered.* In particular, carrier wavelengths in semiconductors are in the 10 nm range, a range now accessible to semiconductor device fabrication technology. This has enabled physicists and device engineers to bestow physical reality upon a host of model textbook quantum mechanics problems. A partial listing of the classic experiments accessible to semiconductor quantum structures includes the particle-in-a-box "quantum well" problem [1], the phenomena of resonant tunnelling through double barriers [2], the Aharonov-Bohm

effect [3], and the Kronig-Penney "superlattice"[4,5].

These experiments, in addition to exhibiting quantum phenomena in a strikingly direct way, have led to new discoveries (e.g., the fractional quantum Hall effect) and useful devices. One particular device, the quantum well semiconductor laser, is now commercially produced and is revolutionizing the telecommunications and industrial laser industries. This revolution has come about as a result of the new technology of confining electrons and holes in nanometer-thick semiconductor layers.

1.2 Quantum wells

Confinement of carriers to nanometer-thick layers is made possible by the precise layer-by-layer growth control available in molecular beam epitaxy (MBE) and organometallic vapor phase epitaxy (OMVPE). In these techniques, crystals are grown at a rate of roughly an atomic layer per second. Mechanical control of the composition of source materials from which the crystal grows is easily achieved at this time scale so that the composition of the crystal may be tailored to sub-nanometer precision.

For several reasons, the GaAs-$Al_xGa_{1-x}As$ material system is extensively used to fabricate these structures. First, the system is nearly perfectly lattice matched over the entire alloy system; so misfit dislocations do not develop in the growth of *heterojunctions* between GaAs and $Al_xGa_{1-x}As$. Second, because GaAs is a direct bandgap semiconductor, electrons and holes injected into a GaAs structure can recombine and radiate light with high efficiency. The bandgap of $Al_xGa_{1-x}As$ increases with the aluminum mole fraction, x, in the alloy. This enables one-dimensional potential wells to be formed by sandwiching a thin layer of GaAs between slabs of $Al_xGa_{1-x}As$ barrier material, as in Fig. 1.1(a). The GaAs

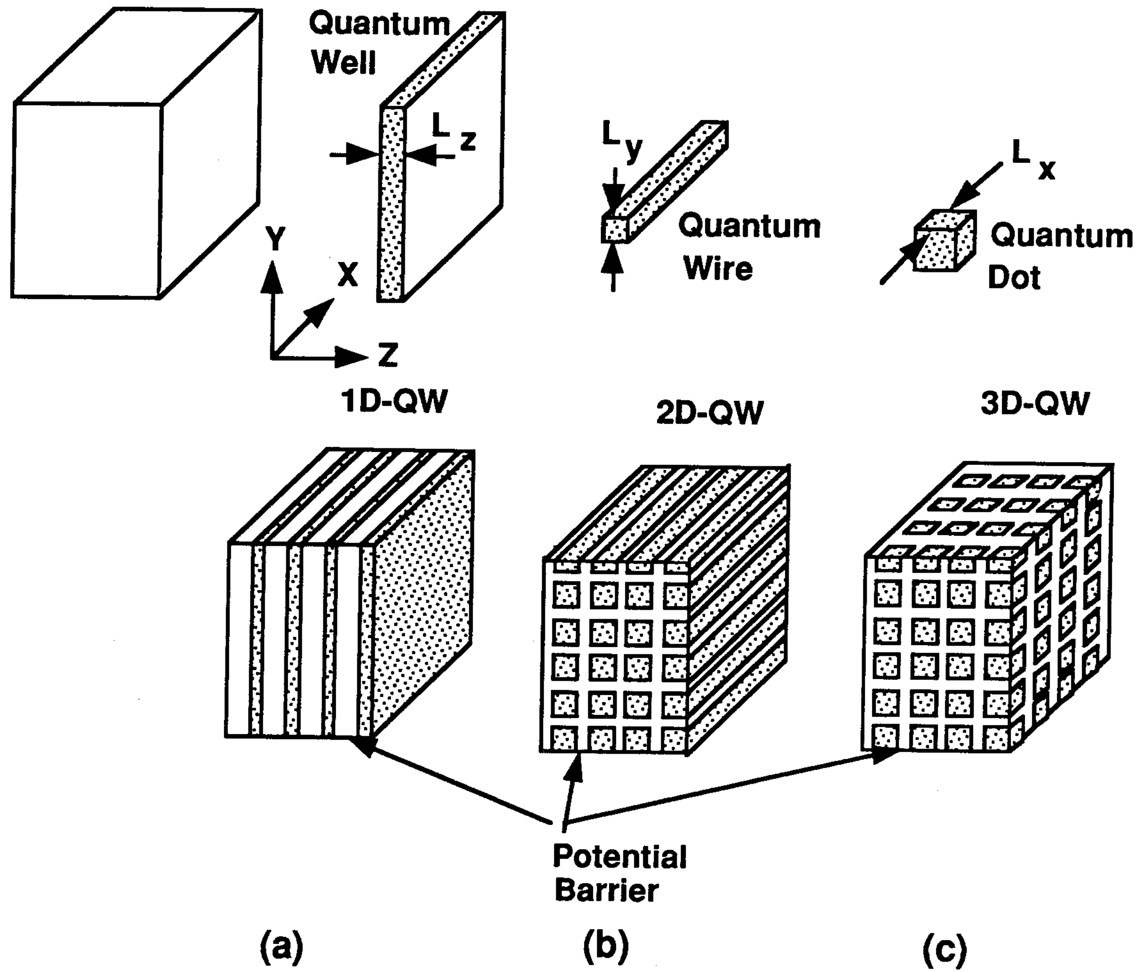

Figure 1.1: Quantum wells, wires and dots. The quantum well, (a), consists of a thin planar slab of low bandgap material, such as GaAs, sandwiched between barrier layers of a higher bandgap material such as $Al_xGa_{1-x}As$. These structures are grown by MBE or OMVPE. Quantum wires and quantum dots, labeled (b) and (c), respectively, are the two- and three-dimensional analogues of the quantum well, in which carriers are confined in the lateral dimensions. The theoretical properties and the experimental effort to fabricate these structures is the subject of this thesis.

wells confine both electrons and holes because at a GaAs-$Al_xGa_{1-x}As$ heterojunction, only 60% of the bandgap difference is offset by the conduction band. This is shown schematically at the top of Figure 1.2. Carriers confined in the GaAs wells occupy discrete energy levels familiar from the particle-in-a-box problem of quantum mechanics. Carrier energies are shifted up from the bulk band edges by a quantity related to the thickness of the well, L_z, the effective mass, m^*, of the carriers, and the particular state, n, occupied in the well. The allowed energies of a carrier in GaAs well relative to the bulk GaAs band edges are given approximately by

$$E = E_n + \frac{\hbar^2}{2m^*}(k_x^2 + k_y^2)^2, \tag{1.1}$$

where

$$E_n = \frac{\hbar^2}{2m^*}(\frac{n\pi}{L_z})^2. \tag{1.2}$$

Here the effective mass, m^*, depends on the carrier type (electron, heavy hole, light hole, etc.). The first term in Eq.(1.1) represents the confinement energy. This is the formula for a particle confined in an infinitely deep square potential well; the effect of finite well depth is easily incorporated. The second term arises from the fact that carriers remain free to move about in the plane of the well, so that the confined electrons and holes behave as two-dimensional particles. In this term, k_x and k_y are the in-plane wavevectors of the carriers. In the quantum well, the bandstructure of the bulk semiconductor is split into a series of *quasi-two-dimensional subbands* each corresponding to a confined state in the well. The energy expressions above accurately describe the electrons in GaAs. For the holes, the expressions apply at zone-center ($k_x = k_y = 0$) but are increasingly inaccurate as the in-plane wavevector increases from zero. This inaccuracy is due to band-coupling effects neglected in this simple model.

The quasi-two-dimensional nature of the carriers has great practical significance because of its effect on the density of states (DOS) and optical properties of a quantum well. The optical properties are affected because absorption and gain are proportional to the DOS. The DOS of a quantum well is step-like, in contrast to the gradual $\sqrt{E}$ dependence of the bulk. This is shown in Figure 1.2. Thus, when carriers are injected into a quantum well, higher values of optical gain occur for a given carrier density than in bulk material. As a result, semiconductor lasers employing quantum well gain media have yielded lower threshold currents [6], higher modulation bandwidths [7] and far higher power levels than possible in bulk material [8].

1.3 Quantum wires and quantum dots

Quantum wires and quantum dots are hypothetical quantum well structures confined laterally in a second or third dimension, respectively. These structures are shown in Figure 1.1. The advances made possible by planar quantum well fabrication technology suggest that if we can create quantum wires and dots, further improvements in semiconductor laser performance is possible. Carriers confined in a quantum wire behave one-dimensionally and, in a one-band model, are thought to have a DOS proportional to $\frac{1}{\sqrt{E}}$. Thus the DOS for the quantum wire is singular at the subband edges. The states in a quantum dot are entirely spatially quantized, so the ideal DOS should be a set of Dirac delta functions. Because of the singularities in the quantum dot and quantum wire DOS, several significant device improvements may ensue if these structures are successfully fabricated and incorporated into semiconductor lasers. Predicted improvements include reduced linewidth, lower threshold current, and higher modulation bandwidth [9]-[11]. Some of these predictions have been

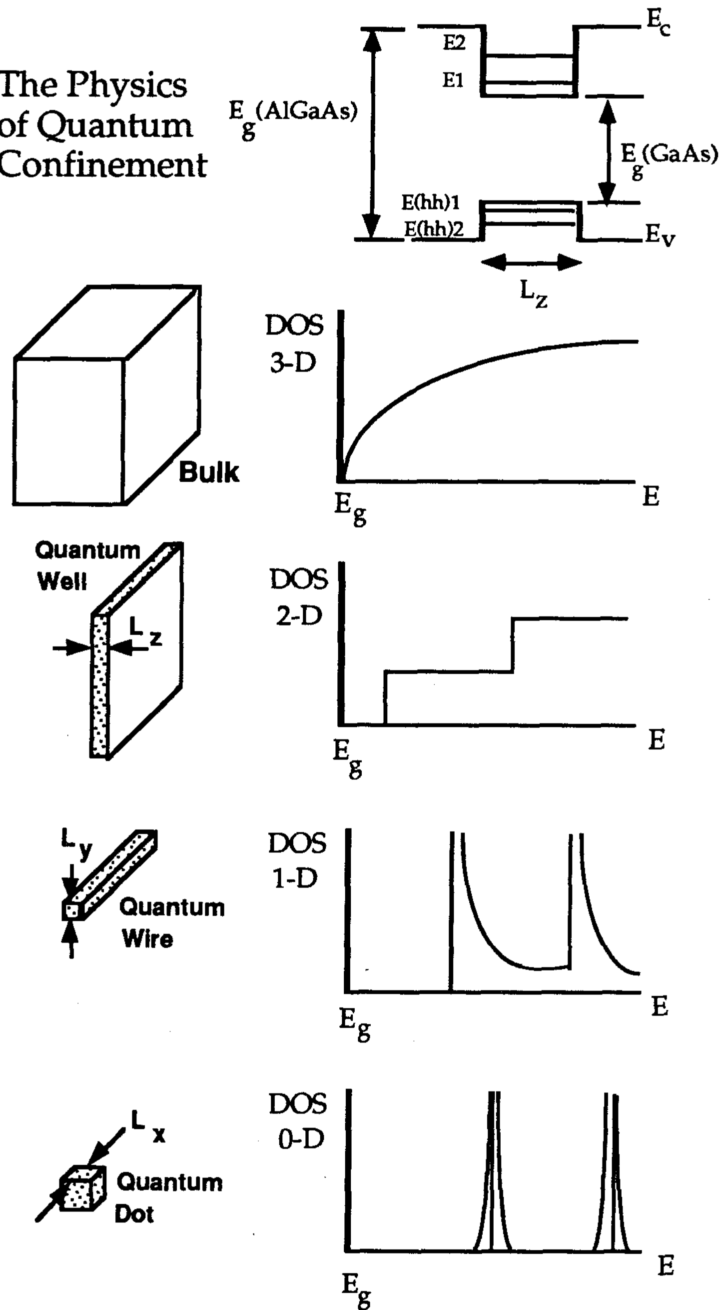

Figure 1.2: The physics of quantum confinement. The DOS of carriers is shown for the bulk and for quantum wells, wires, and dots. The allowed states in a quantum dot are entirely discrete so that its ideal DOS is a set of Dirac delta functions. The quantum dot DOS in the figure is drawn to indicate a slight broadening due to fabricational inhomogeneities.

realized in simulation experiments in which quantum well lasers were subjected to high magnetic fields [12].

1.4 Outline of the thesis

This thesis can be naturally divided into two halves, representing theoretical and experimental efforts to understand the properties of semiconductor quantum wires and quantum dots. Chapters 2 - 4 form a relatively self-contained unit describing the theoretical work. Chapter 2 contains the formulation of an analytical technique for studying the effect of lateral confinement on coupled band systems. Applications of this theory are described in chapters 3 and 4. In chapters 5 - 7, experimental efforts to fabricate and characterize quantum wires and quantum dots by various means are presented.

Chapter 2 presents a new formalism for determining energy eigenstates of spherical quantum dots and cylindrical quantum wires in the multiple band envelope function approximation. The technique is based upon a reformulation of the $\vec{K} \cdot \vec{P}$ theory in a basis of eigenstates of total angular momentum. The bound states are studied for the conduction band and the coupled light and heavy holes as a function of radius for the GaAs-$Al_xGa_{1-x}As$ quantum dot. Quantum wire valence subband dispersion and effective masses are determined for GaAs-$Al_xGa_{1-x}As$ wires of several radii. We find that band-coupling, which is ignored in the one-band analyses such as that employed in Eqs.(1.1- 1.2), is critical to understanding the structure of the valence subbands in quantum wires and dots. This is in distinct contrast to the case of the quantum well, where light- and heavy- hole bands are decoupled at zone-center. The effective masses of the quantum wire valence subbands are determined by inter-subband coupling. These masses are found to be independent of wire

radius in an infinite well model, but strongly dependent on wire radius for a finite well, in which the mass of the highest energy valence subband is as low as 0.16 m_o. I first published the work presented in this chapter in Refs. [13,14].

The techniques developed in chapter 2 for studying quantum confinement in coupled band systems are applied to the InAs-GaSb material system in chapter 3. The unusual type-II, broken gap-band line-up in this system allows charge transfer across the InAs-GaSb interfaces. The analysis, which must account for coupling between the valence and conduction bands, shows that appropriately fabricated nanostructures that contain high free carrier densities are possible without intentional impurity doping. Quantum dots in this system should behave as artificial quasi-atoms, with ionization energy and valence determined by fabricationally determined parameters. Synthetic p-(n-)type semiconductors may therefore be formed from arrays of InAs(GaSb) quantum dots embedded in GaSb(InAs). InAs-GaSb quantum wires are also investigated and predicted to exhibit semimetallic behavior. We have previously published this study in Ref.[15].

In chapter 3, the analysis of polarization dependence of the absorption and gain spectra in cylindrical quantum wires using the results of chapter 2 is reported. This work, which we have presented in Refs.[16] - [17], was the first analysis of the optical properties of quantum wires that included band coupling effects. Contrary to assumptions employed in previous studies, the valence states involved in these transitions are a strong admixture of light and heavy-hole character. Analytical expressions are derived for the polarization dependence of optical matrix elements, and model optical absorption and gain spectra are calculated. Applicability of the results derived for cylindrical quantum wires to the case of wires with lower symmetry is discussed using group theory. It is shown that the optical polarization

anisotropies predicted for cylindrical quantum wires will be qualitatively present in quantum wires of lower symmetry, but that lateral inter-wire coupling in quantum wire arrays will reduce these anisotropies.

In chapter 5 the reader will encounter the first of three chapters describing the experimental work. A logical approach to the synthesis of quantum wires and dots would be to pattern, at a nanometer-scale, prefabricated quantum well material. Structures in the 10 nm size range should be sufficient to observe effects of *lateral* confinement even at room temperature. Unfortunately, existing technologies for creating the necessary lateral confinement are unsatisfactory for a variety of reasons. The pattern generation problem at the nanometer-scale has largely been solved by electron-beam lithography or focussed ion-beam lithography and conventional liftoff procedures. Pattern *transfer*, however, has been more challenging. Anisotropic etch techniques such as reactive ion etching or ion beam assisted etching have been employed to create nanometer-scale mesa structures with embedded quantum wells [18]-[21]. Although the lateral dimensions of the wire and dot structures fabricated in this fashion are in the necessary 10 nm size range, the anisotropic etching step creates a damaged semiconductor surface [22]. Thus, the structures produced have extremely low radiative recombination efficiency. Such structures, although useful for quantum transport experiments in which confinement of only one carrier type is necessary, are useless as quantum sized structures for photonics applications.

An alternate approach to quantum sized structure fabrication is developed in chapter 5. To circumvent the problem of damaged free surfaces, this method utilizes a selectively masked shallow zinc impurity diffusion to locally disorder quantum well material. Strips of less disordered quantum well material are left behind. Cathodoluminescence spectra of

these strips show a systematic blue shift of luminescence as the width of the diffusion mask is reduced in the range from 500 nm to 100 nm. Additionally, we have observed blue shifted luminescence from individual wires demonstrating that the technique can be used to create 100 nm scale lateral bandgap modulation. Unfortunately, considering the size of the wires produced, the observed luminescence peak blue shifts are most likely the result of diffusion of aluminum into the quantum well strips, rather than a quantum size effect. This work has been published in Ref. [23].

A very different approach to the fabrication of quantum dots is adopted in the experiments described in chapters 6 and 7. In these experiments, nanometer-scale III-V quantum dots are fabricated *directly* by homogeneous nucleation from a nonequilibrium vapor phase. Chapter 6 describes two related cluster sources that we have demonstrated. In the first technique, filaments of GaAs or other III-V semiconductors are explosively vaporized in an inert atmosphere, e.g., Ar or He. A non-equilibrium vapor is generated which homogeneously condenses to form stoichiometric, crystalline clusters. Electron micrographs and diffraction measurements show the clusters to be faceted microcrystallites in the 10 nm size range with a zincblende structure. The optical extinction of a colloidal suspension of GaAs clusters differs substantially from that of bulk material in a manner consistent with a quantum confinement effect. We have previously presented these results in Ref. [24]. In the second technique, GaAs clusters are produced by homogeneous nucleation from a nonequilibrium vapor produced by pulsed laser ablation from a GaAs target.

The problem of passivating the surfaces of these clusters to create optically active quantum dots with low surface carrier recombination rates is yet to be solved. The issue of passivation is addressed in more detail in chapter 7. There, a hypothetical experimental

process is described in which an $Al_xGa_{1-x}As$ passivating layer is to be grown on the surfaces of GaAs clusters. A hot-wall OMVPE reactor has been designed and constructed to carry out this experiment and has recently been used successfully to synthesize crystalline GaAs particles. High resolution transmission electron microscopy studies reveal that under atmospheric OMVPE growth conditions using trimethyl-gallium (TMG) and arsine precursors, an aerosol of highly faceted single crystal GaAs particles in the 10 to 20 nm range is formed. The size distribution of the nanometer-scale crystallites can be controlled by variation of reactant concentration and residence time in the reactor. These results have been published in Ref.[25]. Preliminary passivation experiments are then described. However, these experiments have only recently been attempted so that this section should be considered in the spirit of a progress report.

The direction this field will take in the future is uncertain, but it is appropriate to speculate here. For quantum wires and dots to make an impact on the optoelectronic technologies, the problems of fabricationally induced inhomogeneities in these structures will have to be solved. As serial lithographic patterning techniques seem unequal to this task, it seems clear that a technology must be developed that is capable of massively parallel production of quantum structures with self-regulated size. Early efforts to grow quantum wire arrays on vicinal substrates [26] seemed promising, but three years of work have not solved fundamental problems of terrace width nonuniformity. A structure-size feedback mechanism is lacking.

The aerosol techniques described in chapters 6-7 for creating nanometer-scale semiconductor clusters are extremely promising because almost everything that was tried, worked. The aerosol techniques seem to naturally produce quantum size regime clusters with faceted

surfaces. Our early efforts, based upon lithographic patterning, were characterized by a constant struggle to achieve even 100 nm dimensions. One might speculate that a technique may be developed in the future that results in clusters with "magic number" sizes [27]. It is possible that an aerosol or colloidal cluster synthesis process involving an orientationally selective etch will provide the necessary feedback on cluster geometry and size.

A fascinating aspect of nanometer-scale semiconductor physics is that unexpected phenomena occur at these mesoscopic dimensions. An example of such an unexpected phenomenon is the observation of visible photoluminescence both from porous silicon [28] and nanometer-sized silicon clusters produced by gas evaporation methods [29]. The mechanism responsible for these phenomena is still unknown. It seems clear that other surprises await in this emerging field.

References

[1] R. Dingle, W. Wiegmann, and C. H. Henry, *Phys. Rev. Lett.* **33**, 827 (1974).

[2] L.L. Chang, L. Esaki, and R. Tsu, *Appl. Phys. Lett.* **24**, 593 (1974).

[3] S. Datta, M. R. Melloch, S. Bandyopadhyay, and R. Noren, *Phys. Rev. Lett.* **55**, 2344 (1985).

[4] L. Esaki and R. Tsu, *IBM J. Res. Dev.* **14**, 61 (1970).

[5] L. Esaki and L.L. Chang, *Phys Rev. Lett.* **33**, 495 (1974).

[6] P. L. Derry, A. Yariv, K. Y. Lau, N. Bar-Chaim, and J. Rosenberg, *Appl. Phys. Lett.* **50**, 1773 (1987).

[7] K. Uomi, T. Mishima, and N. Chinone, *Appl. Phys. Lett.* **51**, 78 (1987).

[8] Masamachi Sakamoto, David Welch, John G. Endriz, Donald Scifres, and William Streifer, Appl. Phys. Lett., **54**, 2299 (1989).

[9] Yasuhiko Arakawa, Kerry Vahala, and Amnon Yariv, *Appl. Phys. Lett.* **45**, 950 (1984).

[10] Kerry J. Vahala, *IEEE J. Quantum Electron.***24**, 523 (1988).

[11] Hal Zarem, Kerry J. Vahala, and Amnon Yariv, *IEEE J. Quantum Electron.***25**, 705 (1989).

[12] K. Vahala, Y. Arakawa, and A. Yariv, *Appl. Phys. Lett.*, **50**, 365 (1987).

[13] Kerry J. Vahala and Peter C. Sercel, *Phys. Rev. Lett.* **65**, 239 (1990).

[14] Peter C. Sercel and Kerry J. Vahala, *Phys. Rev. B* **42** 3690 (1990).

[15] Peter C. Sercel and Kerry J. Vahala, *Appl. Phys. Lett.* **57**, 1569 (1990).

[16] Peter C. Sercel and Kerry J. Vahala, *Appl. Phys. Lett.* **57**, 545 (1990).

[17] Peter C. Sercel and Kerry J. Vahala, *Phys. Rev. B* **44** 5681 (1991).

[18] M. B. Stern, H. G. Craighead, P.F. Liao, and P. M. Mankiewich, *Appl. Phys. Lett.* **45**, 410 (1984).

[19] M. A. Reed, R. T. Bate, K. Bradshaw, W. M. Duncan, W. R. Frensley, J. W. Lee, and H. D. Shaw, *J. Vac. Sci. Technol. B* **4**, 358 (1985).

[20] K. Kash, A. Scherer, J. M. Worlock, H. G. Craighead, and M. C. Tamargo, *Appl. Phys. Lett.* **49**, 1043 (1986).

[21] R. L. Kubena, R. J. Joyce, J. W. Ward, H. L. Garvin, F. P. Stratton, and R. G. Brault, *J. Vac. Sci. Technol. B* **6**, 353 (1988).

[22] A. Scherer, H. G. Craighead, M. L. Roukes, and J. P. Harbison, *J. Vac. Sci. Technol. B* **6**, 277 (1988).

[23] Hal A. Zarem, Peter C. Sercel, Michael E. Hoenk, John A. Lebens, and Kerry. J. Vahala, *Appl. Phys. Lett.* **54**, 2692 (1989).

[24] Winston A. Saunders, Peter C. Sercel, Harry A. Atwater, Kerry J. Vahala, and Richard C. Flagan, *Appl. Phys. Lett.* **60**, 950 (1992).

[25] Peter C. Sercel, Winston A. Saunders, Kerry J. Vahala, Harry A. Atwater, and Richard C. Flagan, to appear in *Appl. Phys. Lett.*

[26] M. Tsuchiya, J.M. Gaines, R.H. Yan, R.J. Simes, P.O. Holtz, L.A. Coldren, and P.M. Petroff, *Phys. Rev. Lett.* **62**, 466 (1989). *IEEE J. Quantum Electron.***24**, 523 (1988).

[27] Ch.-H. Fischer, H. Weller, L. Katsikas, and A. Henglein, *Langmuir* , **5**, 429 (1989).

[28] L. T. Canham, *Appl. Phys. Lett.* **57**, 1046 (1990).

[29] Peter C. Sercel, Winston A. Saunders, Harry A. Atwater, Kerry J. Vahala, and Richard C. Flagan, unpublished.

Chapter 2

Quantum wire and quantum dot bandstructure

"The more abstract the truth is that you would teach, the more you have to seduce the senses to it" — Nietzche

2.1 Introduction

The rapid progress of experimental efforts to fabricate quantum wires and quantum dots (the two- and three-dimensional analogs of the conventional quantum well in zincblende semiconductors) is a strong impetus to develop theoretical techniques for their study. In this chapter we present a complete account of a new analytical method for this problem, first presented by Sercel and Vahala in Refs. [1,2]. We show how to determine simple expressions for eigenstates and eigenenergies of the spherical quantum dot and the cylindrical quantum wire, rigorously incorporating band coupling effects, through simple dispersion

relations accessible to experimentalists, in contrast to complex numerical procedures previously required.

We begin in Sec. 2.2 with a review of the conventional approaches to the calculation of states in heterostructures, intending to show the shortcomings of existing techniques for studying quantum wires and dots so as to motivate the rest of the discussion. We find in Sec. 2.3 that the analysis of spherical quantum dots and cylindrical quantum wires in the multiband envelope function approximation is simplified due to the high symmetry of these structures and the separable nature of their heterostructure potentials. This simplification is made possible by the observation, originally made in the context of the theory of acceptors, that total angular momentum, defined in section 2.4, commutes with the Hamiltonian in the spherical bandstructure approximation [3,4,5]. We therefore proceed, in Secs. 2.4 and 2.6, to develop the $\vec{K}\cdot\vec{P}$ bandstructure Hamiltonian in representations appropriate to the quantum dot and quantum wire, respectively, based on the eigenstates of this operator. Using the bulk crystal eigenstates that arise in these new repesentations, we construct eigenstates of the spherical quantum dot and cylindrical quantum wire in a piecewise continuous fashion across the heterostructure interface in Secs. 2.5 and 2.7. This leads naturally to exact solutions for the bound states. Representative calculations are performed on the coupled conduction and valence bands in quantum dots and wires to illustrate application of the formalism.

2.2 Conventional techniques for studying quantum confinement effects

Prior to the introduction of our technique, theoretical analyses of conduction and valence band states in quantum wires and dots employed either the simple one band effective mass analysis used initially in this field, or computational approaches based on the standard multiband envelope function theory. The former approach, while of great value in the study of conduction band states, breaks down fundamentally in the study of the valence bands as well as the conduction band in narrow gap semiconductors. Studies which use this technique to calculate optical transition matrix elements and gain [6,7], and exciton states [8]-[10] entirely neglect band-coupling. This effect, which determines the valence subband structure in quantum wells [11], will be shown here to be even more important in quantum dots and quantum wires. In chapter 4, band-coupling will be shown to determine the polarization dependent optical transition matrix elements in quantum wires.

The latter approach, standard multiband envelope function theory, has been applied to the study of confinement in quantum wires in an effort to correct this flaw. However, the calculations that have been performed, while including band-coupling effects, have certain other drawbacks, the foremost of which is mathematical complexity. The problem consists mathematically of a set of coupled, simultaneous, second-order partial differential equations, one for each band included in the analysis, to be solved for envelope functions in conjunction with appropriate boundary conditions. Even the simpler problem of the valence subband dispersion in a quantum well has an analytical solution only in the approximation of an infinite potential barrier [11]. A more realistic model of the quantum well, with finite band

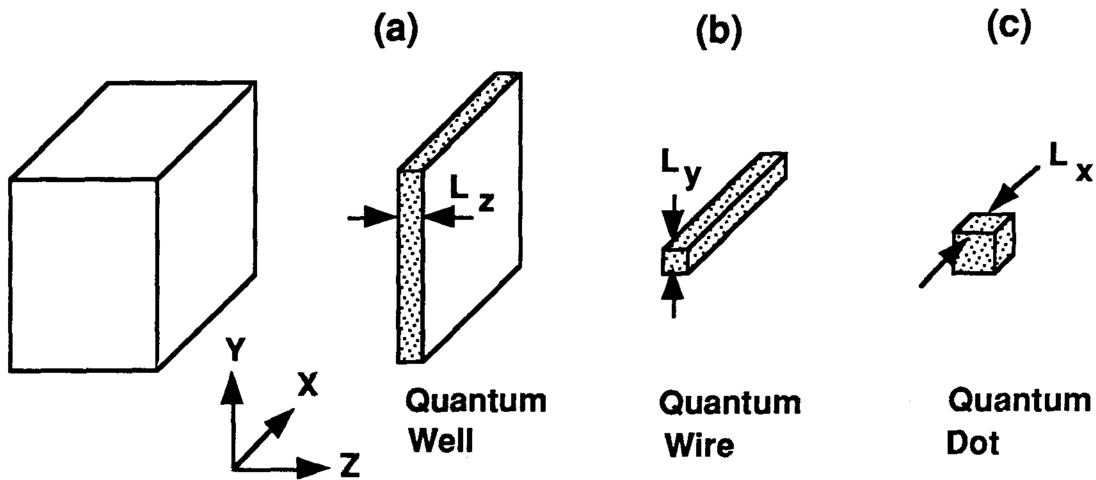

Figure 2.1: Quantum wells, quantum wires and quantum dots. The cube on the left represents bulk semiconductor. The drawings labeled a), b), and c) represent quantum well, quantum wire and quantum dot structures, respectively, with planar boundaries.

discontinuities, requires numerical solution.

The quantum wire and quantum dot problems are more complicated than the quantum well (which is essentially a one-dimensional potential problem), because these structures are multidimensional. This is depicted in Figure 2.1, which shows a geometrical model of the quantum wire and quantum dot employed in much of the work that has been done in this field [12]-[14]. In analogy with the conventional quantum well, there is a well region of low bandgap material with square or rectangular cross-sections imbedded in a higher bandgap barrier region, so that the structures have planar interfaces. However, the finite heterostructure potential is non-separable in this case, a serious complication even in the simple one-band problem. As such, workers studying quantum wires frequently resort to the use of infinite well barriers to simplify the problem mathematically [13] – an approach which

can cause certain interesting physical effects to be overlooked [15,16], while still leaving a complex problem. Other workers have retained finite barriers in their model, employing approximation methods [12], or more computationally intensive approaches [14,17]. While these studies are valuable, the relationship between the physics of the structures and fundamental parameters is therefore somewhat obscured, a quality which reduces usefulness to experimentalists and device engineers.

An alternate approach is to use a model characterized by separable finite potentials, as in the cylindrical quantum wire and the spherical quantum dot depicted in Figure 2.2. These high symmetry geometries greatly simplify the mathematics of the problem to be solved, so that an analytical solution might be expected, while retaining the fundamental features of the problem: namely, two- and three-dimensional quantum confinement, with finite well depths. Furthermore, the cylindrical and spherical configurations are reasonable approximations to actual quantum wire and quantum dot nanostructure geometries which lack the planar interfaces characteristic of the conventional quantum well [18]-[21]. These geometries have therefore been used frequently in one-band calculations [10,15,16]. Additionally, valence band states in quantum wire and dots with these geometries have been studied in the infinite well approximation by an elegant coupled band technique which is specific to the holes [22,23]. In the next section, we will develop a general formalism for incorporating band-coupling effects among the conduction and valence bands in quantum dots and wires, building upon simplifying techniques originally developed for another centrosymmetric problem, that of charged impurities.

Spherical Quantum Dot:

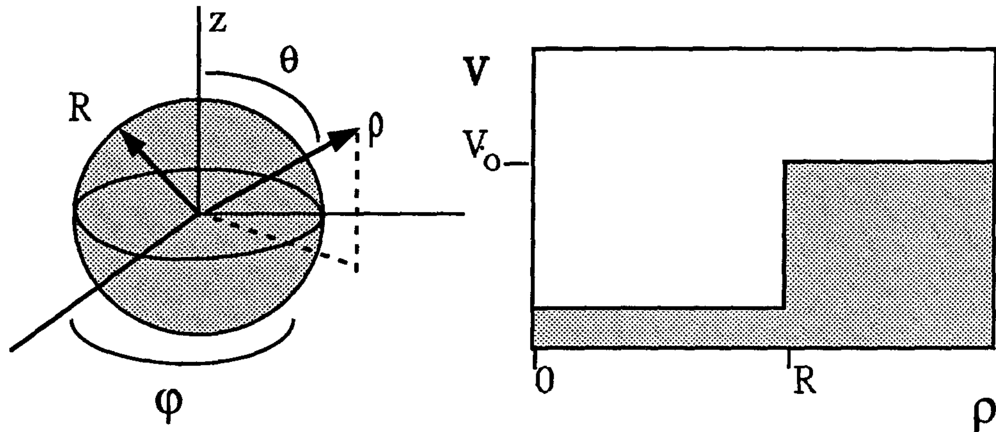

Cylindrical Quantum Wire:

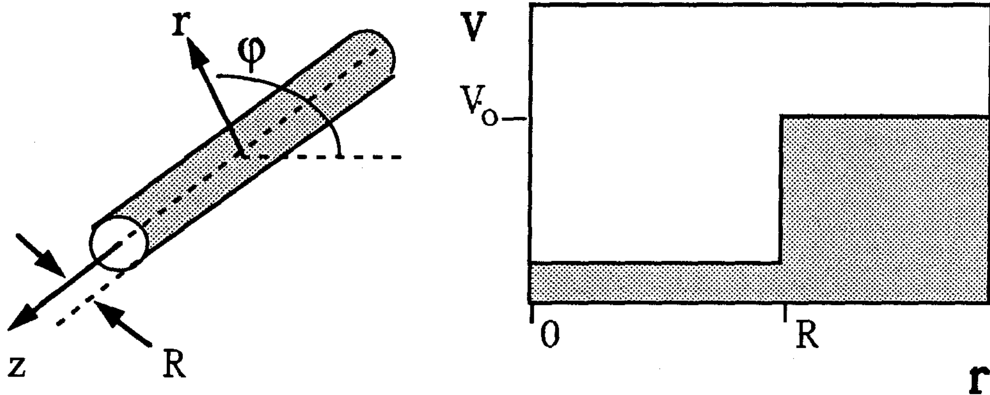

Figure 2.2: A cylindrical quantum wire and a spherical quantum dot. The drawings to the left represent the structures, those to the right represent the confining potential as a function of the radial coordinate in each case. The well depth, V_0 in the figure, represents a discontinuity of the band edges across the heterostructure interface.

2.3 The envelope function method in centrosymmetric problems

The starting point of the envelope function techniques which have been used so effectively in the study of quantum wells and Coulombic impurities is the $\vec{K}\cdot\vec{P}$ theory of bandstructure [24]-[27]. The technique begins with the Bloch form for the energy eigenstates of a periodic potential,

$$\psi^{j}_{\vec{K}} = u^{j}_{\vec{K}}(\vec{r}) \;\; \mathrm{Exp}[i\vec{K}\cdot\vec{r}], \tag{2.1}$$

where $u^{j}_{\vec{K}}(\vec{r})$ has the periodicity of the crystal lattice and j is a band index. At the band edges, these functions are characterized by symmetry arguments as eigenstates $|J, J_z\rangle$ of an angular momentum $\vec{\mathbf{J}}$, which we shall refer to as Bloch angular momentum. These are given for the conduction and valence bands in the Appendix at the end of this chapter. Using these functions as a basis, one can develop a representation $\mathbf{H}(\vec{K})$ for the Hamiltonian governing the conduction and valence bands (such as that given in the Appendix, Table 2.5).

To find heterostructure or impurity states, a potential $V(\vec{r})$ modeling the problem is added to the Hamiltonian. A solution is assumed of the form

$$\psi = \sum_{J,J_z} |J, J_z\rangle \;\; F_{J,J_z}(\vec{r}), \tag{2.2}$$

where F is an envelope function which replaces the plane waves of the perfect periodic crystal, and the sum may include conduction and valence bands. $\vec{K}$ is replaced by $-i\hbar\nabla$ in the Hamiltonian $\mathbf{H}(\vec{K})$, creating a differential operator which acts on the envelope functions.

We are left with an effective envelope Schroedinger equation [11,26,27],

$$\sum_j [H_{ij}(-i\hbar\nabla) + V(\vec{r})] \;\; F_j(\vec{r}) = EF_i(\vec{r}). \tag{2.3}$$

where we use the simplified notation i,j in place of angular momentum quantum numbers, to represent band indices. In conjunction with appropriate boundary conditions this coupled set of equations is solved for the envelope functions.

Extensive work done on the Coulomb impurity problem for degenerate valence bands has established several important results applicable to our problem. The first is that, in most materials of interest (with the notable exception of silicon) it is acceptable, at least as a first order approximation, to replace anisotropic terms in the $\vec{K} \cdot \vec{P}$ Hamiltonian by a suitable spherical average, neglecting "warping" terms of cubic symmetry [4,5]. In such a spherical approximation, the sum of the angular momenta, $\vec{J}$ of the band-edge Bloch functions and $\vec{L}$ of the envelope functions, is a constant of the motion [3,4,5]. We call this conserved operator the total angular momentum, $\vec{F} = \vec{J} + \vec{L}$. Based on this result, Baldereschi and Lipari [4,5] utilized an analogy between $\vec{L}$ and $\vec{J}$ and the L-S coupling scheme used in atomic physics to greatly simplify the acceptor state problem. The role of the atomic orbital wavefunction is assumed by the envelopes. Instead of the electron spin 1/2, the "spin" in the acceptor problem assumes the value J=3/2 which characterizes the underlying band edge Bloch states of the light and heavy holes (the Γ_8 states). The acceptor wavefunctions are then simplified by application of the theory of angular momentum, and computed variationally using Eq.(2.3) without the warping terms. The warping can be added as a small perturbation if desired [5].

Two important features emerge in applying this formalism to a centrosymmetric heterostructure problem. The first is that, whereas the wavefunctions and energy levels of the

acceptor problem must be computed variationally, and then corrected approximately for such effects as the "central cell" overlap of the wavefunction, we can expect exact solutions for a flat band quantum dot or quantum wire heterostructure. Second, the formalism must be generalized if it is to be applicable to problems other than the coupled light and heavy hole bands. In narrow gap semiconductors, for example, coupling between the conduction and valence bands causes appreciable non-parabolicity in the bandstructure [24]. To incorporate such effects it will be necessary to treat the $\vec{K} \cdot \vec{P}$ coupling term between the conduction and valence bands explicitly in developing the envelope Hamiltonian. However, the conduction band is characterized by J=1/2, different from that of the J=3/2 states to which the acceptor problem is restricted, so that in a direct application of the formalism developed for acceptors, the envelope state "spin" evidently has internal variables. In light of this, we have developed a more general analogy. We imagine a two particle system comprised of an "envelope" particle and a "Bloch" particle, with respective angular momenta $\vec{L}$ and $\vec{J}$, and total angular momentum $\vec{F} = \vec{J} + \vec{L}$, as before. Thus the model reduces to the formalism developed for the acceptor problem in the case of the Γ_8 states. However, in contrast to the orbit-spin analogy of Baldereschi and Lipari, we will see that this model incorporates the direct $\vec{K} \cdot \vec{P}$ coupling term between the conduction and valence bands in a natural way, through the kinetic energy of the two-particle couple. Furthermore, the model emerges naturally in the context of the envelope function approximation.

A subtle feature of the theory leading to Eq.(2.3) illustrates the last point. In replacing $\vec{K}$ by the operator $-i\hbar\nabla$ which acts only on the envelope functions F_j, we have implicitly treated the envelopes, F_j, and the underlying Bloch functions, $|J, J_z\rangle$ as functions of spatial coordinates corresponding to different state spaces. Examination of how

wavefunctions developed in the envelope theory are used to calculate observables confirms this interpretation– the envelope and Bloch parts of matrix elements factor into separate integrals. A familiar example is the K-selection rule for band to band optical transitions in bulk semiconductors or quantum wells [28]. This factoring is a result of the separate nature of the envelope and Bloch function state spaces. The Bloch functions $u^{i}_{\vec{K}}$ are defined in a coordinate space "interior" to the unit cell, while the envelope functions F_i are essentially defined over the lattice points, in a coarse-grain approximation valid for describing functions which are slowly varying on the scale of the unit cell of the crystal.

The total wavefunction describing a carrier exists in a composite state space which is a direct sum of the envelope space and the Bloch space. Operators pertaining to the envelope space commute with those belonging to the Bloch space. The two spaces are coupled through the kinetic energy of the carrier they describe. This is given by $\mathbf{T} = |\vec{\mathbf{P}}|^2/2m_o$ where m_o is the free electron mass and $\vec{\mathbf{P}}$ is its momentum, equal to the sum of the momenta of the Bloch and envelope "particles", $\vec{\mathbf{P}} = \vec{\mathbf{P}}_b + \vec{\mathbf{P}}_e$. We note that this seems equivalent to a classical "center of mass" momentum of the two particle couple. However, in contrast to a system of two real particles, there is no relative coordinate in our model, since the envelope and Bloch "particles" pertain to the same physical carrier. Thus, the kinetic energy takes the form

$$\mathbf{T} = |\vec{\mathbf{P}}|^2/2m_o = \frac{|\vec{\mathbf{P}}_b|^2 + |\vec{\mathbf{P}}_e|^2 + 2\vec{\mathbf{P}}_b \cdot \vec{\mathbf{P}}_e}{2m_o}, \tag{2.4}$$

which is invariant with respect to the total angular momentum $\vec{F}$. If we represent this in a basis of the Bloch form, Eq.(2.1), the matrix element of $\vec{\mathbf{P}}_b \cdot \vec{\mathbf{P}}_e$ becomes the $\vec{K} \cdot \vec{P}$ of conventional bandstructure theory, $|\vec{\mathbf{P}}_b|^2$ is incorporated in the band edges E(0), and $|\vec{\mathbf{P}}_e|^2$ enters the free electron kinetic energy term. Thus, the two particle model leads to the full

$\vec{K} \cdot \vec{P}$ Hamiltonian governing valence as well as conduction bands in an intuitive way. As in the (less general) acceptor formalism, the total angular momentum is a constant of the motion in the absence of anisotropic coupling to remote bands.

We can therefore take full advantage of the theory of angular momentum in the centrosymmetric heterostructure problems at hand. For example, a basis of common eigenstates of the Hamiltonian $\mathbf{H}$, the operator $\mathbf{F}^2$ and the projection of total angular momentum along the quantization axis, $\mathbf{F}_z$ will greatly simplify problems with spherical symmetry such as the spherical quantum dot. The common eigenstates of $\mathbf{H}$, $\mathbf{F}_z$ and $\mathbf{P}_z$, the component of envelope linear momentum along the z axis, will similarly aid us in the cylindrical quantum wire problem.

2.4 Bandstructure in a spherical representation

We found in the last section that the set of operators ($\mathbf{H}$,$\mathbf{F}^2$,$\mathbf{F}_z$) form a complete set of commuting observables (CSCO) for the bandstructure Hamiltonian in the absence of anisotropic remote band-coupling. This makes sense intuitively; we expect the Hamiltonian of our two-particle system to be a scalar with respect to the total angular momentum in the absence of anisotropic interactions.

The conceptual model that we have adopted amounts to replacing a finite symmetry group, the space group of the crystal, with the full rotation group. We reiterate that this simplification requires a spherical bandstructure approximation. In the Kane model [24,25], coupling of the valence and conduction bands is isotropic and the effects of remote bands not explicitly included in the analysis are ignored, so that this requirement is automatically satisfied. Many problems, however, necessitate the use of the generalized Hamiltonian given

in the Appendix, which additionally incorporates Luttinger-type coupling terms among the valence bands [27]. These terms represent indirect coupling via remote bands, and generally impart cubic symmetry to the bandstructure. However, many materials are modeled well by setting the Luttinger parameters γ_2 and γ_3 equal, in which case this coupling becomes isotropic [4]. For greater accuracy, band warping terms in $\gamma_2 - \gamma_3$ can be introduced later as a perturbation [5].

In a spherical approximation, the Hamiltonian will be block diagonal in a basis of eigenstates of $\mathbf{F}^2$ and $\mathbf{F}_z$, assuming the form

$$\mathbf{H} = \sum_{\mathbf{F},\mathbf{F_Z}} \mathbf{H}_{\mathbf{F},\mathbf{F_Z}}. \tag{2.5}$$

Using the familiar rules of addition of angular momentum we form such a basis as follows:

$$|\mathrm{K};\mathrm{F},\mathrm{F_z};\mathrm{J},\mathrm{L}\rangle = \sum_{\mathrm{J_z}=-\mathrm{J}}^{\mathrm{J}} \sum_{\mathrm{L_z}=-\mathrm{L}}^{\mathrm{L}} \langle \mathrm{J},\mathrm{J_z};\mathrm{L},\mathrm{L_z}|\mathrm{F},\mathrm{F_z}\rangle \;\; |\mathrm{J},\mathrm{J_z}\rangle \;\; |\mathrm{K};\mathrm{L},\mathrm{L_z}\rangle. \tag{2.6}$$

The first term in the sum is the Clebsch-Gordan coefficient for adding states of angular momenta $\vec{\mathrm{J}}$ and $\vec{\mathrm{L}}$. The states $|\mathrm{J},\mathrm{J_z}\rangle$ as before are the band edge functions of the Bloch state space, explicitly given in the Appendix, and $|\mathrm{K};\mathrm{L},\mathrm{L_z}\rangle$ are envelope functions with angular momentum quantum numbers L and $\mathrm{L_z}$.

We anticipate that the appropriate envelope basis for a flat band region consists of free spherical waves. The envelope kets $|\mathrm{K};\mathrm{L},\mathrm{L_z}\rangle$ therefore have the coordinate representations

$$\langle \rho,\theta,\phi|\mathrm{K},\mathrm{L},\mathrm{L_z}\rangle = \sqrt{\frac{2}{\pi}} \;\; \mathrm{i^L} \;\; \mathrm{h_L}(\mathrm{K}\rho) \;\; \mathrm{Y_L^{L_z}}(\theta,\phi), \tag{2.7}$$

where $\mathrm{h_L}$ is a spherical Hankel function, $\mathrm{Y_L^{L_z}}$ is a spherical harmonic, and K is the radial wavenumber. These envelope functions form a complete set in the envelope state space, obeying the orthonormality relation

$$\langle \mathrm{K},\mathrm{L},\mathrm{L_z}|\mathrm{K}',\mathrm{L}',\mathrm{L_z}'\rangle = \frac{\delta(\mathrm{K}-\mathrm{K}')}{\mathrm{K}^2} \;\; \delta_{\mathrm{L},\mathrm{L}'} \;\; \delta_{\mathrm{L_z},\mathrm{L_z}'}, \tag{2.8}$$

and the envelope space closure relation

$$\mathbf{1}_e = \sum_{L=0}^{\infty} \sum_{L_z=-L}^{L} \int_0^{\infty} K^2 dK \quad |K, L, L_z\rangle\langle K, L, L_z|. \tag{2.9}$$

To obtain the explicit form of the bandstructure Hamiltonian, Eq.(2.5), in the total angular momentum representation $|K; F, F_z; J, L\rangle$, we apply a unitary basis transformation to the Hamiltonian matrix given in the conventional Bloch plane wave basis, $|\vec{K}; J, J_z\rangle = |\vec{K}\rangle|J, J_z\rangle$. We begin by establishing the relationship between the plane wave envelope states $|\vec{K}\rangle$ and the spherical wave envelope states just introduced:

$$|\vec{K}\rangle = \sum_{L,L_z} [Y_L^{L_z}(\Omega_{\vec{K}})]^* \quad |K, L, L_z\rangle. \tag{2.10}$$

In this equation $\Omega_{\vec{K}} = (\theta_{\vec{K}}, \phi_{\vec{K}})$ are the polar coordinates of the vector $\vec{K}$. Projection of this relationship onto the bra $\langle K', L', L'_z|$, using Eq.(2.8), results in the following unitary transformation matrix relating the two envelope bases–

$$\langle K', L', L'_z|\vec{K}\rangle = [Y_{L'}^{L'_z}(\theta_{\vec{K}}, \phi_{\vec{K}})]^* \quad \frac{\delta(K - K')}{K^2}. \tag{2.11}$$

Next, we write the closure relation for the product Bloch plane wave basis:

$$\mathbf{1} = \mathbf{1}_b \otimes \mathbf{1}_e = \{\sum_{J,J_z} |J, J_z\rangle\langle J, J_z| \quad \} \otimes \{ \quad \int K^2 dK \int d\Omega_{\vec{K}} \quad |\vec{K}\rangle\langle\vec{K}| \quad \}, \tag{2.12}$$

where the subscripts e and b denote envelope space and Bloch space respectively. We insert this closure relation into the expression for the components of a state ψ written in the total angular momentum basis:

$$\langle K; F, F_z; J, L|\psi\rangle = \langle K; F, F_z; J, L|$$
$$\{\sum_{J',J'_z} |J', J'_z\rangle\langle J', J'_z| \quad \}\{\int K'^2 dK' \int d\Omega_{\vec{K'}} \quad |\vec{K'}\rangle\langle\vec{K'}| \quad \}|\psi\rangle. \tag{2.13}$$

Using Eqs.(2.6) and (2.11), this results in

$$\langle \mathrm{K},\mathrm{F},\mathrm{F_z};\mathrm{J},\mathrm{L}|\psi\rangle = \sum_{\mathrm{J_z}=-\mathrm{J}}^{\mathrm{J}} \sum_{\mathrm{L_z}=-\mathrm{L}}^{\mathrm{L}} \langle \mathrm{J},\mathrm{J_z};\mathrm{L},(\mathrm{L_z}=\mathrm{F_z}-\mathrm{J_z})|\mathrm{F},\mathrm{F_z}\rangle \int d\Omega_{\vec{K}}\ [\mathrm{Y}_{\mathrm{L}}^{\mathrm{L_z}}(\Omega_{\vec{K}})]^*\ \langle \vec{\mathrm{K}};\mathrm{J},\mathrm{J_z}|\psi\rangle, \tag{2.14}$$

which is the required unitary transformation. We use this to derive an expression giving the matrix elements of the $\vec{K}\cdot\vec{P}$ Hamiltonian in the basis of eigenstates of $\vec{F}$:

$$\langle \mathrm{K},\mathrm{F},\mathrm{F_z};\mathrm{J},\mathrm{L}|\mathrm{H}|\mathrm{K},\mathrm{F}',\mathrm{F}_z';\mathrm{J}',\mathrm{L}'\rangle = \sum_{\mathrm{J_z}=-\mathrm{J}}^{\mathrm{J}} \sum_{\mathrm{J}_z'=-\mathrm{J}'}^{\mathrm{J}'} \langle \mathrm{J},\mathrm{J_z};\mathrm{L},(\mathrm{L_z}=\mathrm{F_z}-\mathrm{J_z})|\mathrm{F},\mathrm{F_z}\rangle\langle \mathrm{J}',\mathrm{J}_z';\mathrm{L}',(\mathrm{L_z}=\mathrm{F}_z'-\mathrm{J}_z')|\mathrm{F}',\mathrm{F}_z'\rangle \int d\Omega_{\vec{K}}\ [\mathrm{Y}_{\mathrm{L}}^{(\mathrm{F_z}-\mathrm{J_z})}(\Omega_{\vec{K}})]^*\ [\mathrm{Y}_{\mathrm{L}'}^{(\mathrm{F}_z'-\mathrm{J}_z')}(\Omega_{\vec{K}})]\ \langle \vec{\mathrm{K}};\mathrm{J},\mathrm{J_z}|\mathrm{H}|\vec{\mathrm{K}};\mathrm{J}',\mathrm{J}_z'\rangle. \tag{2.15}$$

The matrix elements $\langle \vec{K};J,J_z|H|\vec{K};J',J_z'\rangle$ belong to the conventional $\vec{K}\cdot\vec{P}$ Hamiltonian written in the basis of zone center Bloch functions. We used the fact that this matrix does not mix waves of different $\vec{K}$ to eliminate one integration in (2.15). For reference, we give the Hamiltonian in the conventional basis in the Appendix.

Using the transformation equation (2.15), we have derived the explicit representation of the bandstructure Hamiltonian Eq.(2.5) in a spherical wave basis. Since states of different total angular momentum do not couple, it is most useful to present each angular momentum sub-matrix $\mathbf{H_{F,F_z}}$ separately. We begin with the two degenerate sub-spaces corresponding to F=1/2, $F_z = \pm 1/2$. It is simple to show that for the conduction and valence band system, these matrices are each six-dimensional, each sub-space being spanned by the two possible kets from each of the band edges that can be constructed with $F_z = \pm 1/2$. For reference, the explicit form of these basis vectors are shown in Table 2.1. We use the notation $|J,L\rangle$ for our basis with the quantum numbers $F = 1/2$ and $F_z = \pm 1/2$ in $|F,F_z;J,L\rangle$ understood and therefore omitted.

$\mathbf{H}_{1/2,\pm1/2} =$

$$
\begin{array}{c|cccccc}
 & |1/2,1\rangle & |1/2,0\rangle & |3/2,1\rangle & |3/2,2\rangle & |1/2,0\rangle & |1/2,1\rangle \\
\hline
|1/2,1\rangle & E_c + \frac{1}{2}K^2 & 0 & 0 & -i\sqrt{\frac{2}{3}}PK & -i\sqrt{\frac{1}{3}}PK & 0 \\
|1/2,0\rangle & 0 & E_c + \frac{1}{2}K^2 & -i\sqrt{\frac{2}{3}}PK & 0 & 0 & -i\sqrt{\frac{1}{3}}PK \\
|3/2,1\rangle & 0 & i\sqrt{\frac{2}{3}}PK & E_v - (\gamma_1 + 2\gamma_2)\frac{K^2}{2} & 0 & 0 & -2\sqrt{2}\gamma_2\frac{K^2}{2} \\
|3/2,2\rangle & i\sqrt{\frac{2}{3}}PK & 0 & 0 & E_v - (\gamma_1 + 2\gamma_2)\frac{K^2}{2} & -2\sqrt{2}\gamma_2\frac{K^2}{2} & 0 \\
|1/2,0\rangle & i\sqrt{\frac{1}{3}}PK & 0 & 0 & -2\sqrt{2}\gamma_2\frac{K^2}{2} & E_v - \Delta - \gamma_1\frac{K^2}{2} & 0 \\
|1/2,1\rangle & 0 & i\sqrt{\frac{1}{3}}PK & -2\sqrt{2}\gamma_2\frac{K^2}{2} & 0 & 0 & E_v - \Delta - \gamma_1\frac{K^2}{2}
\end{array}
\tag{2.16}
$$

In this expression, $P = -i\langle s|\mathbf{P}_z^b|z\rangle$ is equivalent to the Kane momentum matrix element [24,25]. Atomic units are used throughout this paper. E_c, E_v, $E_v - \Delta$ denote the conduction band edge, heavy-hole and light-hole band edges, and split-off band edges, respectively. The dashed lines delineate regions of the matrix corresponding to the conduction band system (upper left) the upper spin-split-off valence band system (middle) and the lower spin-split-off bands (lower right). The γ parameters in this full matrix are the so-called "modified" Luttinger parameters which are related to the "true" Luttinger coupling parameters by the relations [29]

$$
\begin{aligned}
\gamma_1 &= \gamma_1^{true} - \frac{2P^2}{3(E_c - E_v)} \\
\gamma_2 &= \gamma_2^{true} - \frac{P^2}{3(E_c - E_v)}.
\end{aligned}
\tag{2.17}
$$

In Luttinger's original work [27] the conduction band was treated as remote, hence the above correction is necessary when the conduction band coupling is treated explicitly.

From selection rules for parity, Hamiltonian sub-matrix $\mathbf{H}_{1/2,\pm1/2}$ can be further decomposed to

$$
\mathbf{H}_{1/2,\pm1/2} = \begin{pmatrix} \mathbf{H}^{l=0} & 0 \\ 0 & \mathbf{H}^{l=1} \end{pmatrix},
\tag{2.18}
$$

Basis Vectors For F=1/2, $F_z = +1/2$			
Band	$\|J, L\rangle$	Explicit Representation	Radial Envelope
Conduction	$\|1/2, 0\rangle$	$\|1/2, 1/2\rangle \otimes \|K, 0, 0\rangle$	$f_0(K\rho)$
(Γ_6)	$\|1/2, 1\rangle$	$\sqrt{\frac{1}{3}}\|1/2, 1/2\rangle \otimes \|K, 1, 0\rangle - \sqrt{\frac{2}{3}}\|1/2, -1/2\rangle \otimes \|K, 1, 1\rangle$	$f_1(K\rho)$
Light Holes	$\|3/2, 1\rangle$	$\sqrt{\frac{1}{2}}\|3/2, 3/2\rangle \otimes \|K, 1, -1\rangle - \sqrt{\frac{1}{3}}\|3/2, 1/2\rangle \otimes \|K, 1, 0\rangle$ $+\sqrt{\frac{1}{6}}\|3/2, -1/2\rangle \otimes \|K, 1, 1\rangle$	$f_1(K\rho)$
(Γ_8)	$\|3/2, 2\rangle$	$\sqrt{\frac{1}{10}}\|3/2, 3/2\rangle \otimes \|K, 2, -1\rangle - \sqrt{\frac{1}{5}}\|3/2, 1/2\rangle \otimes \|K, 2, 0\rangle$ $+\sqrt{\frac{3}{10}}\|3/2, -1/2\rangle \otimes \|K, 2, 1\rangle - \sqrt{\frac{2}{5}}\|3/2, -3/2\rangle \otimes \|K, 2, 2\rangle$	$f_2(K\rho)$
Split-Off	$\|1/2, 0\rangle$	$\|1/2, 1/2\rangle \otimes \|K, 0, 0\rangle$	$f_0(K\rho)$
(Γ_7)	$\|1/2, 1\rangle$	$\sqrt{\frac{1}{3}}\|1/2, +1/2\rangle \otimes \|K, 1, 0\rangle - \sqrt{\frac{2}{3}}\|1/2, -1/2\rangle \otimes \|K, 1, 1\rangle$	$f_1(K\rho)$

Table 2.1: Explicit representations for basis states of total angular momentum corresponding to quantum numbers F=1/2 and $F_z = 1/2$. The heavy holes are not contained in the F=1/2 space, as discussed in the text. The $f_l(K\ \rho)$ are spherical Bessel functions or spherical Hankel functions.

where the sub-matrices $\mathbf{H}^{\mathbf{l}=\{\mathbf{0},\mathbf{1}\}}$ take the form

$$\mathbf{H}^{\mathbf{l}=\{\mathbf{0},\mathbf{1}\}} = \begin{array}{c} \\ |1/2,\{0,1\}\rangle \\ |3/2,\{1,2\}\rangle \\ |1/2,\{0,1\}\rangle \end{array} \begin{array}{c} \begin{array}{ccc} |1/2,\{0,1\}\rangle & |3/2,\{1,2\}\rangle & |1/2,\{1,0\}\rangle \end{array} \\ \begin{pmatrix} E_c + \frac{1}{2}K^2 & -i\sqrt{\frac{2}{3}}PK & -i\sqrt{\frac{1}{3}}PK \\ i\sqrt{\frac{2}{3}}PK & E_v - (\gamma_1 + 2\gamma_2)\frac{K^2}{2} & -2\sqrt{2}\gamma_2\frac{K^2}{2} \\ i\sqrt{\frac{1}{3}}PK & -2\sqrt{2}\gamma_2\frac{K^2}{2} & E_v - \Delta - \gamma_1\frac{K^2}{2} \end{pmatrix} \end{array}. \quad (2.19)$$

The envelope angular momentum quantum number is to be read as the first or second number in the braces, $\{i,j\}$. Other than this, the two matrices assume identical forms.

When we diagonalize these matrices, we obtain eigenvalues corresponding to the light holes, split-off holes, and the conduction electrons. This is most easily seen if we make certain simplifications. If we consider the case, equivalent to the Kane model [24,25], in which all the higher band-coupling terms and the free electron energy are neglected, we recover the nonparabolic dispersion relation

$$(\mathrm{E_c} - \mathrm{E})(\mathrm{E_v} - \mathrm{E})(\mathrm{E_v} - \Delta - \mathrm{E}) = (\mathrm{E_v} - \frac{2}{3}\Delta - \mathrm{E})\mathrm{P}^2\mathrm{K}^2, \quad (2.20)$$

which is the well-known result for the split-off, light hole, and conduction bands. If Δ is large, we can describe the coupled electrons and light holes with the two-band dispersion relation

$$(\mathrm{E_c} - \mathrm{E})(\mathrm{E_v} - \mathrm{E}) = \frac{2}{3}\mathrm{P}^2\mathrm{K}^2. \quad (2.21)$$

On the other hand, considering only the Γ_8 states, treating the conduction bands and the split-off bands as remote, we immediately see that the states $|3/2,1\rangle$ and $|3/2,2\rangle$ decouple with eigenvalues $\mathrm{E(K)} = \mathrm{E_v} - (\gamma_1 + 2\gamma_2)\frac{\mathrm{K}^2}{2}$, as we expect for the light holes. Again, the heavy hole states are not found in this sub-space.

These observations lead us to point out that states must be labeled “light hole” or “heavy hole” solely on the basis of the eigenvalue dispersion, E(K), to which the states

correspond, and not on the basis of the quantum number J_z of the Bloch component of the wavefunction, $|J, J_z\rangle$, as some authors prefer. The eigenstates of the conventional Luttinger Hamiltonian for $\vec{K} = K\hat{z}$ correspond to $J_z = \pm 1/2$ for the light holes and $J_z = \pm 3/2$ for the heavy holes [26,27]. However, J_z is generally not a good quantum number and this correspondence does not hold for all directions of the vector $\vec{K}$. In fact, the light hole states $|3/2, 1\rangle$ and $|3/2, 2\rangle$ discussed above are superpositions involving various $|J, J_z\rangle$, as shown in Table 1. (It remains true, however, that a projection of either state onto the space of Bloch eigenstates with $\vec{K} = K\hat{z}$, recovers a superposition of Bloch states characterized by $J_z = \pm 1/2$).

The heavy holes first appear in the four degenerate spaces corresponding to $F = 3/2$, and its four projections $F_z = \pm 1/2$ and $F_z = \pm 3/2$. These are each spanned by eight vectors. As before we find that each of these sets decouple into 2 sub-sets of four vectors, due to parity selection rules. The four degenerate Hamiltonian sub-matrices thus each assume the form

$$\mathbf{H}_{3/2,\pm 1/2 \mathrm{or} \pm 3/2} = \begin{pmatrix} \mathbf{H}^1 & 0 \\ 0 & \mathbf{H}^2 \end{pmatrix}, \qquad (2.22)$$

with the parity sub-matrices given respectively by

$$\mathbf{H}^1 = \begin{array}{c} \\ |1/2,1\rangle \\ |3/2,0\rangle \\ |3/2,2\rangle \\ |1/2,2\rangle \end{array} \begin{array}{c} \begin{array}{cccc} |1/2,1\rangle & |3/2,0\rangle & |3/2,2\rangle & |1/2,2\rangle \end{array} \\ \begin{pmatrix} E_c + \frac{1}{2}K^2 & i\sqrt{\frac{1}{3}}PK & -i\sqrt{\frac{1}{3}}PK & -i\sqrt{\frac{1}{3}}PK \\ -i\sqrt{\frac{1}{3}}PK & E_v - \gamma_1\frac{K^2}{2} & 2\gamma_2\frac{K^2}{2} & 2\gamma_2\frac{K^2}{2} \\ i\sqrt{\frac{1}{3}}PK & 2\gamma_2\frac{K^2}{2} & E_v - \gamma_1\frac{K^2}{2} & -2\gamma_2\frac{K^2}{2} \\ i\sqrt{\frac{1}{3}}PK & 2\gamma_2\frac{K^2}{2} & -2\gamma_2\frac{K^2}{2} & E_v - \Delta - \gamma_1\frac{K^2}{2} \end{pmatrix} \end{array} \qquad (2.23)$$

and

$$
\mathbf{H}^2 = \begin{array}{c} \\ |1/2,2\rangle \\ |3/2,1\rangle \\ |3/2,3\rangle \\ |1/2,1\rangle \end{array}
\begin{array}{c} \begin{array}{cccc} |1/2,2\rangle & |3/2,1\rangle & |3/2,3\rangle & |1/2,1\rangle \end{array} \\
\begin{pmatrix}
E_c + \frac{1}{2}K^2 & i\sqrt{\frac{1}{15}}PK & -i\sqrt{\frac{3}{5}}PK & -i\sqrt{\frac{1}{3}}PK \\
-i\sqrt{\frac{1}{15}}PK & E_v - (\gamma_1 - \frac{8}{5}\gamma_2)\frac{K^2}{2} & \frac{6}{5}\gamma_2\frac{K^2}{2} & \frac{2}{\sqrt{5}}\gamma_2\frac{K^2}{2} \\
i\sqrt{\frac{3}{5}}PK & \frac{6}{5}\gamma_2\frac{K^2}{2} & E_v - (\gamma_1 + \frac{8}{5}\gamma_2)\frac{K^2}{2} & -\frac{6}{\sqrt{5}}\gamma_2\frac{K^2}{2} \\
i\sqrt{\frac{1}{3}}PK & \frac{2}{\sqrt{5}}\gamma_2\frac{K^2}{2} & -\frac{6}{\sqrt{5}}\gamma_2\frac{K^2}{2} & E_v - \Delta - \gamma_1\frac{K^2}{2}
\end{pmatrix} \end{array}, \qquad (2.24)
$$

where the quantum numbers F, F_z have again been omitted in the vectors. Diagonalization of these matrices yields the conduction, light hole, heavy hole, and split-off band eigenvectors for these spaces. It is interesting to examine the form of these matrices after application of a unitary transformation which diagonalizes the inner 2×2 system, which represents the projection of the Hamiltonian onto the Γ_8 band edge. For example, transformation of the inner block in (2.23) using the basis vector definitions: $|LH\rangle = (|3/2,0\rangle - |3/2,2\rangle)/\sqrt{2}$ and $|HH\rangle = (|3/2,0\rangle + |3/2,2\rangle)/\sqrt{2}$, yields

$$
\mathbf{H}^{1'} = \begin{array}{c} \\ |1/2,1\rangle \\ |LH\rangle \\ |HH\rangle \\ |1/2,2\rangle \end{array}
\begin{array}{c} \begin{array}{cccc} |1/2,1\rangle & |LH\rangle & |HH\rangle & |1/2,2\rangle \end{array} \\
\begin{pmatrix}
E_c + \frac{1}{2}K^2 & i\sqrt{\frac{2}{3}}PK & 0 & -i\sqrt{\frac{1}{3}}PK \\
-i\sqrt{\frac{2}{3}}PK & E_v - (\gamma_1 + 2\gamma_2)\frac{K^2}{2} & 0 & 2\sqrt{2}\gamma_2\frac{K^2}{2} \\
0 & 0 & E_v - (\gamma_1 - 2\gamma_2)\frac{K^2}{2} & 0 \\
i\sqrt{\frac{1}{3}}PK & 2\sqrt{2}\gamma_2\frac{K^2}{2} & 0 & E_v - \Delta - \gamma_1\frac{K^2}{2}
\end{pmatrix} \end{array}. \qquad (2.25)
$$

It is clear that the vector $|\mathrm{HH}\rangle$, which is decoupled from all other states, belongs to the heavy hole band. The conduction, light hole and split-off bands are coupled. Interestingly, this is the same matrix that one obtains with the conventional theory, when $\vec{\mathrm{K}}$ is directed along the z axis. In the present case, however, the coupling parameter is the isotropic radial wavenumber K.

As before, it is useful to explore certain simplifying limiting cases. If the spin orbit parameter Δ and the energy gap, $E_c - E_v$, are large compared to the kinetic energies of the light holes, we can treat the split-off and conduction bands as remote. In this case, the

γ's are true Luttinger parameters and we retain only the Γ_8 block of the matrix in (2.25). Then the vector $|LH\rangle$ is rigorously identified as the light hole eigenstate, with the familiar eigenvalue $E(K) = E_v - (\gamma_1 + 2\gamma_2)\frac{K^2}{2}$. On the other hand, in the limit where the terms in K^2 can be neglected, we again retrieve the Kane dispersion relations, Eqs.(2.20- 2.21), plus one more for the heavy holes: $E_{HH} = E_v$. The heavy hole band is entirely flat in this approximation.

Continuing in this fashion, the Hamiltonian could be developed for spaces of higher angular momentum. Having demonstrated that our technique for computing bandstructure in a spherical representation gives the correct bulk crystal dispersion relations within a spherical bandstructure approximation, we now apply the technique to the calculation of states in the spherical quantum dot in the next section.

2.5 Electronic structure of the spherical quantum dot

Since the spherical quantum dot heterostructure is an isotropic potential, F and F_z remain good quantum numbers. Thus the quantum dot may be very simply modeled by considering the bandstructure parameters in our Hamiltonian sub-matrices as functions of the radial coordinate ρ. The states are governed by the Hamiltonian matrices $\mathbf{H}_{F,F_z}$ in each separate total angular momentum subspace. Consequently, the approach is algebraic, and, with only minor exceptions, is identical to that used in standard heterostructure envelope calculations [30].

As a first example, we compute the two lowest energy conduction band states in a GaAs quantum dot of radius R embedded in AlGaAs. We will compare our results against those of the one-band model, which is accurate in this case, as a check of the formalism. In this

simple problem, coupling to remote bands is negligible. We neglect the free electron energy term and coupling to the split-off bands. The lowest states turn out to be contained in the F = 1/2 sub-space. The Hamiltonian in this case becomes a simple two-band, 2 × 2 matrix with bandstructure constants $\mathrm{E_c^I}$, $\mathrm{E_v^I}$ within the structure and $\mathrm{E_c^O}$, $\mathrm{E_v^O}$ exterior to the structure. Eigenvectors of the 2 × 2 Hamiltonian are computed interior and exterior to the quantum dot. We require that the wavefunction be regular at the origin. Boundary conditions are then applied at the interface of the dot to arrive at a relation between spherical wave numbers inside and outside. This condition is combined with the known energy dispersion relations to determine the eigenvalues of the quantum dot. The energy dispersion relations follow from Eq.(2.21) and are given by the expressions

$$\begin{aligned}(\mathrm{E_c^I} - \mathrm{E})(\mathrm{E_v^I} - \mathrm{E}) &= \frac{2}{3}\mathrm{P}^2\mathrm{k}^2 \\ (\mathrm{E_c^O} - \mathrm{E})(\mathrm{E_v^O} - \mathrm{E}) &= -\frac{2}{3}\mathrm{P}^2\lambda^2,\end{aligned} \tag{2.26}$$

where the exterior spherical wavenumber is taken as $i\lambda$ in anticipation of solving for bound energy eigenstates. Eigenvectors resulting from the diagonalization process have the form:

$$|\psi_E\rangle = A \ \ \{|1/2,l\rangle + \sqrt{\frac{E-E_c}{E-E_v}} \ \ |3/2,l+1\rangle \ \} \tag{2.27}$$

where $l = 0, 1$ depending on the parity of the conduction band envelope and where "A" is a constant to be determined by matching boundary conditions and applying normalization. The angular and Bloch space elements of Eq.(2.27) are the same inside and outside the dot, so this vector is projected onto only the envelope space radial coordinate representation. This results in the following two-dimensional column vector:

$$\psi_E(\rho) = A \begin{pmatrix} h_l(k\rho) \\ \sqrt{\frac{E-E_c}{E-E_v}} \ h_{l+1}(k\rho) \end{pmatrix}. \tag{2.28}$$

The form of Eq.(2.26) is such that $\pm k$ ($\pm\lambda$) are degenerate roots. Using these roots and the basic form given by Eq.(2.28), state functions within each region are constructed. The requirement of regularity at the origin leads to combinations of Hankel functions within the quantum dot that are equivalent to spherical Bessel functions of the first kind. Outside the quantum dot, only the Hankel function of imaginary argument which decays for large ρ is retained. Applying continuity of the resulting envelope states at the boundary of the quantum dot leads to the following condition:

$$\frac{j_l(kR)\ h_{l+1}(i\lambda R)}{j_{l+1}(kR)\ h_l(i\lambda R)} = \sqrt{\frac{(E - E_c^I)(E - E_v^O)}{(E - E_v^I)(E - E_c^O)}}. \tag{2.29}$$

Equations (2.26), and (2.29) form a system of three equations in the three unknowns, E, k, and λ. In Figure 3 we present the energy of the conduction state in a quantum dot relative to the bulk crystal conduction band edge, as a function of radius for the two cases of interest (l = 0 and l = 1) in the F = 1/2 subspace. These states are two-fold degenerate. Parameters have been selected so that the band curvature at the zone center yields an effective mass that is equivalent to the conduction band effective mass in GaAs ($m_c^* = 0.067m_o$; E_{gap}(GaAs) = 1.424 eV ; in addition $m_{lh}^* = 0.082m_o \approx m_c^*$ indicating that the two-band model is approximately correct). The band energy constants have been selected to reflect the quantum dot embedded in an $Al_{0.3}Ga_{0.7}As$ barrier ($m_c^* = 0.092m_o$; $E_{gap}(Al_{0.3}Ga_{0.7}As)$ = 1.798 eV, 60/40 conduction/valence energy offset). An important feature of the calculated result is the appearance of a critical quantum dot radius below which no bound states are allowed. This result was previously predicted for quantum dots by solving a simple one band effective mass Hamiltonian in spherical coordinates [15].

As a check of the formalism, the above results are compared in Figure 2.3 with a calculation based on a simple one band effective- mass Hamiltonian. The one band effective-

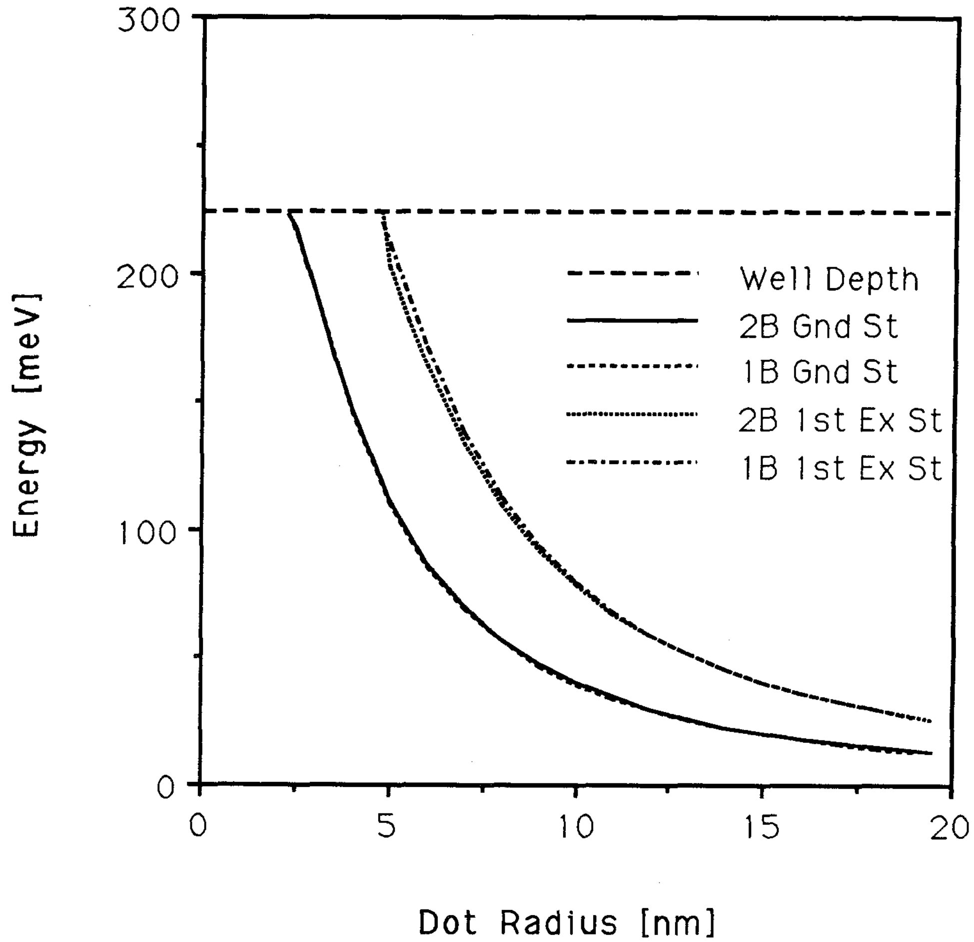

Figure 2.3: Confinement energy of the conduction band states in a spherical GaAs dot embedded in a $Al_{0.3}Ga_{0.7}As$ barrier relative to the bulk GaAs band edge, plotted as a function of dot radius. The ground and first excited states are shown for both the two-band model and the one-band model. The dashed line represents the well depth, equal to 224 meV. The difference between the two curves for the first excited state is due to the neglect of band-coupling in the one band model.

mass Hamiltonian assumes a parabolic bulk dispersion relation and neglects mixing of the zone center conduction band wavefunction with other bands for nonzero wavenumbers. In comparision against the two-band model discussed above, the ground-state energies are in good agreement for all quantum dot radii. Only in the excited state does a slight difference appear, which becomes more pronounced for stronger confinement (i.e., smaller radii). On the whole, however, the two models agree in this case as we expect.

An extreme situation in which the one band model would fail for the conduction band states in a quantum dot is in so-called "type-II", broken gap heterostructures. An InAs dot embedded in GaSb provides an example. In this system, the conduction band edge of bulk InAs is below the Γ_8 valence band edge of GaSb. Thus, coupling between the conduction and valence bands across the heterostructure interface cannot be ignored, so that the assumptions underlying the one-band model break down. To determine the conduction band states in this structure, we employ the two-band formalism that we developed for the GaAs dot. We use the material parameters of Ref. [31] and calculate the position of the lowest conduction band state relative to E_c in InAs as a function of InAs dot radius, in Figure 2.4. For comparison we also plot the results calculated using a one-band model of the conduction band in the same figure. It is clear that the two models disagree significantly in this case, by as much as 100 meV for smaller radii, due to the neglect of band-coupling effects in the one-band calculation. We do not extend the calculation beyond the radius at which the InAs conduction state sinks below the GaSb valence band edge as at this point charge transfer across the surface of the dot may be expected to occur. Quantitative analysis of this interesting effect, which has been observed in InAs-GaSb superlattices [32], must incorporate a self-consistent determination of the band bending as in Ref. [33]. The possibility of using

this effect to create artificial, "self-doping" semiconductor heterostructures is discussed in the next chapter.

We return to the study of type-I systems such as GaAs-AlGaAs, in which the band edges line up closely across the heterostructure, to study the coupled valence band states in a quantum dot. We first consider states characterized by total angular momentum quantum number F=1/2. We neglect the split-off band, retaining only the projection of the Hamiltonian sub-matrix in this space onto the Γ_8 band edge. As discussed in the last section, the Hamiltonian assumes the form:

$$\mathbf{H}^{\Gamma_8}_{1/2,\pm 1/2} = \begin{array}{c} \\ |3/2,1\rangle \\ |3/2,2\rangle \end{array} \begin{array}{c} \begin{array}{cc} \quad |3/2,1\rangle & \qquad\qquad |3/2,2\rangle \end{array} \\ \begin{pmatrix} E_v - (\gamma_1 + 2\gamma_2)\frac{K^2}{2} & 0 \\ 0 & E_v - (\gamma_1 + 2\gamma_2)\frac{K^2}{2} \end{pmatrix} \end{array} . \tag{2.30}$$

The γ's in this matrix are "true" Luttinger parameters. This diagonal matrix contains only light hole eigenvalues since the F=1/2 space contains no heavy hole character. Because of this decoupling, the vectors $|3/2,1\rangle$ and $|3/2,2\rangle$ each form quantum dot bound states with the same energy as that determined in a one band model of the light holes, corresponding respectively to the first and second excited light hole states. It should be noted, however, that the total wavefunctions are very different between the coupled band and one band models. The one-band model of these states predicts a degeneracy of three for l=1 and five for l=2, plus the two-fold spin degeneracy, while the multiple band calculation yields only the two-fold degeneracy in $F_z = \pm 1/2$ for these states. As the radial part of the envelopes happens to be the same in the two models, the energy calculation from this point proceeds in a familiar way so we do not pursue it further.

We expect the uppermost valence states (lowest energy in the hole picture) in the spher-

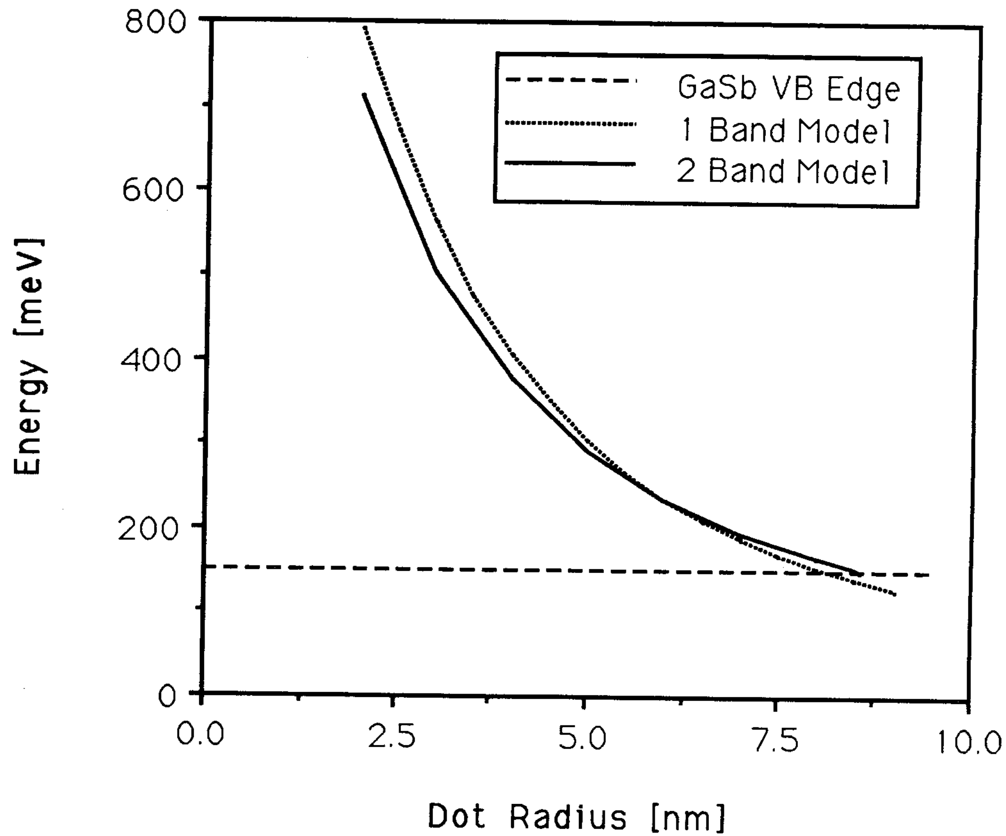

Figure 2.4: Confinement energy of the conduction band states in a spherical InAs dot embedded in a GaSb barrier, plotted as a function of dot radius. The ground state is shown for both the two band model and the one band model. The dashed line is the position of the GaSb valence band edge, 150 meV above the conduction band edge in bulk InAs. The difference between the two curves is far larger than in Figure 2.3 due to the strong band-coupling effects in this type-II structure.

ical quantum dot to have envelopes with a degree of "s" character, which is not contained in the Γ_8 states spanning the F=1/2 space. It is straightforward to show that such states can only appear in the space characterized by total angular momentum F=3/2. We consider the sub-matrix of $\mathbf{H}_{3/2,\pm3/2\text{or}\pm1/2}$, Eq.(2.22), which corresponds to the Γ_8 band edge:

$$\mathbf{H}^{\Gamma_8}_{3/2,\pm3/2\pm1/2} =$$

$$\begin{array}{c} \\ |3/2,0\rangle \\ |3/2,2\rangle \\ |3/2,1\rangle \\ |3/2,3\rangle \end{array} \begin{array}{c} \begin{array}{cccc} |3/2,0\rangle & |3/2,2\rangle & |3/2,1\rangle & |3/2,3\rangle \end{array} \\ \begin{pmatrix} E_v - \gamma_1\frac{K^2}{2} & 2\gamma_2\frac{K^2}{2} & 0 & 0 \\ 2\gamma_2\frac{K^2}{2} & E_v - \gamma_1\frac{K^2}{2} & 0 & 0 \\ 0 & 0 & E_v - (\gamma_1 - \frac{8}{5}\gamma_2)\frac{K^2}{2} & \frac{6}{5}\gamma_2\frac{K^2}{2} \\ 0 & 0 & \frac{6}{5}\gamma_2\frac{K^2}{2} & E_v - (\gamma_1 + \frac{8}{5}\gamma_2)\frac{K^2}{2} \end{pmatrix} \end{array} . \tag{2.31}$$

The matrix is itself block diagonal with the upper left matrix corresponding to even parity states and the lower right, to odd parity states. For each of the four possible values of F_z $(\pm 3/2, \pm 1/2)$ there are therefore four eigenvectors: a heavy hole and a light hole eigenvector of each parity type. The even parity vectors are

$$\begin{aligned} |LH\rangle_{even} &= \sqrt{\frac{1}{2}}\{|3/2,0\rangle - |3/2,2\rangle\} \\ |HH\rangle_{even} &= \sqrt{\frac{1}{2}}\{|3/2,0\rangle + |3/2,2\rangle\} \end{aligned} \tag{2.32}$$

while the odd parity vectors are given by

$$\begin{aligned} |LH\rangle_{odd} &= \frac{1}{\sqrt{10}}\{|3/2,1\rangle - 3|3/2,3\rangle\} \\ |HH\rangle_{odd} &= \frac{1}{\sqrt{10}}\{3|3/2,1\rangle + |3/2,3\rangle\}. \end{aligned} \tag{2.33}$$

As before, we form these states separately for the regions inside and outside the dot. We then project them onto the radial coordinate of the envelope space. We consider the even

parity eigenvectors first. Using Eq.(2.7), and anticipating the requirement of regularity at the origin, we obtain a two-dimensional column vector for the heavy hole eigenvector inside the dot in terms of spherical Bessel functions:

$$\phi_E^{HH}(\rho) = \sqrt{\frac{1}{2}} \begin{pmatrix} j_0[K_{HH}(E)\rho] \\ j_2[K_{HH}(E)\rho] \end{pmatrix} \tag{2.34}$$

and similarly for the light hole eigenvector,

$$\phi_E^{LH}(\rho) = \sqrt{\frac{1}{2}} \begin{pmatrix} j_0[K_{LH}(E)\rho] \\ -j_2[K_{LH}(E)\rho] \end{pmatrix} . \tag{2.35}$$

Here K_{HH} and K_{LH} are the heavy and light hole wavenumbers inside corresponding to the dispersion relations: $E_{HH}(K) = E_v - (\gamma_1 - 2\gamma_2)\frac{K^2}{2}$, and $E_{LH}(K) = E_v - (\gamma_1 + 2\gamma_2)\frac{K^2}{2}$.

If we assume at this point that the confining potential outside the dot is infinite (an infinite valence band discontinuity) the total wavefunction must vanish at the dot surface. Because the radial envelope wavefunctions are in this case two-component vectors, this boundary condition manifests itself as two independent equations. Thus the quantum dot eigenstate generally can not be purely light hole or heavy hole in character. The solution must take the form

$$\psi_E = A\phi_E^{HH}(\rho) + B\phi_E^{LH}(\rho). \tag{2.36}$$

The requirement that ψ vanish at $\rho = R$ leads to the simple dispersion relation

$$j_0[K_{HH}(E)\ R]\ \ j_2[K_{LH}(E)\ R] + j_0[K_{LH}(E)\ R]\ \ j_2[K_{HH}(E)\ R] = 0, \tag{2.37}$$

yielding the valence state eigenenergies E as a function of the dot radius R. Once the energy is known, the constants A and B may be determined, specifying the light and heavy hole amplitudes of the state. It is therefore in general qualitatively incorrect to characterize a quantum dot as having light or heavy hole states: the quantum dot confinement potential

hybridizes these bands. This effect was recently reported for the infinite well quantum dot in Ref.[23]. We will see below that it is also true for the finite well case.

The infinite well dot eigenstates which arise from the odd parity block of Eq.(2.31) are governed by a dispersion relation similar to the one just determined for the even parity states. Proceeding as we did for the even states, we arrive at the dispersion relation

$$9\, j_1[K_{HH}(E)\ R]\ \ j_3[K_{LH}(E)\ R] + j_1[K_{LH}(E)\ R]\ \ j_3[K_{HH}(E)\ R] = 0. \qquad (2.38)$$

For the more realistic case of a dot surrounded by a medium with a finite relative valence band discontinuity, such as GaAs in AlGaAs, these dispersion relations fail. We must construct a non-vanishing wavefunction outside the dot. Light and heavy hole vectors are formed according to Eqs.(2.32- 2.33) outside the dot. Projecting them upon the envelope space radial coordinate as before, we obtain expressions similar to Eqs.(2.34- 2.35) except we use spherical Hankel functions to insure vanishing probability at infinity for the bound states. The wavefunction inside and outside the dot is then written as a linear combination of the HH and LH vectors in each region, yielding a total of four unknown coefficients. Continuity of the wavefunction and probability current are required at the interface at radius $\rho = R$ between well and barrier regions, resulting in four equations. The requirement that a solution to this set of equations exist leads to a four by four determinantal dispersion relation for the allowed eigenenergies. For the even parity states, this is

$$\mathrm{Det}\begin{vmatrix} j_0[K_{HH}(E)\ R] & j_0[K_{LH}(E)\ R] & h_0[i\lambda_{HH}(E)\ R] & h_0[i\lambda_{LH}(E)\ R] \\ j_2[K_{HH}(E)\ R] & -j_2[K_{LH}(E)\ R] & h_2[i\lambda_{HH}(E)\ R] & -h_2[i\lambda_{LH}(E)\ R] \\ j_0'[K_{HH}(E)\ R] & j_0'[K_{LH}(E)\ R] & h_0'[i\lambda_{HH}(E)\ R] & h_0'[i\lambda_{LH}(E)\ R] \\ j_2'[K_{HH}(E)\ R] & -j_2'[K_{LH}(E)\ R] & h_2'[i\lambda_{HH}(E)\ R] & -h_2'[i\lambda_{LH}(E)\ R] \end{vmatrix} = 0. \qquad (2.39)$$

In this expression, "h" is the spherical Hankel function $h^{(1)}$ which decays for imaginary argument, f' denotes derivative of f with respect to ρ, ie $f'(kR) = \frac{df(k\rho)}{d\rho}|_{\rho=R}$. $K_{LH}(E)$ and $K_{HH}(E)$ are defined as before, and $i\lambda_{LH}(E)$ and $i\lambda_{HH}(E)$ are the light and heavy hole wavenumbers outside the dot, taken to be imaginary in anticipation of solving for bound states. A similar dispersion relation follows straightforwardly for the odd parity states:

$$\text{Det}\begin{vmatrix} 3j_1[K_{HH}(E)\,R] & j_1[K_{LH}(E)\,R] & 3h_1[i\lambda_{HH}(E)\,R] & h_1[i\lambda_{LH}(E)\,R] \\ j_3[K_{HH}(E)\,R] & -3j_3[K_{LH}(E)\,R] & h_3[i\lambda_{HH}(E)\,R] & -3h_3[i\lambda_{LH}(E)\,R] \\ 3j_1'[K_{HH}(E)\,R] & j_1'[K_{LH}(E)\,R] & 3h_1'[i\lambda_{HH}(E)\,R] & h_1'[i\lambda_{LH}(E)\,R] \\ j_3'[K_{HH}(E)\,R] & -3j_3'[K_{LH}(E)\,R] & h_3'[i\lambda_{HH}(E)\,R] & -3h_3'[i\lambda_{LH}(E)\,R] \end{vmatrix} = 0. \tag{2.40}$$

We have assumed that the effective masses are the same inside and outside the dot for simplicity. Solution of these dispersion relations gives the allowed energies of the quantum dot with a finite well depth, in the F=3/2 spaces.

The highest states calculated with the finite well quantum dot dispersion relations are plotted in Figure 2.5(a) in the electron picture. The plots reflect a GaAs dot embedded in $Al_{0.3}Ga_{0.7}As$ with a 40 % valence band offset, so the "well depth" is 150 meV. We have assumed $m^*_{lh} = 0.082m_o$ and $m^*_{hh} = 0.45m_o$. The figure displays the energies of even and odd parity states found with Eqs.(2.39, 2.40) respectively, relative to E_v in bulk GaAs. The state with lowest confinement energy (highest curve in the figure) is of even parity as we expected, while the next is an odd parity solution. As in the conduction band calculation, there is a critical radius below which no bound states exist. We point out that each state displayed is four-fold degenerate due to the four-fold degeneracy of F=3/2. In Figure 2.5(b) we compare the energies of the highest even and odd-parity states determined using

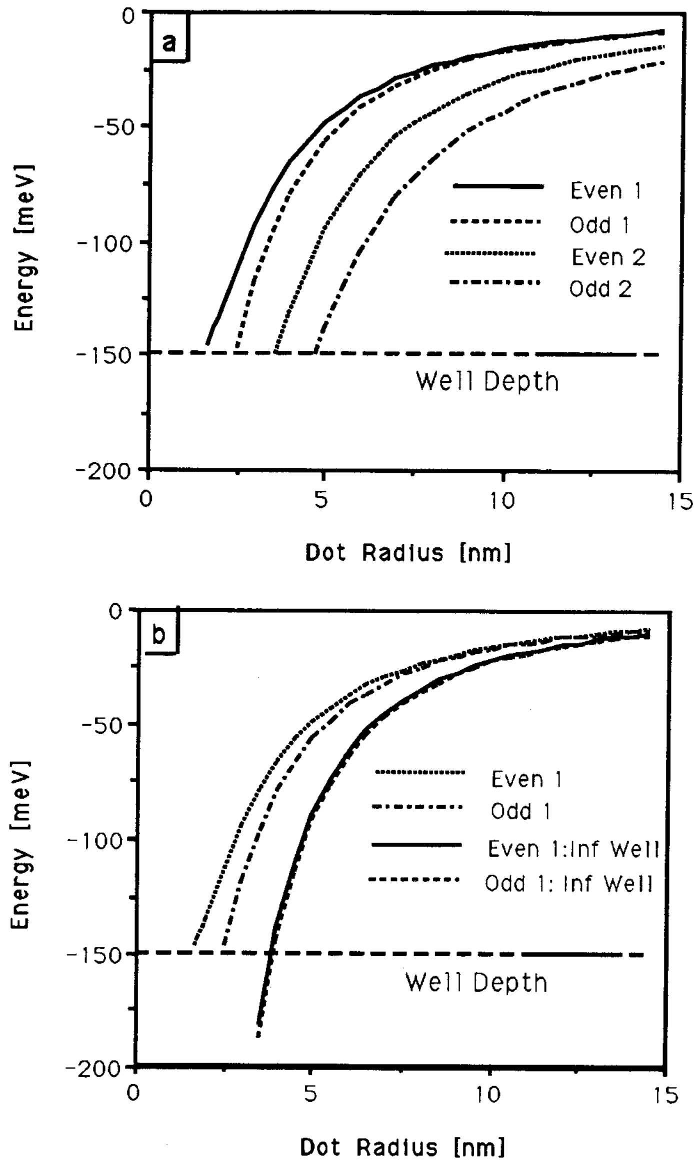

Figure 2.5: Confinement energy of bound valence band states in a spherical GaAs quantum dot plotted versus dot radius, relative to E_v in bulk GaAs. The dot is embedded in an $Al_{0.3}Ga_{0.7}As$ barrier, reflected in a well depth of 150 meV. (a): Coupled band model of the light and heavy holes. The states belong to the F=3/2 space and are labeled according to parity (even/odd) and order in energy (1,2,..). (b): Finite vs. infinite well models for the highest even and odd parity states.

the infinite well dispersion relations, Eqs. (2.37- 2.38), with the results of the finite well calculation. The infinite well causes an overestimation of the confinement energy for both states. Note that in the finite well, the energy separation between the even and odd states is enhanced relative to the infinite well calculation because the odd parity state has higher probability to be in the barrier region than the even state. Thus the infinite well model yields energies for these states that are inaccurate both qualitatively as well as quantitatively.

The results of a one band calculation for the heavy and light hole states in a GaAs quantum dot surrounded by $Al_{0.3}Ga_{0.7}As$, using the same material parameters as in our multiple band calculation, are shown in Figure 2.6 for comparison to the coupled band model used in Figure 2.5. Note the level crossings which occur in the one-band model do not occur when band-coupling effects are included. Furthermore, the highest state in our multiple band calculation is significantly lower than the highest heavy hole state in the one-band model. This is due to the fact that the dot eigenstates are an admixture of light and heavy hole character. Any admixture of lower mass light hole character into the heavy hole ground state would naturally tend to increase the confinement energy, pushing it downwards on the energy scale of Figure 2.6.

This admixture has a significant impact on the electrical properties and optical spectra of these structures, and hence must be taken into account if applications involving quantum dots, such as to semiconductor lasers, are to be accurately studied. Information about the optical properties of the quantum dot may be straightforwardly obtained by using the dot eigenstates, such as Eq.(2.36) for the valence bands, to calculate matrix elements for optical transitions between conduction and valence band states. A calculation of the optical matrix element between the lowest conduction and highest valence band states shows

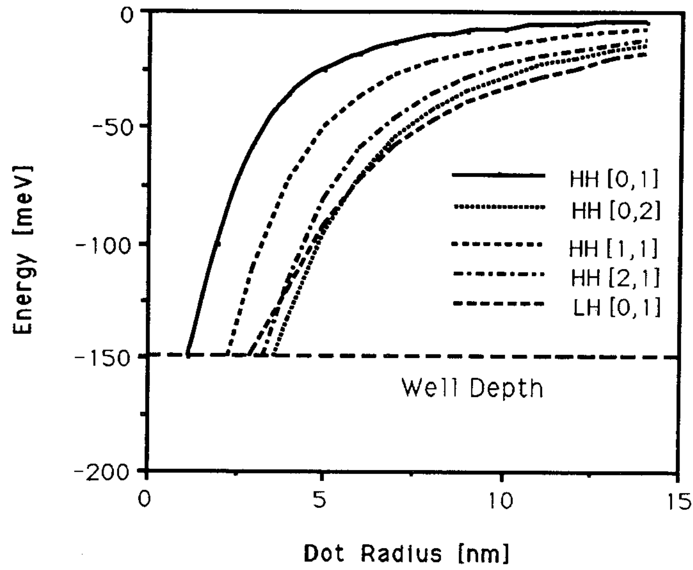

Figure 2.6: Confinement energy of bound valence band states in a spherical GaAs quantum dot plotted versus dot radius, calculated in the one-band model. Energy is plotted relative to E_v in bulk GaAs. The dot is embedded in an $Al_{0.3}Ga_{0.7}As$ barrier, reflected in a well depth of 150 meV. Effective masses are the same as in the previous figure. The states are identified by the band (HH or LH),and [L − z,n], where L − z is the envelope angular momentum and n is the order in energy. Note the level crossings, which do not occur in the coupled band model.

that this transition in the quantum dot is optically isotropic, as we expect in a spherical bandstructure approximation [1]. This result could not be obtained in a one-band model. We mention that all of the calculations presented here were performed either analytically, or where necessary, on a desk top personal computer, implying that incorporation of band-coupling effects into device analyses is simple and therefore warranted. We next turn our attention to the quantum wire.

2.6 Bandstructure in a cylindrical representation

Our success in solving the multiple band quantum dot problem arose from the compatibility of the total angular momentum $\vec{F}$ with the bandstructure Hamiltonian in the spherical approximation. A similar simplification applies in the case of the quantum wire. In contrast to the spherical case, where we used the complete set of commuting observables including $\mathbf{H}$, $\mathbf{F}^2$, and $\mathbf{F}_z$, we now a use a basis of eigenstates shared by $\mathbf{H}$, $\mathbf{F}_z$ and $\mathbf{P}_z$, the component of envelope linear momentum along the z axis. This basis has the desired symmetry for studying the cylindrical quantum wire. F_z is a good quantum number so the Hamiltonian in this basis is again block diagonal:

$$\mathbf{H} = \sum_{\mathbf{F_z}} \mathbf{H}_{\mathbf{F_z}}. \tag{2.41}$$

In contrast to the approach in section IV for the spherically symmetric problem, it is most convenient to work in an "uncoupled" angular momentum representation. We use the fact that $\mathbf{F}_z = \mathbf{J}_z + \mathbf{L}_z$ to construct a basis in the product form

$$|K_z, k, F_z; J, J_z\rangle = |J, J_z\rangle |K_z; k, L_z = F_z - J_z\rangle. \tag{2.42}$$

The envelope vector $|K_z; k, L_z\rangle$, described below, is an eigenstate of $\mathbf{L}_z$, the projection

of envelope angular momentum along the z axis with quantum number L_z. The zone-center Bloch function $|J, J_z\rangle$, as before, has Bloch angular momentum quantum numbers J,J_z. The envelope vectors are simultaneously eigenstates of $\mathbf{P}_z$, the z-component of the envelope momentum operator, with eigenvalue $\hbar K_z$. The envelope states therefore have the cylindrical coordinate representation

$$\langle r, \theta, z | K_z; k, L_z \rangle = \frac{i^{L_z}}{2\pi} \, H_{L_z}(kr) \, e^{iL_z\theta} \, e^{iK_z z}, \tag{2.43}$$

where k is a radial wavenumber and H is a Hankel function. It is clear that the resulting basis has the necessary cylindrical symmetry. It is also an orthonormal basis:

$$\langle K_z', k', F_z'; J', J_z' | K_z, k, F_z; J, J_z \rangle = \delta_{F_z', F_z} \, \delta_{J', J} \, \delta_{J_z', J_z} \, \frac{\delta(k' - k)}{k} \, \delta(k_z' - k_z). \tag{2.44}$$

The process of expressing the bandstructure Hamiltonian in this basis involves a unitary transformation similar to that carried out in the spherical case. It is simple to show that the transformation from the conventional Bloch plane wave basis into the new cylindrical wave basis is

$$\langle K_z, k, F_z; J, J_z | \psi \rangle = \int d\theta_{\vec{K}'} \;\; e^{-i(F_z - J_z)\theta_{\vec{K}'}} \, \langle \vec{K}'; J, J_z | \psi \rangle. \tag{2.45}$$

In this equation, $\langle \vec{K}'; J, J_z | \psi \rangle$ are the components of a wavefunction ψ written in the conventional basis of Bloch plane waves. $\theta_{\vec{K}'}$ is the angular coordinate of the vector $\vec{K}'$ expressed in cylindrical coordinates. Using this unitary transformation we find the matrix elements of the bandstructure Hamiltonian in the new basis in terms of the conventional matrix elements (found in the Appendix):

$$\langle K_z, k, F_z'; J', J_z' | H | K_z, k, F_z; J, J_z \rangle = \frac{1}{2\pi} \int_0^{2\pi} d\theta_{\vec{K}} \;\; e^{i[(F_z - F_z') - (J_z - J_z')]\theta_K} \, \langle \vec{K}; J', J_z' | H | \vec{K}; J, J_z \rangle. \tag{2.46}$$

Employing this transformation equation, we find that each Hamiltonian sub-matrix $\mathbf{H}_{\mathrm{F_z}}$ (see (2.41)) assumes the identical 8×8 form given in Table 2.2. This is the full Hamiltonian governing conduction, light and heavy holes, and the split-off bands. In the table, the basis vectors are written as products of a zone-center Bloch function, $|\mathrm{J}, \mathrm{J_z}\rangle$ and an envelope state, $|\mathrm{F_z} - \mathrm{J_z}\rangle$ so that $L_z = F_z - J_z$. This form ensures that all the basis vectors correspond to the same quantum number $\mathrm{F_z}$. In the envelope vector, k and $\mathrm{K_z}$ are understood and therefore omitted. P is the Kane matrix element. The other terms are given by

$$
\begin{aligned}
-\frac{T}{2} &= (\gamma_1 + \gamma_2)\frac{k^2}{2} + (\gamma_1 - 2\gamma_2)\frac{K_z^2}{2} \\
-(\frac{T}{6} + \frac{2Q}{3}) &= (\gamma_1 - \gamma_2)\frac{k^2}{2} + (\gamma_1 + 2\gamma_2)\frac{K_z^2}{2} \\
-L &= -i2\sqrt{3}\gamma_3\frac{kK_z}{2} \qquad (Axial Approximation) \\
-L &= -i2\sqrt{3}\gamma_2\frac{kK_z}{2} \qquad (Spherical Approximation) \\
-M &= \sqrt{3}\gamma_2\frac{k^2}{2}.
\end{aligned} \tag{2.47}
$$

These sub-matrices are quite similar in structure to the conventional Cartesian coordinate Hamiltonian (see the Appendix), but $\mathrm{K_x}$ and $\mathrm{K_y}$ are everywhere replaced by the radial wavenumber, k. Either the spherical or the axial approximation may be employed as indicated in the expression for the term L. In the more accurate axial approximation, we equate γ_2 and γ_3 only in the term M, so that warping effects are neglected only in the $(\mathrm{K_x}, \mathrm{K_y})$ plane. Thus the energy bands remain cylindrically symmetric about the quantization axis and $\mathrm{F_z}$ remains conserved. The axial approximation is therefore naturally incorporated into the present formalism, in contrast to coordinate free methods which have been previously applied to the cylindrical quantum wire [22]. It is easily shown that the bandstructure relations which result from diagonalizing these sub-matrices agree with those obtained via the

$$
\begin{array}{cccccccc}
|1/2,1/2,(0)\rangle & |1/2,-1/2,(0)\rangle & |3/2,3/2\rangle & |3/2,1/2\rangle & |3/2,-1/2\rangle & |3/2,-3/2\rangle & |1/2,1/2,(1)\rangle & |1/2,-1/2,(1)\rangle \\
\otimes|F_z-1/2\rangle & \otimes|F_z+1/2\rangle & \otimes|F_z-3/2\rangle & \otimes|F_z-1/2\rangle & \otimes|F_z+1/2\rangle & \otimes|F_z+3/2\rangle & \otimes|F_z-1/2\rangle & \otimes|F_z+1/2\rangle
\end{array}
$$

$$
\begin{pmatrix}
E_c+\frac{1}{2}(k^2+K_z^2) & 0 & \frac{-iPk}{\sqrt{2}} & i\sqrt{\frac{2}{3}}PK_z & i\frac{Pk}{\sqrt{6}} & 0 & -i\sqrt{\frac{1}{3}}PK_z & -i\sqrt{\frac{1}{3}}Pk \\
0 & E_c+\frac{1}{2}(k^2+K_z^2) & 0 & -i\frac{Pk}{\sqrt{6}} & i\sqrt{\frac{2}{3}}PK_z & \frac{iPk}{\sqrt{2}} & -i\sqrt{\frac{1}{3}}Pk & i\sqrt{\frac{1}{3}}PK_z \\
\frac{iPk}{\sqrt{2}} & 0 & E_v+\frac{T}{2} & -iL & -M & 0 & \frac{iL}{\sqrt{2}} & \sqrt{2}M \\
-i\sqrt{\frac{2}{3}}PK_z & i\frac{Pk}{\sqrt{6}} & iL^* & E_v+\frac{T}{6}+\frac{2Q}{3} & 0 & -M & \frac{T-2Q}{3\sqrt{2}} & -i\sqrt{\frac{3}{2}}L \\
-i\frac{Pk}{\sqrt{6}} & -i\sqrt{\frac{2}{3}}PK_z & -M^* & 0 & E_v+\frac{T}{6}+\frac{2Q}{3} & iL & i\sqrt{\frac{3}{2}}L^* & -\frac{T-2Q}{3\sqrt{2}} \\
0 & \frac{-iPk}{\sqrt{2}} & 0 & -M^* & -iL^* & E_v+\frac{T}{2} & -\sqrt{2}M^* & \frac{-iL^*}{\sqrt{2}} \\
i\sqrt{\frac{1}{3}}PK_z & i\sqrt{\frac{1}{3}}Pk & \frac{-iL^*}{\sqrt{2}} & \frac{T-2Q}{3\sqrt{2}} & -i\sqrt{\frac{3}{2}}L & -\sqrt{2}M & E_v-\Delta+\frac{T+Q}{3} & 0 \\
i\sqrt{\frac{1}{3}}Pk & -i\sqrt{\frac{1}{3}}PK_z & \sqrt{2}M^* & i\sqrt{\frac{3}{2}}L^* & -\frac{T-2Q}{3\sqrt{2}} & \frac{iL}{\sqrt{2}} & 0 & E_v-\Delta+\frac{T+Q}{3}
\end{pmatrix}
$$

Table 2.2: Matrix representation, $\mathbf{H}_{\mathbf{F_z}}$, of the $\vec{\mathrm{K}}\cdot\vec{\mathrm{P}}$ Hamiltonian in a cylindrical wave basis. This matrix represents coupling among conduction, light and heavy hole, and split-off bands, including indirect coupling through remote bands. The symbols are defined in the text.

conventional $\vec{K} \cdot \vec{P}$ method using the same approximations. However, the eigenvectors have cylindrical symmetry, so that the cylindrical quantum wire problem is now easily solved by the same algebraic method that we used for the spherical quantum dot.

2.7 Electronic structure of the cylindrical quantum wire

By treating the bandstructure parameters such as E_c and E_v as functions of the radial coordinate in the Hamiltonian given in Table 2.2, we can model the cylindrical wire heterostructure just as in the case of the quantum dot. We find that the one-band model is adequate for conduction band states in systems like GaAs-AlGaAs, but fails in the case of type-II systems such as InAs-GaSb.

We narrow our focus now to the more interesting Γ_8 states – the light and heavy holes– and calculate the quantum wire subband dispersion relations, $E(K_z)$, for these bands. For the light and heavy holes, we retain only the middle 4×4 block of the Hamiltonian in Table 2.2, incorporating the effects of coupling to the conduction and split-off bands through the Luttinger parameters in the spherical approximation:

$$
\begin{array}{c} \\ \mathbf{H}^{\Gamma_8}_{\mathbf{F_z}} = \end{array}
\begin{array}{c}
\begin{array}{cccc} |3/2,3/2\rangle|F_z-3/2\rangle & |3/2,1/2\rangle|F_z-1/2\rangle & |3/2,-1/2\rangle|F_z+1/2\rangle & |3/2,-3/2\rangle|F_z+3/2\rangle \end{array} \\
\left(\begin{array}{cccc}
E_v+\frac{T}{2} & -iL & -M & 0 \\
iL^* & E_v+\frac{T}{6}+\frac{2Q}{3} & 0 & -M \\
-M^* & 0 & E_v+\frac{T}{6}+\frac{2Q}{3} & iL \\
0 & -M^* & -iL^* & E_v+\frac{T}{2}
\end{array} \right)
\end{array} . \qquad (2.48)
$$

In Eq. 2.48, the basis vectors are written as products of a zone-center Bloch function, $|J, J_z\rangle$ and the envelope state, $|L_z\rangle$, where $L_z = F_z - J_z$. This form ensures that all the basis vectors correspond to the same quantum number F_z. In the envelope vector, k and k_z are understood and therefore omitted. The terms in the matrix are given by Eq[2.47] where

the parameters γ_1 and γ_2 are the usual Luttinger parameters, and we invoke the spherical approximation ($\gamma_2 = \gamma_3$) [26,27]. E_v denotes the bulk valence band-edge, which will later be taken to be a function of position in modeling the quantum wire heterostructure.

For a given F_z, the heavy and light holes each have two eigenvectors. The heavy hole vectors are

$$|HH\rangle_1 = \begin{pmatrix} \frac{1}{\sqrt{3}}\frac{k^2+4K_z^2}{k^2} \\ \frac{2K_z}{k} \\ 1 \\ 0 \end{pmatrix} \qquad |HH\rangle_2 = \begin{pmatrix} \frac{2K_z}{k} \\ \sqrt{3} \\ 0 \\ 1 \end{pmatrix}, \tag{2.49}$$

where the heavy-hole eigenvalue is $E_{HH}(k) = E_v - (\gamma_1 - 2\gamma_2)\frac{k^2+K_z^2}{2}$. The light-hole vectors are

$$|LH\rangle_1 = \begin{pmatrix} -\sqrt{3} \\ \frac{2K_z}{k} \\ 1 \\ 0 \end{pmatrix} \qquad |LH\rangle_2 = \begin{pmatrix} \frac{2K_z}{k} \\ -\frac{1}{\sqrt{3}}\frac{k^2+4K_z^2}{k^2} \\ 0 \\ 1 \end{pmatrix} \tag{2.50}$$

with eigenvalue $E_{LH}(k) = E_v - (\gamma_1 + 2\gamma_2)\frac{k^2+K_z^2}{2}$. Note that if $K_z = 0$ the Γ_8 Hamiltonian, Eq.(2.48), decouples into two 2×2 matrices of even or odd parity. The vectors subscripted 1 and 2 will then contain separately envelopes of either purely even or purely odd parity, depending on F_z. Thus, by taking the quantum wire axis to be the quantization direction, we not only obtain a simple radial boundary condition for the wavefunctions of the quantum wire, but also a significant simplification in determining subband edge ($K_z = 0$) wavefunctions and energies. This is pointed out because the optical properties of the quantum wire will be dominated by the subband edge states.

As in the quantum dot calculation, we treat the bandstructure parameters as a function of the cylindrical radial coordinate r, form heavy and light-hole vectors separately inside

and outside the quantum wire, and project them onto the envelope space radial coordinate. Inside the wire, the envelopes must be regular so these projections are

$$\phi_{F_z}^{HH1}(r,z) = \begin{pmatrix} \frac{1}{\sqrt{3}}\frac{k^2+4K_z^2}{k^2} J_{F_z-3/2}[k_{HH}(E)r] \\ \frac{2K_z}{k} J_{F_z-1/2}[k_{HH}(E)r] \\ J_{F_z+1/2}[k_{HH}(E)r] \\ 0 \end{pmatrix} \mathrm{Exp}[iK_z z] \quad \phi_{F_z}^{HH2}(r,z) = \begin{pmatrix} \frac{2K_z}{k} J_{F_z-3/2}[k_{HH}(E)r] \\ \sqrt{3} J_{F_z-1/2}[k_{HH}(E)r] \\ 0 \\ J_{F_z+3/2}[k_{HH}(E)r] \end{pmatrix} \mathrm{Exp}[iK_z z] \tag{2.51}$$

and

$$\phi_{F_z}^{LH1}(r,z) = \begin{pmatrix} -\sqrt{3} J_{F_z-3/2}[k_{LH}(E)r] \\ \frac{2K_z}{k} J_{F_z-1/2}[k_{LH}(E)r] \\ J_{F_z+1/2}[k_{LH}(E)r] \\ 0 \end{pmatrix} \mathrm{Exp}[iK_z z] \quad \phi_{F_z}^{LH2}(r) = \begin{pmatrix} \frac{2K_z}{k} J_{F_z-3/2}[k_{LH}(E)r] \\ -\frac{1}{\sqrt{3}}\frac{k^2+4K_z^2}{k^2} J_{F_z-1/2}[k_{LH}(E)r] \\ 0 \\ J_{F_z+3/2}[k_{LH}(E)r] \end{pmatrix} \mathrm{Exp}[iK_z z]. \tag{2.52}$$

For bound states, the wavefunctions outside the wire must be normalizable, so the projections in the barrier region involve Hankel functions $H^{(1)}$ in place of the Bessel functions J appearing in the expressions above.

The quantum wire eigenstates are then formed in each region as a superposition of the bulk light and heavy-hole vectors. If we specialize for the moment to the case of a quantum wire with an infinite well depth, the boundary condition is that the wavefunction inside must vanish at the surface of the wire, r=R. Since the states are four-component vectors, this requirement can be satisfied generally only if the wavefunction is a superposition of the four bulk light and heavy-hole eigenstates for a given F_z, such as

$$\psi_{F_z}(E) = A\ |HH\rangle_1 + B\ |HH\rangle_2 + C\ |LH\rangle_1 + D\ |LH\rangle_2. \tag{2.53}$$

By forcing this state to vanish at R, we obtain a 4×4 determinantal dispersion relation giving the allowed energies for the infinite well quantum wire. This is

$$\det \begin{vmatrix} \frac{1}{\sqrt{3}} \frac{k_{HH}^2 + 4K_z^2}{k_{HH}^2} J_{F_z-3/2}[k_{HH}R] & \frac{2K_z}{k_{HH}} J_{F_z-3/2}[k_{HH}R] & -\sqrt{3} J_{F_z-3/2}[k_{LH}R] & \frac{2K_z}{k_{LH}} J_{F_z-3/2}[k_{LH}R] \\ \frac{2K_z}{k_{HH}} J_{F_z-1/2}[k_{HH}R] & \sqrt{3} J_{F_z-1/2}[k_{HH}R] & \frac{2K_z}{k_{LH}} J_{F_z-1/2}[k_{LH}R] & -\frac{1}{\sqrt{3}} \frac{k_{LH}^2 + 4K_z^2}{k_{LH}^2} J_{F_z-1/2}[k_{LH}R] \\ J_{F_z+1/2}[k_{HH}R] & 0 & J_{F_z+1/2}[k_{LH}xR] & 0 \\ 0 & J_{F_z+3/2}[k_{HH}R] & 0 & J_{F_z+3/2}[k_{LH}R] \end{vmatrix} = 0. \tag{2.54}$$

This dispersion relation is equivalent to one reported in Ref.[22], which was derived using a coordinate free form for the Luttinger Hamiltonian. The formalism presented in this work is more general in that explicit coupling to the conduction and split-off bands is incorporated into the general Hamiltonian. The formalism reduces to that presented in [22] for the case of the isolated Γ_8 states we are presently calculating.

Before returning to the finite well problem, we stop to examine some qualitative features which become apparent in the steps leading to the infinite well dispersion relation. The only possibility for the light and heavy holes to decouple in the wire exists in the spaces corresponding to $F_z = \pm 1/2$ at the zone center ($K_z = 0$) where parity is a good quantum number. In this case, the odd-parity vectors in Eqs.(2.51- 2.52) have two non-zero envelope components, proportional to $J_{\pm 1}[kr]$. Since $J_{-1}[x] = -J_1[x]$, the infinite well boundary condition at the wire interface is equivalent to just one equation: $J_1[kr] = 0$. Thus the light and heavy-hole vectors decouple in this specific case, and the corresponding sub-band edge energies are identical to those predicted by a one-band model. However, for the even-parity vectors corresponding to $F_z = \pm 1/2$, and for all other zone center vectors, both even and odd, with $|F_z| > 1/2$, the indices of the Bessel functions for the two non-zero components are not equal. As a result, light and heavy-hole waves must be mixed to satisfy the boundary conditions at the wire interface, and the one-band model fails even to predict correct subband edge energies. The quantum wire eigenstates are therefore in general hybrids of light and heavy-hole character, even at the zone center. With non-zero

K_z this mixing further increases. This effect, which has been reported for wires of square cross-section [12,14] in addition to the cylindrical wire result reported here, is in distinct contrast to the situation in the conventional planar quantum well, in which light and heavy hole states are always decoupled at the zone center. It is therefore not possible to label quantum wire subbands as light or heavy hole in character as is done in the quantum well.

This remains true for the finite well quantum wire. To solve this problem, we must construct states in the barrier region in addition to the states inside the wire. As indicated above, the barrier states contain Hankel functions which decay as r increases to infinity. The quantum wire eigenstates in the well and in the barrier are formed separately as superpositions of the two light and two heavy hole vectors in the respective regions, leaving four constants in the well and four constants in the barrier to be determined. By requiring continuity of the wavefunctions (four equations) and the probability current (four more equations) across the interface between well and barrier regions, we obtain an 8×8 determinantal dispersion relation which determines the allowed quantum wire eigenenergies and eigenstates. We take the effective mass parameters to be the same in the well and barrier, and write this dispersion relation in the compact form:

$$\det \begin{vmatrix} \Phi_{Inside} & \Phi_{Outside} \\ \Phi'_{Inside} & \Phi'_{Outside} \end{vmatrix} = 0 \qquad (2.55)$$

where the Φ are 4×4 matrices given by

$$\Phi_{\text{Inside}} = \begin{pmatrix} \frac{1}{\sqrt{3}}\frac{k_{HH}^2+4K_z^2}{k_{HH}^2} J_{F_z-3/2}[k_{HH}R] & \frac{2K_z}{k_{HH}} J_{F_z-3/2}[k_{HH}R] & -\sqrt{3} J_{F_z-3/2}[k_{LH}R] & \frac{2K_z}{k_{LH}} J_{F_z-3/2}[k_{LH}R] \\ \frac{2K_z}{k_{HH}} J_{F_z-1/2}[k_{HH}R] & \sqrt{3} J_{F_z-1/2}[k_{HH}R] & \frac{2K_z}{k_{LH}} J_{F_z-1/2}[k_{LH}R] & -\frac{1}{\sqrt{3}}\frac{k_{LH}^2+4K_z^2}{k_{LH}^2} J_{F_z-1/2}[k_{LH}R] \\ J_{F_z+1/2}[k_{HH}R] & 0 & J_{F_z+1/2}[k_{LH}R] & 0 \\ 0 & J_{F_z+3/2}[k_{HH}R] & 0 & J_{F_z+3/2}[k_{LH}R] \end{pmatrix} \qquad (2.56)$$

and

$$\Phi_{\text{Outside}} =$$
$$\begin{pmatrix} \frac{1}{\sqrt{3}} \frac{\kappa_{HH}^2+4K_z^2}{\kappa_{HH}^2} H_{F_z-3/2}[\kappa_{HH}R] & \frac{2K_z}{\kappa_{HH}} H_{F_z-3/2}[\kappa_{HH}R] & -\sqrt{3} H_{F_z-3/2}[\kappa_{LH}R] & \frac{2K_z}{\kappa_{LH}} H_{F_z-3/2}[\kappa_{LH}R] \\ \frac{2K_z}{\kappa_{HH}} H_{F_z-1/2}[\kappa_{HH}R] & \sqrt{3} H_{F_z-1/2}[\kappa_{HH}R] & \frac{2K_z}{\kappa_{LH}} H_{F_z-1/2}[\kappa_{LH}R] & -\frac{1}{\sqrt{3}} \frac{\kappa_{LH}^2+4K_z^2}{\kappa_{LH}^2} H_{F_z-1/2}[\kappa_{LH}R] \\ H_{F_z+1/2}[\kappa_{HH}R] & 0 & H_{F_z+1/2}[\kappa_{LH}R] & 0 \\ 0 & H_{F_z+3/2}[\kappa_{HH}R] & 0 & H_{F_z+3/2}[\kappa_{LH}R] \end{pmatrix} \tag{2.57}$$

and each term in the matrices labeled Φ' is the derivative with respect to r of the corresponding term in Φ. k_{HH} and k_{LH} are the wavenumbers corresponding to $E(k) = E_v - (\gamma_1 \mp 2\gamma_2)\frac{k^2+K_z^2}{2}$, where the minus applies to the heavy holes and the plus to the light holes. κ_{HH} and κ_{LH} are similarly defined in the barrier.

We have solved this dispersion relation for a GaAs wire embedded in an $Al_{0.3}Ga_{0.7}As$ barrier region for several wire radii, using the same bandstructure parameters as in Sec. 2.5. We begin by presenting plots of the subband edge ($K_z = 0$) energies of bound states as a function of wire radius. Figure 2.7(a) shows edge energies for all of the bound subbands corresponding to $F_z = \pm 1/2$ for radii up to R=10 nm, relative to E_v in GaAs. Figures 2.7(b) and 2.8(a) similarly show the bound subband edges in $F_z = \pm 3/2$ and $F_z = \pm 5/2$, respectively. The states are labeled according to parity in Figures 2.7(a)-(b) and 2.8(a) since at the quantum wire zone center, parity is a good quantum number. In Figure 2.8(b) we show the position of the four highest subband edges versus wire radius calculated in a one-band model for heavy and light holes using the same bandstructure parameters as for the coupled band calculations. A comparison of these plots shows the effect of the admixture of light and heavy hole character in the zone center quantum wire states, discussed above. The highest state in Figure 2.7(a) is substantially lower for all radii than the HH0 state in the one-band model, reflecting admixture of light hole character into the wavefunction. The

confinement energies increase as we decrease wire radius, as expected. Also, confinement energies for a given radius tend to be larger for states of higher F_z. The highest subband (lowest confinement energy) corresponds to an even parity state with $F_z = \pm 1/2$. Note that, in contrast to the situation in the quantum dot, there is always at least one bound state in the wire, though as r approaches zero the subband edge of the state approaches the top of the well asymptotically. This was first pointed out for the one-band case in Ref.[16].

In Figures 2.9(a) and 2.9(b) we show the subband dispersion, $E(K_z)$ for bound states corresponding to $F_z = \pm 1/2$ and $F_z = \pm 3/2$, respectively, in a GaAs-$Al_{0.3}Ga_{0.7}As$ quantum wire with radius 5 nm. Reference to Fig. 2.8 shows that there are no bound states for the 5 nm radius wire in the spaces $F_z = \pm 5/2$: Figure 2.9 represents all bound states for this radius. These plots were made by solving Eq.(2.55) numerically on a desk top personal computer. The states are labeled according to the parity of the zone center envelope wavefunction. The strong non-parabolicity of the subband structure is a result of the no-crossing rule for coupled states, reflecting the importance of band-coupling effects in this system. The most extreme result of this coupling is seen in Fig. 2.9(b), in which the highest subband is actually electron-like at zone-center. Similar effects manifest themselves in Figure 2.10, which shows the dispersion of the bound subbands in a wire of radius 2.5 nm. Reference to Figures 2.7- 2.8 shows that these plots describe all bound states for this radius.

It is instructive to examine the effective masses at the subband edges as a function of wire radius. We have determined these masses by performing a quadratic best fit to the subband dispersion curves near the subband edges, as in Ref.[13]. The results for the highest subband, for both infinite and finite well depths, are shown in Table 2.3. The mass is as low

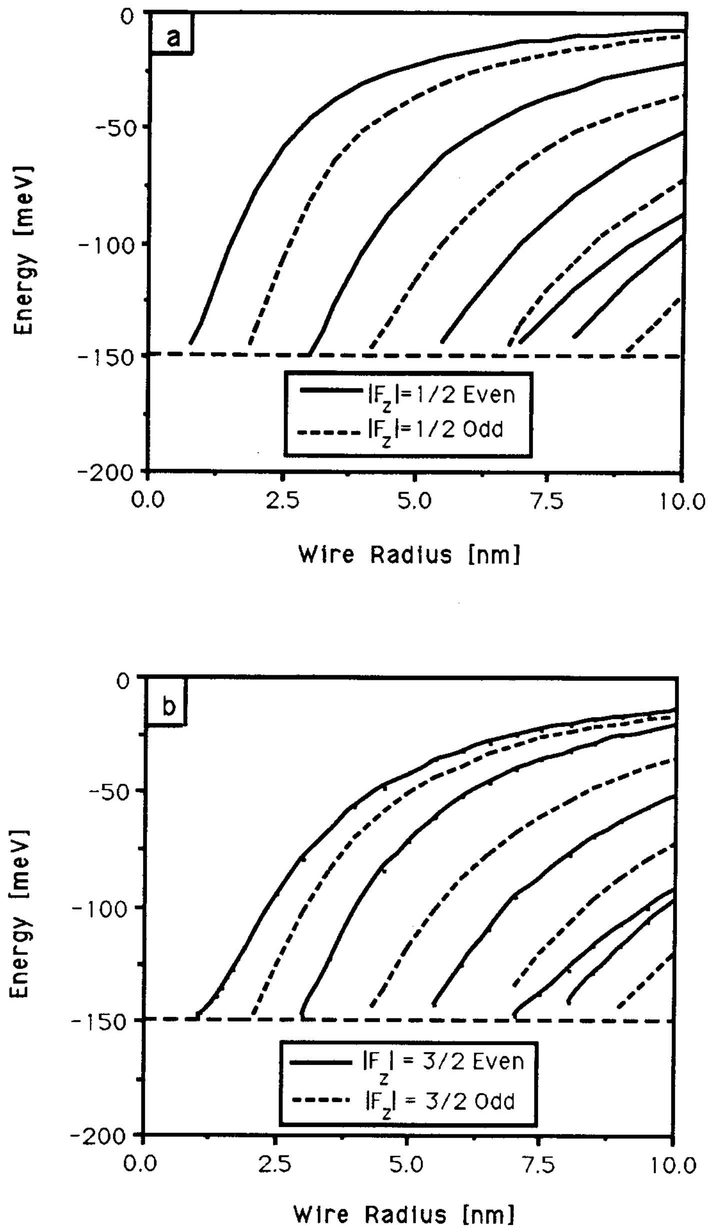

Figure 2.7: Confinement energy at zone-center ($K_z = 0$) for bound valence band states in a cylindrical GaAs quantum wire embedded in an $Al_{0.3}Ga_{0.7}As$ barrier (well depth=150 meV) plotted versus wire radius. (a): Coupled band model, $F_z = \pm 1/2$. (b): $F_z = \pm 3/2$. The states are labeled according to their parity, which is a good quantum number at zone center.

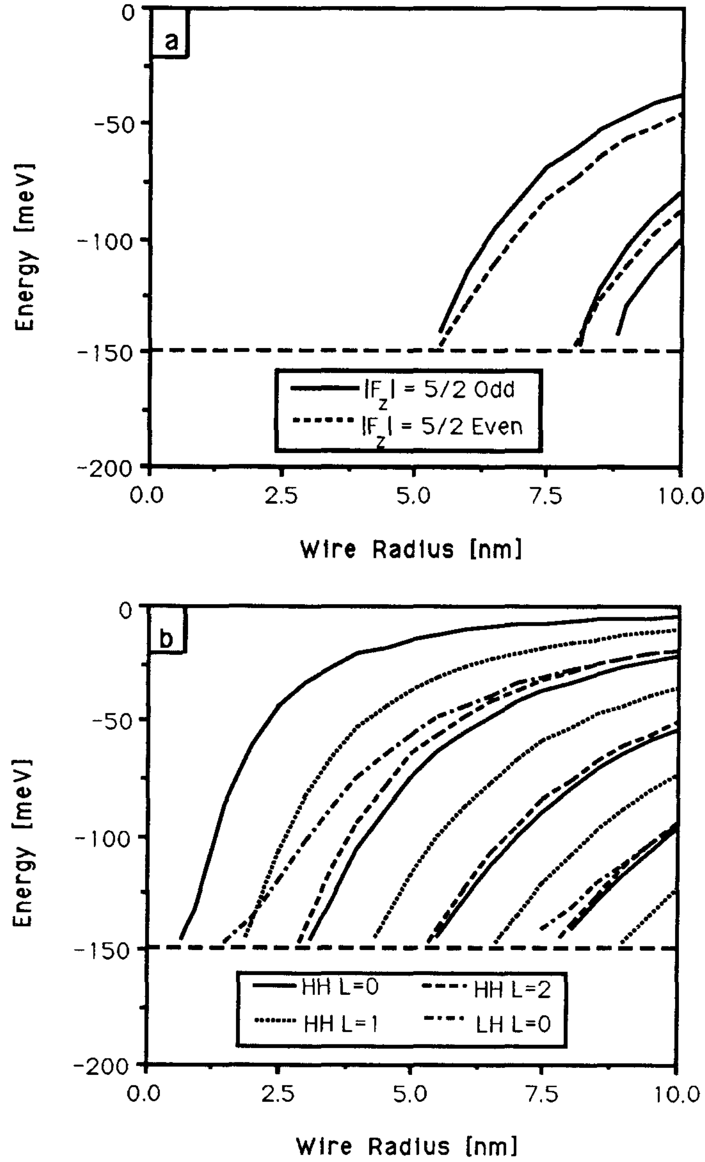

Figure 2.8: Confinement energy at zone-center ($K_z = 0$) for bound valence band states in a cylindrical GaAs quantum wire embedded in an $Al_{0.3}Ga_{0.7}As$ barrier (well depth=150 meV) plotted versus wire radius. (a): Coupled band model, $F_z = \pm 5/2$. (b): One-band model with the same effective masses as in (a). The states are identified by the band (HH or LH) and the quantum number L_z.

Quantum Wire:	Radius		
Well Depth	2.5 nm	5 nm	10 nm
Infinite	0.25 m_o	0.25 m_o	0.25 m_o
150 meV	0.16 m_o	0.19 m_o	0.27 m_o

Table 2.3: Effective mass at the subband edge of the highest valence subband in a GaAs quantum wire embedded in an $Al_{0.3}Ga_{0.7}As$ barrier, for several wire radii. Also included in the table are values determined in the approximation of infinite well depth.

as 0.16 m_o for the 2.5 nm radius wire with finite well depth, and increases somewhat with increasing wire radius. In the approximation of an infinitely deep well, the mass is found to be $m^* = 0.25m_o$, independent of wire radius. A similar result was reported for a quantum wire of square cross-section in the infinite well approximation, in Ref.[13]. However, in that study, the mass of the highest valence subband was found to be $m^* = 0.027m_o$, nearly ten times lighter than our value for the infinite well case. This discrepancy is explained by the fact that the light and heavy hole states are assumed to decouple at the quantum wire zone center in Ref. [13], an assumption which has been shown here to be invalid, as well as in previous studies by other workers [12,14,22].

The effective mass of the highest valence subband in a quantum wire of a given diameter tends to be heavier than that for the corresponding state in a planar quantum well with a comparable thickness. This is best seen in the approximation of infinite well depth. In this approximation, the mass of the highest valence subband in a GaAs quantum well is $m^* = 0.118m_o$, independent of well thickness [11], in contrast to $m^* = 0.25m_o$ for the

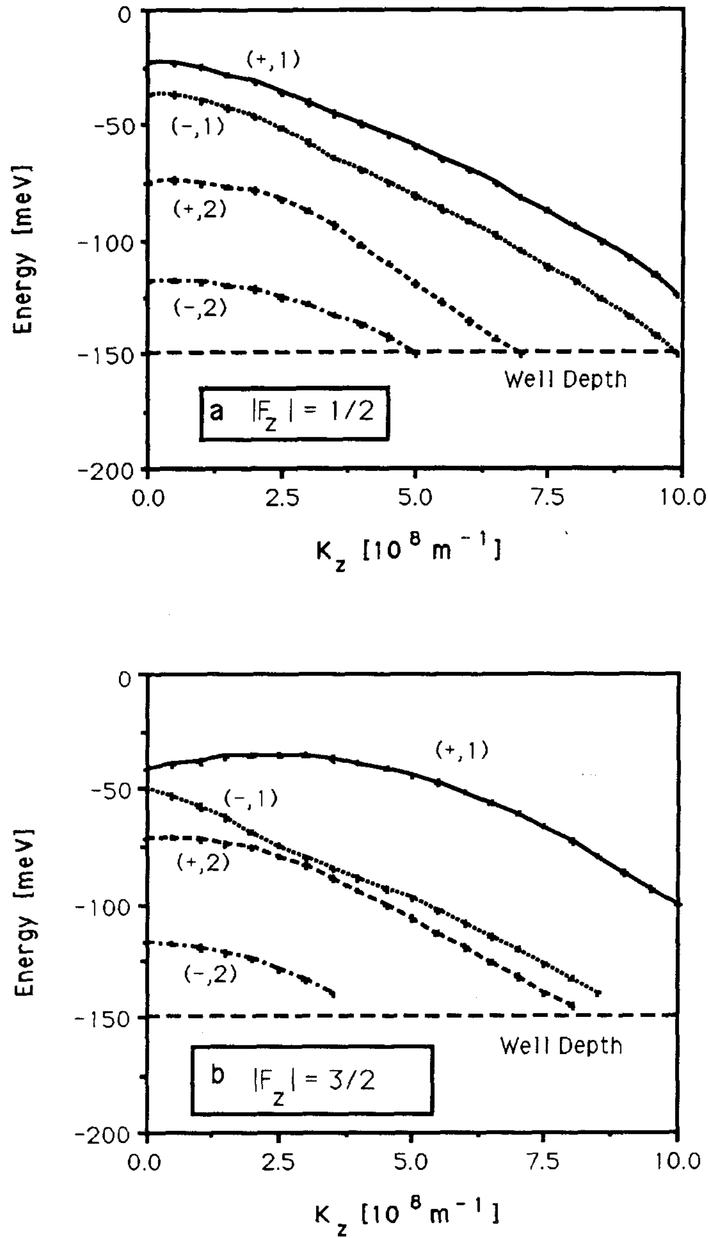

Figure 2.9: Valence subband dispersion $E(K_z)$ for a 5 nm radius GaAs quantum wire embedded in an $Al_{0.3}Ga_{0.7}As$ barrier (well depth =150 meV). The dispersion curves are labeled (π,n) where π is the parity of the zone center state to which the curve corresponds and n is the subband order in energy for given π. (a): $F_z = \pm 1/2$. (b): $F_z = \pm 3/2$. Note that the highest state in this space is electron-like near the subband edge.

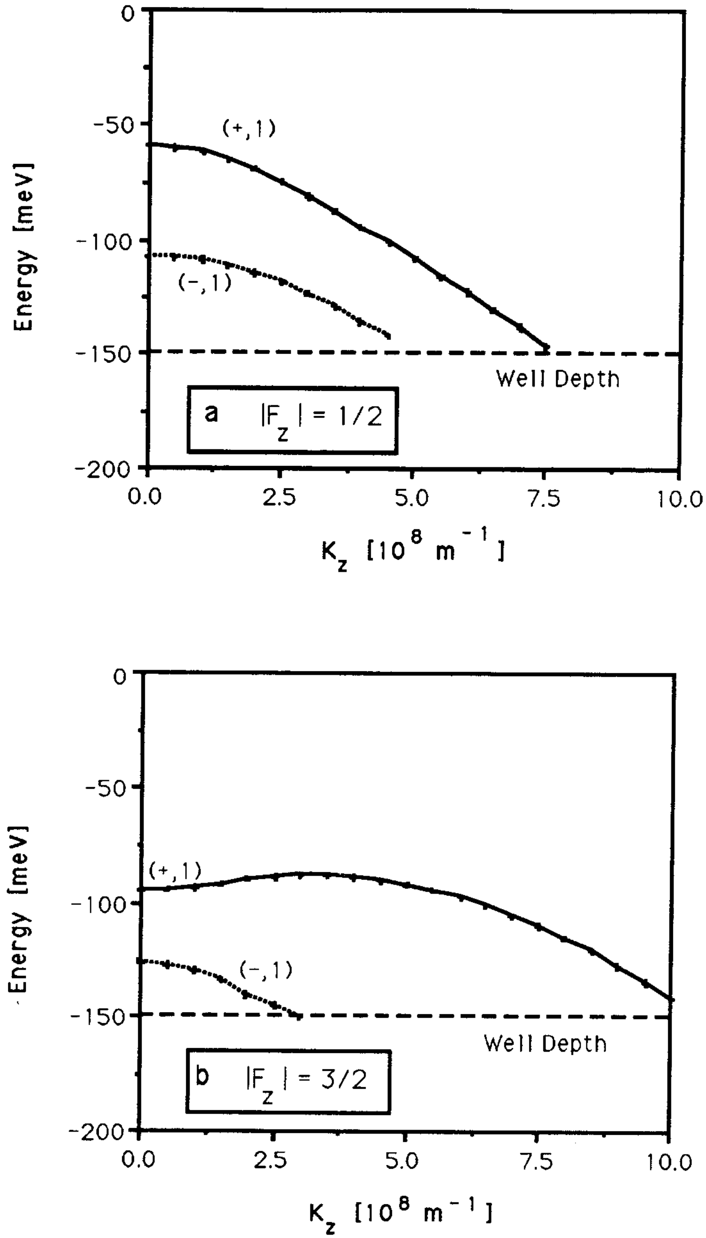

Figure 2.10: Valence subband dispersion $E(K_z)$ for a 2.5 nm radius GaAs quantum wire embedded in an $Al_{0.3}Ga_{0.7}As$ barrier (well depth =150 meV). The dispersion curves are labeled (π,n) where π is the parity of the zone center state to which the curve corresponds and n is the subband order in energy for given π. (a): $F_z = \pm 1/2$. (b): $F_z = \pm 3/2$. Note that the highest state in this space is electron-like near the subband edge.

highest quantum wire subband. The valence subbands in a quantum wire tend to be more numerous and therefore more closely spaced in energy than in a quantum well with comparable thickness due to the additional confinement and band-coupling effects in the wire structure. (This rather counter-intuitive effect is not true in a simple one-band model in which band coupling is neglected). This is seen in Table 2.4. There, the edge energy of the highest valence subband (HH1) in an infinitely deep quantum well of thickness 10 nm is listed, with the energy separation to the next state (HH2) and the effective mass for in-plane dispersion. The corresponding parameters are given for the highest valence state of a 10 nm diameter quantum wire with infinite well depth (which belongs to the $F_z = \pm 1/2$ subspace). The energy separation to the second highest state is lower in the quantum wire than in the planar well by over a factor of two. As a result, the coupling between these levels is stronger in the wire, causing the higher subband to "flatten out" due to the no crossing rule. This is reflected in the mass which is more than two times higher in the wire than in the well.

A more comprehensive study of the subband structure and effective masses in a cylindrical quantum wire would require the incorporation of band warping effects into the calculation. This could be done by employing the axial approximation discussed in Sec. 2.7. In the axial approximation, actual bandstructure in a cubic semiconductor is more accurately reproduced than in the spherical approximation, yet, since F_z remains a good quantum number, the calculation would be only moderately more complicated.

Finally, we point out that it is straightforward to obtain exact, closed form expressions for the quantum wire wavefunctions using the formalism we have presented. This is necessary for studying such important topics as excitons in the quantum wire, and matrix

State	E	$\Delta E_{2,1}$	m^*
Well: HH 1	-8.3 meV	24.9 meV	0.118 m_o
Wire: $F_z = 1/2$ Even 1	-39.6 meV	9.8 meV	0.250 m_o

Table 2.4: A comparison of the effective mass for valence band in-plane dispersion in a GaAs quantum well and down-wire dispersion in a quantum wire. The values are calculated in the approximation of an infinite well depth. The quantum well state labeled HH1 is heavy hole like with even parity at the subband edge. $\Delta E_{2,1}$ is the energy separation between HH1 and HH2, the next highest state, which has odd parity. Corresponding values are given for the highest even and odd-parity states for the quantum wire, which have quantum number $F_z = \pm 1/2$. The larger energy seperation between HH1 and HH2 implies a lighter effective mass in the quantum well.

elements for optical transitions. The band-coupling has a profound effect on these calculations and must not be ignored if realistic results are to be obtained. In chapter 4, the formalism developed here will be applied to the calculation of polarization dependent optical transition matrix elements, absorption, and gain in the cylindrical quantum wire.

2.8 Conclusions

We have demonstrated an analytical formalism for studying bandstructure in quantum dots and quantum wires. The technique is based upon the critical observation that the envelope function approximation is equivalent to a two-particle model of the electrons in a semiconductor. In the spherical approximation, the bandstructure Hamiltonian commutes with the sum of the angular momenta of these particles, which we term Bloch and envelope. The total angular momentum $\vec{F}$ therefore provides good quantum numbers in centrosymmetric systems, a general result previously applied in the more limited context of the acceptor problem. Application of the theory of angular momentum thus greatly simplifies the spherical quantum dot and the cylindrical quantum wire bandstructure calculations. Additionally, for the cylindrical quantum wire, the more accurate axial approximation may be invoked to incorporate band warping effects.

Utilizing the two-particle model to develop unitary basis transformations, we recast the $\vec{K}\cdot\vec{P}$ bandstructure Hamiltonian into a coupled total angular momentum basis for the quantum dot and an uncoupled basis of eigenstates of F_z for the quantum wire. The resulting Hamiltonians are block diagonal, producing eigenstates corresponding to the familiar conduction, light hole, heavy hole, and split-off bands. Quantum dot and wire eigenstates are formed by constructing linear superpositions of the bulk crystal eigenstates inside and out-

side the structures. By matching these functions at the hetero-interface, we obtain simple dispersion relations giving the allowed state energies. A two-band dispersion relation was developed and solved for quantum dot conduction band states in GaAs-AlGaAs and the type-II system, InAs-GaSb. We found good agreement between the two band model and the less accurate one band model for GaAs-AlGaAs, but the one band model failed for the conduction band in the type-II system. In the next chapter we will discuss the possibility of using the unusual band line-up in InAs-GaSb to fabricate novel self-doped quantum transport structures. For the valence band states in GaAs-AlGaAs quantum wires and dots, the one band approximation breaks down completely. The multiple band calculation which we introduced shows that the valence band states in the quantum dot and quantum wire are admixtures of light and heavy hole character. This admixture has a significant affect on the confinement energies in the quantum dot and on valence subband dispersion in quantum wires. This dispersion is highly non-parabolic and electron-like in some cases. Analytical expressions derived in this chapter for quantum dot and wire eigenstates rigorously include band-coupling effects and will be used in chapter 4 to calculate polarization dependent matrix elements for optical transitions.

2.9 Appendix: The conventional $\vec{\mathrm{K}} \cdot \vec{\mathrm{P}}$ Hamiltonian

In this section we present the conventional $\vec{\mathrm{K}} \cdot \vec{\mathrm{P}}$ bandstructure Hamiltonian describing coupling among the two conduction and six valence bands. We use a somewhat different phase convention in our definition of the band-edge Bloch states than that used by other investigators. The states $|\mathrm{J}, \mathrm{J_z}\rangle$ are written below in terms of orbital wave functions transforming as s-states (the conduction bands), p states (the valence bands), and the spin states up and

down. Our phase convention is determined by the reality of the Clebsch Gordan coefficients used to combine the spin and orbital angular momenta to form states of total Bloch angular momentum **J**:

$$
\begin{aligned}
|1/2,1/2,(0)\rangle &= |s\rangle|\uparrow\rangle \\
|1/2,-1/2,(0)\rangle &= |s\rangle|\downarrow\rangle \\
|1/2,1/2,(1)\rangle &= -\sqrt{1/3}[|z\rangle|\uparrow\rangle + (|x\rangle + i|y\rangle)|\downarrow\rangle] \\
|1/2,-1/2,(1)\rangle &= \sqrt{1/3}[|z\rangle|\downarrow\rangle - (|x\rangle - i|y\rangle)|\uparrow\rangle] \\
|3/2,3/2\rangle &= -\sqrt{1/2}[|x\rangle + i|y\rangle]|\uparrow\rangle \\
|3/2,1/2\rangle &= \sqrt{2/3}|z\rangle|\uparrow\rangle - \sqrt{1/6}(|x\rangle + i|y\rangle)|\downarrow\rangle \\
|3/2,-1/2\rangle &= \sqrt{1/6}(|x\rangle - i|y\rangle)|\uparrow\rangle] + \sqrt{2/3}[|z\rangle|\downarrow\rangle \\
|3/2,-3/2\rangle &= \sqrt{1/2}[|x\rangle - i|y\rangle]|\downarrow\rangle.
\end{aligned}
\tag{2.58}
$$

We include the orbital angular momentum quantum number in parenthesis for the conduction and split-off bands to distinguish between the two. For these bands the following correspondences apply between the band edge representations of the crystal double group and the representations of the full rotation group (written D_j, corresponding to the states that transform as angular momentum j): $D_{1/2} \leftrightarrow \Gamma_6$ for conduction band, $D_{1/2} \leftrightarrow \Gamma_7$ for the split-off bands, and $D_{3/2} \leftrightarrow \Gamma_8$ corresponding to the coupled light and heavy holes.

In this basis, the Hamiltonian matrix $\mathbf{H}(\vec{\mathbf{K}})$ takes the form given in Table 2.5. The terms E_c, E_v, Δ have their usual meanings, P is the Kane momentum matrix element, $P = -i\langle s|P_z|z\rangle$, and the other expressions are defined as follows:

$$
\begin{aligned}
K^2 &= K_x^2 + K_y^2 + K_z^2 \\
K_+ &= K_x + iK_y
\end{aligned}
$$

$$\begin{aligned}
K_- &= K_x - iK_y \\
\frac{-T}{2} &= (\gamma_1+\gamma_2)\frac{(K_x^2+K_y^2)}{2} + (\gamma_1 - 2\gamma_2)\frac{K_z^2}{2} \\
-(\frac{T}{6}+\frac{2Q}{3}) &= (\gamma_1-\gamma_2)\frac{(K_x^2+K_y^2)}{2} + (\gamma_1 + 2\gamma_2)\frac{K_z^2}{2} \\
-L &= -i2\sqrt{3}\gamma_3\frac{(K_x - iK_y)K_z}{2} \qquad (AxialApproximation) \\
-L &= -i2\sqrt{3}\gamma_2\frac{(K_x - iK_y)K_z}{2} \qquad (SphericalApproximation) \\
-M &= \sqrt{3}\gamma_2\frac{(K_x - iK_y)^2}{2}.
\end{aligned} \tag{2.59}$$

The γ parameters in these expressions are so-called "modified" Luttinger parameters which are related to the "true" Luttinger coupling parameters [27] by the relations [29]

$$\begin{aligned}
\gamma_1 &= \gamma_1^{true} - \frac{2P^2}{3(E_c - E_v)} \\
\gamma_2 &= \gamma_2^{true} - \frac{P^2}{3(E_c - E_v)} \\
\gamma_3 &= \gamma_3^{true} - \frac{P^2}{3(E_c - E_v).}
\end{aligned} \tag{2.60}$$

In these modified parameters we have effectively subtracted out the effects of valence band-coupling to the conduction bands from the "true" parameters. These effects are included explicitly in this model. Note that we have also assumed inversion symmetry in this Hamiltonian.

We note that a number of simplifications are possible. We can restrict attention solely to the Γ_8 sub-matrix for example, in which case we simply obtain Luttinger's 4×4 Hamiltonian [27] and the "true" Luttinger parameters are used in place of the modified parameters discussed above. In the spherical approximation, this gives isotropic lh and hh dispersions

$$E_{hh}(K) = E_v - (\gamma_1 - 2\gamma_2)\frac{K^2}{2}, \tag{2.61}$$

$$E_{lh}(K) = E_v - (\gamma_1 + 2\gamma_2)\frac{K^2}{2}. \tag{2.62}$$

$$
\begin{array}{cccccccc}
|1/2,1/2,(0)\rangle & |1/2,-1/2,(0)\rangle & |3/2,3/2\rangle & |3/2,1/2\rangle & |3/2,-1/2\rangle & |3/2,-3/2\rangle & |1/2,1/2,(1)\rangle & |1/2,-1/2,(1)\rangle
\end{array}
$$

$$
\begin{pmatrix}
E_c+\frac{1}{2}K^2 & 0 & \frac{-iPK_+}{\sqrt{2}} & i\sqrt{\frac{2}{3}}PK_z & i\frac{PK_-}{\sqrt{6}} & 0 & -i\sqrt{\frac{1}{3}}PK_z & -i\sqrt{\frac{1}{3}}PK_- \\
0 & E_c+\frac{1}{2}K^2 & 0 & -i\frac{PK_+}{\sqrt{6}} & i\sqrt{\frac{2}{3}}PK_z & \frac{iPK_-}{\sqrt{2}} & -i\sqrt{\frac{1}{3}}PK_+ & i\sqrt{\frac{1}{3}}PK_z \\
\frac{iPK_-}{\sqrt{2}} & 0 & E_v+\frac{T}{2} & -iL & -M & 0 & \frac{iL}{\sqrt{2}} & \sqrt{2}M \\
-i\sqrt{\frac{2}{3}}PK_z & i\frac{PK_-}{\sqrt{6}} & iL^* & E_v+\frac{T}{6}+\frac{2Q}{3} & 0 & -M & \frac{T-2Q}{3\sqrt{2}} & -i\sqrt{\frac{3}{2}}L \\
-i\frac{PK_+}{\sqrt{6}} & -i\sqrt{\frac{2}{3}}PK_z & -M^* & 0 & E_v+\frac{T}{6}+\frac{2Q}{3} & iL & i\sqrt{\frac{3}{2}}L^* & -\frac{T-2Q}{3\sqrt{2}} \\
0 & \frac{-iPK_+}{\sqrt{2}} & 0 & -M^* & -iL^* & E_v+\frac{T}{2} & -\sqrt{2}M^* & \frac{-iL^*}{\sqrt{2}} \\
i\sqrt{\frac{1}{3}}PK_z & i\sqrt{\frac{1}{3}}PK_- & \frac{-iL^*}{\sqrt{2}} & \frac{T-2Q}{3\sqrt{2}} & -i\sqrt{\frac{3}{2}}L & -\sqrt{2}M & E_v-\Delta+\frac{T+Q}{3} & 0 \\
i\sqrt{\frac{1}{3}}PK_+ & -i\sqrt{\frac{1}{3}}PK_z & \sqrt{2}M^* & i\sqrt{\frac{3}{2}}L^* & -\frac{T-2Q}{3\sqrt{2}} & \frac{iL}{\sqrt{2}} & 0 & E_v-\Delta+\frac{T+Q}{3}
\end{pmatrix}
$$

Table 2.5: The full 8×8 $\vec{\mathrm{K}} \cdot \vec{\mathrm{P}}$ Hamiltonian $\mathbf{H}(\vec{\mathbf{K}})$ representing coupling between conduction and valence bands as well as indirect coupling through remote bands. The symbols are defined in the text.

where $\mathrm{K} = |\vec{\mathrm{K}}|$. On the other hand, if we neglect the Luttinger coupling parameters and the free electron kinetic energy term $\frac{\mathrm{K}^2}{2}$ entirely, we recover the Kane dispersion relations discussed in the text [24].

References

[1] Peter C. Sercel and Kerry J. Vahala,International Quantum Electronics Conference 1990, paper QThA2, Anaheim.

[2] Kerry J. Vahala and Peter C. Sercel, *Phys. Rev. Lett.* **65**, 239 (1990).

[3] D. Schecter, *J. Phys. Chem. Solids* **23**, 237 (1962).

[4] A. Baldereschi and Nunzio O. Lipari, *Phys. Rev. B* **8**, 2697 (1973).

[5] A. Baldereschi and Nunzio O. Lipari, *Phys. Rev. B* **9**, 1525 (1974).

[6] Masahiro Asada, Yasuyuki Miyamoto and Yasuharu Suematsu, *Jpn. J. Appl. Phys.* **24**, L95 (1985).

[7] Yasuhiko Arakawa, Kerry Vahala, and Amnon Yariv, *Appl. Phys. Lett.* **45**, 950, (1984).

[8] Takeshi Kodama,Yukio Osaka, and Masamichi Yamanishi, *Jpn. J. Appl. Phys.* **24**, 1370, (1985).

[9] Marcos H. Degani and Oscar Hipolito, *Phys. Rev. B* **35**, 9345, (1987).

[10] Jerry W. Brown and Harold N. Specter, *Phys. Rev. B* **35**, 3009 (1987).

[11] A. Fasolino and M. Altarelli, in *Two-Dimensional Systems, Heterostructures, and Superlattices*, New York: Springer Verlag, (1984).

[12] J. A. Brum, G. Bastard, L.L. Chang, and L. Esaki,*Superlattices and Microstructures* **3**, 47 (1987).

[13] Ikuo Suemune and Larry A. Coldren, *IEEE J. Quantum Electron.* **24**, 1778 (1988).

[14] D.S. Citrin and Yia-Chung Chang, *Phys. Rev. B* **40**, 5507, (1989-I).

[15] Kerry J. Vahala,*IEEE J. Quantum Electron.***24**, 523 (1988).

[16] Hal Zarem, Kerry J. Vahala, and Amnon Yariv, *IEEE J. Quantum Electron.***25**, 705 (1989).

[17] G.T. Einevoll and Y.C. Chang, *Phys. Rev. B* **40**, 9683, (1989).

[18] G. R. Olbright, N. Peyghambarian, S.W. Koch, and L. Banyai, *Optics Lett.* **12**, 413, (1987).

[19] Louis Brus, *IEEE J. Quantum Electron.* **QE-22**, 1909 (1986).

[20] E. Kapon, D. M. Hwang, and R. Bhat, *Phys Rev. Lett* **63** 430 (1989).

[21] John A.Lebens, Charles Tsai, Kerry J. Vahala, and Thomas Kuech, *Appl. Phys. Lett.* **56**, 2642, (1990).

[22] Mark Sweeny, Jingming Xu, and Michael Shur, *Superlattices and Microstructures* **4**, 623, (1988).

[23] M. Sweeny and Jingming Xu, *Solid State Commun.* **72**, 301, (1989).

[24] Evan O. Kane, *J. Phys. Chem. Solids* **1**, 249 (1957).

[25] E. O. Kane, in *Physics of III-V compounds,* Vol **1** of *Semiconductors and Semimetals* edited by R.K.Willardson and Albert C. Beer (Academic, New York, 1966) p. 75.

[26] J.M. Luttinger and W. Kohn, *Phys. Rev.* **97**, 869, (1955).

[27] J. M. Luttinger, *Phys. Rev.* **102**, 1030 (1956).

[28] Amnon Yariv, *Quantum Electronics, Third Ed.* (Wiley, New York, 1989) Chapters 11-12.

[29] C. R. Pidgeon and R. N. Brown, *Phys. Rev.* **146**, 575 (1966).

[30] S.R. White and L.J. Sham, *Phys. Rev. Lett.* **47**, 879, (1981).

[31] G. A. Sai-Halasz, R. Tsu, and L. Esaki, *Appl. Phys. Lett.* **30**, 651, (1977).

[32] L.L. Chang,N. Kawai, G. A. Sai-Halasz, R. Ludeke and L. Esaki, *Appl. Phys. Lett.* **35**, 939, (1979).

[33] M. Altarelli, *Phys. Rev. B* **28**, 842, (1983).

Chapter 3

Self-doping semiconductor quantum structures

3.1 Introduction

Progress in the field of nanostructure physics and fabrication has been motivated largely by the prospect of creating a new generation of electronic devices which rely upon quantum transport effects [1]-[3] for their operation. An issue that has not been adequately addressed is the question of how nanometer scale transport structures might be doped. The stochastic nature of impurity dopant distributions is a critical problem in this field because the presence of an ionized impurity in the vicinity of a quantum wire or dot represents a significant electronic perturbation to these nanometer scale structures. This discreteness also translates into uncertainty in whether or not a given nanostructure in fact contains charge carriers.

In this chapter a novel class of nanometer scale semiconductor structures for transport applications is proposed that avoids these problems. Employing the coupled band formalism

developed in chapter 2, we examine analytically the bandstructure of quantum dots and wires based upon the type-II broken gap system InAs-GaSb, and demonstrate the theoretical feasibility of creating "self-doping" quantum dot and quantum wire arrays which contain free charge carriers, without intentional impurity doping. This fact, along with the low effective mass of InAs, which relaxes the size requirements necessary to observe quantum effects, make this new class of nanostructures potentially interesting for quantum transport studies. We conclude by examining the practical issue of how such type-II quantum wires and dots might be fabricated.

3.2 InAs-GaSb heterostructures

The basic physics of InAs-GaSb heterostructures can be understood by reference to the inset of Figure 3.1, which shows the band line-ups of the system. Because the conduction band edge of InAs lies below the valence band edge of GaSb, charge transfer may occur across the interface [4]. Additionally, conduction-valence band mixing across the heterojunction is significant so that a multiple band model is necessary for theoretical calculations. A rigorous analysis should therefore be based on multiple band envelope function theory and should self-consistently include the band-bending due to charge transfer at the InAs-GaSb interface (an example of such a calculation for superlattices is found in Ref.[5]). Such an approach is quite computationally intensive, however. A flat band model is preferable because of its simplicity; and in spite of simplicity, the model successfully explains observations of a semiconductor-to-semimetal transition in InAs-GaSb superlattices [6]. This transition was observed to occur for InAs layer thickness in the neighborhood of 10 nm, in rough agreement with a Kane-type two-band calculation which predicted a transition at 8.5 nm

[6]. The approximate agreement of experiment with the flat band theory lends confidence that this simplified approach may be used as well to determine the essential characteristics of the type-II quantum wire and quantum dot.

Even in a flat band approximation, however, the study of the coupled band states in quantum wires and quantum dots is significantly more complicated than in the planar quantum well problem. The multi-dimensional nature of these heterostructures complicates the boundary conditions, and quantum wires or boxes of square cross-section cannot be dealt with analytically since the finite square well potential is non-separable in two or three dimensions. We therefore employ simpler geometries for which the heterostructure potentials are separable: a cylindrical quantum wire and a spherical quantum dot. The theory developed in chapter 2 permits analytical solution of coupled band problems for these geometries. The approach is based upon the observation that in a spherical bandstructure approximation such as the Kane model [7]-[8], total angular momentum is a conserved quantity. Total angular momentum $\vec{F}$ is defined as the sum of the the angular momenta, $\vec{J}$, of the zone-center Bloch functions and, $\vec{L}$, of the envelope functions. In a cylindrical quantum wire the projection of total angular momentum along the wire axis therefore provides a good quantum number, F_z, while in a spherical quantum dot, the total angular momentum quantum numbers F and F_z are good quantum numbers. The Kane Hamiltonian may therefore be re-expressed in a basis of eigenstates of the operator $\mathbf{F_z}$ for the quantum wire, and in a basis of the eigenstates of $\mathbf{F}^2$ and $\mathbf{F_z}$ for the quantum dot. Bulk eigenvectors in the new bases are then computed in the well and barrier regions just as in the familiar quantum well problem, and the requirement of continuity at the interface [9] results in an eigenvalue equation.

3.2.1 InAs-GaSb quantum dots

We illustrate the method by calculating the energy of the lowest conduction state in an InAs quantum dot embedded in GaSb. The Kane Hamiltonian will be block diagonal with respect to quantum numbers F, F_z, and parity. Using the familiar rules of addition of angular momentum we form a total angular momentum basis as follows:

$$|K;F,F_z;J,L\rangle = \sum_{J_z=-J}^{J} \sum_{L_z=-L}^{L} \langle J,J_z;L,L_z|F,F_z\rangle \; |J,J_z\rangle \; |K;L,L_z\rangle. \qquad (3.1)$$

The first term in the sum is the Clebsch-Gordan coefficient for adding states of angular momenta $\vec{J}$ and $\vec{L}$. The states $|J,J_z\rangle$ are the band edge Bloch functions, where $J = 1/2$ for the conduction bands and $J = 3/2$ for the upper valence bands [7]. The envelope kets $|k;L,L_z\rangle$ are free spherical waves with angular momentum quantum numbers L and L_z. These therefore have the coordinate representations

$$\langle \rho,\theta,\phi|k,L,L_z\rangle = \sqrt{\frac{2}{\pi}} \; i^L \; h_L(k\rho) \; Y_L^{L_z}(\theta,\phi), \qquad (3.2)$$

where h_L is a spherical Hankel function, $Y_L^{L_z}$ is a spherical harmonic, and K is the radial wavenumber.

Since states of different total angular momentum and total parity, π, do not couple, each Hamiltonian sub-matrix $\mathbf{H}_{\mathbf{F},\mathbf{F_z},\pi}$ may be separately diagonalized to obtain bulk eigenstates. We expect the lowest conduction state in a quantum dot to have even parity; this state was shown in last chapter to have quantum numbers F=1/2, $F_z = \pm 1/2$. It is simple to show that for the conduction and upper valence band system, the appropriate Hamiltonian sub-

matrix (Eq. 2.19) assumes the simple form:

$$\mathbf{H_{1/2,\pm1/2,even}} = \begin{array}{c} \\ |1/2,0\rangle \\ |3/2,1\rangle \end{array} \begin{array}{c} \begin{array}{cc} |1/2,0\rangle & |3/2,1\rangle \end{array} \\ \begin{pmatrix} E_c & -i\sqrt{\frac{2}{3}}pk \\ i\sqrt{\frac{2}{3}}pk & E_v \end{pmatrix} \end{array}, \tag{3.3}$$

where the quantum numbers k, F, F_z are understood in the basis vectors $|J,L\rangle$. In the matrix, p is the Kane matrix element $-i\langle s|P_z|z\rangle$ [7]. E_c, E_v denote the conduction and light-hole band edges. Diagonalization gives the familiar Kane two-band energy dispersion relations [8] inside and outside the dot:

$$\begin{aligned} (E_c^I - E)(E_v^I - E) &= \frac{2}{3}|p|^2 k^2 \\ (E_c^O - E)(E_v^O - E) &= -\frac{2}{3}|p|^2 \lambda^2, \end{aligned} \tag{3.4}$$

where superscripts I,O refer to regions inside and outside the dot, respectively. The exterior spherical wavenumber is taken as $i\lambda$ in anticipation of solving for bound energy eigenstates with energy $E \geq E_v^0$. Eigenvectors resulting from the diagonalization process have the form:

$$|\psi_E\rangle = A[|1/2,0\rangle + \sqrt{\frac{E - E_c}{E - E_v}}|3/2,1\rangle], \tag{3.5}$$

where "A" is a constant to be determined by matching boundary conditions and applying normalization. The envelope parts of this vector are projected onto only the radial coordinate representation. This results in the following two-dimensional column vector:

$$\psi_E(r) = A \begin{pmatrix} h_0(kr) \\ \sqrt{\frac{E-E_c}{E-E_v}} h_1(kr) \end{pmatrix}. \tag{3.6}$$

The form of Eq.(3.4) is such that $\pm k$ ($\pm\lambda$) are degenerate roots. Using these roots and the basic form given by Eq.(3.6), state functions within each region are constructed. The requirement of regular behavior at the origin leads to combinations of Hankel functions

within the quantum dot that are equivalent to spherical Bessel functions of the first kind. Outside the quantum dot, only the spherical Hankel function of imaginary argument which decays for large r is retained. Applying continuity of the resulting envelope states at the boundary of the quantum dot leads to the following condition:

$$\frac{j_0(kR)h_1(i\lambda R)}{j_1(kR)h_0(i\lambda R)} = \sqrt{\frac{(E - E_c^I)(E - E_v^O)}{(E - E_v^I)(E - E_c^O)}}. \tag{3.7}$$

Eqs.(3.4- 3.7) form a system of three equations in the three unknowns, E, k, and λ.

The energy determined with this equation is plotted as a function of InAs dot radius in Figure 3.1 using the material parameters of Ref. [4]. We see that for dot diameters *larger* than 17 nm the lowest conduction state sinks below the position of the GaSb valence band edge, implying that electrons transfer from the GaSb barrier into the InAs well region. In essence, the InAs quantum dot is behaving like an artificial acceptor, in this case with a valence of two. The ionization energy is determined by the position of the InAs conduction state with respect to the GaSb valence band edge, a tailorable quantity dependent upon the radius of the InAs quantum dot. In a similar fashion, a GaSb quantum dot embedded in InAs will behave as a donor. These observations suggest the possibility of creating a synthetic extrinsic semiconductor with one mobile carrier type (without intentional impurity doping) by fabricating two- or three-dimensional arrays of InAs(GaSb) quantum dots embedded in GaSb(InAs). Such a system would have an advantage over a conventionally doped semiconductor because individual quantum dots could be located precisely by lithographic means. We call attention to Ref.[2] where it is shown that appropriately tailored miniband structure in quantum dot arrays may be used to suppress polar optical phonon scattering.

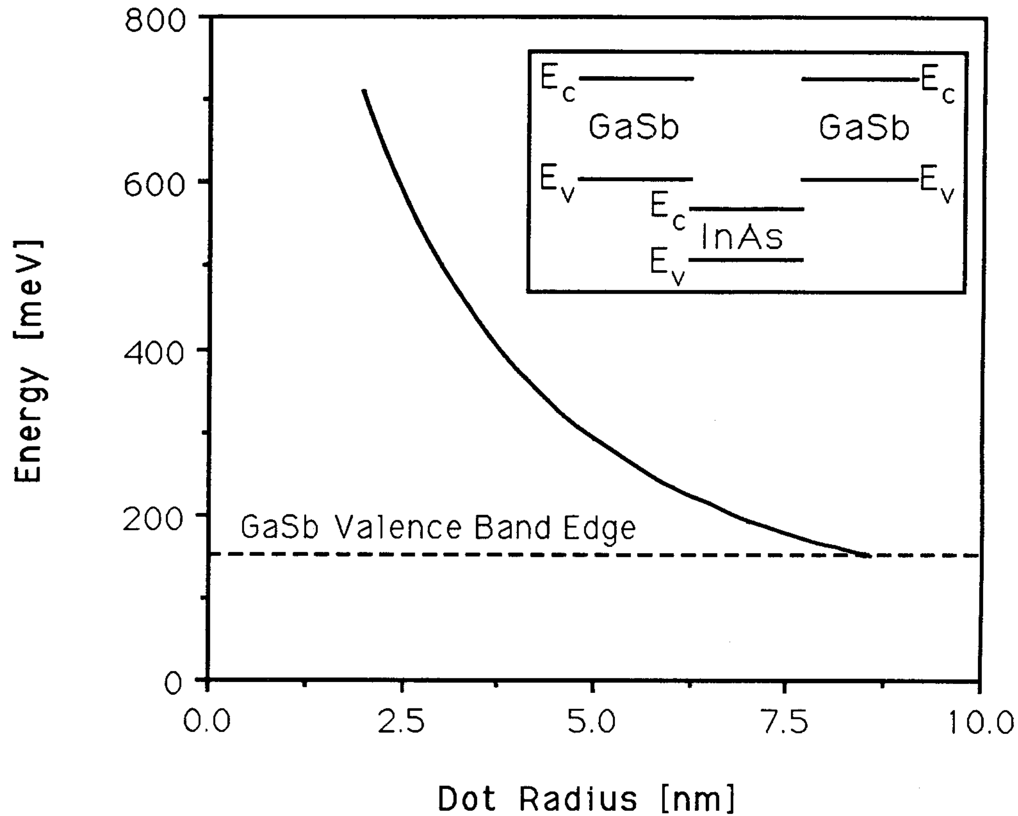

Figure 3.1: Confinement energy of the conduction band states in a spherical InAs dot embedded in a GaSb barrier, plotted as a function of dot radius. The dashed line is the position of the GaSb valence band edge, 150 meV above the conduction band edge in bulk InAs. Inset: schematic drawing of the relative position of bulk InAs and GaSb conduction and valence band edges.

3.2.2 InAs-GaSb quantum wires

The InAs quantum wire embedded in GaSb is studied in a manner similar to the quantum dot. The Kane two-band Hamiltonian is expressed in a basis of eigenstates of the operator F_z in this case. Following a procedure similar to that taken for the quantum dot, we arrive at the eigenvalue equation for the lowest conduction state with $K_z = 0$:

$$\frac{J_0(kR)H_1(i\lambda R)}{J_1(kR)H_0(i\lambda R)} = \sqrt{\frac{(E - E_c^I)(E - E_v^O)}{(E - E_v^I)(E - E_c^O)}}. \tag{3.8}$$

Using this equation, we find that for wire diameters greater than 13 nm, we expect charge transfer to occur across the InAs-GaSb interface. In this manner, quasi-one-dimensional channels may be created which contain high concentrations of free electrons, without intentional impurity doping. Due to the absence of charged impurity scattering centers, the quasi-one-dimensional nature of the electrons in the quantum wire, and the low effective mass of InAs we expect that such a structure would exhibit high mobility. Such a self-doping structure would be ideal for quantum transport experiments which require long scattering lengths.

3.3 Potential fabrication schemes

A possible scheme for fabricating InAs-GaSb quantum wires and dots based upon a selective epitaxial growth process is shown in Figure 2. The process shown has recently been demonstrated in the GaAs-$Al_xGa_{1-x}As$ system resulting in passivated wire and dot structures with excellent morphology [10]. To apply the technique to InAs structures embedded in GaSb, a thin masking layer of SiN would be deposited on a GaSb surface and selectively patterned by electron beam lithography to open holes and lines in the SiN layer. InAs is then grown

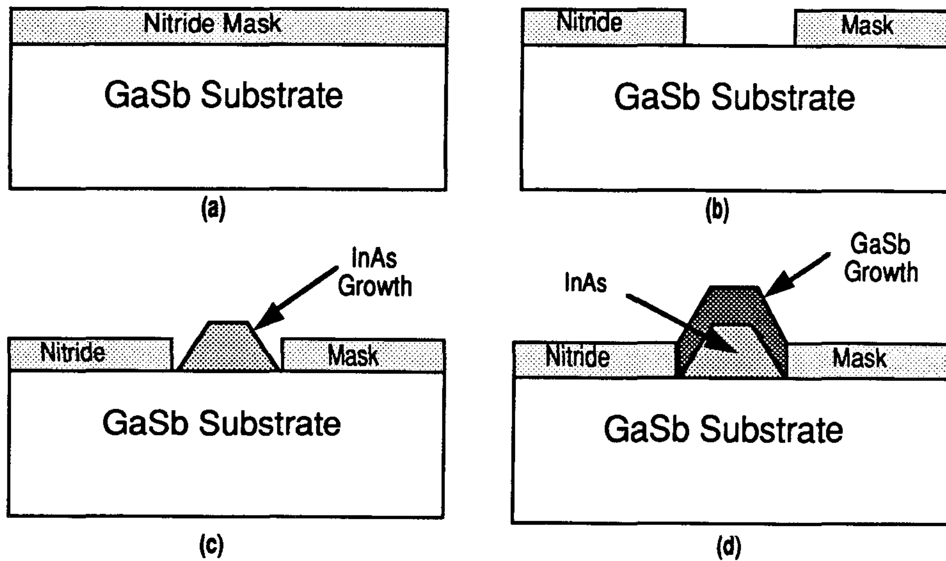

Figure 3.2: Possible scheme for fabricating InAs quantum wires or dots embedded in GaSb using a selective epitaxial growth technique similar to that demonstrated for GaAs-$Al_xGa_{1-x}As$ in Ref.[10]. (a): SiN mask is deposited on a GaSb substrate. (b): Stripes or holes are created in the SiN mask by electron beam lithography followed by a chemical etch process. (c): InAs is grown selectively in the mask openings. (d): GaSb overlayer is grown epitaxially.

selectively in the openings of the SiN layer. Finally the InAs is passivated by overgrowing GaSb. While effort would be required to develop such a selective epitaxy process in the InAs-GaSb material system, the basic feasibility of the process has been demonstrated.

Another possible scheme for fabricating InAs or GaSb quantum dots would be to grow nanometer sized InAs or GaSb clusters by homogeneous nucleation from the vapor phase. The InAs(GaSb) clusters would then be deposited on a substrate of GaSb (InAs) and overgrown with an epitaxial layer of GaSb (InAs). The first step of this process, the growth of

nanometer sized InAs and GaSb clusters by homogeneous nucleation from a supersaturated vapor, is demonstrated in chapter 6. Deposition of these clusters, and their incorporation into a growing epitaxial film, is a challenging research problem for future study.

3.4 Conclusions

In conclusion, we have proposed a novel class of quantum wires and dots based upon the type-II system InAs-GaSb, which are expected to exhibit unique self-doping behavior and high mobilities. This conclusion is based on a coupled band calculation which assumes a flat band condition. A more complete theoretical approach which incorporates band bending effects will be necessary to compute mobilities and carrier densities in such structures. Finally, we have suggested two schemes for fabricating such structures. The first could be realised by extending the technology of selective epitaxy to the InAs-GaSb material system. The second utilizes the cluster generation techniques to be described in chapter 6.

References

[1] Hiroyuki Sakaki, *Japan. J. Appl. Phys.* **19**, L735 (1980).

[2] Hiroyuki Sakaki, *Japan. J. Appl. Phys.* **28**, L314 (1989).

[3] J.N. Randall, M. A. Reed, T. M. Moore, R. J. Matyi, and J. W. Lee, *J. Vac. Sci. Technol. B* **6**, 302 (1988).

[4] G. A. Sai-Halasz, R. Tsu, and L. Esaki *Appl. Phys. Lett.* **30**, 651 (1977).

[5] M. Altarelli *Phys. Rev. B* **28**, 842 (1983).

[6] L.L. Chang,N. Kawai, G. A. Sai-Halasz, R. Ludeke and L. Esaki, *Appl. Phys. Lett.* **35**, 939 (1979).

[7] Evan O. Kane, *J. Phys. Chem. Solids* **1**, 249 (1957).

[8] E. O. Kane, in *Physics of III-V compounds,* Vol **1** of *Semiconductors and Semimetals* edited by R.K.Willardson and Albert C. Beer (Academic, New York, 1966) p. 75.

[9] S.R. White and L.J. Sham, *Phys. Rev. Lett.* **47**, 879 (1981).

[10] John A.Lebens, Charles Tsai, Kerry J. Vahala, and Thomas Kuech, *Appl. Phys. Lett.* **56**, 2642 (1990).

Chapter 4

Optical absorption and gain in quantum wires

4.1 Introduction

Polarization dependent photoluminescence excitation (PLE) spectroscopy has emerged recently as a powerful tool for the characterization of quantum wires [1,2]. In particular, these PLE studies have shown that a strong anisotropy exists in the relative intensity of the two lowest energy exciton lines in quantum wire arrays as a function of polarization of the exciting light. Given the importance of this observation to future application of quantum wires to semiconductor lasers [3]-[4], it is crucial that a rigorous theoretical understanding of this effect be established. However, the theoretical model which has previously been used to interpret this effect, and to calculate polarization dependent gain spectra in quantum wires [5,6], contains two major simplifications which can be shown to be fundamentally invalid. First, for simplicity, band coupling effects are neglected, and second, coherence terms are

neglected in the calculation of the optical transition matrix element.

In this chapter we apply the coupled-band formalism developed in chapter 2 to calculate the polarization dependent linear optical spectra in cylindrical quantum wires correctly. In addition to providing a theoretical framework with which to interpret polarization dependent absorption/emission spectra of quantum wires, these calculations can aid in the design of quantum wire lasers. This is particularly timely since the feasibility of incorporating quantum wires into the active region of a semiconductor laser has recently been experimentally demonstrated [7]. As an example, Figures 4.1(a) and (b) respectively represent lasers in which the quantum wires are oriented parallel and perpendicular to the electric field in the lasing mode.

A determination of the optimal configuration requires calculation of the optical gain spectrum. The interband optical transition matrix elements and joint density of states (JDOS) must be calculated while taking into account the effects of band-coupling. The electron-like structure of the dispersion relations for certain valence subbands which results from these band-coupling effects will be seen to result in a large JDOS for transitions involving these subbands, a fact which has important consequences to the optical spectra in these structures. In the course of developing the gain calculation, the valence subband dispersion relations, densities of states, interband optical transition matrix elements, and absorption spectra of cylindrical quantum wires will be presented. Before the conclusion of the chapter, the applicability of the model to quantum wires of lower symmetry, e.g., wires with square, rectangular, and triangular cross-sections, will be examined through application of group theory. In the next section, we begin with a brief review of the formalism necessary to calculate these quantities.

Quantum Wire Laser

[a] Quantum Wires Parallel to Electric Field

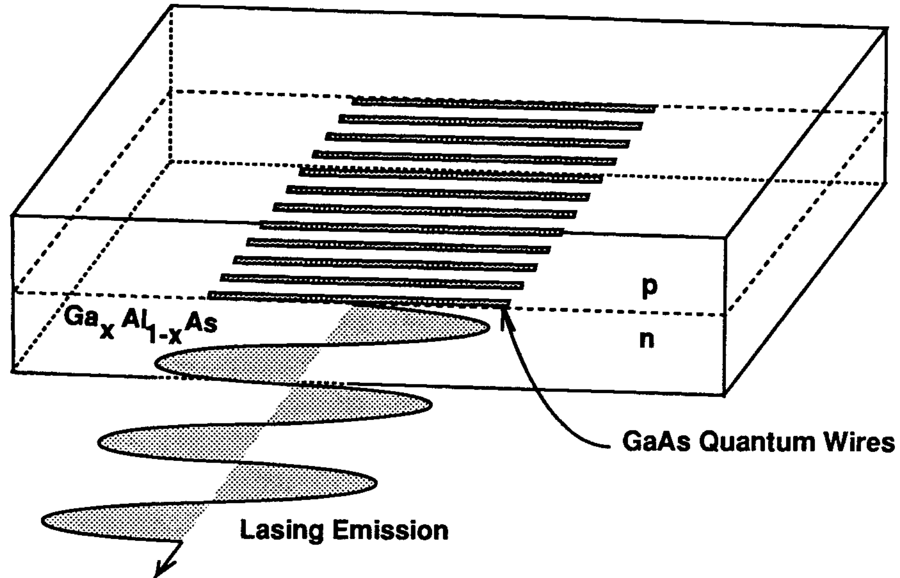

[b] Quantum Wires Perpendicular to Electric Field

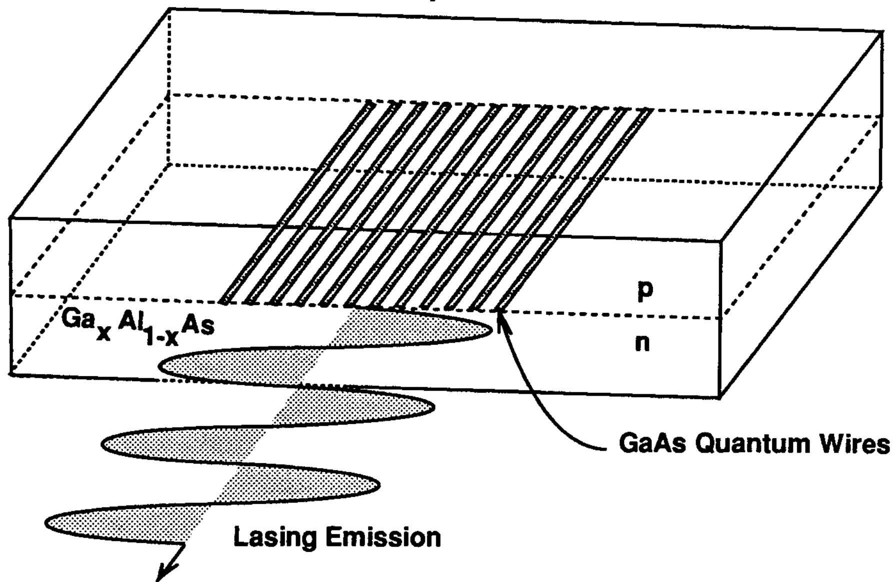

Figure 4.1: Two possible schemes for a quantum wire laser. (a): quantum wires are oriented parallel to the cavity facets (b) quantum wires oriented parallel to the cavity axis. In both structures the quantum wires are situated inside a graded index region and the laser is assumed to operate in TE mode.

4.2 Electronic structure of the cylindrical quantum wire

The determination of the optical properties of the quantum wire involves several distinct steps. First, it is necessary to determine the conduction and valence subband dispersion relations and wavefunctions. For the conduction band states, this step may be accomplished by invoking simple one-band effective mass theory, in which the quantum wire is modeled as a two-dimensional potential well. This method is analogous to the calculation that was presented in chapter 1 for the conventional one-dimensional quantum well [4]. The more complicated coupled valence band problem must then be solved to yield valence subband wavefunctions and dispersion relations. Once these steps are carried out, it is then straightforward to calculate matrix elements and JDOS for interband optical transitions. The calculations which follow assume a cylindrical quantum wire with a finite well depth. The high symmetry permits us to describe the polarization dependence of optical transitions with simple trigonometric expressions. Despite the simplicity of the model, the analysis retains the essential physics of the problem – namely, two-dimensional quantum confinement with finite well depths in a coupled-band system.

4.2.1 Conduction subbands

The conduction subband wavefunctions and energies in the cylindrical quantum wire may be calculated in a straightforward manner with one-band effective mass theory [4]. The conduction wavefunction takes the form

$$\Psi^{C}_{L_z,\pm\frac{1}{2}}[k_z] = \frac{1}{N_c}\begin{pmatrix} J_{L_z}[k_{L_z,n}r](r<R) \\ H_{L_z}[\sqrt{k^2_{L_z,n}-V_c}\; r](r>R) \end{pmatrix} Exp[iL_z\theta]Exp[ik_z z]|\frac{1}{2},\frac{\pm 1}{2}\rangle, \qquad (4.1)$$

where J and H are Bessel functions and Hankel functions, and the radial wavenumber $k_{L_z,n}$ is a discrete quantity determined by the requirement of continuity of the envelope and its derivative across the interface between the well and barrier regions. The radius of the wire is R and the conduction band offset is V_c. The energy of the state is given by $E_c[k_z] = \frac{\hbar^2}{2m_c^*}(k_{L_z,n}^2 + k_z^2)$. N_c is a coefficient which normalizes the wavefunction. The term $|\frac{1}{2}, \frac{\pm 1}{2}\rangle$ is simply the conduction band Bloch function with spin up or down. In what follows we will adopt the convention whereby the conduction subband which corresponds to a particular value of $|L_z|$ is labeled "C(L_z)." The envelope component of the wavefunction of lowest subband, C(0), has even parity in the plane perpendicular to the wire, and is only doubly degenerate (due to the spin degeneracy of the Bloch function). The next subband, C(1), has quantum number $L_z = \pm 1$ and therefore is four-fold degenerate. This state has odd envelope parity in the plane perpendicular to the wire axis. As a matter of terminology, from this point on when we refer to envelope parity, it will be understood to mean parity in the plane perpendicular to the wire axis.

4.2.2 Valence subbands

The valence band states of the quantum wire represent a more challenging problem than the conduction states just discussed. In the simplest approximation, the two split-off bands are assumed to be decoupled from the four Γ_8 bands (the light- and heavy-holes). However, coupling among the remaining four bands still may not be neglected. Thus, a multi-band envelope function technique must be employed. We adopt the approach of chapter 2, in which the bulk Luttinger Hamiltonian is expressed in a representation of the appropriate *cylindrical waves* rather than of Bloch *plane waves.* (The approach used here employs an

explicit representation of the Hamiltonian but is equivalent to the coordinate-free approach of Ref.[8]). This basis is simply the set of eigenstates of the projection of total angular momentum along the z axis. The total angular momentum operator is the sum of the angular momenta of the envelope and Bloch components of the total wavefunction. It is defined by the relation $\vec{F} = \vec{J} + \vec{L}$, where $\vec{J}$ is the angular momentum which characterizes the familiar zone-center Bloch functions $|J, J_z\rangle$, (J=3/2 for the light- and heavy-hole states), and $\vec{L}$ is the angular momentum of the envelope part of the wavefunction. Since $\mathbf{F_z} = \mathbf{J_z} + \mathbf{L_z}$, the necessary basis may be written in the product form

$$|k_z, k, F_z; J, J_z\rangle = |J, J_z\rangle |k_z; k, L_z = F_z - J_z\rangle. \tag{4.2}$$

Here the envelope vector $|k_z; k, L_z\rangle$, which has angular momentum L_z about the z-axis, is represented in cylindrical coordinates by

$$\langle r, \theta, z | k_z; k, L_z\rangle = \frac{i^{L_z}}{2\pi} H_{L_z}(kr)\, e^{iL_z\theta}\, e^{ik_z z}. \tag{4.3}$$

In this expression, k is a radial wavenumber, H_{L_z} is a Hankel function of order L_z, and k_z is the component of crystal momentum along the z-axis.

The process of expressing the bulk bandstructure Hamiltonian in this basis involves a unitary transformation from the conventional Bloch plane wave representation and is described in detail in Section 2.7. It is found that the Hamiltonian is block diagonal in F_z, with sub-blocks corresponding to a given quantum number F_z taking the identical form :

$$\begin{array}{cccc} |3/2,3/2\rangle|F_z-3/2\rangle & |3/2,1/2\rangle|F_z-1/2\rangle & |3/2,-1/2\rangle|F_z+1/2\rangle & |3/2,-3/2\rangle|F_z+3/2\rangle \end{array}$$

$$\mathbf{H}^{\Gamma_8}_{\mathbf{F_z}} = \begin{pmatrix} E_v + \frac{T}{2} & -iL & -M & 0 \\ iL^* & E_v + \frac{T}{6} + \frac{2Q}{3} & 0 & -M \\ -M^* & 0 & E_v + \frac{T}{6} + \frac{2Q}{3} & iL \\ 0 & -M^* & -iL^* & E_v + \frac{T}{2} \end{pmatrix}. \tag{4.4}$$

In Eq.(4.4), the basis vectors are written as products of a zone-center Bloch function, $|J, J_z\rangle$ and the envelope state, $|L_z\rangle$, where $L_z = F_z - J_z$. This form ensures that all the basis vectors correspond to the same quantum number F_z. In the envelope vector, k and k_z are understood and therefore omitted. The terms in the matrix are given by

$$\begin{aligned} -\frac{T}{2} &= (\gamma_1 + \gamma_2)\frac{k^2}{2} + (\gamma_1 - 2\gamma_2)\frac{k_z^2}{2} \\ -(\frac{T}{6} + \frac{2Q}{3}) &= (\gamma_1 - \gamma_2)\frac{k^2}{2} + (\gamma_1 + 2\gamma_2)\frac{k_z^2}{2} \\ -L &= -i2\sqrt{3}\gamma_2\frac{kk_z}{2} \\ -M &= \sqrt{3}\gamma_2\frac{k^2}{2}, \end{aligned} \quad (4.5)$$

where the parameters γ_1 and γ_2 are the usual Luttinger parameters, and we have invoked the spherical approximation ($\gamma_2 = \gamma_3$) [9,10]. E_v denotes the bulk valence band-edge, which will later be taken to be a function of position in modeling the quantum wire heterostructure.

To calculate the eigenstates and eigenenergies of the quantum wire which correspond to a given total angular momentum quantum number F_z, we model the heterostructure by a method similar to the conduction band calculation. This is accomplished by introducing a radial potential V_v in the barrier region equal to the valence band discontinuity across the interface at $r = R$. Inside and outside the quantum wire, we find the heavy-hole and light-hole eigenvectors for a given quantum number F_z corresponding to a given energy and down-wire momentum k_z. We then form in each region the most general possible linear combination of these bulk eigenvectors and impose appropriate boundary conditions. To begin with, the wavefunction must be regular at the origin, so that the solution in the region $r < R$ takes the general form

$$\psi_{F_z} = \left\{A_1\phi_{F_z}^{HH1}(r,z) + A_2\phi_{F_z}^{HH2}(r,z) + A_3\phi_{F_z}^{LH1}(r,z) + A_4\phi_{F_z}^{LH2}(r,z)\right\}, (r < R), \quad (4.6)$$

where the $\phi_{F_z}(r, z)$ are the bulk light- and heavy-hole eigenvectors which are regular at r = 0, given in Eqs. 2.51 and 2.52 in chapter 2. The wavefunction in the region r > R is

$$\psi_{F_z} = \left\{ A_5 \phi_{F_z}^{HH1}(r, z) + A_6 \phi_{F_z}^{HH2}(r, z) + A_7 \phi_{F_z}^{LH1}(r, z) + A_8 \phi_{F_z}^{LH2}(r, z) \right\}, (r > R), \qquad (4.7)$$

where for bound states, the $\phi_{F_z}(r, z)$ are the bulk light- and heavy-hole eigenvectors which vanish at infinity, given in Equations 2.51 and 2.52 in chapter 2.

By requiring continuity of the wavefunction (four equations) and the probability current (four more equations) across the interface between well and barrier regions at r = R, we obtain an 8×8 homogenous, linear system of equations for the eight unknown mixing coefficients $A_1 ... A_8$. The requirement that the determinant of the matrix must vanish for a solution to exist supplies an implicit relation determining the allowed quantum wire eigenenergies for a given F_z and k_z. This relation appears in chapter 2, Equation 2.55.

In Figure 4.2 we show the subband dispersion, $E(k_z)$ for bound states corresponding to $F_z = \pm 1/2$ and $F_z = \pm 3/2$, respectively, in a GaAs quantum wire with radius 5 nm embedded in $Al_{0.3}Ga_{0.7}As$. Bandstructure parameters have been chosen to reflect $m_{hh}^* = 0.45 m_o$ and $m_{lh}^* = 0.082 m_o$. Figure 4.2 represents all bound light- and heavy-hole states for this radius because there are no bound valence states for the 5 nm radius wire with $|F_z| > 3/2$. Since eigenstates in a quantum wire are admixtures of light- and heavy-hole character even at zone-center, these band labels are not useful. The subbands in the figure are therefore labeled by the irreducible representation, $E_{F_z,n}^{\pm}$, to which they correspond. The subband index, n, is assigned on the basis of the energy at zone-center. The superscript '±' is a reminder of the *zone-center envelope* parity of the subband. Note that this is *not* the parity of the total wavefunction, but only of the envelope, and that off of zone-center parity is *not* a good quantum number.

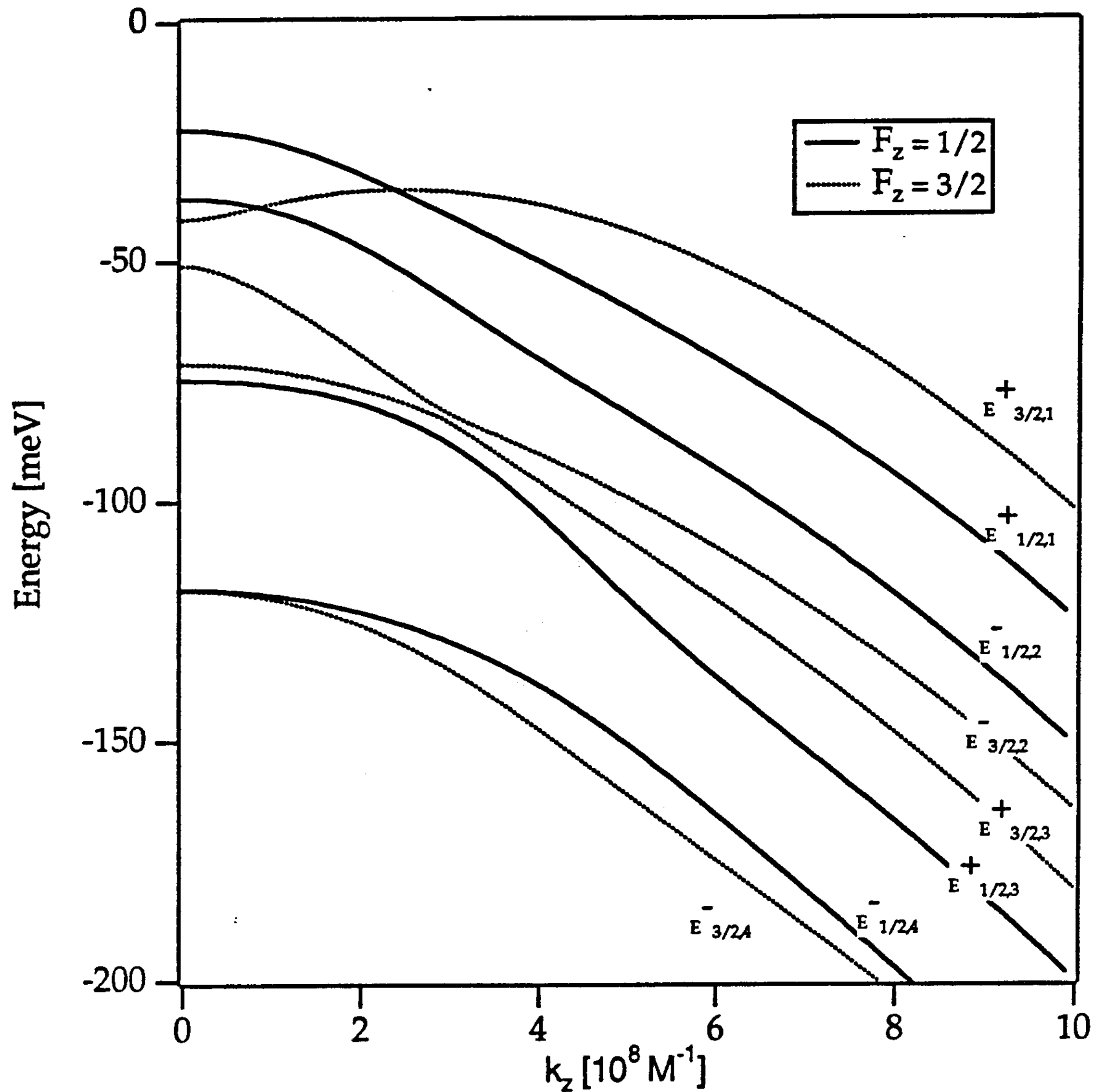

Figure 4.2: Valence subband dispersion $E(k_z)$ for a 5 nm radius GaAs quantum wire embedded in an $Al_{0.3}Ga_{0.7}As$ barrier (well depth =150 meV). The dispersion curves are labeled $E^{\pm}_{F_z,n}$, where $\pm$ denotes the envelope parity of the zone center state, and n is a subband index. The subbands with quantum number $F_z = \pm 1/2$ and $F_z = \pm 3/2$ and drawn with solid and dashed lines, respectively.

The strong non-parabolicity of the subband structure in Figure 4.2 is a result of the no-crossing rule for coupled states, reflecting the importance of band-coupling effects in this system. The most extreme result of this coupling is seen in the structure of the highest subband, $E^+_{3/2,1}$, which is actually electron-like at zone-center. Note that subbands with different F_z cross, because they are not coupled. Similar results have been obtained by others for quantum wires of cylindrical [8] and rectangular [11,12] cross-section.

Having determined the subband dispersion relations of the coupled valence states of the quantum wire, it is a simple matter to derive the DOS. For a one-dimensional structure, it is well known that the DOS per unit length is given by

$$D(E) = \sum_i g_i \frac{1}{\pi} \left| \frac{dk^i_z[E]}{dE} \right|, \tag{4.8}$$

where index i runs over all subbands, $g_i = 2$ is the Kramer's degeneracy of each subband, and $k^i_z[E]$ satisfies $E_i[k^i_z] = E$. In Figure 4.3(a-b) we separately present the calculated DOS corresponding to the $F_z = 1/2$ and $F_z = 3/2$ subbands, whose dispersion relations are plotted in Figure 4.2. The peaks in these plots represent singularities at the subband edges, and are labeled according to the subbands to which they correspond. To smooth out these singularities, the DOS functions have been convoluted with a normalized Gaussian lineshape function, g(E), with a line width, $\delta E =$ of 0.5 meV:

$$g(E) = \frac{1}{\sqrt{\pi}\delta E} exp[-\frac{(E-E')^2}{\delta E^2}]. \tag{4.9}$$

The dominant feature in these plots is the large peak in Figure 4.3(b) corresponding to the electron-like subband denoted $E^+_{3/2,1}$ in Figure 4.2(b). In Section 4.4 we will see that this feature has a pronounced effect upon the polarization dependence of the optical spectra of a quantum wire.

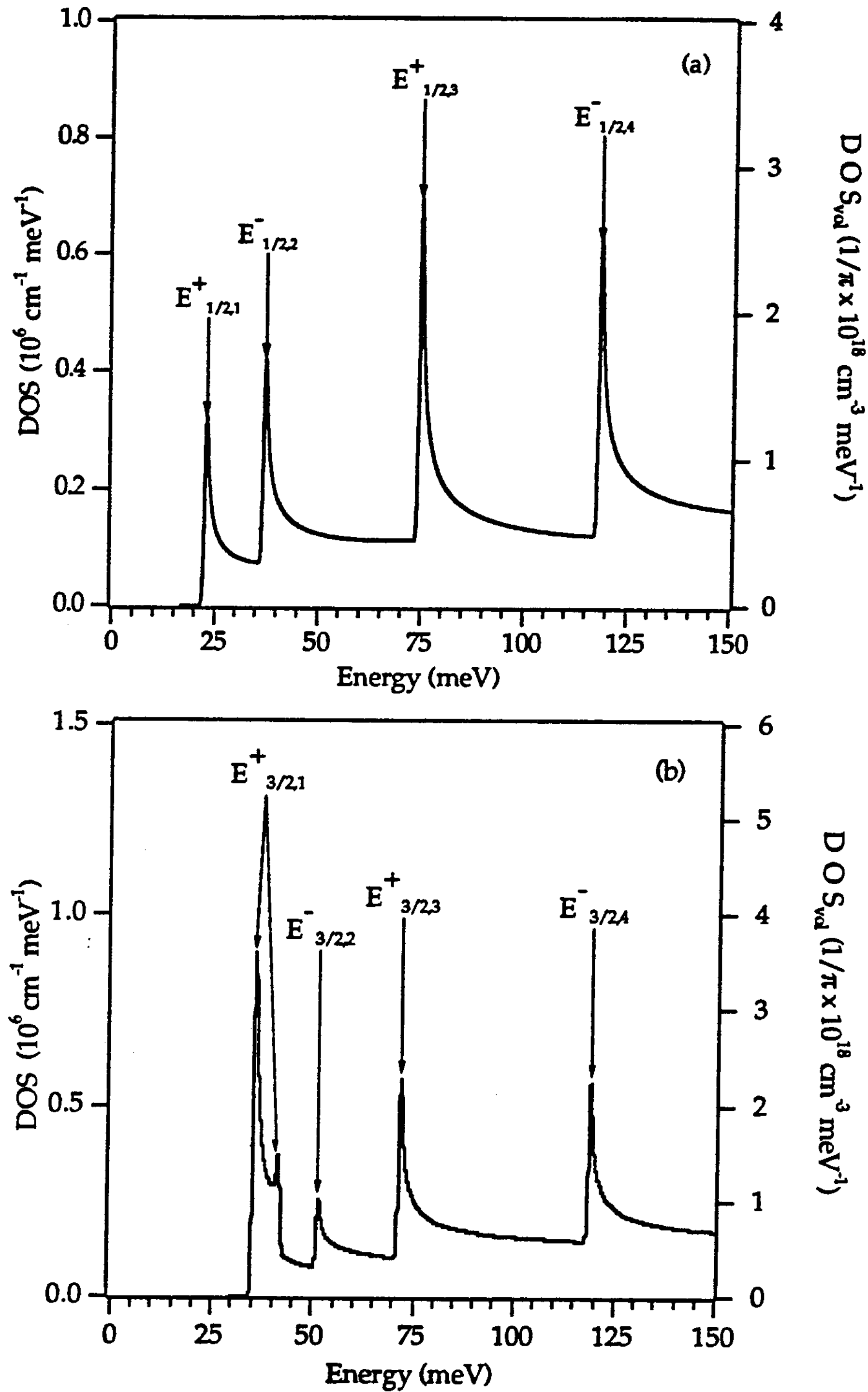

Figure 4.3: Valence band DOS for a 5 nm radius GaAs quantum wire embedded in an $Al_{0.3}Ga_{0.7}As$ barrier (well depth =150 meV). (a): $F_z = \pm 1/2$. (b): $F_z = \pm 3/2$.

4.3 Interband optical transitions in cylindrical quantum wires

4.3.1 Polarization dependence of the optical matrix element

The technique outlined in the last section for determining the valence subband wavefunctions of the quantum wire permits us to calculate the interband optical transition matrix elements. For a given valence subband $\mathrm{E_{F_z,n}}$ we determine the coefficients $\mathrm{A_1 ... A_8}$ in Eqs. (4.6, 4.7) and obtain a normalized wavefunction of the following general form

$$\Psi^{\mathrm{v}}_{\mathrm{F_z,n}}[\mathrm{k_z}] = \begin{pmatrix} f_n^1(r)Exp[i(F_z - \frac{3}{2})\theta] \\ f_n^2(r)Exp[i(F_z - \frac{1}{2})\theta] \\ f_n^3(r)Exp[i(F_z + \frac{1}{2})\theta] \\ f_n^4(r)Exp[i(F_z + \frac{3}{2})\theta] \end{pmatrix} \mathrm{Exp[ik_z z]}. \tag{4.10}$$

This vector is written in the basis of zone-center Bloch functions $|\mathrm{J, J_z}\rangle$, taken in the order $|\frac{3}{2},\frac{3}{2}\rangle ... |\frac{3}{2},-\frac{3}{2}\rangle$. These Bloch function are given explicitly at the end of chapter 2. The radial functions $\mathrm{f_n^1(r)}$ ... $\mathrm{f_n^4(r)}$ denote the radial components of Eqs.(4.6, 4.7) determined for a given subband of quantum number $\mathrm{F_z}$ and subband index n (see Figure 4.2) and are parametrically dependent on $\mathrm{k_z}$. The conduction states involved in the optical transition are much simpler and are given explicitly in Eq.(4.1).

The polarization dependent interaction of a quantum wire with an optical field may be represented by the $\vec{\mathrm{A}} \cdot \vec{\mathrm{P}}$ interaction Hamiltonian. Here $\hat{\mathrm{A}}$ is the polarization vector of a linearly polarized optical wave, which we take to be $\vec{\mathrm{A}} = \mathrm{Cos}(\theta)\hat{\mathrm{z}} + \mathrm{Sin}(\theta)\hat{\mathrm{x}}$ where z is the wire axis. Using the wavefunctions given in Eqs.(4.1, 4.10) for conduction subband $C(L_z)$ and valence subband $\mathrm{E_{F_z,n}}$, we therefore write a $\mathrm{k_z}$-dependent squared transition matrix element of the general form,

$$|\mathrm{M}|^2_{\mathrm{C(L_z)-E_{F_z,n}}} = \{|\langle\psi^{\mathrm{C}}_{\mathrm{L_z},-\frac{1}{2}}[\mathrm{k_z}]|\vec{\mathrm{P}}|\psi^{\mathrm{v}}_{\mathrm{F_z,n}}[\mathrm{k_z}]\rangle \cdot \hat{\mathrm{A}}|^2 + |\langle\psi^{\mathrm{C}}_{\mathrm{L_z},\frac{1}{2}}[\mathrm{k_z}]|\vec{\mathrm{P}}|\psi^{\mathrm{v}}_{\mathrm{F_z,n}}[\mathrm{k_z}]\rangle \cdot \hat{\mathrm{A}}|^2\}. \tag{4.11}$$

Examination of Eqs.(4.1, 4.10- 4.11) reveals two important selection rules that vastly simplify our analysis. The first is that k_z is conserved (k-selection). The second is that there is a strict envelope angular momentum selection rule. For example, consider transitions involving the lowest conduction subband C(0) ($L_z = 0$) and any of the quantum wire valence subbands $E_{F_z,n}$ with quantum number $F_z = 1/2$. In this case, integration over the coordinate θ eliminates all but the second component of the vector Eq.[4.10]. The squared matrix element for these transitions thus simplifies to the following expression:

$$|M|^2_{C(0)-E_{\frac{1}{2},n}} = (|\langle 1/2, 1/2|\vec{P}|3/2, 1/2\rangle \cdot \hat{A}|^2 + |\langle 1/2, -1/2|\vec{P}|3/2, 1/2\rangle \cdot \hat{A}|^2) I^2_{0,(\frac{1}{2},n)}[k_z], \quad (4.12)$$

where all of the information about the envelopes is now contained in the radial overlap integral for the particular transition, $I^2_{0,(\frac{1}{2},n)}[k_z]$. Utilizing the explicit representations $|1/2, 1/2\rangle = |s\rangle \uparrow$, $|1/2, -1/2\rangle = |s\rangle \downarrow$, and $|3/2, 1/2\rangle = \sqrt{\frac{2}{3}}|z\rangle \uparrow - \sqrt{\frac{1}{6}}(|x\rangle + i|y\rangle) \downarrow$, the matrix element assumes the remarkably simple, analytical, form

$$|M|^2_{C(0)-E_{\frac{1}{2},n}} = (\frac{2}{3}\,\mathrm{Cos}^2(\theta) + \frac{1}{6}\,\mathrm{Sin}^2(\theta))|P|^2 I^2_{0,(\frac{1}{2},n)}[k_z]. \quad (4.13)$$

Here P is the matrix element of the momentum operator between orbital 's' and 'p' states: $P = -i\langle s|P_z|z\rangle$ [13]. In this work we use the value $\frac{2}{m_o}|P|^2 = 28.2$ eV, where m_o is the free electron mass [14]. All of the polarization dependence is contained in a simple trigonometric expression, and is the same for all transitions between the lowest conduction subband and the valence subbands with $|F_z| = 1/2$. The energy dependence of the matrix element is entirely contained in the overlap integral for each transition through its dependence on k_z.

Similar simplifications apply for transitions between C(0) and the valence subbands $E_{F_z,n}$ with quantum number $F_z = 3/2$. In this case, using $|3/2, 3/2\rangle = -\frac{1}{\sqrt{2}}(|x\rangle + i|y\rangle) \uparrow$,

we find the result

$$|\mathrm{M}|^2_{\mathrm{C(0)-E_{\frac{3}{2},n}}} = \frac{1}{2}\,\mathrm{Sin}^2(\theta)|\mathrm{P}|^2\ \ \mathbf{I}^2_{0,(\frac{3}{2},n)}[\mathrm{k_z}], \tag{4.14}$$

again a remarkably simple analytical form.

In Figure 4.4 we show the polarization dependence of the relative squared optical transition matrix elements for these transitions. Note that the polarization dependence is independent of the size or composition of the quantum wire. It is clear that transitions involving the $F_z = 1/2$ subbands are four times stronger for an electric field vector oriented along the wire than they are for the perpendicular orientation. For the $F_z = 3/2$ valence subbands, the trend is the reverse; in this model these states do not interact at all with optical waves polarized along the axis of the wire. This is perhaps a surprising result, but one which we will see in Section 4.5 could have been anticipated on the basis of group theory. The importance of this result arises from the fact that the two lowest energy allowed optical transitions are respectively the $C(0) - E^{\pm}_{\frac{1}{2},1}$ and $C(0) - E^{\pm}_{\frac{3}{2},1}$ transitions. Figure 4.4 shows that the matrix elements for these transitions have a pronounced relative anisotropy. This will have a significant effect on the absorption and gain of quantum wires.

In Figures 4.5(a-b) we show the dependence on k_z of the overlap integrals in equations 4.13 and 4.14, which describe transitions involving C(0) and each of the bound valence subbands with quantum number $F_z = 1/2$ and $F_z = 3/2$, respectively. These calculations were performed for a GaAs quantum wire of radius 5 nm, embedded in $Al_{0.3}Ga_{0.7}As$. In contrast to the *polarization* dependence (Fig. 4.4), the magnitude and energy dependence of the matrix elements depend on the size and composition of the wire. Note that certain transitions are forbidden at zone-center ($k_z = 0$) due to an additional selection rule on envelope parity. These transitions become allowed as we move away from zone-center because

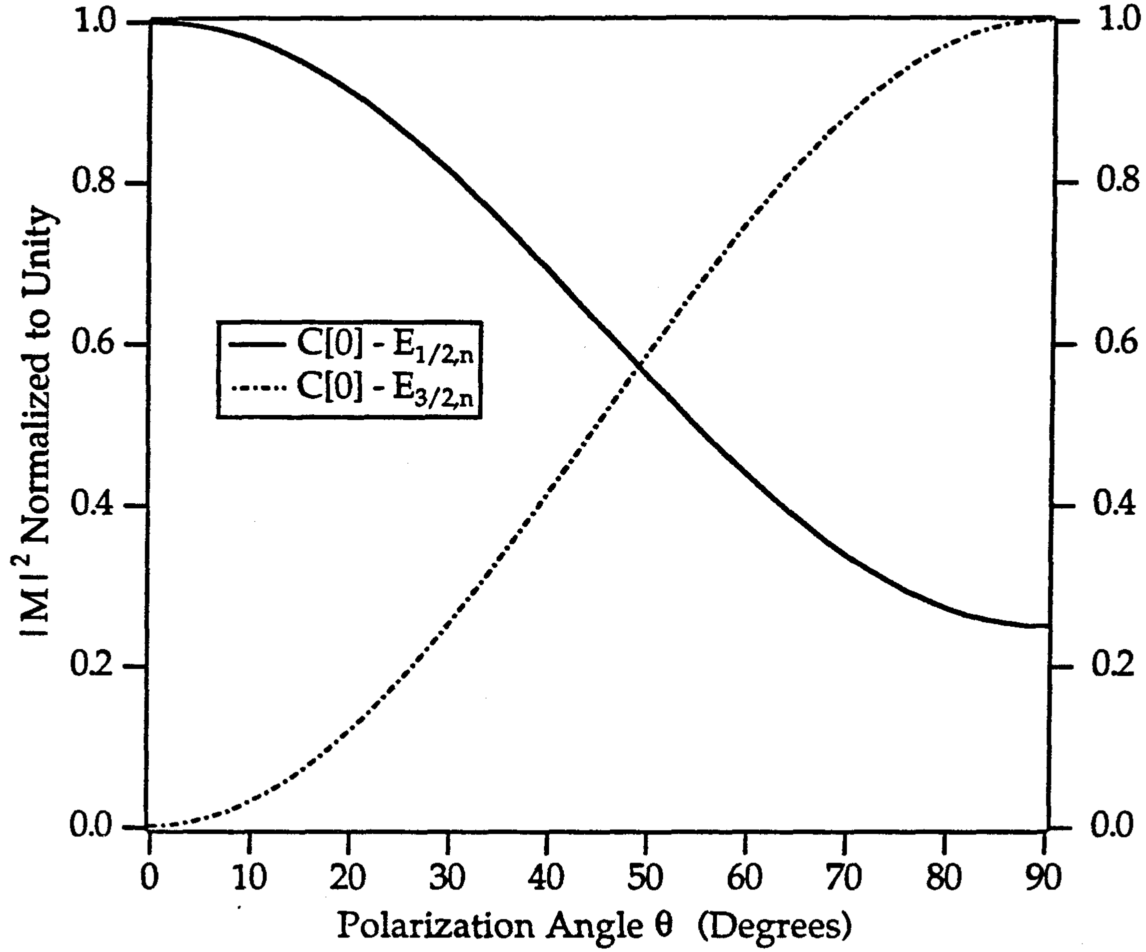

Figure 4.4: Polarization dependence of the squared optical transition matrix element for transitions between the lowest electron subband, C(0), and the highest two valence subbands, respectively $E^{+}_{1/2,1}$ and $E^{+}_{3/1,1}$. The matrix elements are normalized to unity and are plotted versus the polarization angle θ measured from the wire axis (ie, at $\theta = 0$, $\vec{E}$ is parallel to the wire axis). The polarization dependence is independent of the size or composition of the quantum wire.

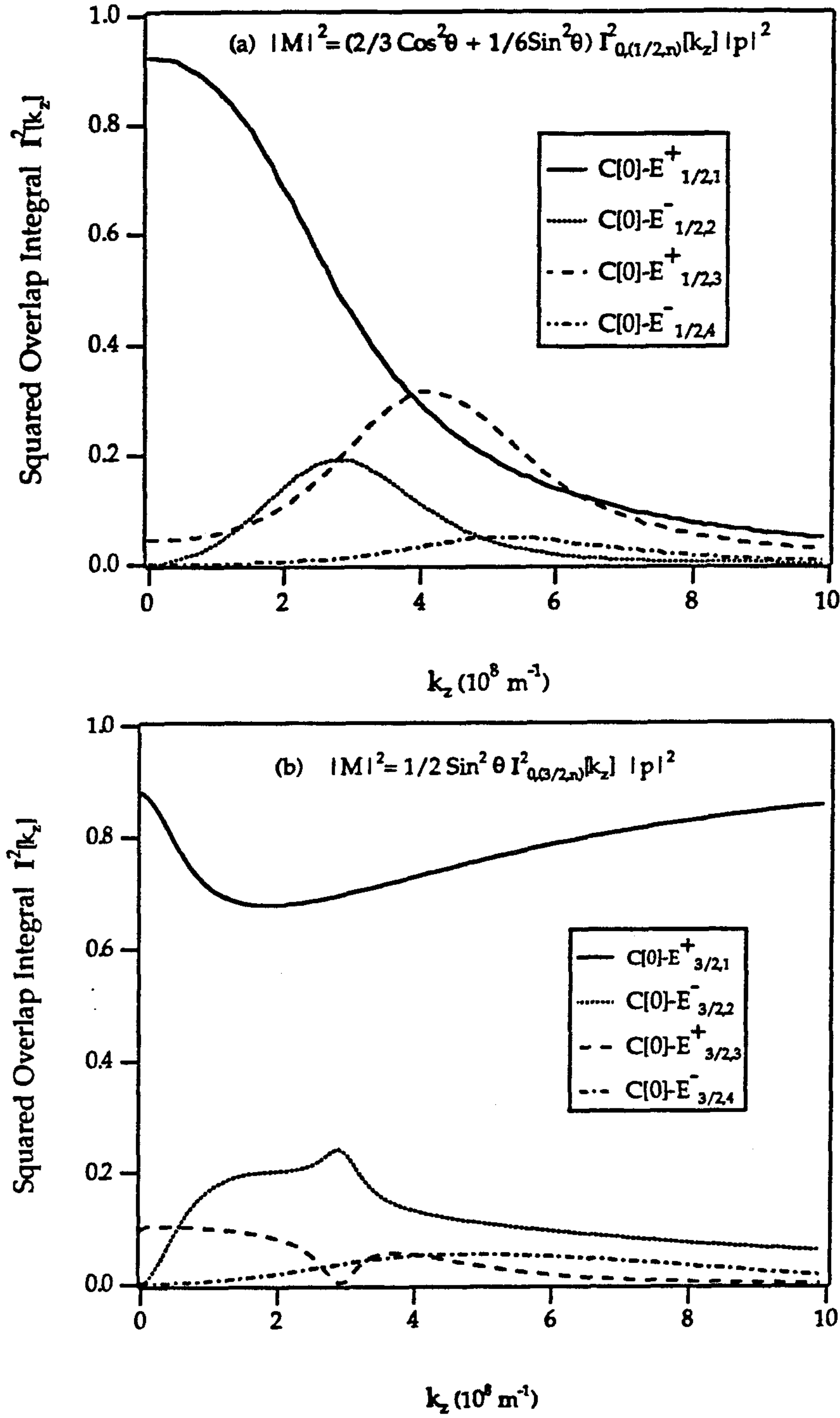

Figure 4.5: Squared overlap integral for transitions between C(0) and valence subbands with quantum number (a): $F_z = \pm 1/2$ and (b): $F_z = \pm 3/2$. The calculation is performed for a 5 nm radius GaAs quantum wire embedded in $Al_{0.3}Ga_{0.7}As$.

there, envelope parity is no longer a good quantum number. Physically, band-mixing effects cause subbands with odd envelope parity at zone-center pick up an increasing degree of even parity character as k_z is increased from zero. Conversely, strongly overlapping transitions at zone-center generally becomes weaker as k_z increases.

Continuing in this fashion, we can derive expressions for the matrix element for transitions involving higher conduction subbands. For a 5 nm radius GaAs quantum wire embedded in $Al_{0.3}Ga_{0.7}As$, there is only one other bound conduction subband, C(1), which corresponds to quantum number $L_z = \pm 1$. This subband is actually four-fold degenerate due to the additional two-fold spin degeneracy. Application of the calculational procedure just developed leads to the following results:

$$|M|^2_{C(1)-E_{\frac{1}{2},n}} = \frac{1}{2}\,\mathrm{Sin}^2(\theta)|P|^2\;\mathbf{I}^2_{-1,(\frac{1}{2},n)}[k_z] + (\tfrac{2}{3}\,\mathrm{Cos}^2(\theta)|P|^2 + \tfrac{1}{6}\,\mathrm{Sin}^2(\theta)|P|^2)\;\mathbf{I}^2_{1,(\frac{1}{2},n)}[k_z] \quad (4.15)$$

$$|M|^2_{C(1)-E_{\frac{3}{2},n}} = (\tfrac{2}{3}\,\mathrm{Cos}^2(\theta)|P|^2 + \tfrac{1}{6}\,\mathrm{Sin}^2(\theta)|P|^2)\;\mathbf{I}^2_{1,(\frac{3}{2},n)}[k_z]. \quad (4.16)$$

Note that, in contrast to the transitions involving the ground conduction subband, the polarization dependence in Eq.(4.15) involves the overlap integrals, and thus depends upon the radius and composition of the wire, as well as on k_z. The overlap integrals in these equations are defined as follows: $\mathbf{I}_{-1,(\frac{1}{2},n)}$ is the radial overlap between the first excited conduction state C(1) and the component $f^1_n(r)$ of valence state $E_{1/2,n}$, $\mathbf{I}_{1,(\frac{1}{2},n)}$ is the radial overlap of C(1) and the component $f^3_n(r)$ of valence state $E_{1/2,n}$, and $\mathbf{I}_{1,(\frac{3}{2},n)}$ is the radial overlap between C(1) and the component $f^2_n(r)$ of valence state $E_{3/2,n}$. In Figures 4.6(a-b), we plot the squared transition matrix element for transitions involving the $F_z = 1/2$ valence states and C(1) for electric fields oriented parallel and perpendicular to a 5 nm radius GaAs quantum wire embedded in $Al_{0.3}Ga_{0.7}As$ as a function of down-wire momentum, k_z. Figure 4.7 shows the k_z-dependence of the matrix element connecting C(1) to the various $F_z = 3/2$

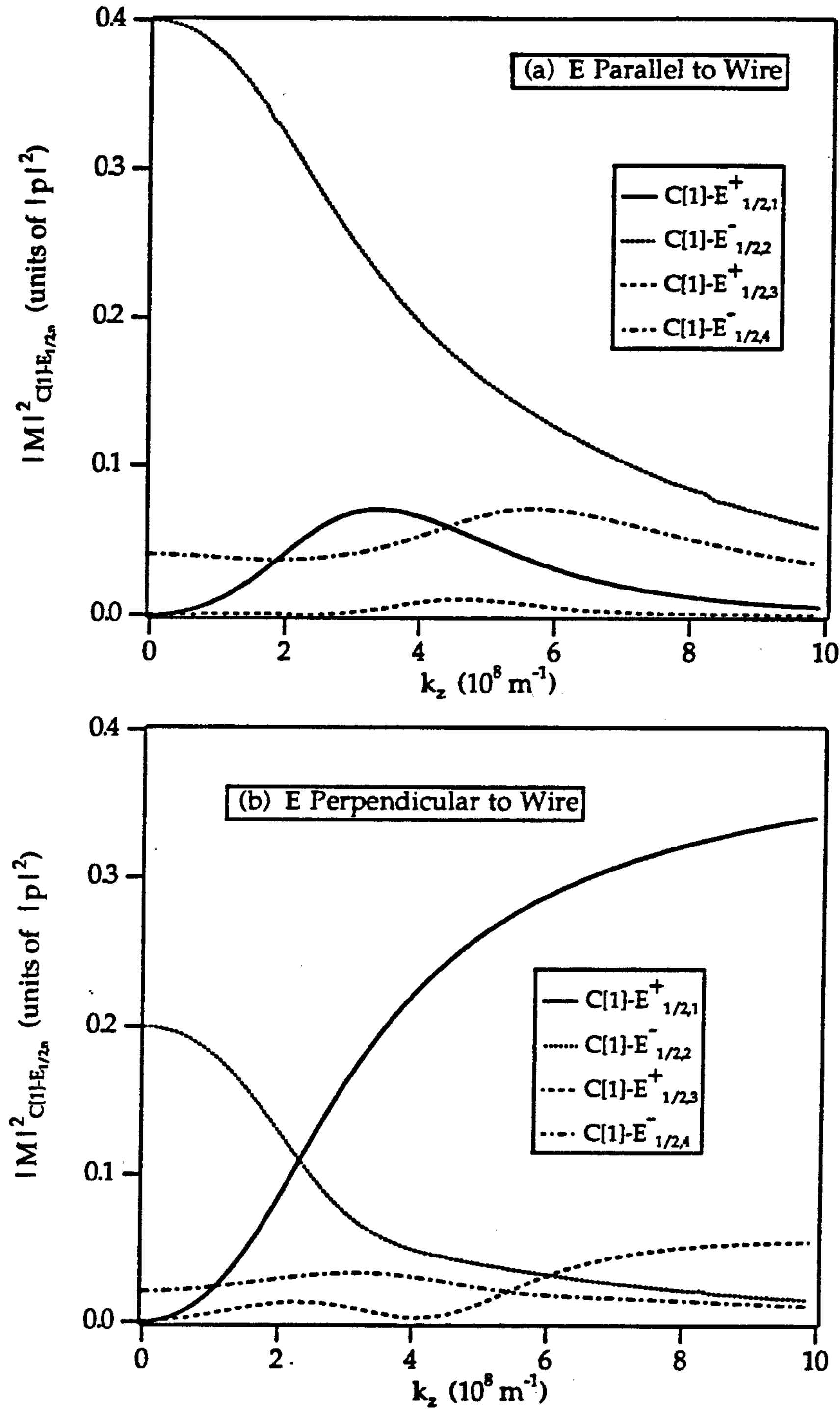

Figure 4.6: Squared optical matrix element for the transitions between C(1) and valence subbands with quantum number $F_z = \pm 1/2$. Electric field is oriented in (a), parallel, and in (b), perpendicular, to the wire. The curves are plotted in units of $|P|^2$, versus k_z.

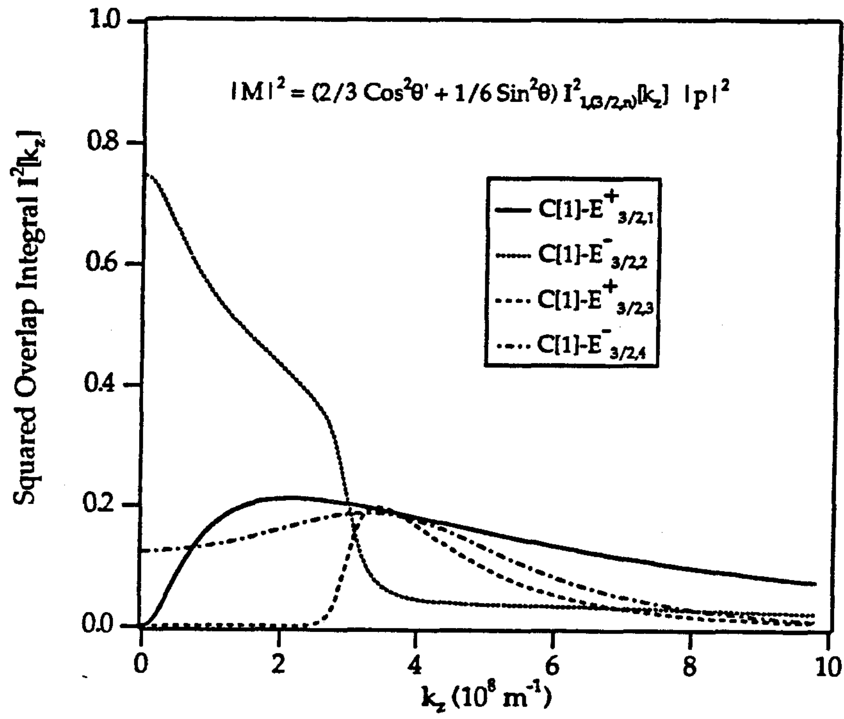

Figure 4.7: Squared overlap integral for transitions between C(1) and valence subbands with quantum number $F_z = \pm 3/2$, plotted versus down-wire momentum k_z. The calculation is performed for a 5 nm radius GaAs quantum wire embedded in an $Al_{0.3}Ga_{0.7}As$ barrier.

states. The polarization dependence for these transitions is the same as that depicted in Figure 4.4 for the transitions connecting the C(0) conduction subbands to the $F_z = 1/2$ valence subbands.

4.3.2 Joint density of states

Figures 4.4- 4.7 describe the polarization dependent optical transition matrix elements between all bound conduction and valence subbands for a 5 nm radius GaAs quantum wire embedded in $Al_{0.3}Ga_{0.7}As$. We now calculate the joint density of states (JDOS) for these transitions. For k_z conserving transitions, the JDOS may be written

$$J[\hbar\omega] = \sum_{c,v} \frac{2}{\pi} \left| \frac{dk_z}{dE_{c,v}} \right|_{E_{c,v}=\hbar\omega}, \tag{4.17}$$

where c and v symbolize conduction and valence subband indices, and k_z satisfies $E_{c,v} = E_c[k_z] - E_v[k_z]$. The factor of 2 accounts for the two-fold Kramer's degeneracy. In Figures 4.8(a) and (b) we separately plot the JDOS for transitions involving the valence subbands corresponding to $F_z = 1/2$ and $F_z = 3/2$, respectively. The figure actually shows a convolution of the JDOS with a Gaussian lineshape function of width $\delta E = 0.5$ meV. The peaks in the figure are labeled according to the zone-center transition to which they correspond. It is interesting to compare the JDOS at the onset of the lowest energy transition in Figure 4.8(a), denoted C(0) - $E^+_{1/2,1}$, with that of the lowest transition in Figure 4.8(b), C(0) - $E^+_{3/2,1}$. Due to band repulsion effects, the JDOS for the latter transition is nearly three times larger at its peak than for the lower energy transition. This ratio will, however, be lower for larger δE. The effect of increased δE on the optical absorption spectra is examined below.

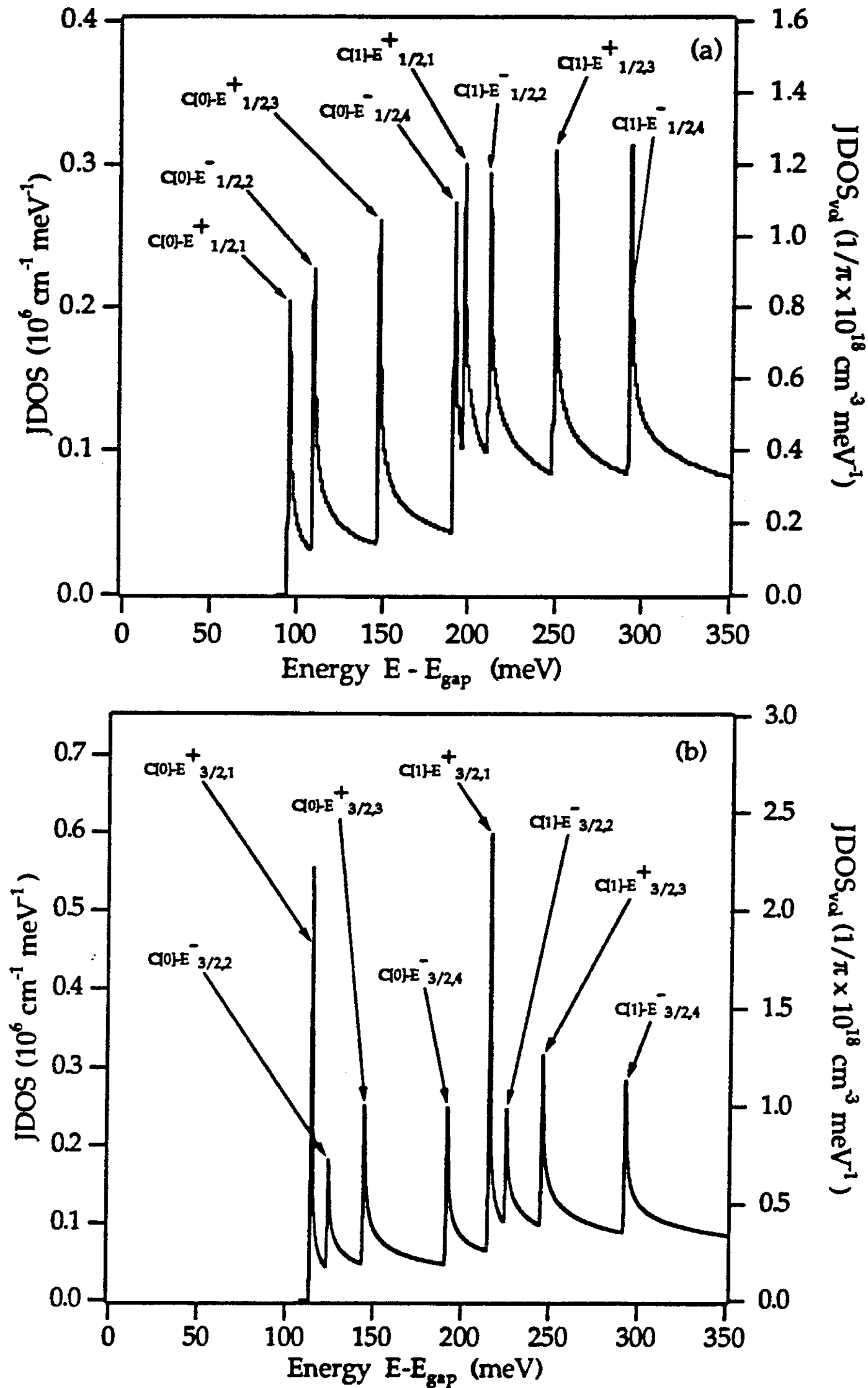

Figure 4.8: Joint density of states for k_z-conserving optical transitions in a 5 nm radius GaAs quantum wire embedded in $Al_{0.3}Ga_{0.7}As$. JDOS for transitions involving valence subbands with quantum number $F_z = \pm 1/2$ and $F_z = \pm 3/2$ are shown in (a) and (b), respectively. Peaks are labeled according to the zone-center transition to which they correspond.

4.4 Optical spectra

4.4.1 Absorption spectra

With the JDOS and transition matrix elements determined, we can calculate polarization-dependent absorption spectra according to the formula,

$$\alpha(\hbar\omega) = \frac{\alpha_0}{\omega} \sum_{c,v} \alpha_{c,v}(\hbar\omega). \quad (4.18)$$

Here, the constant α_0 is given by

$$\alpha_0 = \frac{\pi e^2}{\epsilon_0 c n m_0^2} \text{ (MKS units)}, \quad (4.19)$$

where n is the refractive index, c is the speed of light in vacuum, ϵ_0 is the permittivity of vacuum, and m_0 is the free electron mass. The partial absorption $\sum_{c,v} \alpha_{c,v}(\hbar\omega)$ on the transition between conduction and valence states indexed by c,v is given by

$$\alpha_{c,v}(\hbar\omega) = |M|^2_{c,v} \frac{2}{\pi} \frac{1}{\pi R^2} \left|\frac{dk_z}{dE_{c,v}}\right|_{E_{c,v}=\hbar\omega}. \quad (4.20)$$

The transition matrix element, $|M|^2_{c,v}$, is obtained from Eqs.[4.13- 4.16] and again k_z satisfies $E_{c,v} = E_c[k_z] - E_v[k_z]$. The factor $\frac{1}{\pi R^2}$ gives a volumetric JDOS.

In Figures 4.9(a) and (b) we show calculated absorption spectra for a 5nm radius quantum wire with the same material parameters as above for an electric field oriented parallel and perpendicular to the wire, respectively. The spectra shown were convoluted with a Gaussian linewidth function with $\delta E = 0.5$ meV. The peaks arise from singularities in the JDOS at the subband edges, and should not be confused with excitonic effects, which are not included in this analysis. The peaks are labeled according to the zone-center transition to which they correspond. The effects of the polarization dependence given in Eqs.(4.13- 4.16) are clear in these figures. In particular, there is a large polarization

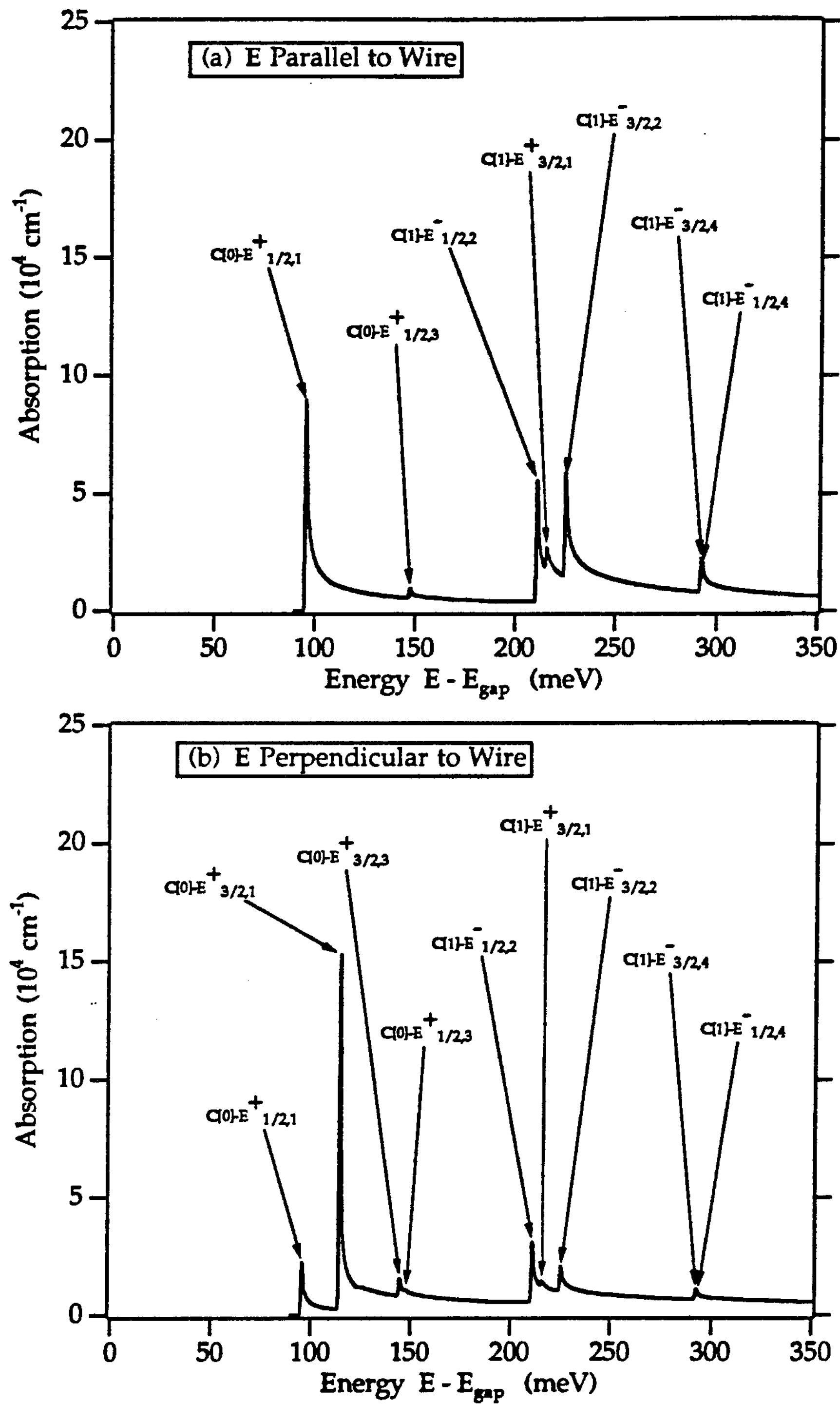

Figure 4.9: Absorption spectra calculated for a 5 nm radius GaAs quantum wire embedded in an $Al_{0.3}Ga_{0.7}As$ barrier. (a): Electric field polarized parallel to the quantum wire. (b): Electric field polarized perpendicular to the wire.

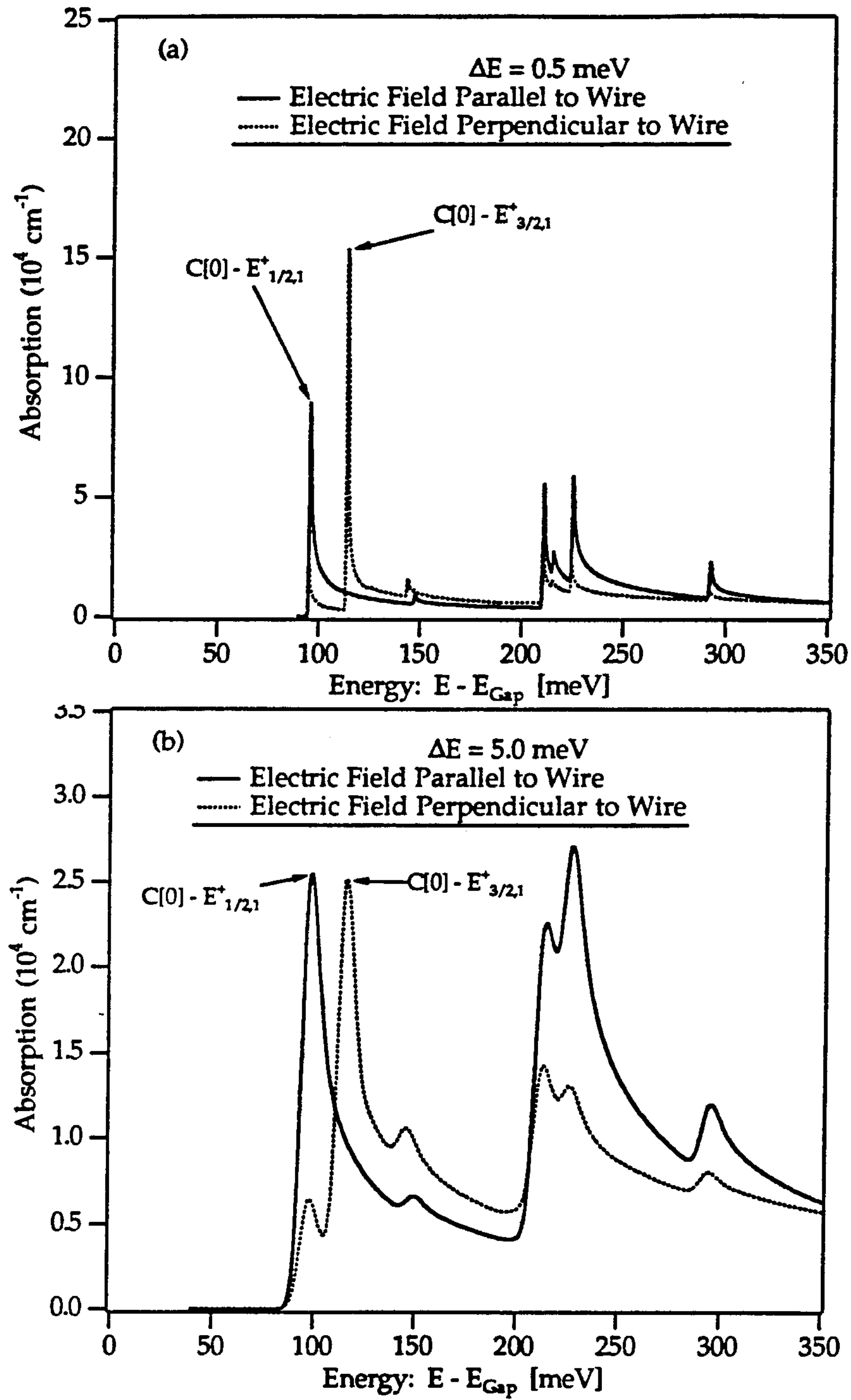

Figure 4.10: Calculated polarization dependent absorption spectra for a 5 nm radius GaAs quantum wire embedded in an $Al_{0.3}Ga_{0.7}As$ barrier. The spectra are broadened with a Gaussian lineshape function with $\delta E = 0.5$ meV in (a), and 5.0 meV in (b).

anisotropy between the two lowest energy peaks, denoted C(0)-$E_{1/2,1}$, and C(0)-$E_{3/2,1}$, in Figures 4.9(a) and (b).

It must be pointed out, however, that the height of the calculated peaks depends upon the linewidth used to broaden the spectra. Figures 4.10 (a) and (b) compare the absorption spectra of a 5 nm radius GaAs wire convoluted with Gaussian lineshape functions with linewidths $\delta E = 0.5$ meV and $\delta E = 5.0$ meV. These figures demonstrate the reduction of peak height with increased broadening, which is particularly pronounced for the C(0)-$E_{3/2,1}$ peak. The anisotropy of the C(0)-$E_{1/2,1}$ and C(0)-$E_{3/2,1}$ peaks in these figures is plotted with respect to the polarization angle between electric field vector and the wire axis in Figure 4.11. The figure shows that the relative polarization anisotropy depends upon the degree to which the quantum wire optical transitions are broadened. Even so, the anisotropy shown in this figure qualitatively fits experimental PLE results in which relative anisotropy of the two lowest energy optical transitions in quantum wire arrays was studied as a function of the polarization of incident light relative to the wires [1,2].

4.4.2 Gain spectra

We now are close to answering the question posed in the introduction of this chapter concerning the optimal geometry for a quantum wire laser. Given that the lowest energy transition in the absorption spectra shown in Figures 4.8- 4.9 is strongest when the electric field is parallel to the quantum wire, the optimal geometry of a quantum wire laser would seem to correspond to Figure 4.1(a). There, the wires are oriented parallel to the end-facets of the laser so as to be aligned with the electric field vector of the lasing TE mode. However, due to the strength of the transition to the next highest energy valence

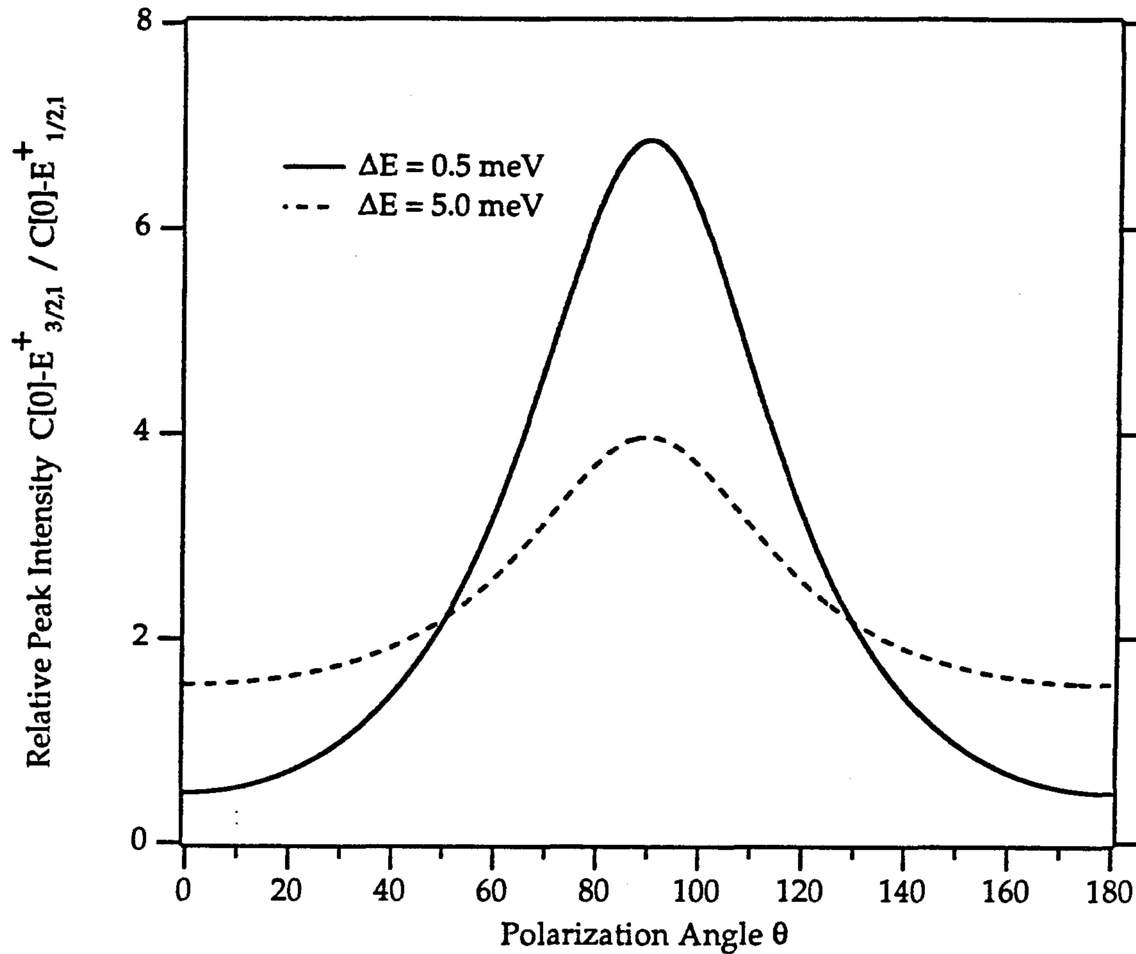

Figure 4.11: Relative polarization dependence of the two peaks labeled "C(0)-$E^+_{1/2,1}$" and "C(0)-$E^+_{3/2,1}$" in Figures 4.9 and 4.10, for two different linewidths. With increasing broadening, the polarization anisotropy is increasingly washed out.

subband this conclusion may be incorrect. In fact, the energy difference between the two lowest energy transitions is only 19 meV, which is less than kT at room temperature. The optimal configuration for a quantum wire laser might therefore be represented by Figure 4.1(b), in which the wires are parallel to the optical axis.

To settle this question, we have performed calculations of the optical gain for different values of the injected carrier density. The gain spectrum for fixed carrier density is given by

$$\gamma(\hbar\omega) = \frac{\alpha_0}{\omega} \sum_{c,v} \gamma_{c,v}(\hbar\omega), \tag{4.21}$$

where the partial gain $\gamma_{c,v}(\hbar\omega)$ on the transition between conduction and valence states indexed by c,v is given by

$$\gamma_{c,v}(\hbar\omega) = |M|^2_{c,v} \; \frac{1}{\pi R^2} \frac{2}{\pi} \; |\frac{dk_z}{dE_{c,v}}|_{E_{c,v}=\hbar\omega} \;\; \{f_c - f_v\}\,. \tag{4.22}$$

Here, $|M|^2_{c,v}$ is obtained from Eqs.[4.13- 4.16]. The momentum k_z satisfies $E_{c,v} = E_c[k_z] - E_v[k_z]$. The f_c and f_v are Fermi functions for the conduction and valence bands. The quasi-Fermi levels of the conduction and valence bands are adjusted such that the total electron and hole concentrations in the wire are equal.

The calculated polarization resolved gain spectra are shown in Figure 4.12 for carrier injection levels of $3.0 \times 10^{18}\text{cm}^{-3}$ and $6.0 \times 10^{18}\text{cm}^{-3}$. The spectra are broadened with a Gaussian lineshape function with δE= 5 meV. This approximately corresponds to a Lorentzian lineshape function with a dephasing time of 0.1 pSec – a value typical of GaAs laser diodes. The peak gains for the given carrier densities are over an order of magnitude larger than corresponding values calculated for GaAs quantum well lasers. This results from several factors, the most important of which is the existence of subband edge singularities

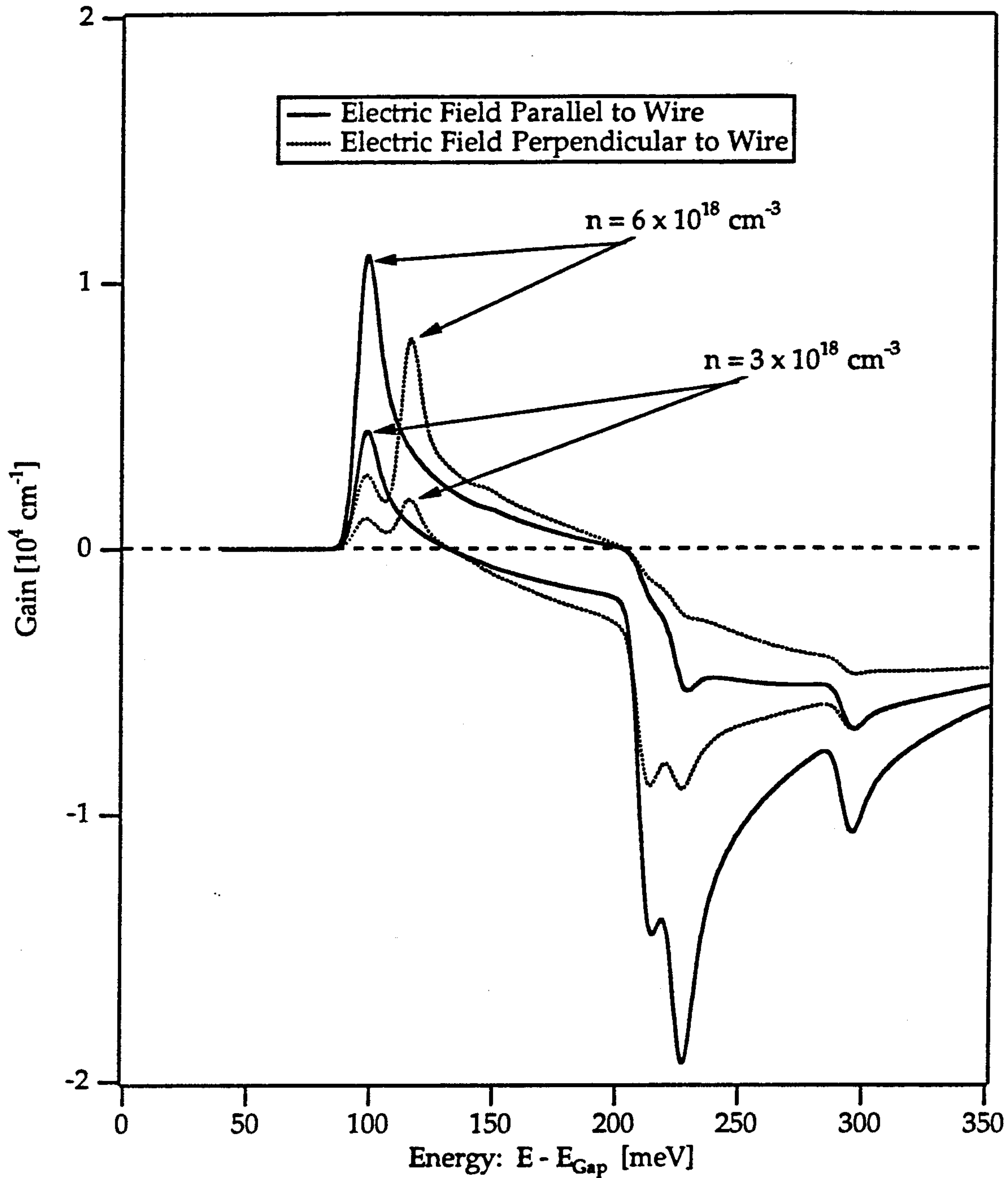

Figure 4.12: Calculated polarization dependent gain spectra for different field orientations for a 5 nm radius GaAs quantum wire embedded in an $Al_{0.3}Ga_{0.7}As$ barrier, for carrier concentrations of $3.0 \times 10^{18} cm^{-3}$ and $6.0 \times 10^{18} cm^{-3}$. The spectra are broadened with a Gaussian lineshape function with δE= 5 meV.

in the DOS of the quantum wire. Also, the effective mass of the uppermost valence subband, which was reported in the last chapter to be $0.16m_0$, is significantly reduced over the bulk heavy hole mass. Lastly, the optical transition matrix element for the lowest energy transition is larger than that in a quantum well by a factor of 4/3, and larger by a factor of 2 over that in bulk GaAs.

The figure shows that at low carrier injection levels, the peak gain is obtained for an electric field oriented parallel to the quantum wires. This indicates that the optimal geometry of a low threshold laser with a quantum wire array active region corresponds to the configuration of Figure 4.1(a), where the wires are fabricated parallel to the end-facets of the laser. At higher injection levels, the ratio of the peak gain calculated for the two polarization directions tends towards unity. Thus, laser configurations which require large material gain, such as would be the case in lasers incorporating a single quantum wire, would be best designed with the quantum wires aligned parallel to the lasing direction.

4.5 Quantum wires of lower symmetry

Our discussion of the subband dispersion, DOS, and interband optical transition matrix elements has been vastly simplified due to the high symmetry of the cylindrical model we have chosen for the quantum wire. The prime reason for choosing such a symmetrical geometry is simply that the problem becomes extremely complex when lower symmetry structures are considered. However, it is possible to use the theory of symmetry groups to make certain judgements regarding the applicability of results obtained in this model to structures of lower symmetry, in particular quantum wires of four-fold, three-fold, and two-fold rotational symmetry about the wire axis. Examples include wires with square,

triangular, or rectangular cross-section (Figure 4.13), and wire arrays with weak lateral inter-wire coupling (Figure 4.14). This is important since several promising fabrication technologies produce wires of these lower symmetries. For instance, growth of quantum wire arrays on vicinal substrates, a technique which results in quantum wires of four-fold or two-fold rotational symmetry, has been recently demonstrated [1,2]. Also, GaAs wires with equilateral triangular cross-section have been fabricated by selective organometallic vapor phase epitaxy [15].

To address the question of applicability of our model, we must apply the arguments of group theory to characterize the symmetry of the states in these lower symmetry structures. If we imagine adiabatically deforming a cylindrical quantum wire into the shape of a square, triangular, or rectangular wire, it is reasonable to assume that the lowest lying states (which we have now completely characterized) will adjust themselves adiabatically to the perturbation. The quantum wire eigenstates will then adopt new symmetries and degeneracies. These can be determined by decomposing the irreducible representation of the cylindrical group, $C^*_{\infty,v}$, to which the state originally belonged, into the irreducible representations of the new group, e.g., $C^*_{4,v}$, $C^*_{3,v}$ and $C^*_{2,v}$, which describe the quantum wire of square, triangular, and rectangular cross-section, respectively. This is shown schematically in Figure 4.13.

The case of a four-fold perturbation is illustrative. The two spin degenerate conduction states of the cylindrical quantum wire with envelope angular momentum $L_z = 0$, i.e., the states we have referred to as C(0), span the irreducible representation $E^+_{1/2}$ of the group $C^*_{\infty,v}$. Use of the group character tables given in Ref. [16] shows that these states are distorted by the four-fold "square" perturbation into new states which belong to the Γ_6

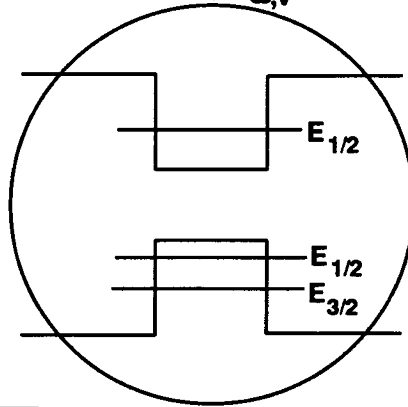

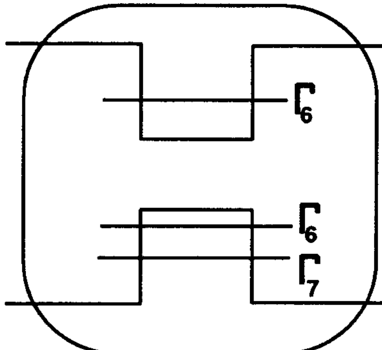

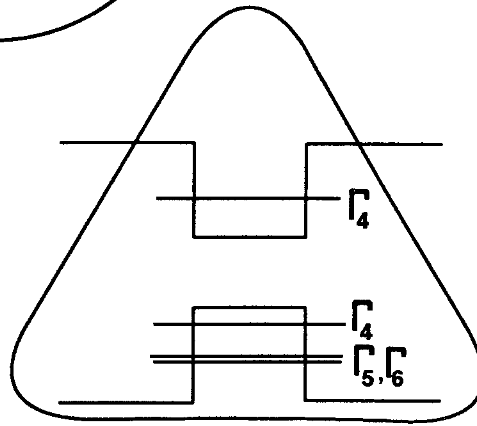

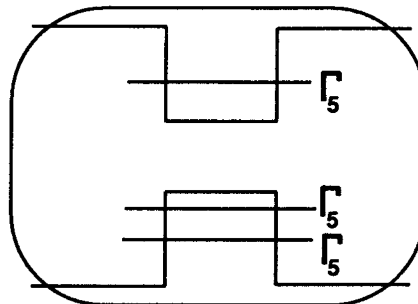

Figure 4.13: Schematic representation of the effect of imposing square, triangular, and rectangular symmetry upon a cylindrical quantum wire. The states are labeled for the cylinder according to the irreducible representations of the group $C^*_{\infty,v}$ to which they correspond. The resulting symmetry of the states in $C^*_{4,v}$, $C^*_{3,v}$ and $C^*_{2,v}$ are labeled following the notation of Ref.[16].

representation of $C^*_{4,v}$, with no loss of degeneracy. Similarly, valence states $E^+_{1/2}$, with total angular momentum $F_z = \pm 1/2$, and $E^+_{3/2}$, with $F_z = \pm 3/2$, deform into new states with Γ_6 and Γ_7 symmetries, respectively, also with no loss of degeneracy.

Two important consequences therefore follow. The first is that the new Γ_6 and Γ_7 valence subbands will not couple because they have different symmetry. Thus, Figure 4.2 will qualitatively describe the valence subband dispersion of the square quantum wire. In particular, the level crossings seen in that figure will still occur. The second consequence is the existence of optical transition selection rules. Consider the dipole operator P_z. This operator is invariant under all operations of the symmetry group of a quantum wire. For instance, a rotation of $\frac{\pi}{2}$ about the wire axis, z, takes P_z into itself. It is well known that the matrix element of an invariant operator vanishes between states belonging to different irreducible representations. Therefore, transitions between the Γ_6 conduction state and the Γ_7 valence states will be strictly forbidden for electric fields polarized parallel to the wire axis. On the other hand, it can be shown that these states couple through electric fields polarized perpendicular to the wire. Additionally, the Γ_6 conduction and valence states can couple through electric fields polarized in any direction. Hence, the polarization anisotropies shown in Figures 4.8- 4.12 will qualitatively apply to the two lowest energy transitions in the square quantum wire.

The validity of this adiabatic relaxation argument is confirmed by comparison with the work reported in Ref.[12] in which the valence subband structure of square GaAs quantum wires is calculated using conventional envelope function theory. The subbands $E^+_{1/2,1}$ and $E^+_{3/2,1}$ shown in Figure 4.2 correspond well, both in energy and in shape, to the highest lying states labeled Γ_6 and Γ_7 in Ref.[12]. This similarity indicates that the absorption and

gain spectra calculated here will apply qualitatively to the square quantum wire.

The same conclusions are obtained in the case of a quantum wire with three-fold rotational symmetry. Use of the character tables of Ref.[16] leads to the conclusion that the lowest spin degenerate conduction subbands, C(0), and the valence subbands with quantum number $F_z = \pm 1/2$, adiabatically deform into states of symmetry Γ_4 of the $C^*_{3,v}$ group. In contrast, the states characterized by $F_z = \pm 3/2$ are split into new states belonging to representations Γ_5 and Γ_6, different from Γ_4. As a result, the states which originate from the subband $E^+_{3/2,1}$ in the cylinder have zero interaction with the lowest conduction state through optical transitions involving z-polarized light. Thus, the basic conclusions found for cylindrical wires remain valid for the triangular quantum wire.

We consider next the case of a quantum wire of two-fold rotational symmetry, which has symmetry $C^*_{2,v}$. This situation would be realized in a quantum wire of rectangular cross-section, or in a planar array of wires positioned in close enough proximity that weak, lateral inter-wire coupling exists (Figure 4.14). Applying the same perturbation argument as above, we find that the $F_z = \pm 1/2$ and $F_z = \pm 3/2$ valence states of the cylinder both decompose into the same irreducible representation Γ_5 of group $C^*_{2,v}$. The subband C(0) also transforms into Γ_5 symmetry. Thus, the valence subbands now may couple, and the crossing behavior seen in the subband dispersion curves, Figure 4.2, may be replaced by anticrossing behavior. Additionally, the polarization anisotropies found in the cylindrical quantum wire will be washed out with increasing aspect ratio in the case of the rectangular wire, or increased interwire coupling in the case of a quantum wire array. This result makes intuitive sense, since in the limit of infinite aspect ratio or interwire coupling, the system is indistinguishable from a planar quantum well.

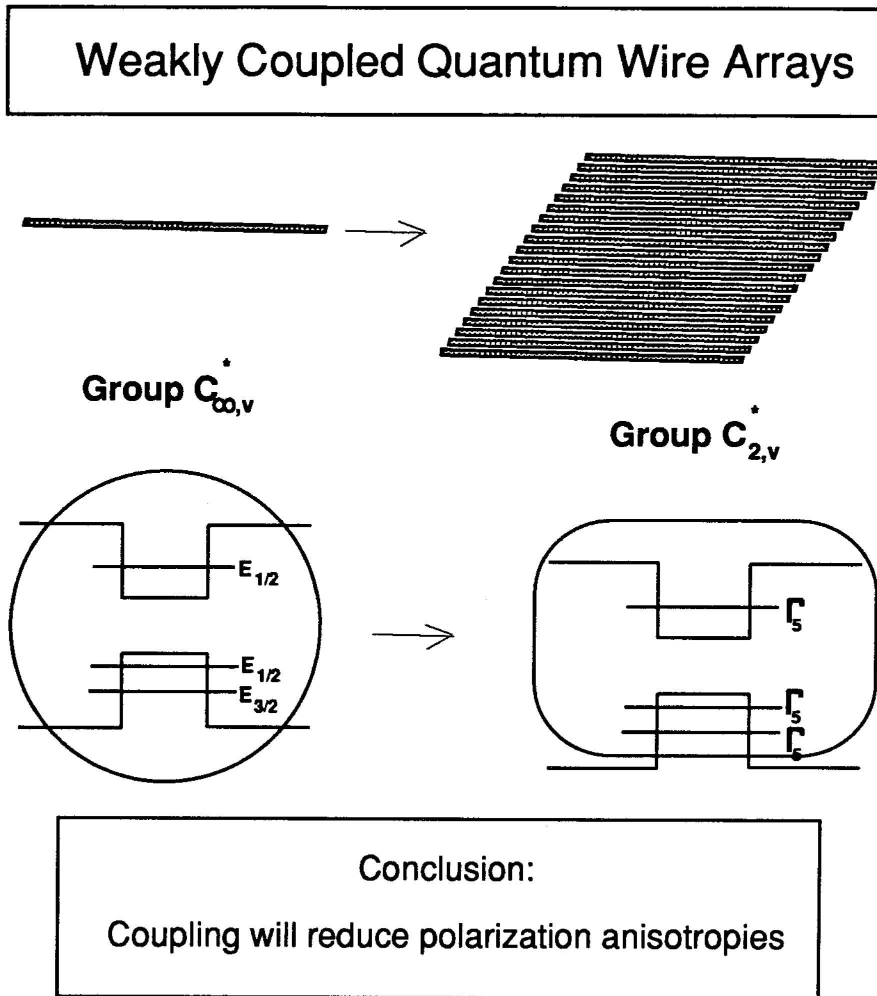

Figure 4.14: Schematic representation of the effect of weak lateral coupling on the states in a quantum wire array. The unperturbed states in the isolated cylindrical wire are labeled according to the irreducible representations of the group $C^*_{\infty,v}$ to which they correspond. The lateral coupling reduces the symmetry of the system to $C^*_{2,v}$. It can be shown that the perturbed states in the wire array all belong to the irreducible representation Γ_5 of $C^*_{2,v}$ and therefore can couple. The polarization anisotropy shown in Figure 4.9-4.12 is therefore reduced by the lateral perturbation.

4.6 Conclusions

We have presented an analytical study of the density of states, interband optical transition matrix elements and optical absorption and gain spectra in cylindrical GaAs quantum wires. Band-coupling effects have been shown to be critical for a correct analysis of these properties. We have derived simple trigonometric expressions for the polarization dependence of the optical transition matrix elements. Polarization dependent absorption spectra have been calculated which should aid in the interpretation of polarization resolved optical spectra of quantum wires. In particular, the results obtained can explain polarization anisotropies observed in PLE spectra performed on quantum wire arrays [1,2].

Polarization resolved gain calculations performed here indicate that for minimum threshold current, a semiconductor laser with a quantum wire array active region should be designed so that the electric field is parallel to the wires. We showed by application of group theory that the analysis for cylindrical quantum wires presented here remains qualitatively valid in quantum wires of four-fold and three-fold rotational symmetry. In rectangular quantum wires, and in planar arrays of quantum wires with lateral inter-wire coupling, important qualitative features of the model are predicted to break down as the cross-sectional aspect ratio or the lateral inter-wire coupling become large.

4.7 Appendix: One-band models of polarization anisotropies

Utilizing polarization dependent photoluminescence excitation (PLE) spectroscopy, a strong relative anisotropy between the two lowest energy optical transitions in quantum wire arrays has recently been observed [1,2]. We have shown in this chapter that the optical polarization

anisotropy reported in Refs. [1,2] is well explained by the coupled band model presented in chapter 2. However, these experimental results have also been interpreted in the context of a one-band model, in which the two transitions are identified as conduction-to-heavy-hole and conduction- to-light-hole exciton lines, under the assumption that the valence states are decoupled at the zone-center of the quantum wire [1,2,5,6]. The neglect of band coupling effects in these previous analyses is incorrect, despite the reported agreement of the one-band theory with experiment. Furthermore, a critical examination of the one-band model used in Refs.[1,2,5,6], finds an unjustified neglect of coherence terms in the transition matrix element. When these coherence terms are retained, the one-band model does not explain the observed polarization anisotropy.

These studies model a quantum wire structure of square or rectangular cross-section as a two-dimensional potential well with infinite well depth. The squared transition matrix element was computed between electron and hole Bloch waves corresponding to the four wavevectors $\vec{k}_i$ propagating into each of the four corners of the well, and then averaged:

$$|M|^2 = \sum_i |\langle 1/2, 1/2|\vec{P}|U_v(\vec{k}_i)\rangle \cdot \hat{A}|^2. \tag{4.23}$$

Here, $|U_v(\vec{k}_i)\rangle$ is the zone-center Bloch function for a heavy or light-hole wave corresponding to wavevector $\vec{k}_i$ [13]. This approach leads to the following expression for the relative squared matrix elements of the [e-lh] and [e-hh] transitions:

$$\frac{|M|^2_{e-lh}}{|M|^2_{e-hh}} = \frac{\frac{1}{2}\mathrm{Cos}^2(\theta) + \frac{5}{4}\mathrm{Sin}^2(\theta)}{\frac{3}{2}\mathrm{Cos}^2(\theta) + \frac{3}{4}\mathrm{Sin}^2(\theta)}, \tag{4.24}$$

which is equivalent to Eq. (1) of Ref.[1]. However, since the waves involved in the summation in Eq.(4.23) are part of a coherent superposition ($\mathrm{Cos}[k_x x]\mathrm{Cos}[K_y y]$) forming a stationary state in a quantum wire, it is incorrect to treat them as independent. Equations

(4.23, 4.24) neglect this coherence, and should therefore be corrected. This is accomplished by performing the summation in Eq.(4.23) *before* squaring. For the light and heavy waves, this results in the corrected formula:

$$\frac{|\mathrm{M}|^2_{\mathrm{e-lh}}}{|\mathrm{M}|^2_{\mathrm{e-hh}}} = \frac{\frac{2}{3}\mathrm{Cos}^2(\theta) + \frac{1}{6}\mathrm{Sin}^2(\theta)}{2\mathrm{Cos}^2(\theta) + \frac{1}{2}\mathrm{Sin}^2(\theta)} = \frac{1}{3} \tag{4.25}$$

which is *constant* with respect to polarization. The one-band model is therefore incapable of explaining the polarization dependent absorption observed in Refs. [1,2]. The observed polarization dependence must be explained by the coupled band approach developed in this chapter.

References

[1] M. Tsuchiya, J.M. Gaines, R.H. Yan, R.J. Simes, P.O. Holtz, L.A. Coldren, and P.M. Petroff, *Phys. Rev. Lett.* **62**, 466 (1989).

[2] Masaaki Tanaka and Hiroyuki Sakaki, *Appl. Phys. Lett.* **54**, 1326 (1989).

[3] Yasuhiko Arakawa, Kerry Vahala, and Amnon Yariv, *Appl. Phys. Lett.* **45**, 950 (1984).

[4] Hal Zarem, Kerry J. Vahala, and Amnon Yariv, *IEEE J. Quantum Electron.***25**, 705 (1989).

[5] Masahiro Asada, Yasuyuki Miyamoto, and Yasuharu Suematsu, *Japan. J. Appl. Phys* **24**, L95 (1985).

[6] Masahiro Asada, Yasuyuki Miyamoto, and Yasuharu Suematsu, *IEEE J. Quantum Electron.* **9**, 1915 (1986).

[7] E. Kapon, D. M. Hwang, and R. Bhat, *Phys. Rev. Lett* **63** 430 (1989). Also, E. Kapon, S. Simhony, R. Bhat, and D.M. Huang, *Appl. Phys. Lett.*, **55**, 2715 (1989).

[8] Mark Sweeny, Jingming Xu, and Michael Shur, *Superlatt. Microstruc.* **4**, 623 (1988).

[9] J.M. Luttinger and W. Kohn, *Phys. Rev.* **97**, 869 (1955).

[10] J. M. Luttinger, *Phys. Rev.* **102**, 1030 (1956).

[11] J. A. Brum, G. Bastard,L.L. Chang, and L. Esaki, *Superlattices and Microstructures* **3**, 47 (1987).

[12] D.S. Citrin and Yia-Chung Chang, *Phys. Rev. B* **40**, 5507 (1989).

[13] Evan O. Kane, *J. Phys. Chem. Solids* **1**, 249 (1957).

[14] R. Eppenga, M. F. H. Schuurmanns, and S. Colak, *Phys. Rev. B* **36**, 1554 (1987).

[15] John A.Lebens, Charles Tsai, Kerry J. Vahala, and Thomas Kuech, *Appl. Phys. Lett.* **56**, 2642 (1990).

[16] George F. Koster, John O. Dimmock, Robert G. Wheeler, and Hermann Statz, "Properties of the Thirty-Two Point Groups," (MIT Press, Cambridge, 1963).

Chapter 5

Nanometer-scale wire structures fabricated by diffusion induced selective disordering of a GaAs-$Al_xGa_{1-x}As$ quantum well

5.1 Introduction

A logical approach to the synthesis of quantum wires and dots is the patterning, at a nanometer-scale, of prefabricated quantum well material. This strategy, which has been dubbed the "cookie cutter" approach, requires two independent steps to succeed. The first is pattern generation of some kind at the nanometer-scale, to create a stencil for the production of the quantum wires and dots. The second is pattern transfer – the transfer of the nanometer scale stencil into the quantum well material.

The first approaches to the creation of nanometer-scale lateral confinement potentials employed pattern generation by electron-beam lithography or focussed ion-beam lithography and conventional liftoff procedures to create a Cr or NiCr etch mask on the surface of a sample. Pattern transfer was accomplished in these experiments by using anisotropic etch techniques such as reactive ion etching or ion beam assisted etching to create nanometer-scale mesa structures with embedded quantum wells [1]-[4]. Although the lateral dimensions of the wire and dot structures (more accurately, ribbon and disk structures) fabricated in this fashion are in the 10 nm size range, the anisotropic etching step creates a damaged semiconductor surface. This causes the structures to have extremely low radiative recombination efficiency [5].

An alternate approach that has been developed to circumvent the problem of damaged free surfaces is to selectively disorder a quantum well in such a way as to leave behind a quantum wire. In this scheme, the quantum wire would consist of a buried strip of GaAs quantum well surrounded on all sides by $Al_xGa_{1-x}As$ material. The technique was first implemented by Cibert *et al.* using ion implantation followed by rapid thermal annealing to selectively disorder the quantum well material [6]. Electron-beam lithography and liftoff were used in that experiment to create a Ti/Au-Pd mask for selective Ga^+ beam implantation. After the rapid thermal annealing step, wire structures with lateral dimensions as small as 60 nm were formed which exhibited a blue shift of the luminescence spectra relative to the unpatterned quantum well material [6]. A similar approach in which a focussed Ga^+ beam is used to directly disorder quantum well material without a mask has been employed to create wire structures with lateral dimensions down to 50 nm [7]. The photoluminescence spectra of these structures exhibit fine structure at a temperature of 4 K which is attributed

to lateral quantization.

In this chapter we report a new technique for selective disordering of quantum well material to produce wire structures with lateral dimensions in the 100 nm range. The method utilizes a selectively masked shallow zinc impurity diffusion to locally disorder quantum well material, leaving behind strips of undisordered (or less disordered) quantum well material. Cathodoluminescence spectra are presented which show a systematic blue shift of luminescence as the width of the diffusion mask is reduced in the range from 500 nm to 100 nm. Additionally, blue shifted luminescence from individual wires is shown which demonstrates that the technique can be used to create 100 nm scale lateral bandgap modulation. Considering the size of the wires produced, the luminescence peak blue shifts observed are most likely the result of diffusion of aluminum into the quantum well strips, rather than a quantum size effect.

5.2 Disorder of GaAs-$Al_xGa_{1-x}As$ heterostructures by zinc diffusion

The GaAs-$Al_xGa_{1-x}As$ heterostructure interface is nearly lattice matched and is ordinarily stable to very high temperatures. It is possible, however, to induce layer interdiffusion by thermal annealing at temperatures in the neighborhood of 900 °C. This technique has been used, for example, to shift the emission wavelength of GaAs-$Al_xGa_{1-x}As$ quantum well heterostructure laser diodes [8]. It has recently been shown, however, that zinc diffusion into GaAs-$Al_xGa_{1-x}As$ heterostructures causes the GaAs-$Al_xGa_{1-x}As$ interface to become unstable and to disorder at temperatures as low as 500 °C [9]. The activation energy of the

Al-Ga interdiffusion coefficient is lowered from the impurity free value of 3.6 eV to 1.0 eV in the presence of zinc at concentrations above $10^{18}cm^{-3}$ [10].

An important feature of the zinc diffusion process is that the diffusion coefficient of zinc in GaAs is proportional to the square of the zinc concentration [11]. As a result, the zinc concentration drops off abruptly across the diffusion front. When zinc is applied to interdiffuse GaAs-AlGaAs heterostructures at low temperatures (500-600 ^oC), this leads to relatively sharp definition of the interface between disordered and non-disordered regions.

To utilize the zinc-impurity-enhanced interdiffusion process to create lateral bandgap modulation, it is important that an appropriate diffusion mask be identified. It has been demonstrated experimentally that silicon deposited by electron beam evaporation on the surface of GaAs samples makes an excellent diffusion mask with nearly unity lateral to depth diffusion rate [12]. Selective zinc-impurity-induced disordering with a silicon diffusion mask has been successfully applied at the 1 μm scale to fabricate a number of integrated optical components including waveguides and phase modulators [13]. In contrast, in our experiment, a silicon diffusion mask with *nanometer scale* dimensions is fabricated using electron-beam lithography followed by silicon evaporation and liftoff.

5.3 Selective disordering of a shallow quantum well to produce 100 nm scale wire structures

A schematic diagram illustrating the goal of the present experiment is shown in Figure 5.1. The sample contains a GaAs quantum well 50 nm below the surface, with $Al_xGa_{1-x}As$ barrier layers on both sides. Electron-beam lithography and conventional liftoff procedures

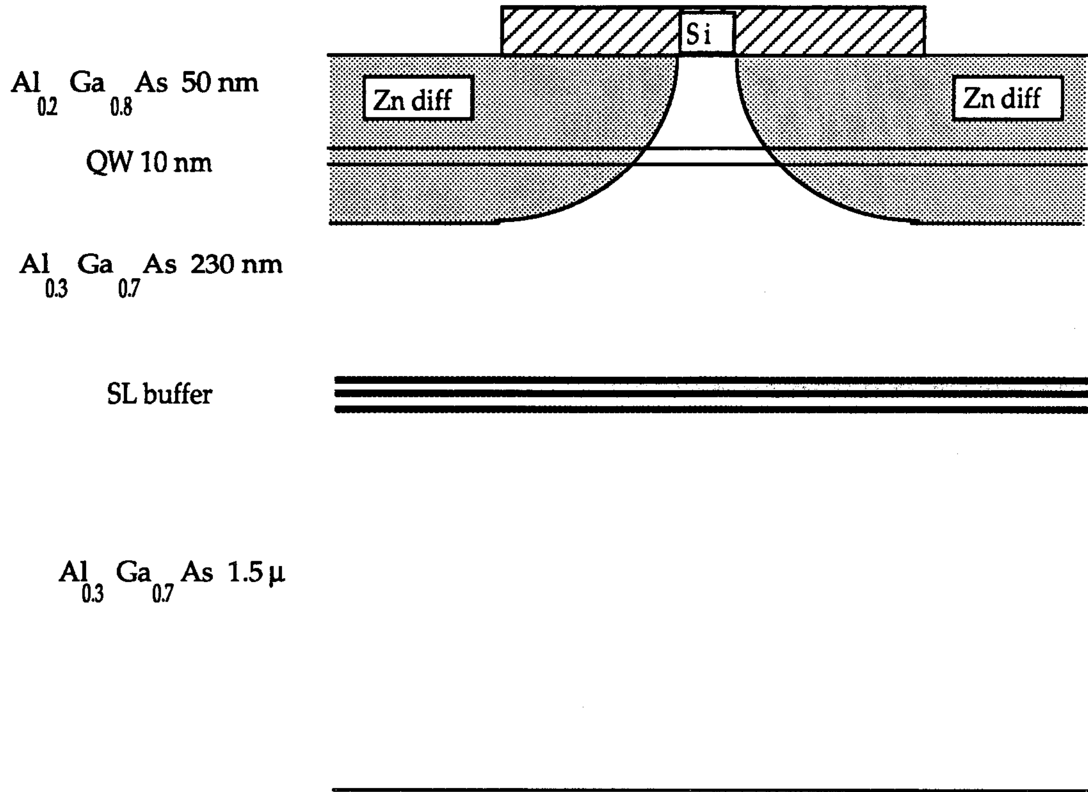

Figure 5.1: Schematic of selective impurity diffusion experiment. The sample structure is described in the text. A quantum well near the surface of the sample is selectively disordered by diffusion of zinc. Narrow silicon diffusion masks are fabricated on the sample surface by electron-beam lithography and liftoff. The quantum well remains relatively undisordered beneath the diffusion masks, producing a lateral bandgap modulation at the 100 nm scale.

are employed to create silicon diffusion masks of various widths on the surface of the sample. Zinc is diffused into the sample, disordering the unmasked material, and hopefully leaving a narrow strip of quantum well material beneath the diffusion masks.

The sample used in our experiment was grown by molecular beam epitaxy in a Riber 2300 RD system. The layers were grown in the following order: a 1 μm buffer layer, a 50 nm AlAs blocking layer, a 1.5 μm $Al_{0.3}Ga_{0.7}As$ buffer layer, a superlattice buffer layer nominally consisting of three 7.0 nm GaAs layers separated by 7.0 nm $Al_{0.3}Ga_{0.7}As$ layers, a 0.23 μm $Al_{0.3}Ga_{0.7}As$ layer, a 10.0 nm GaAs quantum well, and a 50 nm $Al_{0.17}Ga_{0.83}As$ cap layer. All layers were undoped. The luminescence spectrum of the sample is shown in Figure 5.5 and is discussed below.

5.3.1 Electron-beam lithography

To address the problem of pattern generation at the submicron scale, we have converted a Cambridge SE-240 scanning electron microscope (SEM) into an electron-beam lithography system. This system is shown in Figure 5.2. A Mac-II personal computer is used to generate patterns, which are converted into a data set fixing the position of the electron beam as a set of (x,y) coordinates as a function of time. This data set is output through two 16 bit digital to analogue converters to drive the (x,y) scanning coils of the SEM. The electron beam is thus driven in a vector scan over the sample. The sample is spin coated with an electron beam sensitive resist, polymethylmethacrylate (PMMA). Upon exposure to 30 keV electrons, chemical bonds are broken in the PMMA layer, rendering the exposed material soluble in a developer. Since the spot size in the SE-240 SEM is approximately 20 nm, a nanometer-scale pattern can be written into the PMMA resist layer.

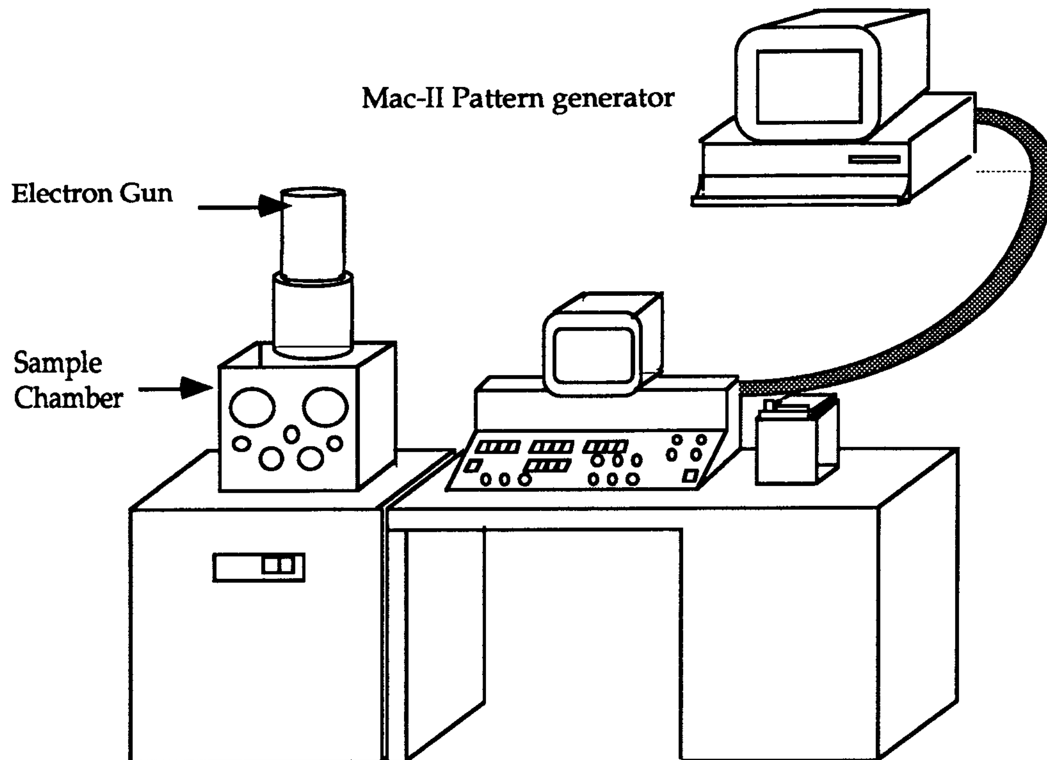

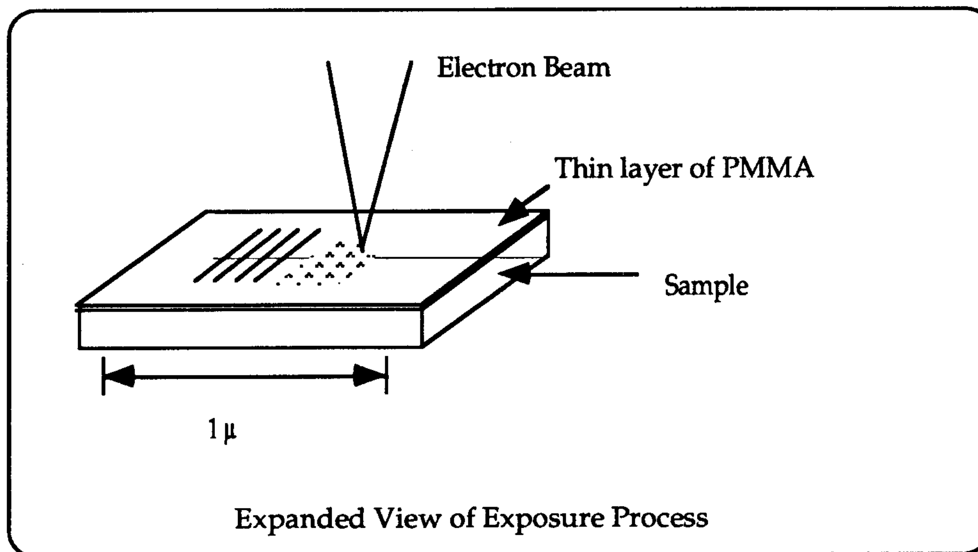

Figure 5.2: Schematic of electron beam lithography system. A Mac-II computer is used as a pattern generator to drive the scanning coils of a Cambridge SE-240 SEM. Samples are spin coated with PMMA, an electron sensitive resist.

The resist solution used in our experiments was 3 % PMMA in chlorobenzene. The solution was spun onto the samples at 3500 rpm for 30 seconds. Typical beam exposures were in the range from 3.5 to 35 nCoulombs per cm of beam travel, using a beam current of 10 pAmperes (measured with a Faraday cup). After developing the resist in a solution of cellosolve:methanol, the sample is ready for conventional liftoff processing to produce the Si diffusion mask.

5.3.2 The diffusion

Using the electron-beam lithography system just described, narrow lines, 4.5 μm in length, ranging from 160 nm to 500 nm in width, were written in array patterns and as isolated lines in the PMMA resist. In addition, a 40 μm square was exposed uniformly to provide a broad area mask for comparison. After development in a solution of cellosolve:methanol (3:7), the sample was placed in an electron-beam evaporator and a 50 nm layer of silicon was deposited. Liftoff was done in dichloromethane. Figure 5.3 shows a typical array of silicon diffusion mask stripes on the surface of the sample.

Following the standard procedure for zinc diffusion in GaAs, the sample was sealed in an evacuated, fused-quartz ampoule with solid ZnAs as the diffusion source. The sample was placed in a tube furnace at 535 °C for 1 hour. Zinc diffusion at this temperature in GaAs-AlGaAs heterostructures is known to enhance the interdiffusion of Ga and Al and disorder the regions with a high concentration of zinc while leaving other areas unaffected [9]. From the CL measurements (described in a later subsection), we know that the diffusion was deep enough to disorder the quantum well but not so deep as to completely disorder the superlattice. This places the disorder front at a depth of between 60 nm and 280 nm.

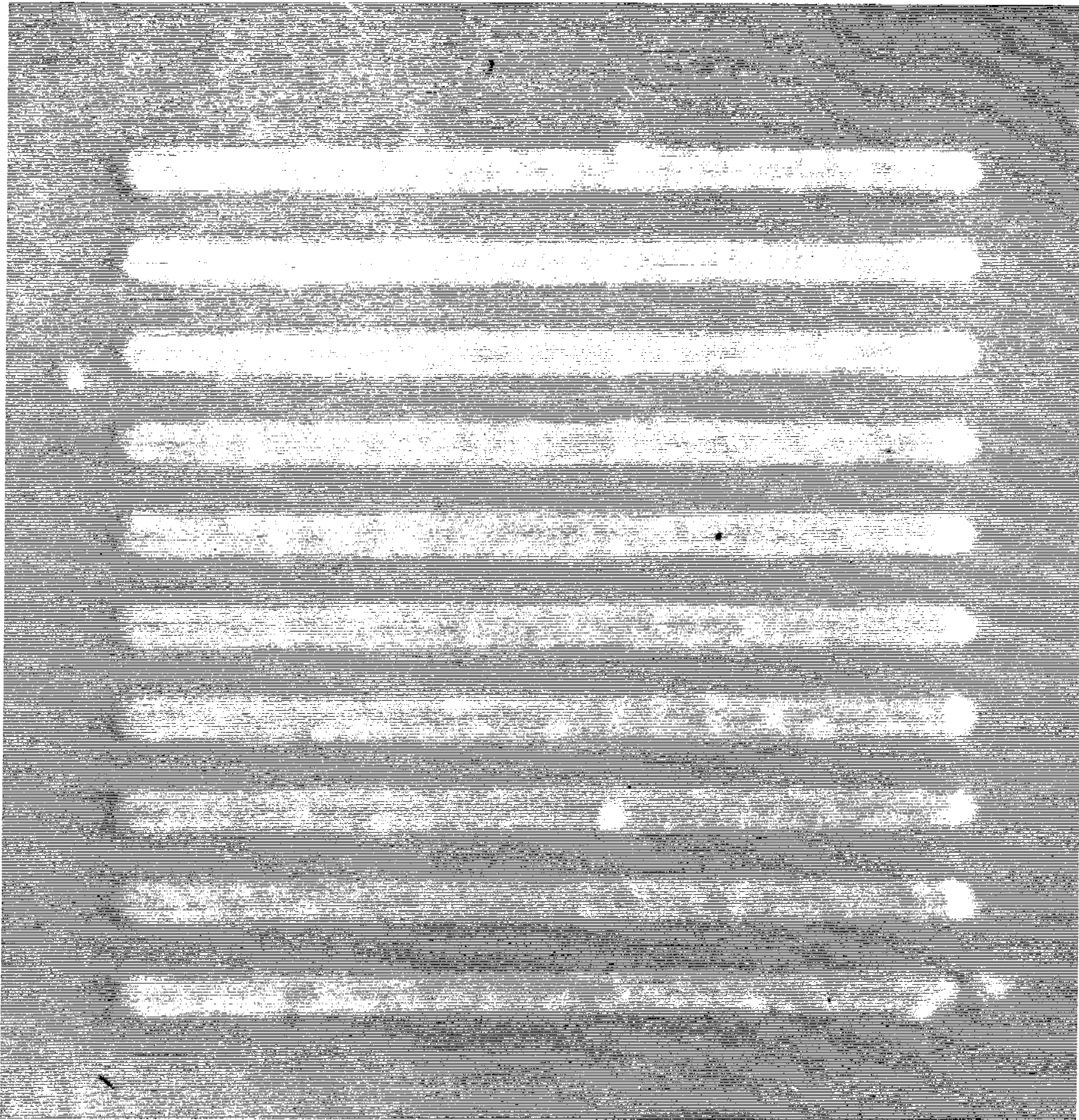

Figure 5.3: Scanning electron micrograph of a typical array of silicon-stripe diffusion masks.

5.3.3 Cathodoluminescence

Investigation of the effects of the zinc diffusion on the band structure of the sample was done by cathodoluminescence (CL) imaging and spectroscopy. Cathodoluminescence is a term indicating the emission of light from a sample bombarded by cathode rays. In a SEM, energetic electrons incident on a semiconductor sample lose energy by creating electron-hole pairs. In a direct-bandgap semiconductor, these carriers can recombine radiatively, producing a cathodoluminescence spectrum characteristic of the sample. By performing CL in an SEM, one can fix the electron beam on a specific region and obtain a local spectrum. Alternatively, one can choose a particular wavelength and raster the beam across the sample to obtain a spatially resolved cathodoluminescence image (SRCL) [14]. In either case, the spatial resolution of the technique is generally determined by the carrier diffusion length.

We have equipped the SEM in our laboratory with a unique optical-fiber-based CL imaging system [14] and a continuous flow cryogenic cold stage for performing low temperature spectroscopy. Figure 5.4 shows a schematic diagram of the system [14]. An optical fiber with a 100 μm diameter core and a numerical aperature of 0.2 is placed in close proximity to the sample using a motorized x-y-z translation stage. The surface of the optical fiber is coated with a thin (5 nm) film of gold to prevent charging. A fraction of the light emitted from the sample enters the optical fiber and is guided out of the SEM sample chamber to a monochromator. The signal output from the monochromator is detected with a photomultiplier tube and is preamplified. The signal can then be sent through a video amplifier and used to generate SRCL images, or lock-in detection can be employed to measure spectra. The cold stage can be used with liquid helium, or liquid nitrogen.

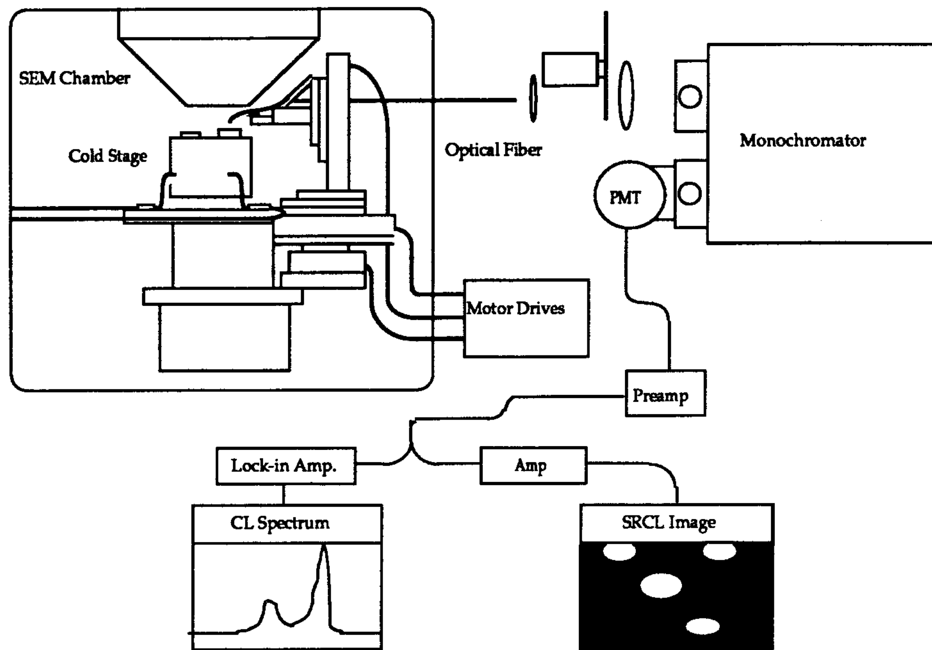

Figure 5.4: Schematic of cathodoluminescence (CL) imaging system. The sample is mounted in the SEM chamber on a cold stage capable of operation at liquid helium or liquid nitrogen temperature. Cathodoluminescence from the sample is collected by a 100 μm core diameter, large numerical-aperature optical fiber which is positioned close to the sample using motorized translation stages. The light is coupled into a monochromator and detected with a photomultiplier tube. The system may be used to generate spectrally resolved cathodoluminescence (SRCL) images, or CL spectra from individual structures on the sample.

5.3.4 Experimental results

The cathodoluminescence spectra taken at 12 K from regions of the sample located under the 40 μm square mask, and an unmasked region, are shown in Figure 5.5. The electron energy used in these measurements was 10 keV and the beam current was approximately 20 nA. The peak at 785 nm in the spectrum of the masked region is identified as the emission from the quantum well. In the spectrum of the unmasked region, the quantum well emission peak is entirely absent, suggesting that the diffusion has completely disordered the quantum well. The peaks labelled SL1 (722 nm) and SL2 (765 nm) originate from wells of different thickness in the superlattice. By depth profiling the sample it was determined that the SL1 (722 nm) peak emanates from the bottom one or two wells, while the peak SL2 (765 nm) originates from the top well (closest to the surface of the sample). The depth profiling was done by measuring cathodoluminescence spectra at different beam energies. The beam energy determines the penetration depth of the electrons and thus permits non-destructive depth profiling. Our interpretation of the energy dependent CL measurements is confirmed by etch profiling. The peaks at 727 nm and 767 nm in the spectrum of the unmasked region originate from the SL1 and SL2 wells, respectively.

The reduction of the emission intensity of the 767 nm peak is probably due to diffusion of zinc into the superlattice. This observation is consistent with previous studies which show that zinc doping at the levels produced in this experiment ($\approx 10^{18}\text{cm}^{-3}$) significantly lowers the radiative recombination efficiency of bulk GaAs [15]. Note that the presence of zinc at these concentrations is expected to lead to a band-gap shrinkage of about 15 meV [16], corresponding to a 7 nm redshift of the superlattice. The 5 nm shift of the SL1 peak is consistent with this expectation. The smaller 2 nm redshift of the SL2 peak suggests

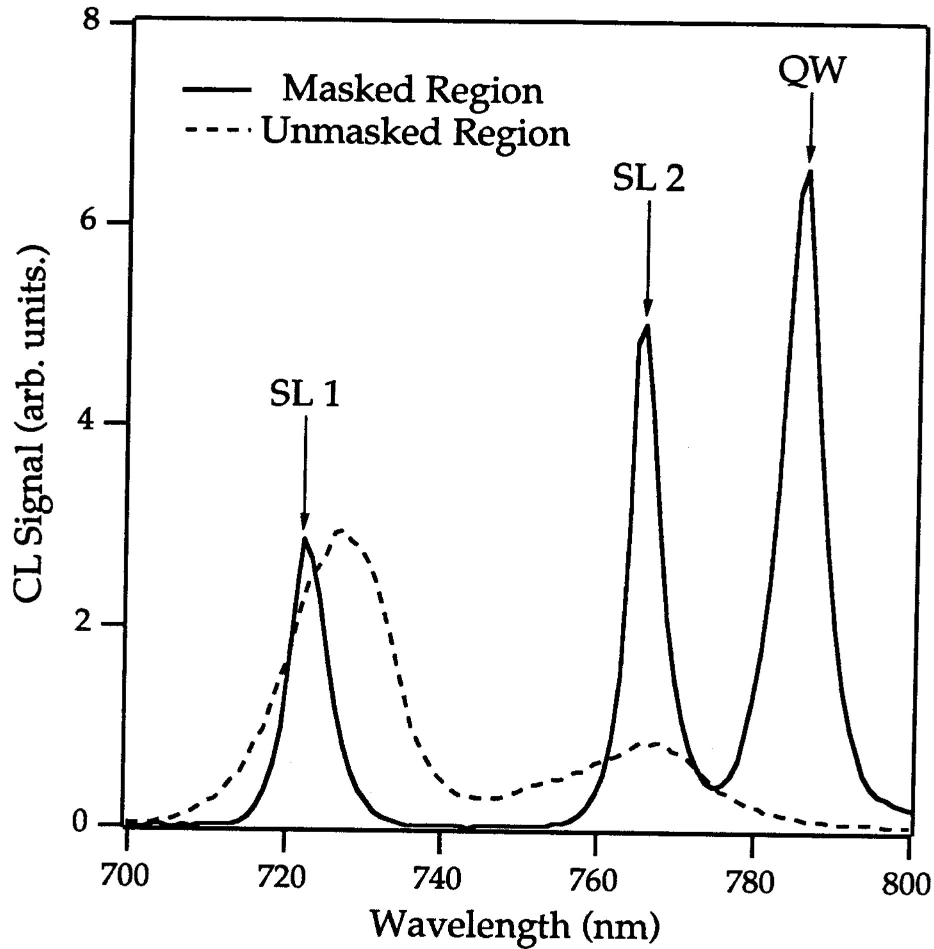

Figure 5.5: Cathodoluminescence spectra of a uniformly masked region (40μm $\times$ 40μm square mask) and an unmasked region. SL1, SL2, and QW locate the emission peaks from the superlattice and quantum well, respectively (see text). The sample temperature is 12 K. Electron beam energy is 10 keV.

that a small amount of aluminum has been introduced into the top well which effectively compensates for the bandgap shrinkage effect. Since the top superlattice well is slightly disordered and the quantum well is completely disordered, this would place the disorder front at a depth slightly less than 280 nm.

Figure 5.6 shows both the secondary electron and CL images of a region containing several arrays. The left half shows several arrays of silicon wires similar to those of Fig. 5.3. The width of the diffusion masks in each array increases from 160 nm in the lower right array to 370 nm in the upper left array. To the right of the array on the lower left is the widest wire in the field of view with a width of 0.5μ. The right half of Fig. 5.6 is the spatially resolved CL taken at a sample temperature of 77 K and an emission wavelength of 780 nm, which is between the peak emission wavelength of the undisordered quantum well and superlattice at this temperature. At this wavelength, the contrast between the arrays and the background is the greatest. Note that individual wires in the arrays are not resolved in the SRCL image due to carrier diffusion, but that the single 0.5 μ wire is resolved. These results suggest that the zinc diffusion has resulted in a lateral modulation of the bandgap of the sample on a 100 nm scale.

Luminescence spectra of individual arrays were taken by placing the electron beam at the center of an array. Spectra of arrays with mask stripe widths of 370 nm and 160 nm are shown in Fig. 5.7 along with the spectra from beneath the broad area mask and an unmasked region. The wire spectra each contain a peak at 730 nm which is redshifted from the SL1 peak of the masked spectrum by 8 nm. As discussed above, such a shift is expected due to the bandgap shrinkage effect caused by the heavy zinc doping of the sample. The wire spectra each contain a second peak in the region indicated 'A' in the figure. These

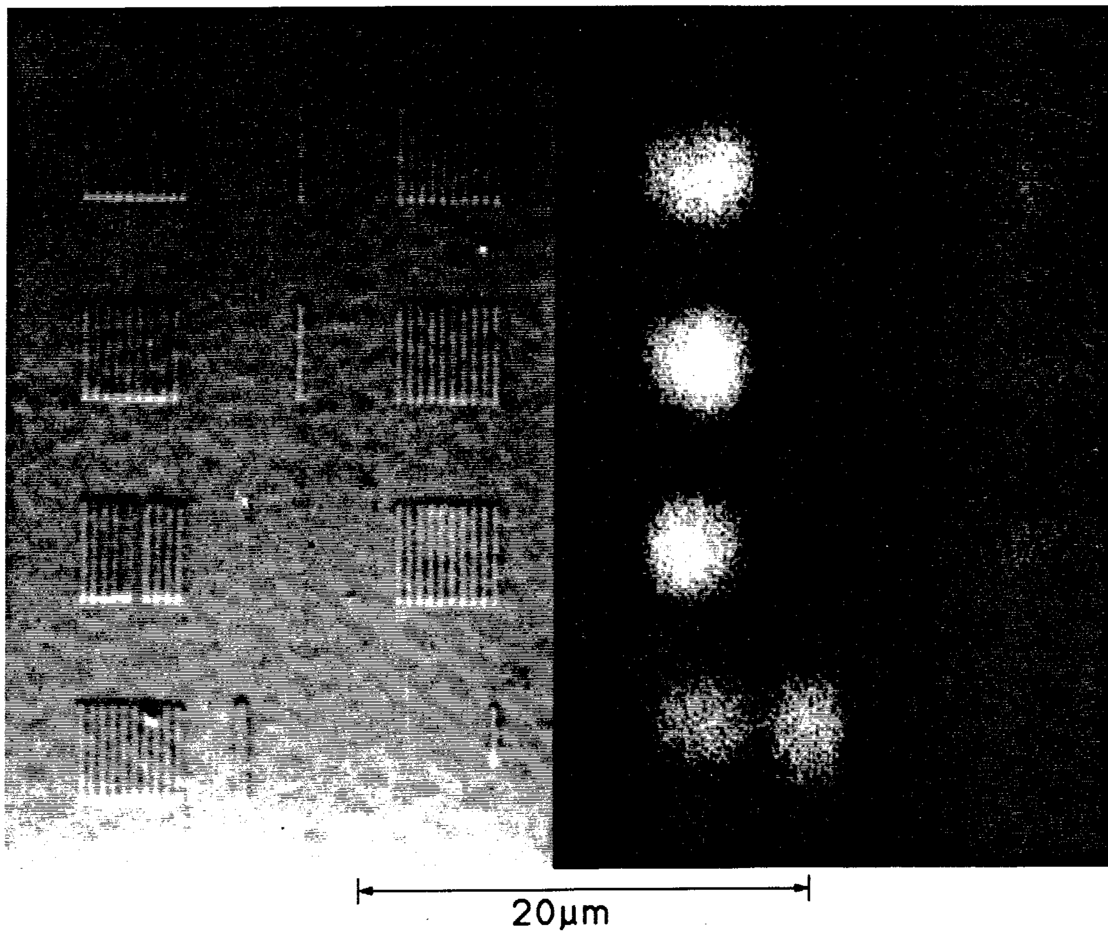

Figure 5.6: Secondary electron and cathodoluminescence images of several wire arrays and an isolated wire. The width of the silicon stripes in each array varies from 370 nm on the upper left, to 160 nm on the lower right. The width of the single line mask on the lower left is 0.5 μm. The luminescence image is taken at 780 nm. Sample T=77 K.

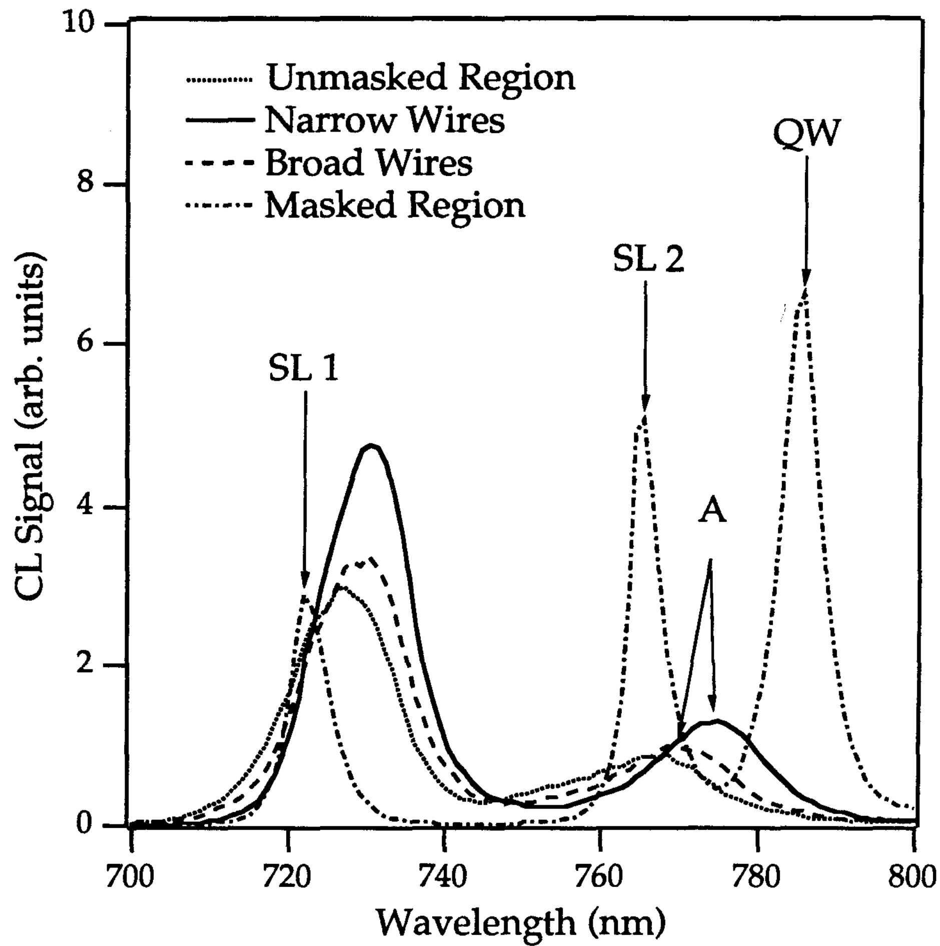

Figure 5.7: Cathodoluminescence spectra of 370 nm wide wire masked region (broad wires), and 160 nm wide wire masked regions (narrow wires). Sample T=12 K. Electron beam energy is 10 keV. For reference, the emission peaks of the quantum well and superlattice from the large area mask are indicated with arrows. The origin of the peaks from the wires, labeled A, are discussed in the text.

peaks, located at 774 nm and 768 nm for the broad wires and narrow wires, respectively, are of less certain origin. In the discussion that follows these peaks will be referred to as the 'A' peaks.

Several possible interpretations of this feature can be made. One interpretation is that the quantum well peak is blue shifting with decreased wire size and coalescing with the superlattice peak to produce the 'A' peaks. A possible mechanism for blue shifting of the quantum well emission peak is lateral quantum confinement. Shifts of 22 meV and 32 meV are seen in the broad and narrow wire arrays as compared to the quantum well. The shape of the confining potential being unknown, no width can be assigned to it from these shifts. However, partial disordering of GaAs-AlAs superlattices over a scale of 100 nm occurs at the temperature range used in these experiments [10]. Thus, a more likely mechanism for producing a shift of the quantum well would be the introduction of a small amount, approximately 2 percent, of aluminum. It is also possible that the 'A' peaks originate from the top superlattice well. The apparent blueshift with reduced wire size would then be explained by partial disordering of the top superlattice well superimposed upon a bandgap shrinkage of about 15 meV due to the zinc doping.

In an effort to clarify the origin of these peaks, additional CL spectra were taken at a lower beam energy of 3 keV. The shallower electron penetration depth at this energy should enhance the quantum well emission peak relative to the superlattice peaks SL1 and SL2 and thereby enable us to determine the origin of the 'A' peaks. These spectra, which were measured at 77 K, are plotted in Figure 5.8. For clarity, the spectra are shown over a range which includes only the SL2 and QW peak. The uniform redshift in this figure relative to the spectra in Figures 5.5 and 5.7 is due to the temperature dependence of the

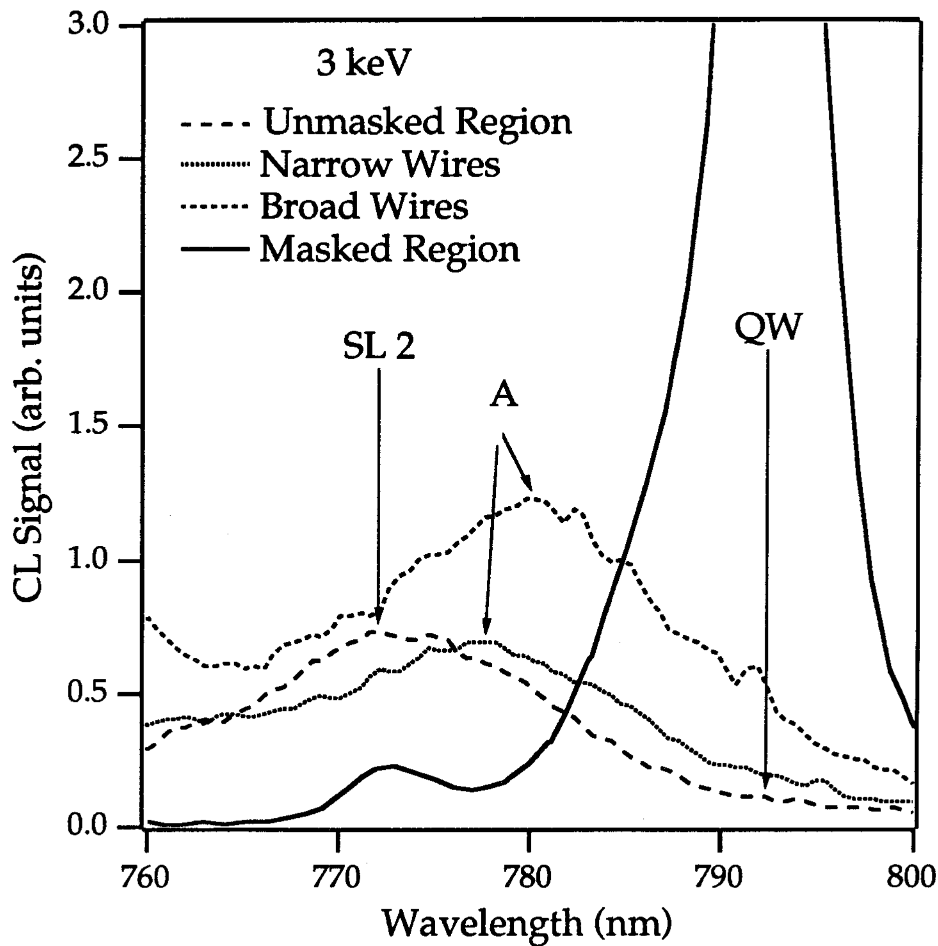

Figure 5.8: Cathodoluminescence spectra of 370 nm wide wire masked region (broad wires), and 310 nm wide wire masked regions (narrow wires). Sample T=77 K. Electron beam energy is 3 keV. Spectra of a uniformly masked region (40μm x 40μm square mask) and an unmasked region are shown as well. For reference, the peak emission wavelength of the quantum well and the top well of the superlattice from the large area mask are indicated with arrows. The 'A' peaks from beneath the wires are discussed in the text.

bandgap of GaAs. The spectrum of the masked region shows a pronounced enhancement of quantum well emission as expected at this energy. The SL1 peak (not shown in the plot) does not appear in the masked spectrum, placing an upper limit of 280 nm on the electron penetration depth at this energy. (Recall that the SL1 peak originates from the bottom well of the superlattice). The spectra from beneath the wires and the unmasked region are of comparable intensity and appear similar to the plots in Figure 5.7. The lack of enhancement of the wire 'A' peaks relative to the SL2 peak in the unmasked spectrum seems to suggest that the wire 'A' peaks originate from the top superlattice well. This determination is not conclusive, however. If the 'A' peaks originate from the quantum well, the volume of the undisordered quantum well material beneath the wires is certainly small, and the zinc impurity concentration high. Both effects would tend to decrease the emission intensity. To distinguish between the two proposed interpretations, it would be necessary to fabricate samples large enough for analysis by cross-sectional transmission electron microscopy. Regardless of the origin of the shifts, it is clear from the CL image, Figure 5.6, that this technique has produced lateral variations in the bandgap on a 100 nanometer scale.

5.4 Conclusions

In conclusion, a technique for selective disordering of GaAs quantum well material to produce 100 nm scale wires has been demonstrated. Silicon diffusion masks as narrow as 120 nm are fabricated using electron beam lithography. Masked samples were diffused with zinc which disordered the quantum well around the masked region and shifted the luminescence peak from the area under it. Spatially and spectrally resolved cathodoluminescence were

presented indicating changes in the bandgap on a 100 nanometer scale. This method could also be useful in creating nanometer-scale waveguides and doping structures.

References

[1] M. B. Stern, H. G. Craighead, P.F. Liao, and P. M. Mankiewich, *Appl. Phys. Lett.* **45**, 410 (1984).

[2] M. A. Reed, R. T. Bate, K. Bradshaw, W. M. Duncan, W. R. Frensley, J. W. Lee, and H. D. Shaw, *J. Vac. Sci. Technol. B* **4**, 358 (1985).

[3] K. Kash, A. Scherer, J. M. Worlock, H. G. Craighead, and M. C. Tamargo, *Appl. Phys. Lett.* **49**, 1043 (1986).

[4] R. L. Kubena, R. J. Joyce, J. W. Ward, H. L. Garvin, F. P. Stratton, and R. G. Brault, *J. Vac. Sci. Technol. B* **6**, 353 (1988).

[5] A. Scherer, H. G. Craighead, M. L. Roukes, and J. P. Harbison, *J. Vac. Sci. Technol. B* **6**, 277 (1988).

[6] J. Cibert, P.M. Petroff, G. J. Dolan, S. J. Pearton, A. C. Gossard, and J. H. English, *Appl. Phys. Lett.* **49**, 1275 (1986).

[7] Y. Hirayama, S. Tarucha, Y. Suzuki, and H. Okamoto, *Physical Review B* **37**, 2774 (1988).

[8] M. D. Camras, N. Holonyak, R. D. Burnham, W. Streifer, D. R. Scifres, T. L. Paoli, and C. Lindstrom, *J. Appl. Phys.* **54** 5637 (1983).

[9] W.D. Laidig, N. Holonyak, M.D. Camras, K.Hess, J.J. Coleman, P.D. Dapkus, and J. Bardeen, *Appl. Phys. Lett.* **38**, 776 (1981).

[10] J. W. Lee and W. D. Laidig, *J. Electron. Mater.* **13** 147 (1984).

[11] Brian Tuck, *J. Phys. D.: Appl. Phys.* **18** 557 (1985).

[12] E. Omura, G.A. Vawter, L. Coldren, and J. L. Mertz *Electron. Lett.* **22** 23 (1986).

[13] T. Hausken, T. C. Huang, K. W. Lee, R. J. Simes, N. Dagli, and L. A. Coldren, *Appl. Phys. Lett.* **53** 728 (1988).

[14] M. E. Hoenk and K. J. Vahala, *Rev. Sci. Instrum.* **60** 226 (1989).

[15] D. B. Darby, P. D. Augustus, G. R. Booker, and D. J. Stirland, *J. Microsc.* **118**, 343 (1980).

[16] H. C. Casey and M. B. Panish, "Heterostructure Lasers," (Academic Press, , San Diego, 1978), p. 150 ff.

Chapter 6

Nonequilibrium vapor phase synthesis of nanometer-scale III-V semiconductor clusters

6.1 Introduction

The challenge of engineering artificial semiconductor structures which exhibit quasi-atomic photonic properties has stimulated a world-wide experimental effort in the last ten years devoted to the fabrication and optical characterization of quantum dots. The effort in the semiconductor device physics community has been characterized by a succession of heroic efforts to extend conventional lithography tools into the nanometer size regime. These efforts have resulted in highly refined lithographic technologies based on electron and focused ion beams, and have led to the development of new concepts such as the use of scanning tunneling microscopes for lithography.

Unfortunately, progress in solving the difficult problem of pattern transfer at the nanometer-scale has lagged behind the impressive achievements in the area of pattern generation. Anisotropic etch techniques such as reactive ion etching create structures with unavoidable surface damage which leads to electrical depletion. Such structures, although useful for quantum transport experiments in which confinement of only one carrier type is necessary, have been singularly unsuccessful in the area of quantum sized structures for photonics applications. Efforts to avoid this surface damage problem by employing selective quantum well disordering, e.g., the selective impurity induced disordering technique described in the last chapter, have been of limited success due to the inherent lack of spatial resolution found in a stochastic diffusion process.

These observations have led our research group to try a very different approach to quantum dot fabrication from the lithographic patterning methods which have previously been applied in this field. In this chapter, we describe a new approach for the *direct* fabrication of nanometer-scale III-V quantum dots by nonequilibrium *vapor phase* synthesis. Our efforts were motivated in part by the success of physical chemists in synthesizing nanometer sized II-VI semiconductor crystallites by "arrested precipitation" in glasses and in solution [1], which exhibit distinctive quantum size effects in optical absorption spectra. The chief drawback of these chemical synthesis routes is that the clusters are typically produced in colloidal form or embedded in highly dissimilar host materials such as silica glasses. As a result, if the clusters exhibit luminescence, it results from surface traps rather than from intrinsic interband transitions.

Recently reported syntheses of nanometer-scale GaAs clusters, though representing important steps forward, have not provided entirely satisfactory results. Using organometallic

solution phase chemistry, Olshavsky *et al.* [2] and Uchida *et al.* [3] have grown GaAs clusters which appear in transmission electron microscopy (TEM) and x-ray diffraction to be of good crystalline quality. However, elemental analysis of the particles reveals a significant incorporation of nitrogen and carbon and nonstoichiometric abundances of Ga and As. Additionally, molecular species mask the optical properties of the clusters produced by this method [3]. A different approach has been employed by Sandroff *et al.* [4], who have grown nanometer-scale GaAs particles on high surface area silica using molecular beam epitaxy (MBE). The MBE technique produces particles which are stoichiometric and crystalline. However, the particle shapes produced by this method are highly nonuniform, implying severe inhomogeneous broadening of their optical transition energies. Furthermore, the influence of the silica substrate on the cluster properties is unknown, leading to potential complications in the interpretation of optical data.

The direct fabrication of nanometer-scale III-V quantum dots by nonequilibrium *vapor phase* synthesis has several intrinsic advantages over other techniques, including guaranteed high chemical purity, a free cluster surface which is available for subsequent growths of epitaxial passivation layers, and facility of size classification. However, vapor phase synthesis is technically challenging from the standpoints of both stoichiometry and crystallinity. At low temperatures, defect mobilities are low and the formation of crystalline clusters is difficult. At the higher temperatures conventionally employed in GaAs epitaxy, the differential between the partial pressures of Ga and As is large and stoichiometry is not preserved [5].

Two related approaches will be described which circumvent these problems. In the first technique, by explosively vaporizing "wires" of highly doped GaAs or other III-V semiconductors in an inert atmosphere, e.g., Ar or He, a non-equilibrium vapor is generated which

homogeneously condenses to form stoichiometric, crystalline clusters. Electron micrographs and diffraction measurements are presented which show the clusters to be faceted micro-crystallites in the 10 nm size range with a zincblende structure. The optical extinction of a colloidal suspension of GaAs clusters differs substantially from that of bulk material in a manner consistent with a quantum confinement effect. In the second technique, GaAs clusters are produced by homogeneous nucleation from a nonequilibrium vapor produced by pulsed laser ablation from a GaAs target. The problem of passivating the surfaces of these clusters so as to create optically active quantum dots with a low surface carrier recombination rate is yet to be solved; however, the vapor phase nature of the techniques presented here should facilitate the epitaxial growth of a passivating surface layer. The issue of passivation is addressed in more detail in the next chapter.

6.2 Cluster sources

6.2.1 The exploding wire cluster source

We have developed a technique for producing stoichiometric, crystalline III-V semiconductor clusters from a non-equilibrium vapor generated by the explosive vaporization of bulk semiconductor wires. Our apparatus is adapted from those used to study the exploding wire phenomenon [6]. Shown in Fig. 6.1 is a schematic diagram of our apparatus.

The wires, typically $0.2 \times 0.2 \times 10\text{mm}^3$, are made from $\langle 100 \rangle$ oriented n - doped GaAs wafers using standard photolithography and etch techniques. Alternatively, $\langle 100 \rangle$ wafers of GaAs or other semiconductors are lapped to the desired thickness and cleaved into thin filaments. Ohmic contacts are made at the ends of the wire by applying In with a soldering iron. The wire is then soldered into its holder using a Ga/In eutectic solder. The holder

Exploding Wire Cluster Source

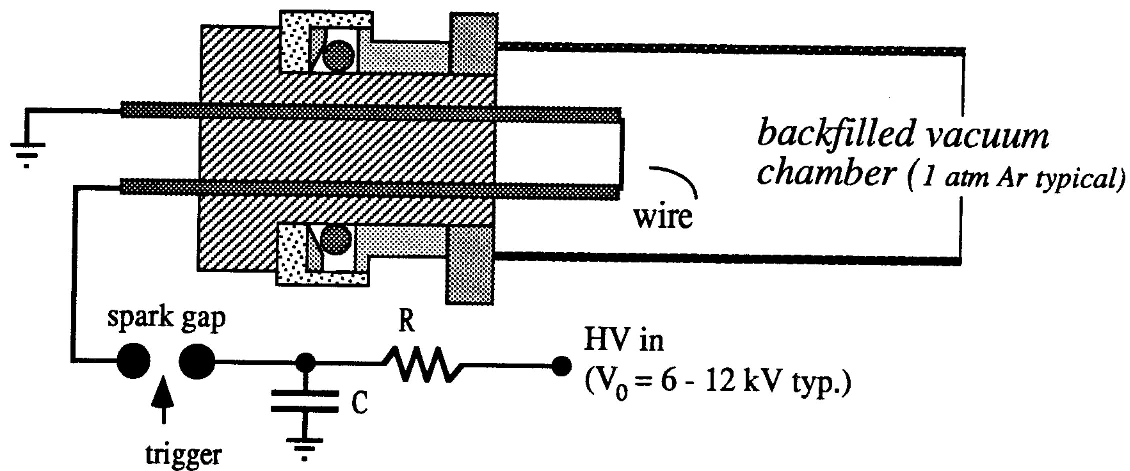

Figure 6.1: Schematic diagram of the exploding wire apparatus. By discharging the capacitor through the semiconductor wire, e.g., a wire of GaAs, a stoichiometric vapor, e.g., of Ga and As, is produced which subsequently nucleates to form crystalline clusters. Typically V is 6 - 12 kV and C = 1 μ F. The stored energy corresponds to approximately 100 eV/atom. The explosion is performed in a vacuum chamber back filled with high purity argon or helium.

is installed in a vacuum chamber which is evacuated and back-filled with high purity gas (typically 99.999 % Ar) to a pressure of approximately 1 atm. With the capacitor, C, charged to 6 - 12 kV, the spark gap is triggered, completing the circuit and vaporizing the wire. The vaporization is expected to occur in a few tens of nanoseconds [7], a result which we have confirmed by analysis of the IV characteristic of the exploding wire measured with a digital sampling oscilloscope. The total energy stored in the capacitor corresponds to roughly 100 eV per atom in the wire. Though not all this energy is dissipated directly into the wire, it appears that sufficient energy is deposited to cause complete vaporization. The details of aerosol formation by exploding wires is not completely understood [8]. However, it is plausible that the background gas quenches the vapor and induces the homogeneous cluster nucleation before vapor-solid equilibrium is established. While explosions of GaAs in inert gases such as argon and helium produce clusters with the zincblende structure, we have found that clusters produced in H_2 do not.

An analysis of GaAs particles produced under typical explosion conditions (capacitor charged to 6 kV with a background gas of Ar at 1 atmosphere pressure) shows that the size distribution is approximately log-normal with a mean cluster diameter of 8.3 nm and a standard deviation of 40 %. The most probable cluster size is 6 nm. We have not directly measured the amount of recoverable aerosol, though under similar experimental conditions, recovery efficiencies exceeding 80 % have been reported [9]. Taking these numbers as typical, we estimate that approximately 10^{15} clusters are produced per wire explosion.

A transmission electron micrograph of the GaAs clusters is shown in Figure 6.2. The particles are collected on a copper electron microscope grid with a holey carbon film by attaching the grid directly to a liquid nitrogen temperature cold finger which inserts into

the vacuum system. Typically, the grid is exposed to the cluster aerosol for 10 minutes. The micrograph, taken near Scherzer focus (first contrast minimum) with 300 kV electrons, clearly shows the atomic order of the clusters. Due to the high density of particles generated by the exploding wire and the small volume of the experimental apparatus, individual clusters agglomerate into long chains, up to several microns in length, on time scales used for particle collection. This has the advantage that the agglomerates will sometimes span holes in the carbon film, permitting the imaging and diffraction measurements on the particles without interference from the carbon background. Within several of the individual particles in the micrograph, atomic rows are easily recognized. The particle shapes are reasonably uniform and roughly spherical. In several places, hexagonal features are readily apparent, suggesting that the cluster growth is not mass transport limited.

The relative orientations of the particles appear to be random, providing strong evidence that particle nucleation occurs on a time scale much shorter than the time scale for agglomeration. The absence of lattice fringes which extend to the particle boundary suggests that a native oxide layer, approximately 1.5 nm thick, surrounds each particle. The formation of an oxide layer is expected since the microscope grid is transfered in air. Figure 6.3 shows the measured interplanar spacings plotted versus bulk interplanar spacings for the GaAs clusters of Figure 6.2. The plot demonstrates that the clusters have the bulk cubic zincblende structure and lattice constant (within the 5% uncertainty of the electron diffraction measurement).

The exploding wire method is readily adapted to the production of nanometer sized clusters of any conductive material which may be obtained in bulk form. We have applied the technique to produce clusters of InAs, GaSb, InP, Si and metals such as Cu and Au.

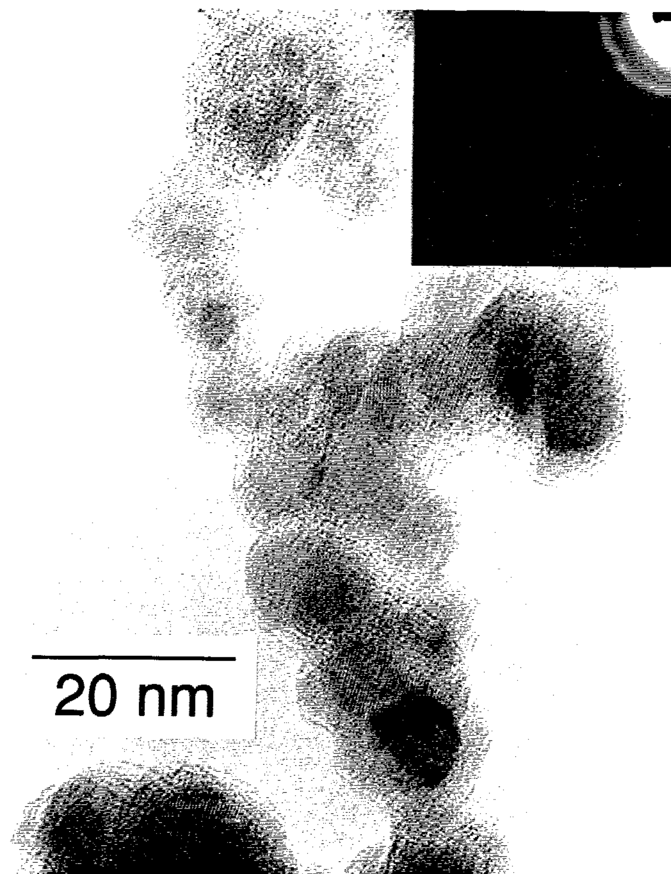

Figure 6.2: A high resolution transmission electron micrograph of GaAs clusters. Due to a high cluster density and small volume of the experimental apparatus, the clusters agglomerate into micron length chains. This has the advantage that the agglomerates may span holes in the carbon film, permitting measurements without interference from the carbon background. Lattice fringes and hexagonal features, suggesting faceting, are apparent. Inset: Electron diffraction pattern which indexes to the zincblende structure.

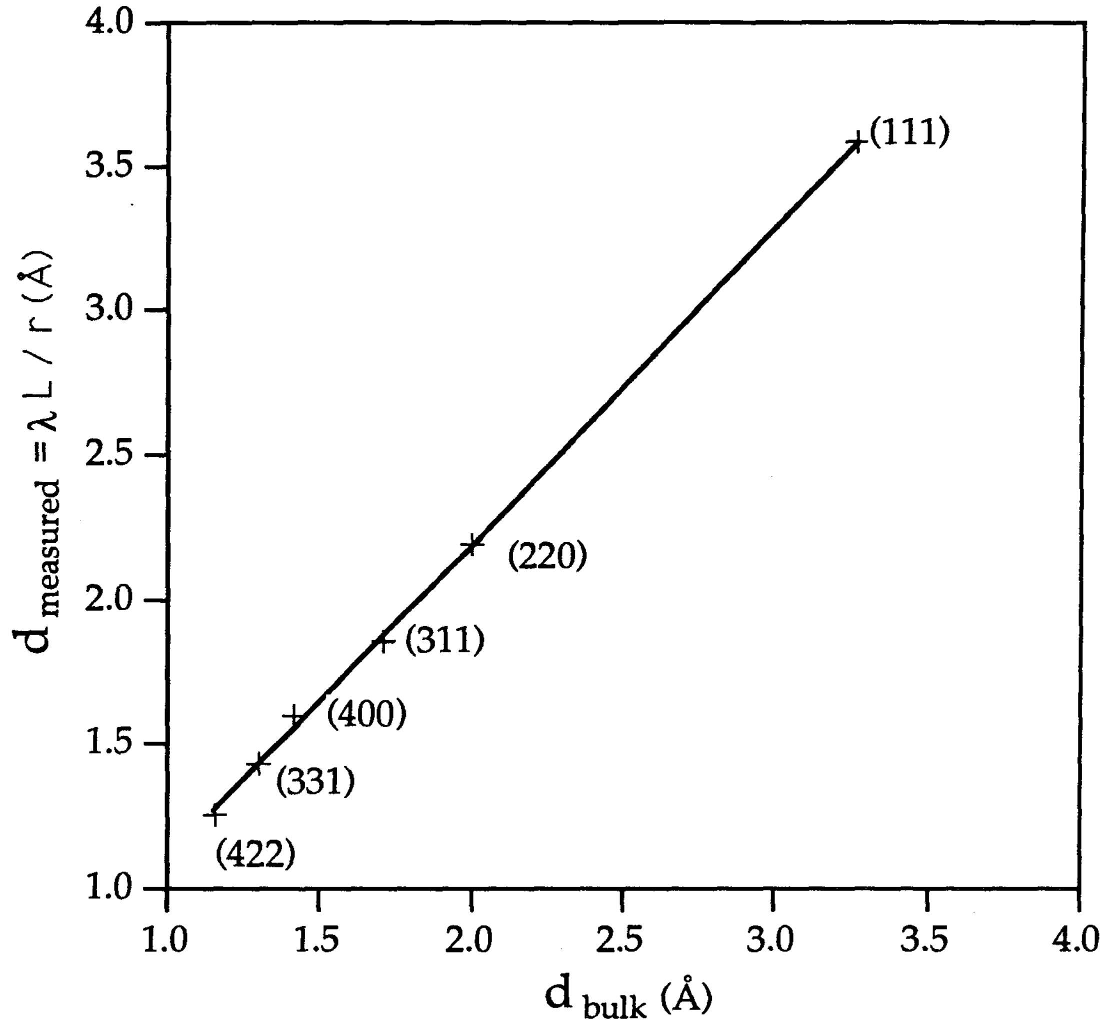

Figure 6.3: Measured interplanar spacings for GaAs clusters shown in Figure 6.2 versus bulk interplanar spacings. Measured values correspond to the ring radii R according to the equation $d_{measured} = \frac{\lambda L}{R}$, where λL is the camera constant. The lattice constant of the GaAs clusters is equal to the bulk value to within experimental uncertainty (5 %).

Figure 6.4 shows a high resolution transmission electron micrograph of an InAs cluster produced by the exploding wire technique. The particle is approximately 20 nm x 30 nm. Lattice fringes are plainly visible and reveal the existence of a grain boundary in the cluster. In general, we rarely observe stacking faults or grain boundaries, and never observe them in clusters smaller than about 10 nm. This observation concurs with that of Sandroff *et al.* who observe stacking faults in GaAs particles in the size regime near 30 nm.

Micrographs of InP clusters generated by exploding InP wires of equal size at different energies in one atmosphere of helium are shown in Figure 6.5. In Figure 6.5(a), the capacitor was charged to 7 kV, while in Figure 6.5(b) the capacitor was charged to 10 kV, thus increasing the energy of the explosion by a factor of two. InP was used for these experiments owing to the relative ease and reproducibility of making ohmic contacts to InP as compared to GaAs. The figure demonstrates that increasing the explosion energy results in a reduction of the mean size of the primary particles produced by the explosion. This phenomenon, which has been observed in the production of aerosols of various metals and metal oxides by the exploding wire technique [10], is presumably due to increased shock wave velocity in higher energy explosions, resulting in more rapid rarefaction of the exploded wire vapor and smaller cluster sizes. In both cases electron diffraction revealed that the clusters possess the bulk zincblende crystal structure.

6.2.2 Clusters formed by pulsed laser ablation

The successful application of the exploding wire method to the synthesis of nanometer-scale, stoichiometric III-V clusters suggests that other techniques which induce rapid vaporization (vaporization on a time scale of 10 to 100 nSec) might be also employed to advantage in

Figure 6.4: A high resolution transmission electron micrograph of an InAs cluster produced by the exploding wire method. A grain boundary is plainly visible.

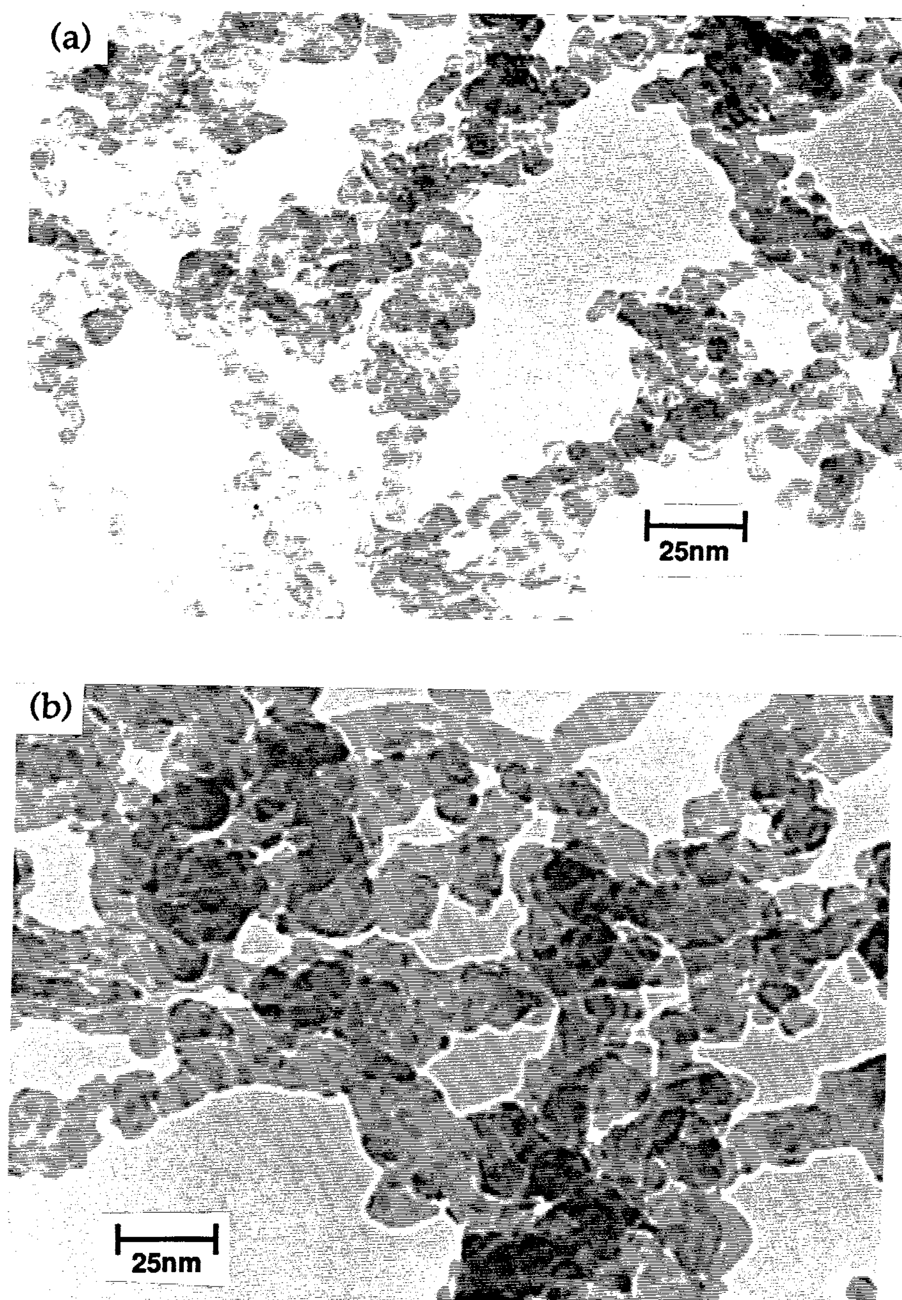

Figure 6.5: Bright field transmission electron micrograph of InP clusters produced by the exploding wire method at two different explosion energies. Increasing the energy of the explosion reduces the mean particle size. The discharge voltage is 7 kV and 10 kV in (a) and (b), respectively. Clusters were produced in one atm. of helium.

synthesis of stoichiometric III-V clusters. Laser ablation is commonly used as a non-thermal evaporation source for compound materials such as high-Tc superconductors, where the preservation of bulk stoichiometry is important. In these applications, laser ablation is done in vacuum or near-vacuum conditions. We have done preliminary experiments with laser ablation of bulk GaAs in a one atmosphere argon ambient. In our experiment, a pulsed, frequency doubled Nd:YAG laser was used to ablate material from a GaAs target mounted in a vacuum chamber back filled with high purity argon gas (99.999 % purity). Clusters are produced by homogeneous nucleation from the plume of ablated material. We believe that the hot plume intersects the ambient gas, which serves to confine and cool the vapor in much the same fashion as in the exploding wire method, inducing homogeneous nucleation of stoichiometric clusters.

The apparatus used in our experiment is shown in Figure 6.6. A portable vacuum chamber was constructed using standard quick-flange components and was equipped with an optical grade quartz window, a target mounting fixture, and a cryogenic feedthrough for cluster collection. The ablation target was a ⟨100⟩ GaAs substrate. A copper TEM grid coated with a holey carbon film was mounted inside the chamber on the cryogenic collection fixture. The chamber was pumped out and purged with argon several times and finally filled with one atmosphere of high purity argon gas. The valve was then closed and the chamber was detached from the vacuum pump - gas fill apparatus and transported to the laser facility which was situated in another laboratory.

The flash lamp pumped Nd:YAG laser was operated with a KDP frequency doubling crystal and produced 120 mJ pulses at 532 nm with a spot area of 10 mm^2 and a repetition frequency of 10 hz. A total of 300 shots were delivered to the target. We estimate the total

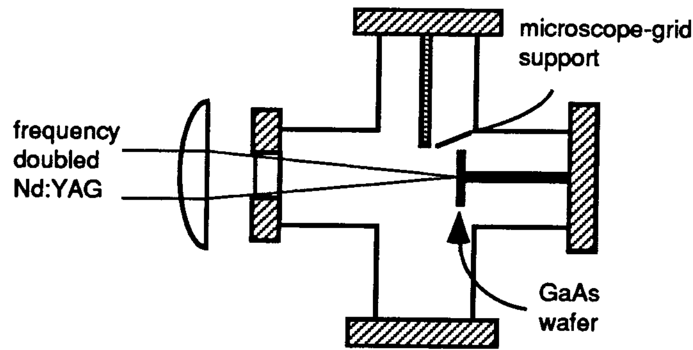

Figure 6.6: Apparatus used for laser ablation experiment. A pulsed, frequency doubled Nd:YAG laser is used to ablate material from a GaAs target in 1 atm. of high purity Argon gas. Clusters are collected thermophoretically on a copper TEM grid coated with a holey carbon.

volume of ablated GaAs to be approximately 0.3 mm^3 based upon an assumed ablation layer thickness of 100 nm per shot. Note that this is approximately the same volume of material as a single wire used in the exploding wire experiment. Clusters were collected by thermophoretic deposition onto the collection fixture which was cooled to liquid nitrogen temperature prior to beginning the laser ablation. We find that laser ablation produces particles in the same size regime as that of the exploding wire, though with a qualitatively broader distribution of cluster sizes. A bright field transmission electron micrograph of the collected clusters is shown in Figure 6.7. The bottom of Figure 6.7 shows an electron diffraction pattern of the clusters which indexes to the bulk zincblende structure of GaAs (Figure 6.8).

The technique of producing nanometer-scale clusters by pulsed laser ablation has a number of significant advantages over other cluster synthesis techniques such as the exploding

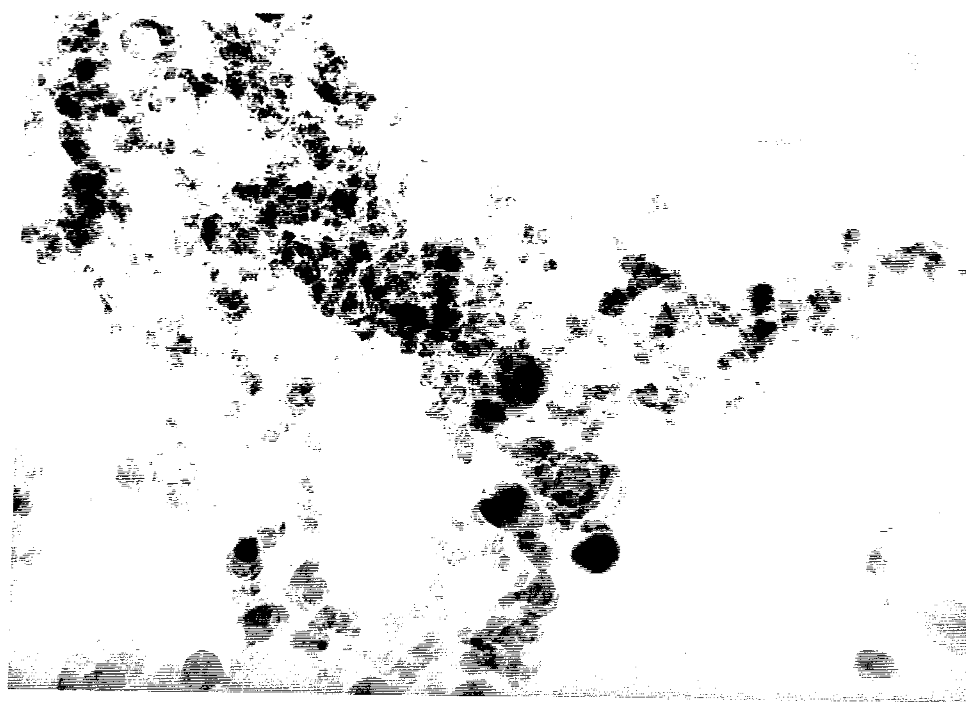

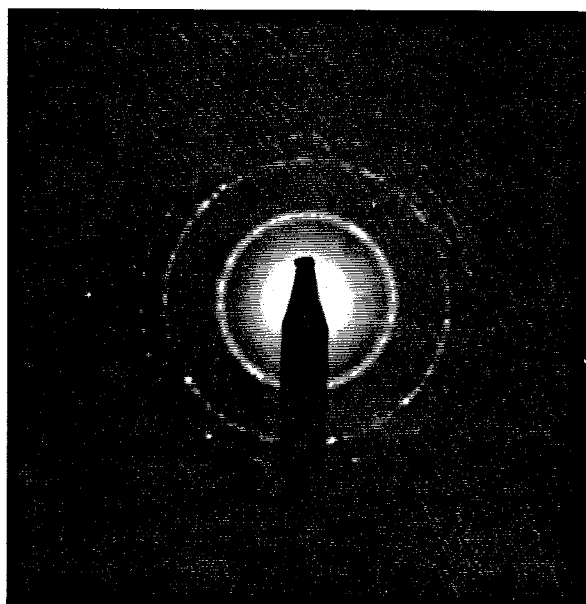

Figure 6.7: Bright field transmission electron micrograph of GaAs cluster produced by pulsed laser ablation. Bottom: Electron diffraction pattern.

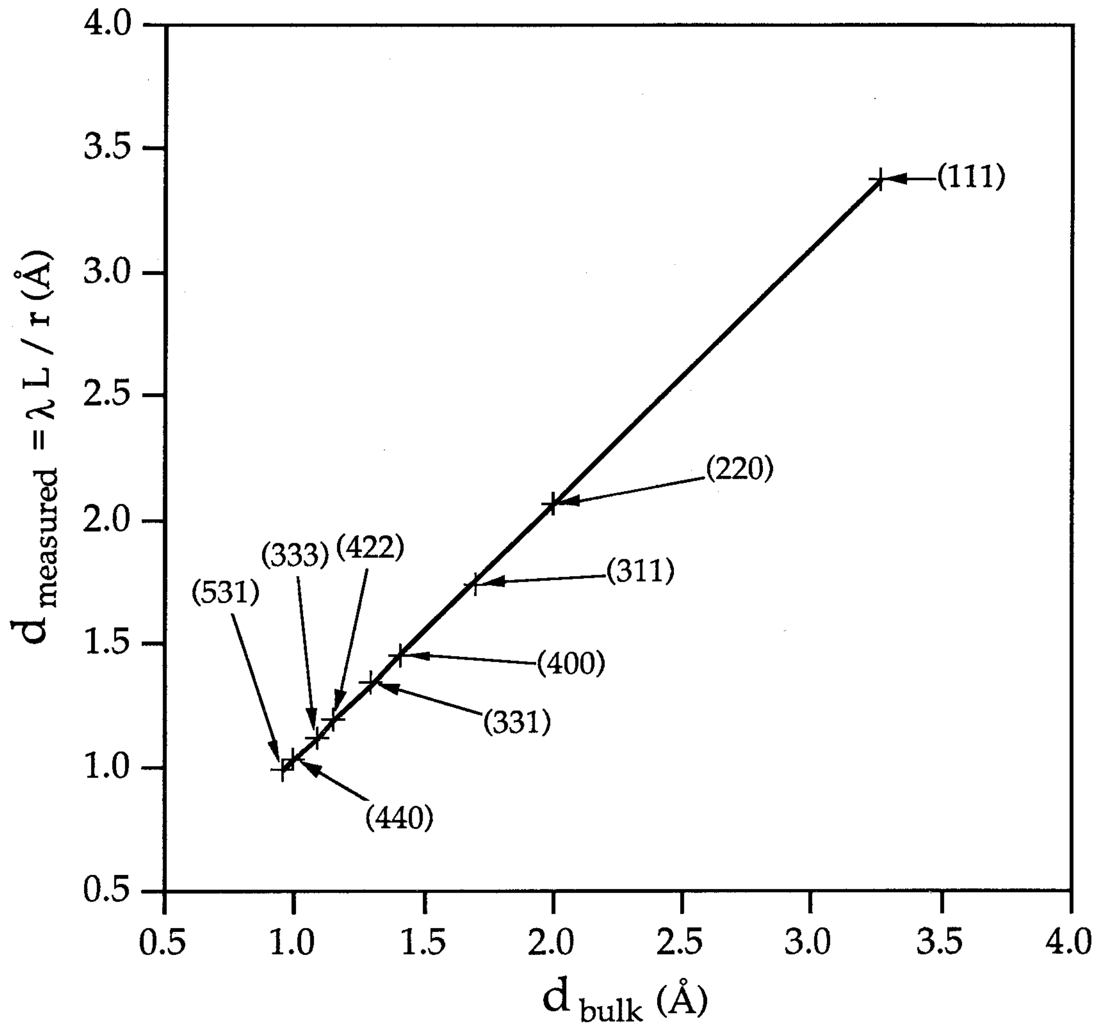

Figure 6.8: Measured interplanar spacings for GaAs clusters shown in Figure 6.7 versus bulk interplanar spacings. Measured values correspond to the ring radii R according to the equation $d_{\text{measured}} = \frac{\lambda L}{R}$, where λL is the camera constant. The lattice constant of the GaAs clusters is equal to the bulk value to within experimental uncertainty (5 %).

wire method. The most important advantage is the flexibility of target materials inherent in the method. Many interesting materials that cannot yet be obtained in bulk ingot or wafer form, such as ternary or quaternary alloy semiconductors, and many of the II-VI semiconductors, are readily obtained as epitaxially grown films. These films, if grown thicker than the ablation depth of the laser, would make suitable pulsed laser ablation targets. Additionally, there are many wide gap semiconductors and insulators which are not readily doped, making application of the exploding wire technique, which requires conducting filaments of material, difficult or impossible. Pulsed laser ablation would be the method of choice to investigate quantum size phenomena in such systems. Another advantage of pulsed laser ablation over the exploding wire method is that cluster production may be done in an on-line, semi-continuous fashion. The major disadvantage of the technique is the requirement of a high cost, high power pulsed laser source. The experiment described here employed a borrowed laser system; the technique has to date not been pursued further because of the cost of obtaining a dedicated laser system.

6.3 Optical characterization of GaAs clusters

Optical extinction measurements on GaAs clusters produced by the exploding wire method described above are strongly suggestive of quantum confinement effects. The clusters are collected for these measurements by entraining them in a flow of Ar saturated with iso-propyl alcohol vapor and then concentrating the flow onto a cooled collector, producing a cluster colloid which is sufficiently dense for measurements with a commercial spectrophotometer. The measured extinction for a GaAs cluster sample produced by the exploding wire technique is shown in Figure 6.9.

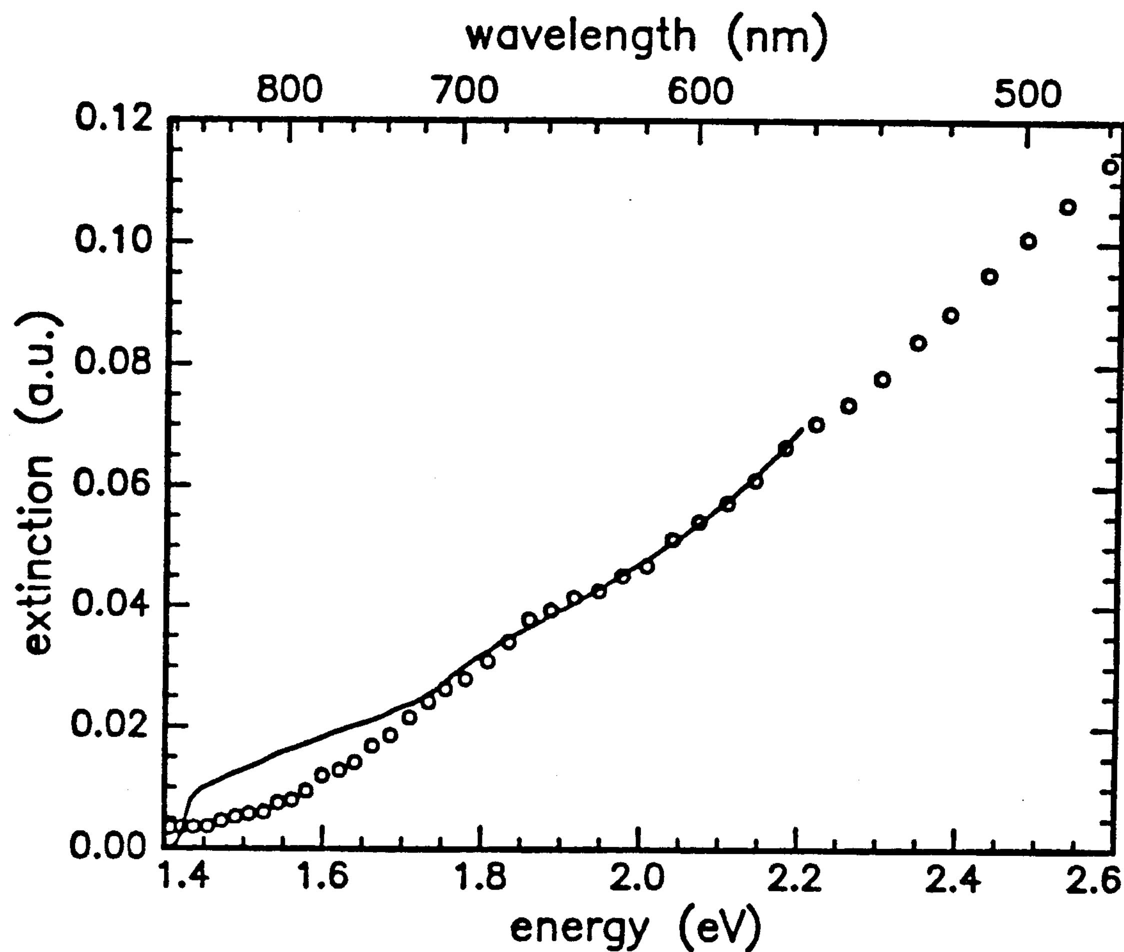

Figure 6.9: The measured optical extinction of a colloidal suspension of GaAs particles produced by the exploding wire technique (-o-). The absorption efficiency of bulk GaAs (—), showing the rise in optical absorption at the bulk band gap at 1.42 eV, is included for comparison. The absorption of the GaAs clusters rises slowly, with no measureable feature at the bulk band gap, and is suggestive of quantum confinement effects. A slight feature in the cluster absorption curve is apparent at 1.9 eV.

For comparision, the bulk absorption coefficient of GaAs is also plotted. The optical extinction of the clusters rises gradually with increasing photon energy with the only remarkable feature being a broad rise in absorption near 1.9 eV, with inflection points at 1.8 and 2.0 eV. The spectrum shown was taken within 10 minutes of the wire explosion. Over a period of an hour, the extinction spectrum loses even this slight feature and scattering increases, presumably due to continued coagulation of clusters in the colloid. For clusters whose radius, $R << \lambda$ where λ is the wavelength of light, Q_{ext}, the optical extinction efficiency, [11] is given by

$$Q_{ext} = -8\pi R/\lambda \, \mathrm{Im}[(m^2 - 1)/(m^2 + 2)]$$
$$\approx 12\alpha n R/(n^2 + 2)^2, \tag{6.1}$$

where $\alpha = 4\pi k/\lambda$ is the bulk absorption coefficient, and n and k are the real and imaginary parts of the complex refractive index, $m = n - ik$. In deriving (6.1), it is assumed that $k << n$. For GaAs, $m = 3.64 - i\,0.079$ at a photon energy of 1.5 eV ($\lambda = 827$ nm) [12]. Since n varies by less than 5 % over the range of Fig. 6.9, to a good approximation the extinction efficiency of the clusters, Q_{ext}, should be proportional to α, provided the dielectric response of clusters and bulk are identical. Conversely, one may conclude that the observed difference between the cluster and bulk data of Fig. 6.9, notably the absence of an abrupt step at the bulk band edge (1.42 eV), implies that the cluster and bulk dielectric response are not the same. The measurement suggests that the absorption edge in the clusters is shifted to higher energy, which is consistent with the qualitative behavior expected for quantum size effects. Furthermore, the position of the 1.9 eV feature is consistent with the confinement energy expected for GaAs clusters in the 5 - 10 nm size range [1,13]. Although

sharp spectral features are expected for a monodisperse cluster sample, a distribution of particle sizes tends to broaden them since the exact position of the spectral feature depends strongly on the particle size. Thus, while definitive measurements on quantum confinement in these systems will require more refined experimental technique, our results suggest that quantum confinement effects are indeed playing a role in the optical properties of these systems.

The absorption spectrum of Fig. 6.9 shares some common qualitative features with the absorption spectrum reported by Sandroff *et al.* [4], who noted a smooth increase in absorption without a sharp onset at the bulk bandgap. However, presumably because of the broad size and shape distribution in that sample, and also possibly uncharacterized interaction with the supporting silica, no features attributable to quantum size effects were observed. On the other hand, Olshavsky *et al.* [2] and Uchida *et al.* [3] report a sharp peak in cluster absorbance near 500 nm which is due to the presence of a molecular species in the colloid rather than the GaAs clusters themselves [3].

6.4 Conclusion

In conclusion, we have demonstrated for the first time the vapor phase synthesis of crystalline nanometer-scale clusters of GaAs and other III-V semiconductors including InAs, InP and GaSb. The exploding wire method relies on the rapid condensation of a non-equilibrium vapor (containing equal numbers of group III and group V atoms) produced by the explosive vaporization of a semiconductor wire in an inert atmosphere (argon or helium). Electron microscopy and diffraction show that the cluster sizes fall well within the quantum size regime and that they are crystalline with the bulk zincblende crystal structure. Pulsed

laser ablation from GaAs targets in an inert gas has also been shown to result in the formation of nanometer-scale, zincblende clusters. The success of these two techniques, combined with optical measurements which are suggestive of quantum confinement effects, imply that a major technological hurdle in the vapor phase synthesis of semiconductor quantum dots has been overcome.

Further work toward characterizing the influences of parameters such as gas pressure, explosion/ablation energy, and vaporization time scale on aspects of cluster production such as size distribution and crystallinity will no doubt be required if the technique is to mature into a viable quantum dot synthesis technology. Additionally, the clusters produced by the exploding wire method and by pulsed laser ablation have free, unpassivated surfaces and have not exhibited photoluminescence. However, among the most important advantages of vapor phase synthesis is that the surfaces of the clusters are undamaged and accessible. A next important step toward producing light emission from semiconductor clusters is to reduce non-radiative carrier recombination at the cluster surface by coating the cluster surface with epitaxial passivating overlayers.

References

[1] M. G. Bawendi, M. L. Steigerwald, and L. E. Brus, *Annu Rev. Phys. Chem.* **41**, 477 (1990), and references therein.

[2] M. A. Olshavsky, A. N. Goldstein, and A. P. Alivisatos, *J. Am. Chem. Soc.* **112**, 9438 (1990).

[3] Hiroyuki Uchida, Calvin J. Curtis, and Arthur J. Nozik, *J. Phys. Chem.* **95**, 5382 (1991).

[4] C.J. Sandroff, J. P. Harbison, R. Ramesh, M. J. Andrejco, M. S. Hedge, D. M. Hwang, C. C. Chang, E. M. Vogel, *Science* **245**, 391 (1989).

[5] Gerald B. Stringfellow, "Organometallic Vapor-phase Epitaxy" (Academic Press, San Diego, 1989) Chapter 3.

[6] W. G. Chace, "Exploding Wires," edited by W. G. Chace and H. K. Moore (Plenum Press, New York, 1959), pp. 7-14.

[7] R. J. Reithel, J. H. Blackburn, G. E. Seay, and S. Skolnick, "Exploding Wires" edited by W. G. Chace and H. K. Moore (Plenum Press, New York, 1959), pp. 19-32.

[8] T. Vijayan and V. K. Rohatgi, *J. Appl. Phys.* **63**, 2576 (1988).

[9] F. G. Karioris and B. R. Fish, *J. Col. Sci.*, **17**, 155 (1962).

[10] F. G. Karioris, B. R. Fish, and G.W. Royster,Jr. "Exploding Wires" edited by W. G. Chace and H. K. Moore (Plenum Press, New York, 1962), pp. 299-311.

[11] H. C. van de Hulst, "Light Scattering by Small Particles," (Dover, New York, 1981), p. 66 ff.

[12] D. D. Sell, H. C. Casey, and K. W. Wecht, *J. Appl. Phys* **45**, 2650 (1974).

[13] K. J. Vahala and P. C. Sercel, *Phys. Rev. Lett.* **65**, 239 (1990).

Chapter 7

Nanometer-Scale GaAs Clusters from Organometallic Precursors

"The surface was invented by the devil." — Wolfgang Pauli

7.1 Introduction

In the last chapter, a new vapor phase synthesis technique was demonstrated for producing nanometer-scale clusters of GaAs and other III-V semiconductors. The success of the exploding wire method in producing structures in the quantum size regime is particularly notable considering the simplicity of the process. However, while the clusters produced by this method exhibit quantum size effects in optical absorption, they show no detectable luminescence under conditions of photoexcitation or electron beam excitation. This is not surprising considering the tremendous surface to volume ratio in a nanometer sized cluster. It has been observed that a ⟨100⟩ surface of GaAs with submonolayer oxide coverage has

a surface density of mid-bandgap traps on the order of $10^{12}cm^{-2}$ [1], and that even GaAs surfaces freshly prepared by molecular beam epitaxy in an ultra high vacuum environment exhibit mid-bandgap surface Fermi level pinning [2]. These surface trap states, which arise from unsaturated bonds at the crystal surface, have the undesirable property that they act as efficient nonradiative carrier recombination centers. Thus a bare GaAs cluster is not expected to luminesce under photoexcitation.

One way to avoid the nonradiative loss of excited carriers at the surface of a GaAs cluster is to prevent the carriers from "seeing" the surface. In principle, an excellent way to accomplish this is to epitaxially grow a wider bandgap semiconductor barrier layer on the cluster surface. The ternary alloy semiconductor $Al_xGa_{1-x}As$ is an ideal candidate for such a surface passivation layer because the lattice mismatch with GaAs is minimal over the whole range of aluminum mole fraction, and the technology for epitaxial growth of $Al_xGa_{1-x}As$ from gaseous precursors is well developed. In addition, it has long been suspected that homogeneous nucleation of GaAs occurs in GaAs OMVPE due to the reduction in the efficiency of the overall growth reaction with increasing temperature above approximately 700 ° C.

We have therefore constructed a novel hot wall OMVPE reactor with two goals in mind. The first is the synthesis of nanometer-scale GaAs clusters by homogeneous nucleation from volatile organometallic and hydride precursors. The second is the epitaxial growth of a passivating layer of $Al_xGa_{1-x}As$ on the surfaces of these clusters to produce optically active quantum dots. The process is shown schematically in Figure 7.1.

We have determined conditions under which nearly defect free, 10-20 nm scale GaAs microcrystallites form. These particles are in the quantum size regime which suggests

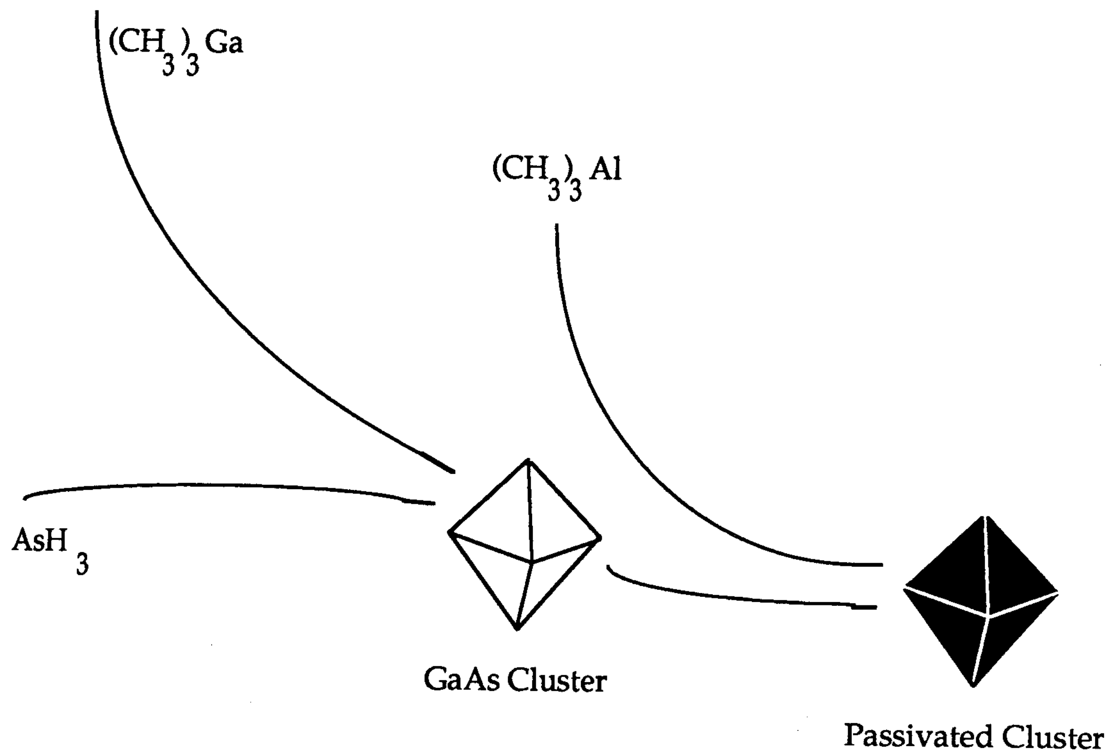

Figure 7.1: Conceptual schematic of gas-phase synthesis of passivated nanometer-scale GaAs clusters from organometallic precursors. Trimethyl gallium and arsine react homogeneously to produce nanometer scale GaAs clusters. Subsequent vapor phase growth of a passivating layer of AlAs or $Al_xGa_{1-x}As$ on the cluster surface occurs by reaction of trimethyl aluminum and arsine.

that the process may be used to form optically active quantum dots [3]. Thus gas-phase homogeneous nucleation in OMVPE, which has been regarded as a troublesome parasitic reaction until now, may ultimately form the basis of an aerosol technology for the fabrication of novel optoelectronic devices such as a quantum dot laser [4]. In this chapter, the design and results of this experiment will be described. We will conclude by discussing progress made so far on the ultimate goal of passivation by vapor phase epitaxial growth of an $Al_xGa_{1-x}As$ layer on the GaAs clusters.

7.2 Reactor design

7.2.1 Process configuration

The aerosol particle reactor is designed to produce GaAs clusters by homogenous nucleation from gaseous precursors and subsequently to passivate the clusters by vapor phase epitaxial growth of $Al_xGa_{1-x}As$ on the cluster surfaces. The growth nutrients used in the process are trimethyl gallium (TMG), trimethyl aluminum (TMA), and arsine (AsH_3). These precursors are carried in hydrogen gas and introduced into a horizontal, hot wall quartz process tube where the gas is heated. Reactant pyrolysis and subsequent gas-phase reactions occur, producing the GaAs clusters. The actual process tube configuration has evolved as the experiment has progressed. As a result, detailed discussion of the tube geometry will vary according to the particular experiment under discussion.

The piping and instrumentation diagram corresponding to the present reactor configuration is shown in Figure 7.2. In this configuration, the process tube is heated by a multizone tube furnace. The tube consists of three main sections. Zone 1 is the GaAs cluster nucleation zone into which a mixture of TMG and arsine in hydrogen are injected. Clusters

formed by homogeneous nucleation in this zone flow into zone 3, the passivation zone. TMA, TMG and arsine are introduced into the main process tube at this point through the heated injector, zone 2. Particles flow into zone 5 and are collected thermophoretically on a demountable fixture. Zone 4 is used to inject hydrogen to dilute the cluster aerosol so as to prevent gas phase agglomeration.

The gas injection system utilizes precision mass flow controllers (MFC) for the two TMG sources, the TMA source, and the arsine, hydrogen, and nitrogen sources. The organometallics are introduced into the reactor by bubbling hydrogen through liquid source material. Pneumatic control valves for these gases are interlocked through a relay board to prevent unsafe operation and to handle abort conditions. The reactor is controlled by a programmable controller located on the control panel on the front of the reactor. The piping and instrumentation diagram for the reactor, shown in Figure 7.2, will illustrate the complexity of the process and the need for computer control.

7.2.2 Safety issues and reactor construction

Each of the materials used in the OMVPE process has significant hazards. Hydrogen is an inflammable gas, while the organometallics are pyrophoric liquids at room temperature. The most dangerous substance used is arsine, which is a potent hemolytic toxin. Brief exposure to as little as 10 parts per million of arsine is deadly, and the safe occupational exposure limit is 50 parts per billion [5]. The design of an OMVPE reactor must incorporate features to prevent the possibility of operator exposure to these chemical hazards. To ensure that the design of our reactor conformed to state-of-the-art industrial safety practices, we contracted with Caleb Corporation (Torrance, California) to design and construct

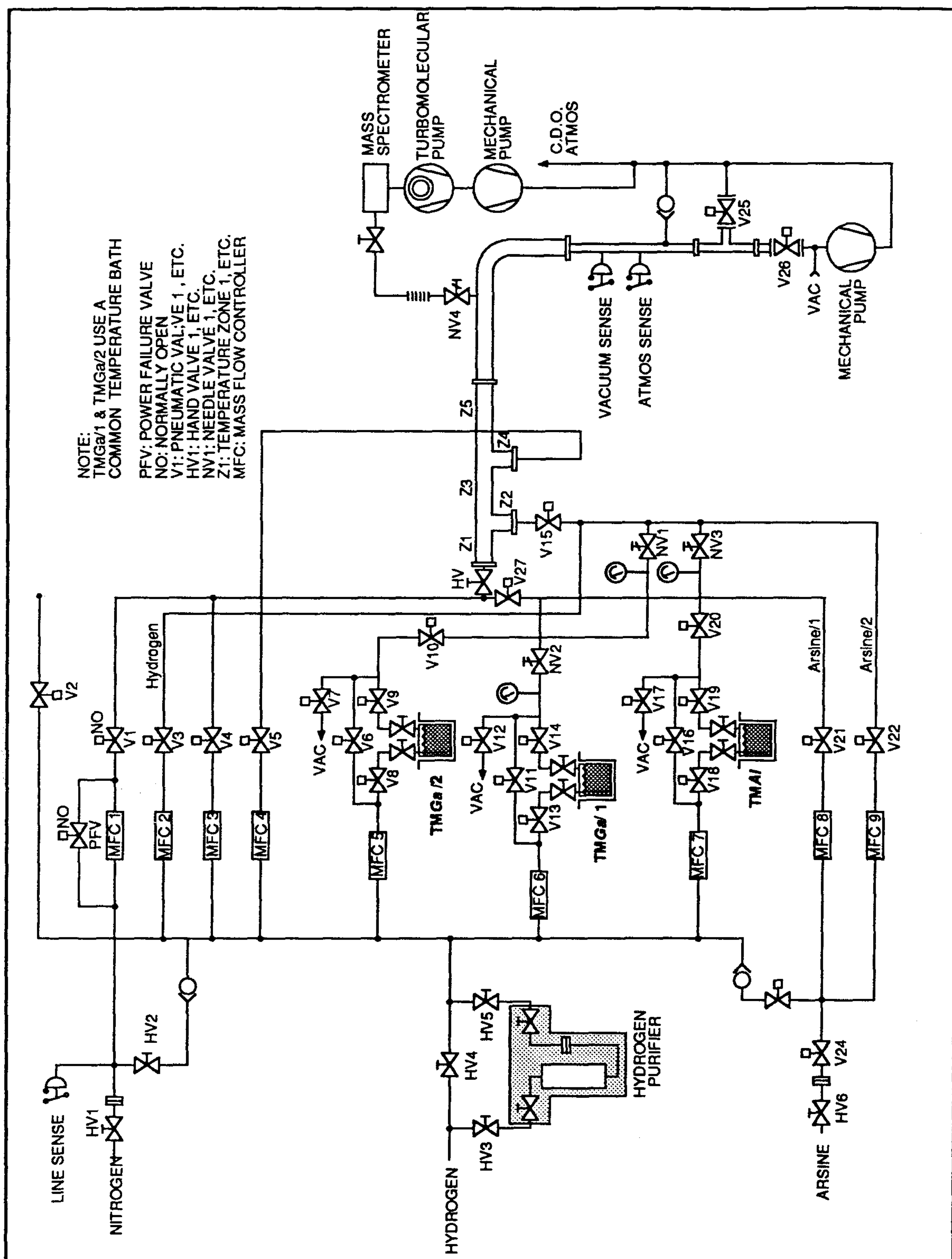

Figure 7.2: Plumbing diagram of OMVPE reactor used for gas-phase synthesis of nanometer-scale GaAs clusters.

the ventilated reactor enclosure, gas source cabinet, failsafe relay safety interlock system, and pneumatic valve control system. The actual process tube and gas mixing manifolds were designed and constructed at Caltech. The reactor is located at the arsine qualified Microdevices Laboratory located at the Jet Propulsion Laboratory in Pasadena.

The primary hazardous gas containment system in the reactor is the process tube itself, along with associated gas feed and exhaust lines. All gas lines are 316L stainless steel tubing with weld joints and VCR connections. The hydrogen and 10 % arsine gas cylinders are located in a separate gas bunker and are connected to the reactor via coaxial gas lines with a counter flow of nitrogen purge gas in the line jackets. All valves are Nupro BN series bellows sealed valves. Quartz components comprising the process tube have all been annealed for 24 hours at 700°C to relieve stress. Glass/metal seals utilize viton O-rings and Ultra-Torr fittings. KF fittings with viton O-rings are utilized in the exhaust system and elsewhere in the process cabinet. The second line of protection is the vented, enclosed, process cabinet, gas cabinet, and vacuum pump area. The reactor is equipped with local combustible gas sensors interlocked to the relay control board to shut off the flow of all hazardous gases in the event of a breech of the process tube. Additionally, sampling tubes leading to a toxic gas monitor are located at several points both inside the reactor and in the laboratory space around the reactor. This monitor is interlocked to shut off the flow of all hazardous gases in the laboratory building and to trigger evacuation alarms in the event of detection of arsine at a level of 20 parts per billion. Exhaust gas from the reactor is treated in a controlled decomposition and oxidation unit (CDO) and passes through a wet chemical scrubber before being exhausted to the outside air.

7.3 Synthesis of nanometer-scale GaAs clusters from organometallic precursors

We report the first direct observation of gas-phase homogeneous nucleation of GaAs by the thermophoretic collection of an aerosol of nanometer-scale microcrystallite GaAs clusters in an atmospheric organometallic vapor-phase epitaxy (OMVPE) reactor. In addition to shedding light on a fundamental question about the reaction kinetics involved in OMVPE, this is the first report of gas-phase synthesis of nanometer-scale III/V clusters from volatile precursor molecules. We have determined conditions under which 10-20 nm scale GaAs microcrystallites form. Thus, gas-phase homogeneous nucleation in OMVPE, which has been regarded in the past as a troublesome parasitic reaction [6,7], may be useful for the fabrication of quantum size regime structures.

A simplified schematic of the reactor configuration used in these experiments is depicted in Figure 7.3. Note that this configuration is different from that shown in Figure 7.2, which represents the present state of the reactor and is designed for $Al_xGa_{1-x}As$ passivation experiments to be described in Section 6.5. In Figure 7.3, a 34 mm diameter, 700 mm long quartz process tube is mounted in a multizone furnace. TMG was introduced by bubbling hydrogen through a liquid source held at -10 ° C. Heated injectors (Z1, Z2) permit TMG and 10 % AsH_3 in hydrogen to be introduced into the process tube separately, allowing for the possibility of precracking the precursor molecules. Alternatively, the reactants can be mixed prior to injection by rerouting the arsine flow as shown in Figure 7.3. The nucleation zone, Z3, is 18 cm long. Aerosol particles are collected thermophoretically on a holey carbon film which is mounted on a stainless steel fixture aligned coaxially in the collection zone,

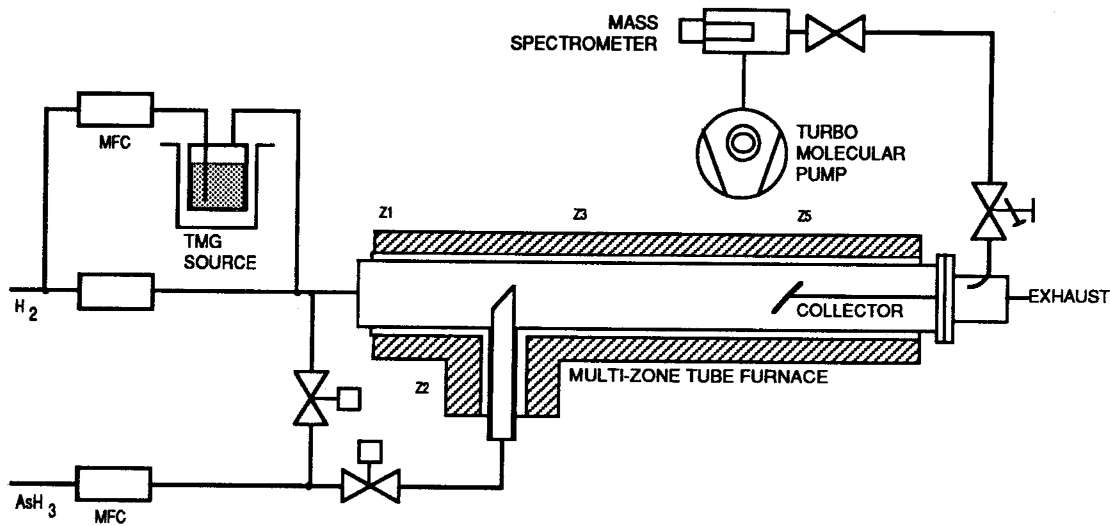

Figure 7.3: Schematic of the experimental apparatus for gas-phase synthesis of nanometer-scale GaAs clusters. The group III precursor (TMG) is introduced into the hot wall reactor by bubbling H_2 carrier gas through a liquid source. The group V precursor, AsH_3, can be mixed with the TMG outside the furnace (at room temperature) or inside the furnace (at elevated temperature). All flows are regulated by mass flow controllers (MFC's). The process runs at atmospheric pressure. A quadrupole mass spectrometer connected to the exhaust of the process tube by a sampling line is used to monitor reactant concentrations.

Z5, of the process tube (Fig. 7.3). Z5 is held at a temperature of 350°C in all experiments to prevent the condensation of arsenic on the collection apparatus. Hydrogen, purified with a resin filter, is used as the carrier gas. The composition of the gas exiting the process tube is monitored with a quadrupole mass spectrometer (QMS).

In a typical experiment the TMG and AsH_3 are preheated to 400°C in Z1 and Z2, respectively, before being introduced into the reaction zone. At this temperature negligible pyrolysis of the TMG or AsH_3 occurs as previously determined by infrared absorption spectroscopy and mass spectroscopic analysis [8,9]. This is verified by negligible decreases in the arsine partial pressure and no CH_4 partial pressure detected on the QMS. The total flow is 2 SLM, with the partial pressures of TMG and arsine typically 1.25×10^{-4}atm and 6.25×10^{-3} atm, respectively. For these flow conditions, the residence time in the reaction zone (Z3) is 5 seconds.

When the temperature in the nucleation zone (Z3) is held at 700 °C, solid GaAs deposits on the reactor walls within the first 10 cm of the nucleation zone, indicating that the TMG is entirely consumed within approximately 3 seconds of entering Z3. Downstream of this point, in Z5, a semitransparent yellow deposit is observed on the walls of the reactor tube and on the collection fixture. A TEM micrograph of the collected deposit reveals it to consist of individual GaAs microcrystallites and some chain-like agglomerates (Fig. 7.4). The electron diffraction pattern of the particles, shown in the inset of Figure 7.4, indexes to cubic zincblende structure, as shown in Figure 7.5.

Figure 7.6 shows a high resolution transmission electron micrograph (HRTEM) of an agglomerate of smaller primary particles. In practice, HRTEM is easier to perform on the agglomerated clusters than on individual particles, owing to the fact that the agglomerates

Figure 7.4: Bright field transmission electron micrograph of GaAs clusters collected on a holey carbon substrate. The temperature in Z3 was 700°C, the partial pressure of TMG was $1.25\text{x}10^{-4}$atm, the V/III ratio was 50, and the total flow was 2 SLM. Inset: electron diffraction pattern of the clusters. The pattern indexes to zincblende (see Figure 7.5).

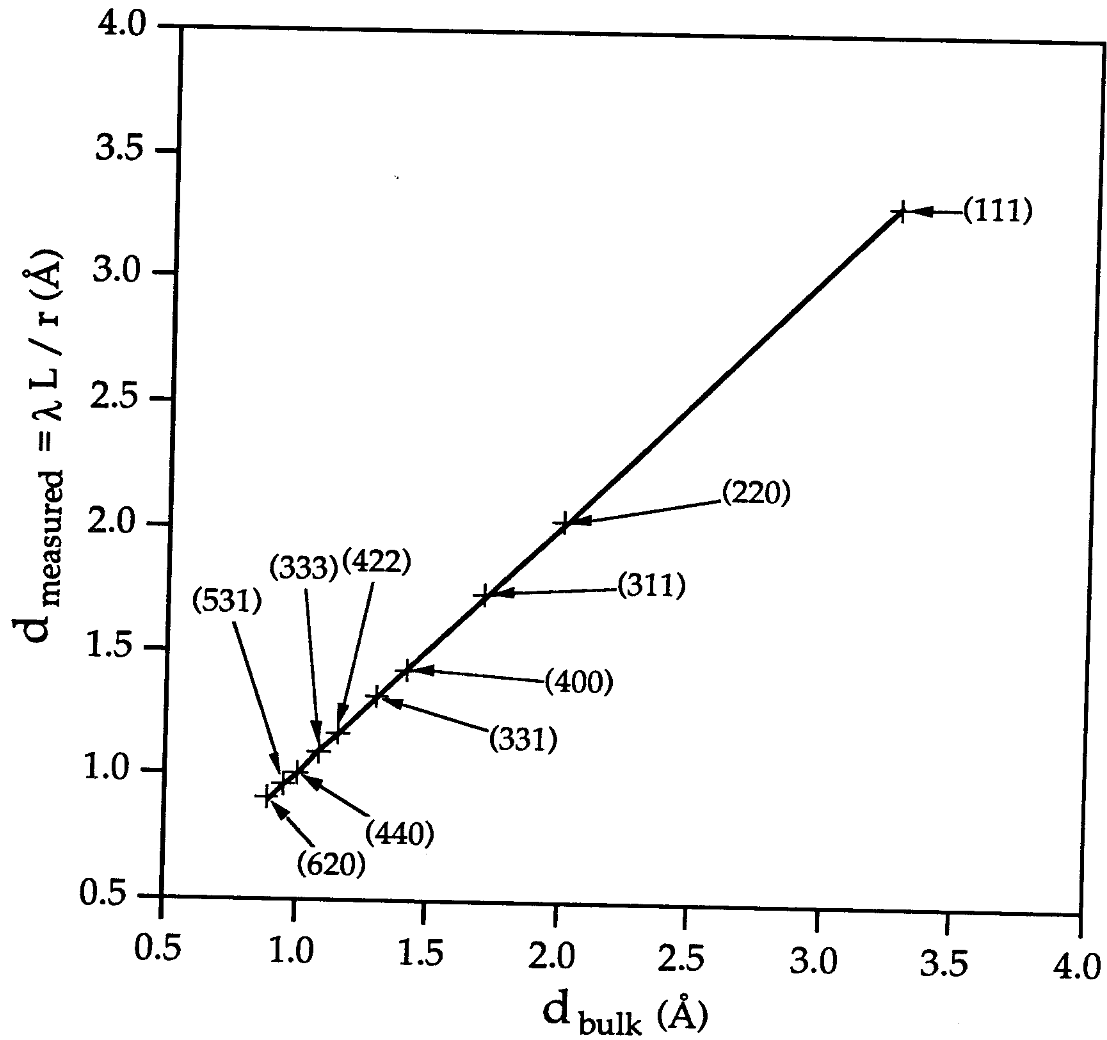

Figure 7.5: Interplanar spacings for GaAs clusters shown in Figure 7.4 versus bulk interplanar spacings. Measured values correspond to the ring radii R according to the equation $d_{\text{measured}} = \frac{\lambda L}{R}$, where λL is the camera constant. The lattice constant of the GaAs clusters is equal to the bulk value to within experimental uncertainty (5 %).

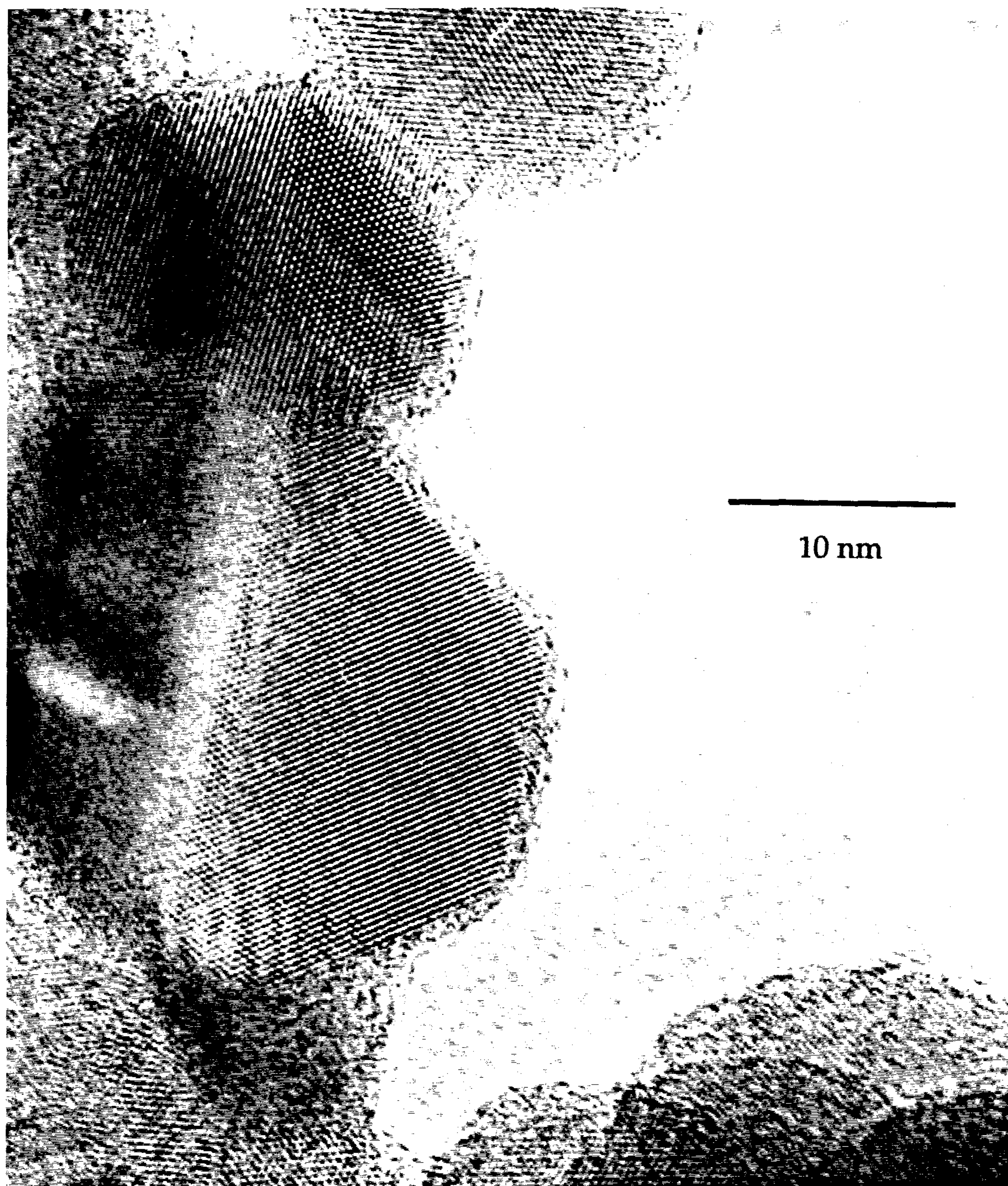

Figure 7.6: High resolution transmission electron micrograph of a chain agglomerate produced under the same conditions as Figure 7.4.

are better able to dissipate excess charge and heat induced by the electron beam than are individual particles. Within several of the clusters shown, lattice fringes and faceting indicative of ⟨111⟩ bounding planes are clearly evident. Some of the crystalline faces have as few as 30 atomic rows. The lattice fringes on the particles extend to within 1 nm of the cluster surface, consistent with the formation of an amorphous oxide layer on the particles on exposure to air.

We have investigated the role of growth temperature and reactant concentration on the nucleation and morphology of the clusters. By analyzing low magnification micrographs, such as Fig. 7.4, we have measured the size distributions of the primary particles for runs at different growth temperatures in the nucleation zone (Z3). We find that the mean particle diameter is strongly influenced by the growth temperature. By fitting the measured particle size distributions to a log-normal distribution, a median particle diameter, $\bar{D}_{pg}$, and geometric standard deviation, σ_g, for the distribution are found. Geometric standard deviations are in the range $\sigma_g = 1.2 - 1.3$. A typical data set and its fit are shown in Figure 7.7. Figure 7.8 shows the behavior of the median crystallite diameter and σ_g as a function of reciprocal temperature. As the temperature in the nucleation zone (Z3) is increased from 600 °C (1000/T = 1.14 K^{-1}) to 800 °C (1000/T = 0.93 K^{-1}), the median particle diameter rises continuously from 12 nm to 19 nm. Doubling the input TMG and AsH_3 concentrations relative to the conditions of Figures 7.4 - 7.5, the mean particle diameter is increased by approximately 10 % with no noticable change in particle morphology. Additionally, we have generated clusters by mixing TMG and arsine both at room temperature and at 400 °C and find no difference in particle morphology.

Several important questions remain regarding the growth mechanism of the primary

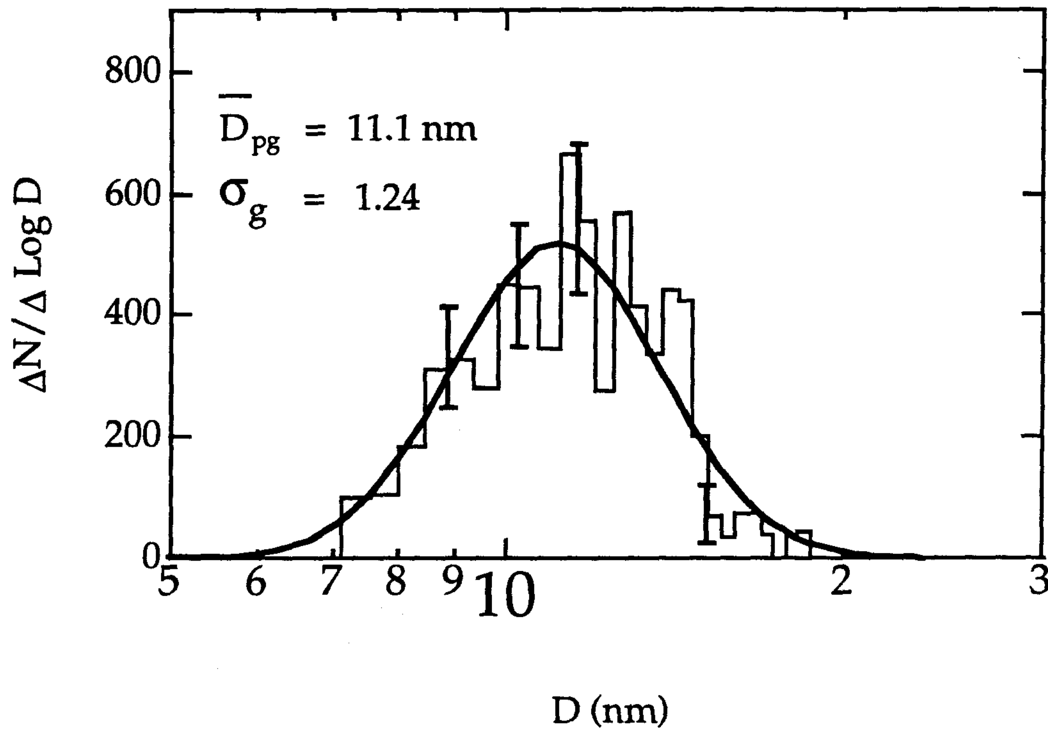

Figure 7.7: Analysis of the size distribution of GaAs clusters produced at a growth temperature 600 ° C, plotted as a histogram $\Delta N/\Delta \mathrm{LogD_p}$ versus D_p, the particle diameter. The solid line is a best fit to a log-normal distribution.

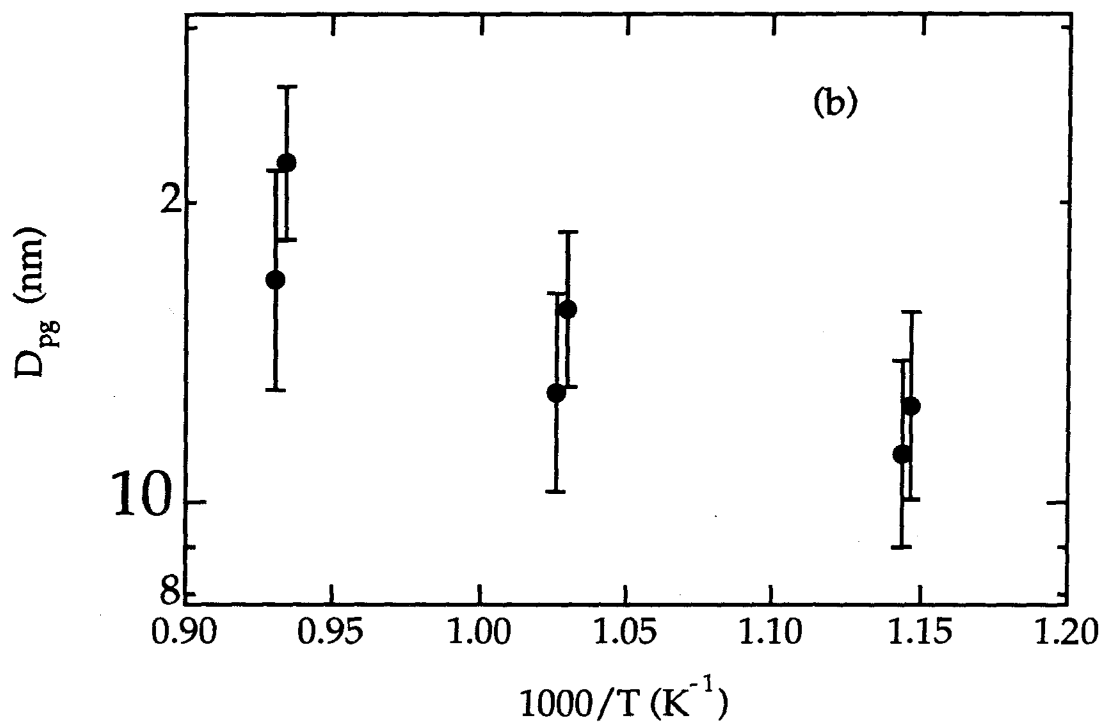

Figure 7.8: Analysis of the size distribution of GaAs clusters produced at various temperatures. Semi-log plot of median particle diameter, $\bar{D}_{pg}$, versus reciprocal temperature. The geometric standard deviation, σ_g, determined for each point is represented on the plot as a vertical bar of height 2 σ_g.

GaAs clusters. Gas-phase infrared absorption measurements showing the presence of TMG–AsH_3 adducts [8], suggest that GaAs may form homogeneously, nucleating $(GaAs)_n$ clusters with n in the range 10 - 20 [10]. This possibility is supported by the observation of GaAs clusters in the 2-50 atom size range produced in a supersonic beam by pulsed laser ablation from a GaAs target [11]. These clusters may then increase to the 10 nm size range by coagulation. Subsequent grain boundary migration through the sintered particle may consolidate the agglomerate into the single crystal, faceted clusters seen in Figures 7.4 - 7.5. Alternatively, further growth to the observed sizes in the 10 nm range may proceed by epitaxial deposition from the supersaturated vapor phase. Since the microscopic crystal planes of the clusters are much smaller than surface diffusion lengths, adsorbed Ga and As atoms can diffuse to fast growing crystal planes, leaving the cluster bounded by slow growth planes as observed in Figure 7.6 [12]. With the present data, it is impossible to distinguish between these two mechanisms, although the particle size distributions are somewhat narrower than would be expected if coagulation were the dominant growth mechanism ($\sigma_g \approx 1.46$) [13]. It is also possible that GaAs cluster growth occurs through a two step process by the reaction of nanometer-scale droplets of Ga or poly-monomethyl gallium polymer with the AsH_3 ambient.

To investigate the possibility of the latter reaction mechanism, a set of experiments was performed in which TMG was precracked at 600 °C to induce the formation of nanometer-scale Ga droplets *prior* to reaction with AsH_3. Pyrolysis of TMG at a temperature of 600 °C leads to the formation of an aerosol of Ga droplets which leaves a diffuse white film on the walls of the TMG precracking zone (Z1 in Figure 7.3). Monomethyl-gallium polymer, which would result in black wall deposits [14], is not observed at these temperatures, indicating

complete reaction to elemental gallium. Samples of the gallium aerosol (formed with no arsine present) were collected as before and examined by TEM. Figure 7.9, which shows a bright field image of the collected particles, shows that Ga droplets in the size range from 10 to 100 nm are formed in this manner. The larger particles probably resulted from Brownian coagulation of the aerosol in transit from Z1 to the collection zone. Next, AsH_3 preheated to 400 °C was injected into the Ga aerosol and the mixture subsequently introduced into the reaction zone held at 700 °C.

A positive test for growth mediated by Ga droplet formation would consist of the observation of GaAs clusters of the same morphology as in the previous runs. However, the bright field micrograph of the collected particles, Figure 7.10, shows that this is not the case. The particles are elongated, and irregular in shape in contrast to Figures 7.4 and 7.6. Although the median particle size was roughly 50 nm, some particles in the 10 nm range were observed. The electron diffraction pattern is consistent with cubic zincblende structure. The whisker morphology seen in some of the clusters is indicative of the vapor-liquid-solid growth mode [15], entirely different from the observed cluster morphology in Figs. 7.4 and 7.6. This suggests that the GaAs cluster growth described in the previous experiment is not mediated by Ga droplet formation.

7.4 Passivation experiments

The results described in the last section provide encouragement that the ultimate goal of producing passivated GaAs clusters is achievable. In particular, the observation that the GaAs clusters are bounded by slow growth planes is consistent with a growth mechanism involving vapor phase condensation on smaller nucleii to produce the observed cluster sizes

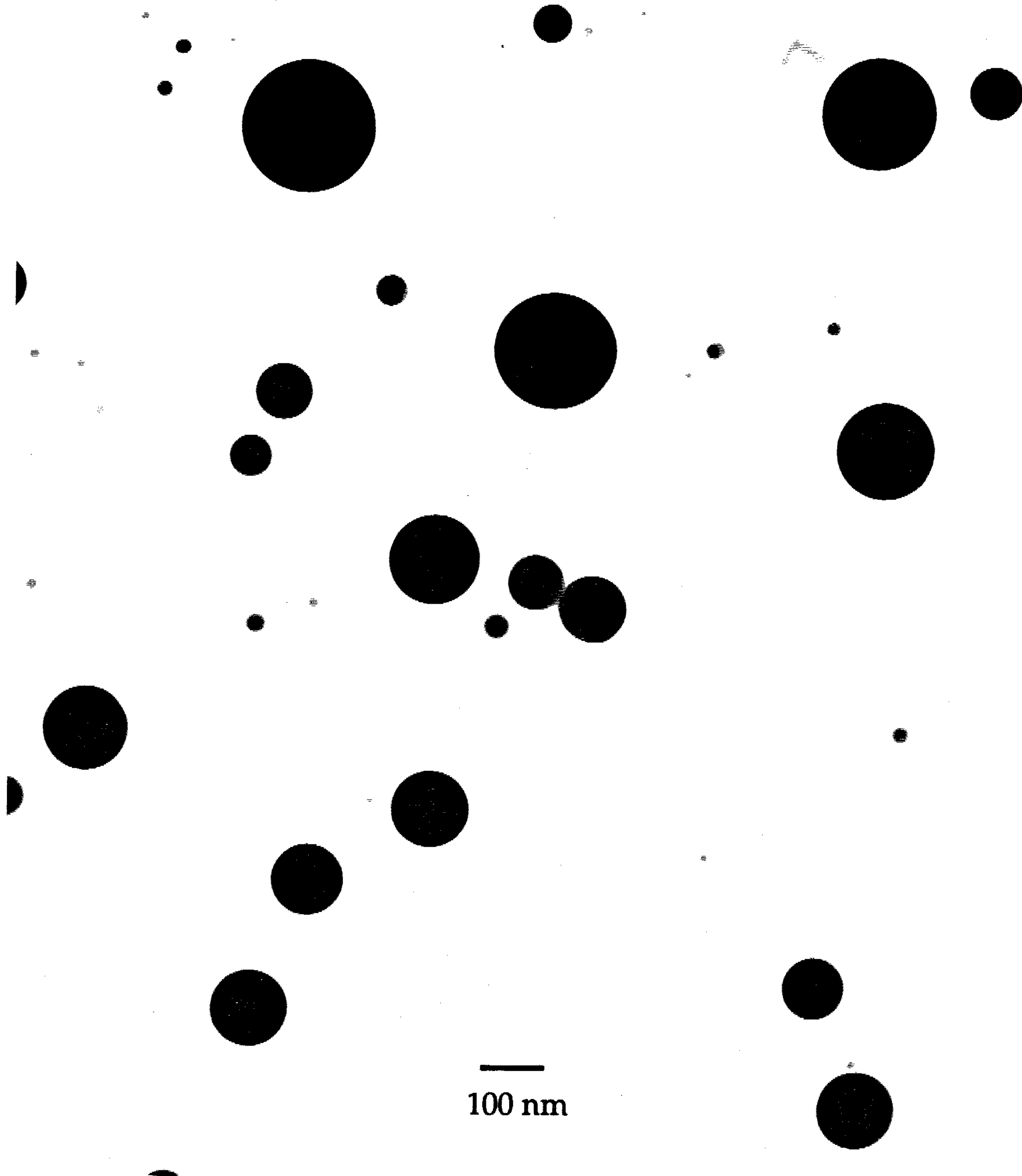

Figure 7.9: Bright field transmission electron micrograph of Ga droplets produced by pyrolysis of TMG at 600 ° C, collected on a holey carbon substrate.

Figure 7.10: Bright field transmission electron micrograph of GaAs clusters produced by reaction of nanometer-scale Ga droplets with arsine. Ga droplets were produced by pryrolysis of TMG (cracking temperature 600 ° C). The reaction with arsine was performed at a temperature of 700 ° C in Z3.

of 10-20 nm. This interpretation was supported by the analysis of cluster size distributions. By changing the composition of the reactant vapor, it should thus be possible to grow an epitaxial $Al_xGa_{1-x}As$ passivating layer on the surfaces of the clusters.

To implement this concept, we have had to significantly modify the reactor from its original configuration. In its original form, the reactor had two separate process zones. The front process zone was to have been used for GaAs cluster nucleation, while the second zone was to have been used for the passivation experiments. In between these two zones we intended to install an electrostatic particle mobility classifier to enable the selection of a mono-sized aerosol for subsequent passivation. Unfortunately, it was discovered early on in the experiment that the temperature drop of the gas stream upon exiting from the front process zone was sufficient to induce the homogeneous nucleation of arsenic clusters. The extremely dense arsenic aerosol produced renders subsequent mobility classification and passivation of the GaAs clusters impossible. As a result, a multizone, single process tube design has been implemented for both GaAs cluster nucleation and passivation. Figure 7.2 shows the piping and instrumentation diagram of the reactor in its new configuration which implements these changes. For greater clarity, Figure 7.11 shows a drawing of the new process tube.

The tube consists of three main sections. Zone 1 is the GaAs cluster nucleation zone into which a mixture of TMG and arsine in hydrogen are injected. Clusters formed by homogeneous nucleation in this zone flow into zone 3, the passivation zone. TMA, TMG and arsine are introduced into the main process tube at this point through the heated injector, zone 2. Particles flow into zone 5 and are collected thermophoretically on a demountable fixture. Zone 4 is used to inject hydrogen to dilute the cluster aerosol so as to prevent gas

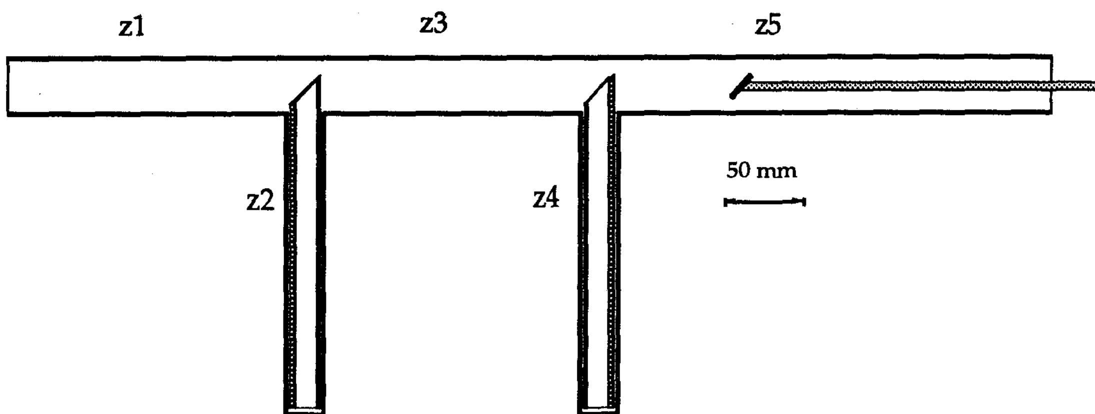

Figure 7.11: Drawing of OMVPE reactor process tube used for passivation experiments. In this configuration, zone 1 (z1) is used for GaAs cluster nucleation, and zone 2 (z2) is used to inject TMA into the passivation zone (z3). Zone 4 (z4) is used to inject diluent hydrogen to prevent aerosol particle agglomeration. Zone 5 (z5) is the collection zone where particles are collected thermophoretically.

phase agglomeration.

We have performed preliminary passivation experiments using the new reactor configuration. Reactant concentrations and flow velocities in the nucleation zone were identical to those used in the nucleation experiments in the last section, and the nucleation zone temperature was held at 650 °C. TMA, TMG and AsH_3 were introduced into the passivation zone in concentrations expected to lead to a passivation layer of composition $Al_{0.3}Ga_{0.7}As$ and thickness 3 nm, if all of the material was incorporated into the growing clusters. The temperature in the passivation zone was varied between 750 °C and 800 °C, consistent with common practice in $Al_xGa_{1-x}As$ growth by OMVPE. Unfortunately, under these conditions, the collected clusters contained no aluminum as determined by energy dispersive x-ray analysis. The $Al_xGa_{1-x}As$ appears to have deposited on the injector wall, rather than creating an epitaxial layer on the GaAs "seed" clusters. In an attempt to prevent deposition of the $Al_xGa_{1-x}As$ on the walls of the injector, we have performed experiments in which arsine and TMA are injected into the reactor separately. Arsine is injected into zone 1, and TMA and TMG are injected through zone 2. Under these conditions, the $Al_xGa_{1-x}As$ homogeneously nucleates to form clusters. The presence of aluminum in the clusters was verified by energy dispersive x-ray analysis. Further study will doubtless be required to determine conditions under which an $Al_xGa_{1-x}As$ passivating layer can be grown on the surfaces of GaAs seed clusters without homogeneous nucleation of uniform $Al_xGa_{1-x}As$ clusters.

7.5 Conclusions

The present aerosol technique has several significant advantages over previous methods for producing nanometer-scale GaAs clusters. For example, synthesis in quinoline solution produces GaAs clusters with significant impurities and unequal Ga and As abundances [16,17], while GaAs MBE on silica substrates produces irregular particles in intimate contact with a foreign substrate [18]. Synthesis of nanometer-scale GaAs clusters by homogeneous nucleation from an exploding wire vapor has been recently demonstrated [19]. However, the process described here is more readily compatible with the incorporation of the GaAs clusters in a passivating medium of AlGaAs, both in the aerosol phase [20] and ultimately in a growing epitaxial structure.

References

[1] T. E. Kazior, J. Lagowski, and H. C. Gatos, *J. Appl. Phys.* **54**, 2533 (1983).

[2] T.T. Chiang and W.E. Spicer, *J. Vac. Sci. Technol. A* **7**, 724 (1989).

[3] L.E. Brus, *J. Chem. Phys.* **80**, 4403 (1984).

[4] Kerry J. Vahala, *IEEE J. Quantum Electron.*, **QE-24**, 523 (1988).

[5] John Doull, Curtis Klaassen, and Mary O. Amdur, "Toxicology," (Macmillan, New York, 1980), p. 437 ff.

[6] G. B. Stringfellow, *J. Crystal Growth* **68**, 111 (1984).

[7] M.R. Leys and H. Veenvliet, *J. Crystal Growth* **55**, 145 (1981).

[8] J. Nishizawa and T. Kurabayashi, *J. Electrochem. Soc.* **130**, 413 (1983).

[9] M. Yoshida, H, Watanabe, and F. Uesugi, *J. Electrochem. Soc.* **132**, 677 (1985).

[10] Y. Takahashi, T. Soga, S. Sakai, M. Umeno, and S. Hattori, *Japan. J. Appl. Phys.* **23**, 709 (1984).

[11] C. Jin, K. J. Taylor, J. Conceicao, and R. E. Smalley, *Chem. Phys. Lett.*, **175**, 17 (1990).

[12] S. Hersee, E. Barbier, and R. Blondeau, *J. Crystal Growth* **77**, 310 (1986).

[13] James D. Landgrebe and Sotiris E. Pratsinis, *Ind. Eng. Chem. Res.* **28**, 1474 (1989).

[14] C. A. Larson, N. I. Buchan, and G. B. Stringfellow, *Appl. Phys. Lett.* **52**, 480 (1988).

[15] Gerald B. Stringfellow "Organometallic Vapor Phase Epitaxy," p. 85 (Academic Press, San Diego, 1989).

[16] M.A. Olshavsky, A.N. Goldstein, and A. P. Alivisatos, *J. Am. Chem. Soc.* **112**, 9438 (1990).

[17] Hiroyuki Uchida, Calvin J, Curtis, and Arthur Nozik, *J. Phys. Chem.* **95**, 5382 (1991).

[18] C. J. Sandroff, J.P. Harbison, R. Ramesh, M. J. Andrejco, M.S. Hedge, D. M. Huang, C.C. Chang, and E. M. Vogel, *Science*, **245** 391 (1989).

[19] Winston A. Saunders, Peter C. Sercel, Harry A. Atwater, Kerry J. Vahala, and Richard C. Flagan, *Appl. Phys. Lett.* **60**, 950 (1992).

[20] Peter C. Sercel, Winston A. Saunders, Kerry J. Vahala, Harry A. Atwater, and Richard C. Flagan, to appear in *Appl. Phys. Lett.*